Evaluation and Design of Wicking Geotextile for Pavement Applications

By

Jun Guo

Submitted to the graduate degree program in Civil, Environmental, and Architectural Engineering and the Graduate Faculty of the University of Kansas in partial fulfillment of the requirements for the degree of Doctor of Philosophy.

_____

Dr. Jie Han, Chairperson

_____

Dr. So-Min Cheong

_____

Dr. Robert L. Parsons

_____

Dr. Steven D. Schrock

_____

Dr. C. Bryan Young

Date Defended: 08/24/2017

The Thesis Committee for Jun Guo

certifies that this is the approved version of the following thesis:

Evaluation and Design of Wicking Geotextile for Pavement Applications

_____

Dr. Jie Han, Chairperson

Date Approved:

Abstract

Geotextiles are often included in roadway structures as substituting drainage layers for gravel or sand drainage layers. When water infiltrates through pavements and enters base courses, it increases water content of base courses with fines, which leads to a decrease in base resilient modulus and accelerates development of deformation and eventually shortens the pavement structure service life. A geotextile allows free water to flow in the geotextile in its plane direction more easily than through its surrounding geomaterial. Thus, the geotextile placed at the interface between the base course and the subgrade shortens the drainage path and accelerates the drainage rate in a pavement structure. However, conventional geotextiles can only provide drainage for free water (i.e., water that flows under action of gravity). In unsaturated soils, suction (also called capillary force) between soil particles holds water and conventional geotextiles cannot provide drainage to capillary water within base courses.

A new type of geotextile, wicking geotextile, was recently developed to remove water from soil via capillary action or suction. This wicking geotextile includes special deep-groove fibers in the cross-machine direction of the geotextile. The hydrophilic and hygroscopic deep-groove fibers can induce high capillary force to "wick" water out from unsaturated soil. Few case studies have shown the wicking geotextile could maintain or reduce the water content of the base course after compaction. However, the effectiveness of wicking geotextile depends on many factors which have not been fully evaluated. Currently, there is no design method or guideline available to incorporate the water content reduction benefit of the wicking geotextile.

A series of laboratory tests, including demonstration tests, water removal tests, small box tests, and soil column tests, were conducted in this study to investigate the hydraulic characteristics of the wicking geotextile when in contact with free water and/or soil. Six large-scale cyclic plate loading tests with rainfall simulation were conducted to evaluate the effect of the wicking geotextile on the permanent deformations of base courses over weak subgrade. Based on the test results, the mechanisms of the wicking geotextile in removing water from base courses were investigated. The small box tests, the soil column tests, and the large-scale cyclic plate loading tests provided relationships between base course water content and drainage time. Design guidelines that incorporate the water content reduction benefit of the wicking geotextile were developed by modifying the 1993 AASHTO Pavement Design Guide and the Mechanistic-Empirical Pavement Design Guide.

Acknowledgement

First of all, I would like to express my sincere gratitude to my advisor and mentor, Prof. Jie Han. His guidance, support, and encouragement that extended beyond the field of academic have helped me make it through nearly every difficult moment. I have learned much from his knowledge and wisdom in the past seven years when I studied under him, and my learning will continue. It has been a great pleasure and privilege to be one of Prof. Han's students.

I would like to thank my Ph.D. committee members, Profs. Robert L. Parsons, Steven D. Schrock, Bryan Young, and So-Min Cheong for their valuable advice and encouragement. I would like to extend my gratitude to Profs. Bruce McEnroe, Joshua Roundy, and Masoud Darabi for their advice and Prof. Xiong Zhang at the Missouri University of Science and Technology for his advice and help.

This study was sponsored by TenCate Geosynthetics. I would like to express my gratitude to Mr. Brett Odgers and Mr. John Lostumbo for the great advice and valuable support they provided. I would also like to thank the Geosynthetic Institute for the GSI Fellowship provided to me.

The members of the KU Geotechnical Society, especially Dr. Fei Wang and Dr. Xiaohui Sun provided me with great support both academically and personally. Without their advice, this study would not be completed. I would like to thank the department lab managers and technicians, Mr. Matthew Maksimowicz, Mr. Kent Dye, and Mr. David Woody. Three undergraduate research

assistants, Davd Rivero, Gregory Overmohle, and Zexia Li, also played important role in helping me completing all the experiments.

Finally, I offer my sincere gratitude to my parents for their support and encouragement.

Table of contents

List of figures

List of tables

CHAPTER 1 Introduction

1.1 The wicking geotextile

Wicking geotextile manufactured by TenCate Geosynthetic (North America) is a new geotextile material that contains both high modulus polypropylene yarns as conventional woven geotextiles and deep-grooved nylon wicking yarns for absorbing and transporting water from soil under unsaturated conditions. The nylon wicking yarns are manufactured with deep grooves on the surface along the fiber direction, as shown in Figure 1.1. The wicking yarns have diameters between 30 and 50 μm and the width of each groove is approximately 5 to 12 μm (Zhang and Connor, 2015). The grooves on the wicking yarn act like channels for water to flow easily along the yarn. On the other hand, the small equivalent diameters of the channels can generate suction. As a result of the suction, the deep-grooved nylon yarns enable the geotextile to remove water from the soil even if the soil becomes unsaturated.

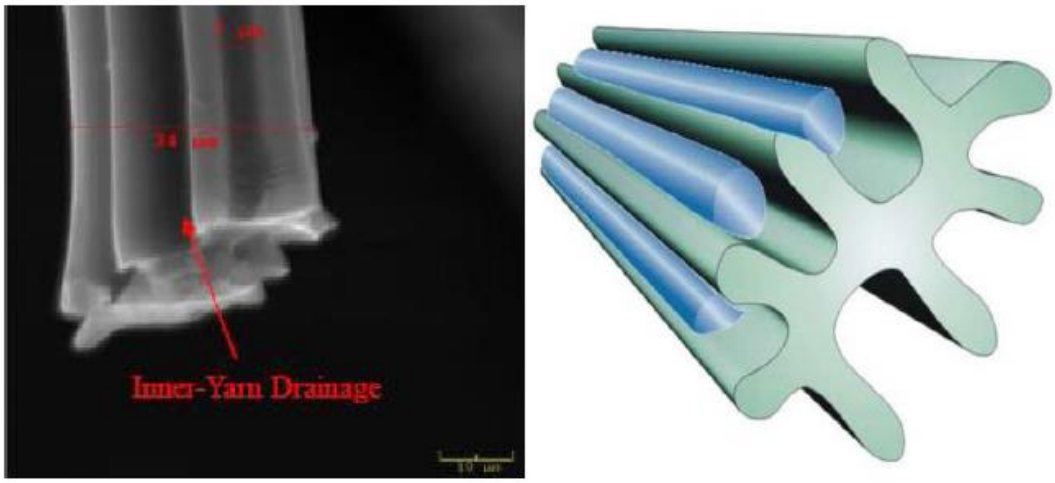

Figure 1.1 Microscopic (left) and schematic (right) pictures of deep-grooved nylon wicking yarn (Lin et al., 2016)

The deep-grooved fibers are weaved into the geotextile in the machine direction. For roadway applications, these deep-grooved fibers are perpendicular to the traffic direction. Compared with conventional woven geotextiles, wicking geotextile presents two advantages: (1) greater transmissivity under saturated conditions, and (2) the ability to "wick" water out of the soil when the soil is unsaturated. As a result, the inclusion of wicking geotextile in roadway structures not only provides reinforcement as conventional woven geotextiles but also enhances the drainage under both saturated and unsaturated conditions.

1.2 Effect of moisture on unbound aggregate base and roadway design

Moisture content of unbound aggregate base has a significant impact on both resilient and permanent strains of the material. Lekarp et al. (2000 a and b) concluded from numerous previous studies that a combination of high degree of saturation and low permeability leads to high pore-pressure and low effective stress and consequently low stiffness, strength, and deformation resistance. They further added that the presence of moisture in an aggregate matrix has some lubricating effect.

The AASHTO Guide for Design of Pavement Structures (AASHTO, 1993) and the Mechanistic-Empirical Pavement Design Guide (MEPDG) (AASHTO, 2008), the two most used design methods for pavements in the United States, both reply on the resilient modulus of the aggregate base to design a pavement. Both methods also consider the moisture effect on the aggregate base. In the 1993 AASHTO method, a drainage factor for the base layer is required in the calculation. In the MEPDG method, the resilient modulus of an unbound base is adjusted by the environmental effect model, which also takes the moisture of the base into consideration.

1.3 Problem statement

Case studies and laboratory tests (Zhang et al., 2014; Zhang and Connor, 2015; and McCartney and Zornberg 2010) have qualitatively confirmed the effectiveness of wicking geotextile and investigated the mechanism of this geotextile.

However, the previous studies did not quantify the water removing ability of wicking geotextile. Lack of quantitive effectiveness of wicking geotextile limits the development of design guidelines to incorporate the benefits of wicking geotextile into pavement design.

1.4 Research objectives and scope

The objectives of this study are to: (1) further investigate the mechanism of wicking geotextile removing water from soil; (2) quantify the relationship between water removal ability of wicking geotextile and environmental parameters, such as relative humidity, temperature, and soil moisture content; (3) evaluate the drainage and reinforcement combined effect of the wicking geotextile in base stabilization; and (4) develop design guidelines to incorporate the benefits of wicking geotextile into pavement design.

Experiments conducted for this study are designed to investigate four aspects between wicking geotextile and the environment: (1) the interaction between wicking geotextile and free water; (2) the interaction between wicking geotextile and water in soil; (3) the interaction between wicking geotextile and air (i.e., evaporation); and (4) the overall stabilization effect of wicking geotextile.

This study established relationships between the water removal ability of wicking geotextile and important environmental factors. These relationships are then used in the

development of design guidelines which incorporate the benefits of wicking geotextile. The design guidelines were developed by adjusting parameters in both 1993 AASHTO and MEPDG design methods.

1.5 Organization of this dissertation

This dissertation comprises seven chapters. Following this chapter, a literature review in Chapter two presents previous studies on wicking geotextiles, evaporation theories, and AASHTO 1993 and MEPDG design methods. Chapters three through five present laboratory experiments, their results, and analyses. Chapter six presents the development of guidelines for designing pavements with wicking geotextile. Chapter seven presents the conclusions and recommendations for future studies.

CHAPTER 2 Literature review

This chapter presents the review of literature regarding the following subjects: (1) Mass-transfer-based evaporation theory; (2) Laboratory and field performances evaluation and investigation on the wicking geotextile; and (3) A brief introduction to the 1993 AASHTO and MEPDG pavement design methods.

2.1 Methods for evaporation rate

Water can exist in the phase of solid, liquid, vapor, or supercritical fluid depending on its temperature and pressure. The relationships between the phases can be explained by thermodynamics. However, due to the number of factors that influence the phase changes and the difficulty to measure them, it is impractical to construct a physical model for civil engineering use. From a civil engineering perspective, water is typically considered in three phases: solid, liquid, and vapor (i.e. gaseous state). And usually, the phase changes between solid and water (i.e. freeze and thaw) as well as between water and vapor (i.e. evaporation and condensation) are concerned in practice of civil engineering. In this study, the evaporation process is a key aspect of the wicking geotextile ability to remove water. Thus a literature review on methods to estimate the rate of evaporation is necessary.

The rate of water evaporation depends on many parameters, such as temperatures of both air and water, air pressure, relative humidity and so on. Some basic terms and assumptions involved in evaporation should be explained. In the civil engineering practice, the air pressure can be assumed to be approximately 1 atmospheric pressure (i.e. 101 kPa or 14.7 psi). At this air pressure, air can be saturated with water vapor at a certain temperature, which is called the dew

point temperature. When the air temperature is lowered to the dew point temperature, the rate of water evaporation into the air equals the rate of water condensation on the water surface. Thus an equilibrium is achieved. Under the condition that the air is saturated with water vapor, the relative humidity of the air is 100%. If the air is at 100% relative humidity and its temperature is further lowered below the dew point temperature, more water starts to condense on solid or water surface, and the total amount of moisture in the air is reduced. Above the dew point temperature, more water starts to evaporate into the air, and the total amount of water in the air increases. The relative humidity is the ratio of the partial pressure of water vapor in the air (e_a) to the equilibrium vapor pressure of water (i.e., saturated vapor pressure, e_s) at a given temperature. The partial pressure of water vapor thus is also an indirect indicator of the evaporation potential of water. Air of higher relative humidity has more moisture, consequently, the potential of evaporation is lower and vice versa. The saturated vapor pressure is a function of air temperature and can be calculated with the equation (Singh and Xu, 1997):

$$e_s = 6.11 \times 10^{\frac{7.5T}{237.3+T}} \tag{2.1}$$

where T is the air temperature in ℃. Thus, the partial vapor pressure can be expressed as:

$$e_a = \frac{RH}{100} \times e_s \tag{2.2}$$

where RH is the relative humidity (%). The dew point temperature, T_{dp}, can be expressed as follows (Parish and Putnam, 1977):

$$T_{dp} = \frac{c\left(\ln\left(\frac{RH}{100}\right) + \frac{bT}{c+T}\right)}{b - \ln\left(\frac{RH}{100}\right) - \frac{bT}{c+T}} \tag{2.3}$$

where T_{dp} is the dew point temperature (°C), T is the air temperature (°C), RH is the relative humidity (%), b is 17.62, and c is 243.12 °C for -45°C ≤ T ≤ +60°C.

The evaporation from free water surface is first investigated by civil engineers in the field of hydrology to estimate the evaporation from large water bodies, such a lake or reservoir. In a natural environment, evaporation depends on temperature, wind speed, atmospheric pressure, solar radiation, quality of water, and the shape of the evaporation surface (Singh and Xu, 1997). As stated previously, due to the number of factors and the difficulty to measure them, a physical model based on thermodynamic is impractical. Thus the empirical mass-transfer method to estimate the evaporation rate from a free water surface was proposed by Dalton (1802):

$$E_0 = f(u)(e_s - e_a) \tag{2.4}$$

where E_0 is the evaporation rate from a free water surface, e_s is the saturation vapor pressure, e_a is the vapor pressure in air, and $f(u)$ is a function of horizontal wind velocity. The mass-transfer method, although proposed many years ago, is still a valuable method due to its simplicity and provides reasonably accurate estimation of evaporation rate (Singh and Xu, 1997).

Penman (1948) conducted an experiment under the natural evaporation condition and showed that the mass-transfer-based method could provide a reasonable prediction of evaporation from water surface by the equation:

$$E_0 = 0.35(1 + 9.8 \times 10^{-3} u_2)(e_s - e_a)(mm/day) \tag{2.5}$$

where u_2 is the wind speed measured in miles per hour. He also concluded that the ratio of the evaporation from a free water surface to that from a bare soil surface under the same condition was approximately 0.9.

Linacre (1977) simplified the Penman formula to the following form:

$$E_0 = \frac{\frac{700T_m}{100-A}+15(T-T_d)}{80-T}(mm/day) \quad (2.6)$$

where $T_m = T+0.006h$, h is the elevation in meters, T is the mean temperature, A is the latitude (in degree), and T_d is the mean dew point temperature. The equation is a modified mass-transfer method that also considers the geological location of an interested area. The advantage of Linacre's equation is the estimation of evaporation based on temperature data alone.

In the following research, modifications were made based on observation. Factors, such as air temperature, dew point temperature, relative humidity, and water temperature, were added into the estimation of evaporation from a free water surface. Singh and Xu (1997) concluded some of mass-transfer methods:

Table 2.1 Mass-transfer-based evaporation equations for estimation of evaporation (after Singh and Xu, 1997)

Author	Equation	Remarks
Dalton (1802)	$E(in/mo) = a(e_s - e_a)$	a=15 for small shallow water a=11 for large deep water
Fitzgerald (1886)	$E(in/mo) = (0.4 + 0.199u)(e_s - e_a)$	
Meyer (1915)	$E(in/mo) = 11(1 + 0.1u)(e_s - e_a)$	e_a measured at 30ft above surface
Horton (1917)	$E(in/mo) = 0.4[(2 - \exp(-2u))(e_s - e_a)]$	
Rohwer (1931)	$E(in/da) = 0.77(1.465 - 0.0186p_b)(0.44 + 0.118u)(e_s - e_a)$	p_b=barometric pressure in inches of Hg
Penman (1948)	$E(in/da) = 0.35(1 + 0.24u_2)(e_s - e_a)$	
Harbeck et al. (1954)	$E(in/da) = 0.0578u_8(e_s - e_a)$ $E(in/da) = 0.0728u_4(e_s - e_a)$	
Kuzmin (1957)	$E(in/mo) = 6(1 + 0.21u_8)(e_s - e_a)$	
Harbeck et al. (1958)	$E(in/da) = 0.001813u(e_s - e_a)(1 - 0.03(T_a - T_w))$	T_a=average air temperature ℃ T_w=average water temperature ℃
Konstantinov (1968)	$E(in/da) = 0.024(\frac{t_w - t_2}{u_1} + 0.166u_1)(e_s - e_a)$	
Romanenko (1961)	$E(cm/mo) = 0.0018(T_a + 25)^2(100 - hn)$	hn=relative humidity
Sverdrup (1946)	$E(cm/s) = (0.623\rho K_0^2 u_8(e_0 - e_8))/(p\left(\frac{ln800}{z}\right)^2)$	K_0=von Karman's Const. ρ=density of air p=atmospheric pressure
Thornthwaite and Holzman (1939)	$E(cm/s) = (0.623\rho K_0^2(u_8 - u_2)(e_2 - e_8))/(p\left(\frac{ln800}{200}\right)^2)$	

The water surface temperature T_w can be replaced by the dew point temperature. Then Singh and Xu (1997) concluded that the mass-transfer method could be generalized into the following forms:

(a) $E = a \times (e_0 - e_a)$

(b) $E = a \times u \times (e_0 - e_a)$

(c) $E = a \times (1 - \exp(-u) \times (e_0 - e_a))$

(d) $E = a \times (1 + b \times u) \times (e_0 - e_a)$

(e) $E = a \times u \times (e_0 - e_a) \times (1 - b \times (T_a - T_d))$

(f) $E = a \times (Ta + 25)^2 \times (100 - hn)$

(g) $E = a \times (1 + b \times u) \times (e_0 - e_a) \times (1 - c \times (T_a - T_d))$

where a, b, and c are the parameters, hn is the relative humidity, u is the wind speed. In these mass-transfer-based equations, four factors that have been mostly considered are the wind speed, temperature, relative humidity, and the difference between practical vapor pressure in the air and the saturated water vapor pressure. Singh and Xu (1997) evaluated the above formulae with evaporation data from climatological stations in north-western Ontario, Canada. Based on their evaluation, the difference between saturated and partial vapor pressure was the dominant factor in estimating evaporation. Wind speed was found to have a much less significant impact on the estimation. They also concluded that the more complicated formulae were not necessarily more accurate to predict the evaporation. Xu and Singh (2001) found that the prediction accuracy of the formulae can be improved by calibrating the constant values in these equations.

On conclusion, the mass-transfer-based methods can reasonability predict evaporation from free water surfaces. Wind speed, temperature of the air, dew point temperature, the difference

between partial vapor pressure and saturated vapor pressure, and relative humidity are the major parameters for mass-transfer methods to estimate the evaporation from free water surfaces. Among the parameters, the difference between partial and saturated vapor pressure presents the most significant influence on the predcted evporation rate. Calibration of the constants in these formulae can help improve the prediction accuracy. On the other hand, the mass-transfer method can also be modified to estimate the evaporation from other material under natural condition.

2.2 Application of wicking geotextile in pavement design

Water in roadway structure

Water can enter a roadway structure due to pavement infiltration, rising of the water table, seepage from higher ground, capillary action, and vapor movement as shown in figure 2.1. The source of pavement infiltration is typically precipitation. Water accumulated on the pavement can enter the base through existing cracks and joint in the pavement. FHWA (1992) identified the pavement infiltration to be the major source of water-causing pavement problems. The rising of water table caused by the seasonal fluctuation of precipitation is another significant source of water into the roadway system. With a shallow ditch along the side of the roadway structure and a flat longitudinal grade of the road, water seepage may carry the water from the higher ground into the roadway structure. Capillary action can also transport water above the water table. Based on (FHWA, 1992), the capillary action can transport water over 20 ft above the water table in clayey soils. The capillary action is the primary cause for frost-heave damage. The vapor movement is caused by the temperature gradient. Under temperature change, the water vapor in the voids can migrate and condense.

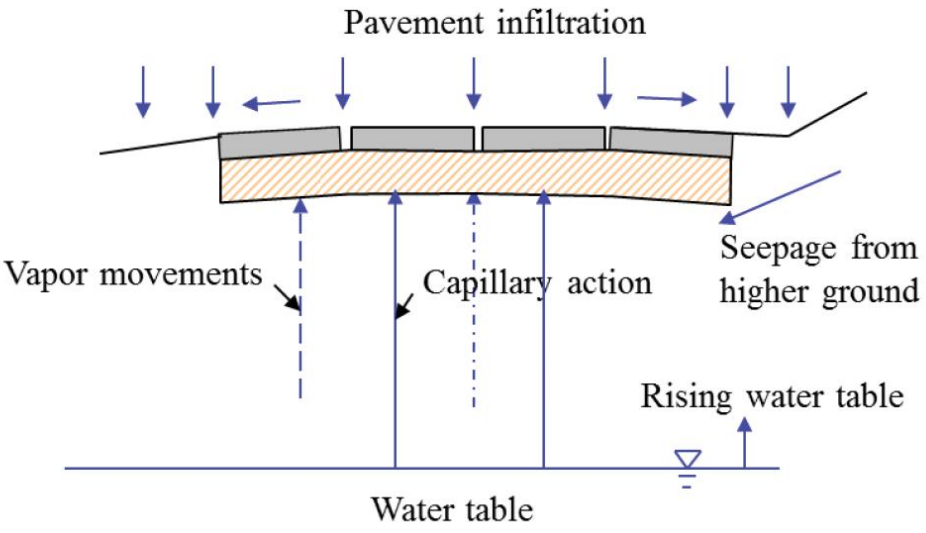

Figure 2.1 Sources of water (Han, 2015 based on FHWA, 1992)

Water in the soil exists in four forms: vapor, bounded water, capillary water and, gravitational water (or free water). The water vapor in most analysis is neglected. The bounded water is the thin film of water attached to the soil particle surface due to the polarity of water molecules and the negative charge carried by the soil particles. This part of the water is strongly bounded to the soil particles thus cannot be removed from the soil due to gravity and is often considered as part of the soil particle. The capillary water is the water exists above the water table. The capillary water occupies the pore space between soil particles due to the surface tension of water and is not affected by gravity. Different from the bounded water, the capillary water can be removed from the soil by introducing of suction. The most common form of water in the soil is the gravitational water. The flow of gravitational water follows Darcy's law.

Effect of moisture on roadway structures

The effect of water in a roadway structure is well studied. Han (2015) identified a series of the detrimental effect of water such as reduction in geomaterial strength and stiffness, expansion of geomaterial, erosion of soil particles and rock, migration of fine, freeze-thaw, stripping of asphalt pavement, and durability cracking of concrete. The detrimental effect of water often damage the performance and reduce the service life of roadway structures. Table 2.2 presents a list of some moisture relation issues in the performance of roadway structures.

Table 2.2 List of some moisture related issue in the performance of roadway structures (after NCHRP, 2004)

Type	Distress Manifestation	Climatic factor	Structural defect begins in		
			Pavement	Base/unbounded subbase	subgrade
Asphalt Concrete Pavement					
Surface deformation	Bump or distortion	Frost heave	No	No	Yes
	Stripping	Moisture	Yes	No	No
	Rutting	Moisture	Yes	Yes	Yes
	Depression	Suction & material	No	No	Yes
	Potholes	Moisture & temperature	Yes	Yes	Yes
Cracking	Alligator (fatigue)	Spring-Thaw strength loss	Yes, mix	Yes	Yes
	Slippage	No	Yes, bond	No	No
Portland cement Concrete Pavement					
Surface defects	Spalling	Freeze-thaw cycles	Yes	No	No
	D-cracking	Freeze-thaw cycles	Yes	No	No
Surface deformation	Pumping & erosion	Moisture	No	Yes	Yes
	Faulting	Moisture-suction	No	Yes	Yes
	Curling/wrapping	Moisture & temperature	Yes	No	No
Cracking	Corner	Moisture	No	Yes	Yes
	Diagonal transverse longitudinal	Moisture	No	Yes	Yes
	Punchout	Moisture	No	Yes	Yes

From a geotechnical perspective, properties such as modulus and stiffness of most of the geomaterials are effected by moisture. Water can reduce strengths, moduli, and stiffness of granular bases and subgrade (Haynes and Yoder, 1963) and induces roadway distresses (Zhang et al., 2014). Most granular bases contain 5% to 15% fine (Qian et al., 2013; Zhang et al., 2014);

therefore, they are sensitive to moisture. The change of strengths and moduli of granular bases and subgrade with the change of water contents has been observed in both laboratory and field. Several researchers (e.g., Haynes and Yoder, 1963; Hicks and Monismith, 1971; Barksdale and Itani, 1989; and Dawson et al., 1996) studied the behavior of granular materials at various water content. They found that soil resilient modulus is dependent to water content. For instance, Haynes and Yoder (1963) observed a 50% decrease in resilient modulus of gravel when the degree of saturation increased from 70% to 97%. Lekarp et al. (2000a) concluded based on previous studies that the resilient behavior of unbound aggregate can be significantly affected by water content when it approaches saturation.

More than altering the properties of geomaterials, the water phase change also damages the performance of roadway structures. Freeze and thaw-induced deformation is a major water-related issue in roadway structures. In regions where roadways structures experience subfreezing temperature and groundwater table is close to the road structure, frost heave and thaw weakening tend to occur. In a freezing period, water in large pore space freezes into ice crystals. During the freezing process, water expands 9% of its volume and became an impermeable particle which induced negative pore-water pressure or suction. As freezing occurs from the top of the roadway structure, the negative pore-water pressure draws water from below the freezing plane via capillary action. As the freezing continues, the ice crystals fed by the capillary water increase in size. Eventually, the ice crystals join together to form an ice lens. Pressure induced by the formation of ice lens heaves the surface. Then in the thawing period, the ice lens melts into water, increases the water content of geomaterials. The increase in water content weakens the material and causes deformation.

In addition, the movement of water often results in the loss of fine particles in the geomaterial thus increases the void ratio in the geomaterials. As a result of the detrimental effects of excess moisture in roadway structures, the moisture-related damage is a major concern in designing pavement structures. Controlling the moisture damage in a roadway structure can be achieved by: 1. Restricting the moisture from entering the roadway structure; 2. Using non-moisture-sensitive material; 3. Incorporating design features to minimize moisture damage, and 4. Removing moisture that enters the pavement system quickly (NCHRP, 2004).

Geotextiles in unsaturated geomaterials

According to Han (2015), geotextiles have the functions of separation, filtration, drainage, reinforcement, erosion protection, and barrier. Among the multiple functions, geotextiles is often used as a drainage layer in a roadway structure. The higher transmissivity in the plane of geotextile allows pavement water move through the plane of geotextiles faster than in the surrounding geomaterials thus increase the rate of drainage. Geotextiles are now commonly used to replace conventional sand or gravel drainage layers. Past studies on the behavior of geotextiles focused on three aspects: (1) hydraulic properties of geotextile in different geomaterials (Stormont et al., 1997; Ho 2000; Iryo and Rowe, 2004, 2005); (2) design methods and criteria for geotextiles (Holtz et al., 1997; Lee and Bourdeau, 2006); and (3) capillary barrier effect of geotextile (Henry, 1996; McCartney and Zornberg, 2010; Zornberg et al., 2010).

The majority of the studies focused on design methods identified gravity or hydraulic gradient in the water to be the driving force for geotextile drainage. In other words, drainage of water through geotextiles requires high degree of saturation of the geomaterial. Many researchers found the hydraulic properties of geotextiles change significantly when the geomaterial or geotextile is unsaturated. One noticeable effect of the geotextile is the capillary barrier effect: the

inclusion of geotextile results in the increase in water storage capacity of geomaterial above the geotextile beyond the level that would normally drain under gravity. As a result, the geotextile will only collect water when the overlaying geomaterial is nearly saturated (McCartney and Zornberg, 2010). Ho (2000) experimentally determined the geotextile water characteristic curves, which exhibited a steep and hysteretic drying and wetting path. The water characteristic curves suggest that the maximum hydraulic conductivity during wetting of a geotextile under low suction head was much lower than the value of the reference saturated hydraulic conductivity. Iryo and Rowe (2003) showed as the geomaterials become unsaturated the drainage efficiency of geotextile decreases significantly. Iryo and Rowe (2003) also found the air and water entry values of geotextiles are very small thus geotextile can change from a permeable to an impermeable material due to very small suction change. Bouazza et al. (2006) concluded that a capillary barrier could develop at the interface of geotextile and unsaturated soil. The capillary barrier results in a restriction to flow and accumulation of water above the drainage interface. A 5 kPa suction in the geotextile was needed to break through the capillary barrier. Bouazza et al. (2006) also pointed out that the water retention characteristic of geotextiles is hysteretic. The retention curve of geotextile shows nearly constant of water content up to an air entry point. Then a sharp reduction in water content was observed when suction was beyond the air entry point. Garcia et al. (2007) conducted a series of model embankment tests under rainfall infiltration. They found the geotextile placed in the embankment worked as a capillary barrier and a high degree of saturation was observed in the geomaterial above the geotextile. Bathurst et al. (2007) developed a column apparatus to investigate the unsaturated to saturated response of a sand-geotextile system. They observed transient ponding of water above the surface of the geotextile layer due to the initial unsaturated condition of the geotextile. Koerner (2012) pointed out that geotextiles are generally

hydrophobic and there is no wicking action across the plane of the geotextile. There is only minor intimate contact of water with the fiber until the voids are saturated.

The capillary barrier effect of geotextile can prevent capillary action of transporting water into a roadway structure. This function of geotextile is especially important in controlling frost heave where the capillary barrier effect of geotextile prevents capillary action of transporting water to the pavement structure. However, the capillary barrier effect also restricts drainage from the geomaterial above into the geotextile.

Wicking geotextile

The hydrophobic nature of geotextile presents drawbacks in conventional geotextile. The capillary barrier effect of geotextile, although can prevent capillary water entering the roadway structure, limits the drainage from geomaterial above the geotextile. The drainage through a conventional geotextile can only occur at high degree of saturation and presence of hydraulic gradient. However, the condition required for drainage may not exist in the field even after a rainfall. In addition, water ponding due to an unleveled interface between base course and subgrade may reduce or even reverse the hydraulic gradient.

A new type of geotextile, the wicking geotextile, was introduced to not only provide drainage in saturated geomaterials but also continue removing water when the geomaterial becomes unsaturated. The wicking geotextile contains both high modulus polypropylene yarns as conventional geotextiles and deep-grooved nylon wicking yarns (i.e., 4DG^{TM} fibers). The 4DG fibers are manufactured with deep grooves on the surface along the fiber direction, as shown in Figure 1.1. The multichannel cross section gives the fiber large specific surface area which generates large capillary force (i.e., suction). The wicking yarns have diameters between 30 and

50 μm and the width of each groove is approximately 5 to 12 μm (Zhang and Connor, 2015). The specific surface area of the wicking geotextile is 0.365 m^2/g and it has a permittivity of 0.24 s^{-1} (Han and Zhang, 2014). As a result of the capillary force, the 4DG fibers are both hydrophilic and hygroscopic. The suction generated by the 4DG fiber allows the capillary water to be wicked into the fiber from adjacent voids. The inclusion of 4DG fibers in the wicking geotextile alters the hydrophobic character of conventional geotextile to hydrophilic and enables the wicking geotextile to remove water from unsaturated geomaterial.

Figure 2.2 illustrates the mechanism of wicking geotextile removing water from a roadway structure. Since the relative humidity of the air around the roadway is relatively low (typically lower than 50%) and the relative humidity of the soil and the wet geotextile is high (close to 100%), this relative humidity difference can generate a large suction in the geotextile. Zhang et al. (2014) pointed out that the suction in an unsaturated soil within a pavement system is typically lower than 1000 kPa and the suction in the geotextile induced by the relative humidity difference can be mostly ranged from 1000 to 100000 kPa. This suction difference between the geotextile and the soil can draw water out of the soil and transport it to the exposed portion of the geotextile. Also, due to the relative humidity difference between the geotextile and the air, the water evaporates into the air. This process continues until the water content of soil decreases and the soil suction equals to the suction in the geotextile. Azevedo and Zornberg (2013) performed small soil column capillary model tests and found the geotextiles with 4DG fibers reduced the moisture buildup formed by a capillary barrier. They contributed the reduction in moisture buildup to the horizontal drainage ability of the 4DG fibers.

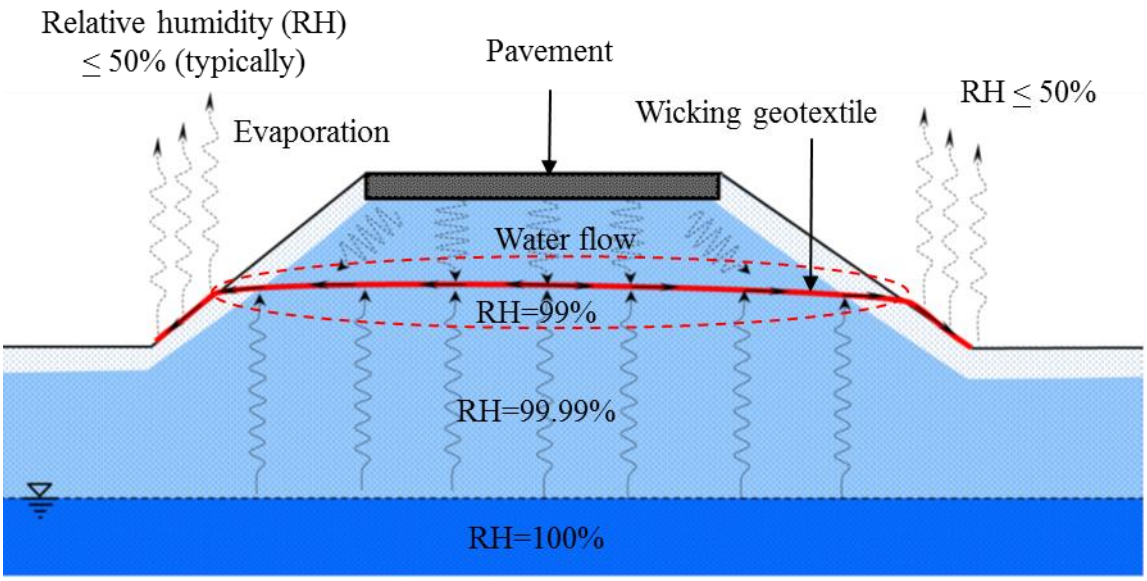

Figure 2.2 Mechanisms of water removal by wicking geotextile in a pavement system (Guo et al., 2016)

The wicking geotextile has already been applied in serval roadway projects. Zhang et al. (2014) reported the application of wicking geotextile to prevent frost heave in Alaska Pavements. This project was to repair a section of the Dalton Highway, which was unpaved and suffered from heavy truck traffic. The extensive damage to the road was caused by frost heaving and thaw weakening. Geocomposite has been used to rehabilitate the section of the Dalton Highway and proven unsuccessful. Two layers of wicking geotextile were installed 45 cm apart with the top layer of wicking geotextile approximately 1 m below the pavement surface. After 5 years of monitoring, the wicking geotextile successfully eliminated the frost heave and thaw weakening issue. The road in Coldfoot, AK experienced a similar frost heave problem. In 2012, a 19-kilometer test section was constructed with 9.5-km wicking geotextile and 9.5 kilometers without geotextile. In the treated section, one lane was constructed with 0.3 m thick aggregate over the wicking geotextile and one lane was constructed with 0.15 m thick aggregate over the geotextile.

The test section showed the wicking geotextile successful prevented water from rising up from the subgrade via capillary action as shown in Figure 2.3. In St. Louis County, MO, the wicking geotextile was used to remove water from underneath the pavement. The original design consisted of a pavement over 100 mm thick base aggregate and 100 mm thick drainable aggregate. The inclusion of wicking geotextile was expected to reduce the aggregate base thickness by 50 mm. Observation showed the geotextile successfully wicked the water out of the aggregate.

Figure 2.3 Wicking geotextile as a capillary break during spring thaw (TenCate, 2013)

Although case studies prove the effectiveness of the wicking geotextile in improving the performance of pavement structures, no design method for the wicking geotextile has been developed for this application.

2.3 1993 AASHTO pavement design method

The American Association of State Highway Officials (AASHTO) initiated research projects in 1948 aiming to provide pavement design guidelines based on the concept of serviceability performance. The AASHTO road test conducted in the 1950s established the relationship between the number of repetitions of specified axle loads of different magnitudes and the performance of different thicknesses of flexible and rigid pavements (Huang, 1993). These relationships were used to develop the serviceability performance-based design method which was named the AASHTO Guide for Design of Pavement Structures (AASHTO, 1993). This design guide is later known as the 1993 AASHTO design guide. The 1993 AASHTO design method considers: pavement performance, traffic, roadbed soil, materials of construction, environment, drainage, reliability, life-cycle costs, and shoulder design (AASHTO, 1993). The serviceability of a pavement is expressed by the term present serviceability index (PSI) on a scale from 0 through 5. The PSI is related to the roughness, distress, cracking, patching, and rut depth. A pavement loses serviceability over its life and the PSI of this pavement decreases. The loss of serviceability of a pavement can be caused by traffic, age, and environment. The 1993 AASHTO pavement design guide provides a design guide for both flexible and rigid pavement. In this review, the flexible design method will be discussed because wicking geotextile has not been used for rigid pavements.

The 1993 AASHTO design guide measures the traffic volume with the unit of equivalent single axle load or ESAL. The damage to pavement inflicted by a vehicle depends on its axle load and axle configuration. Traffic on a pavement consists of different type of vehicles thus the damage of each type vehicles to the pavement is different. To account for damage to the pavement from different types of vehicles, it is necessary to evaluate the damage inflicted by varying axles

in reference to the damage inflicted by a standard axle. Equivalent axle load factor (EALF) defines the damage per pass to a pavement by an axle relative to the damage per pass of a standard axle load, i.e. 18 kip single axle load (Huang, 1993). The EALF is calculated based on the load and the configuration of the axle. The EASL then can be calculated with the following equation:

$$EASL = \sum_{i=1}^{m} F_i n_i \tag{2.7}$$

where m is the number of axle load groups, F_i is the EALF for the *i*th-axle load group, and n_i is the number of passes of the ith-axle load group for the design period.

The 1993 AASHTO pavement design method presented a relationship between traffic volume and loss of serviceability. The relationship for designing a flexible pavement can be expressed as follows:

$$\log_{10}(W_{18}) = Z_r \times S_o + 9.36 \times \log_{10}(SN+1) - 0.2 + \frac{\log_{10}\left(\frac{\Delta PSI}{4.2+1.5}\right)}{0.4+\frac{1094}{(SN+1)^{5.19}}} + 2.32 \times \log_{10}(M_R) - 8.07 \tag{2.8}$$

where W_{18} is the predicted number of 18-kip equivalent single axle load applications; Z_r is standard normal deviate; S_o is the combined standard error of the traffic prediction and performance prediction; ΔPSI is the difference between the initial and terminal serviceability index (p_0-p_t); M_R is resilient modulus (psi); and SN is the structural number.

The structural number is defined as an abstract number expressing the structural strength of a pavement structure needed for a given combination of soil support (M_R, resilient modulus), traffic expressed in equivalent single 18 kip axle (ESAL), final serviceability, and environment (AASHTO, 1993). The layer coefficient is an essential parameter in the 1993 AASHTO design

for determining the thickness of each layer. Some of the environmental factors are also represented in the structural number. The structural number is calculated based on all layers of the pavement:

$$SN = a_1 D_1 + a_2 D_2 m_2 + a_3 D_3 m_3 \tag{2.9}$$

where a_i is the i^{th} layer coefficient, D_i is the i^{th} layer thickness (in inches), and m_i is the i^{th} layer drainage coefficient.

The structural layer coefficients for different geomaterials are calculated differently. The 1993 AASHTO design guide provided the layer coefficient of dense-graded asphalt concrete based on its elastic modulus, as shown in Figure 2.4.

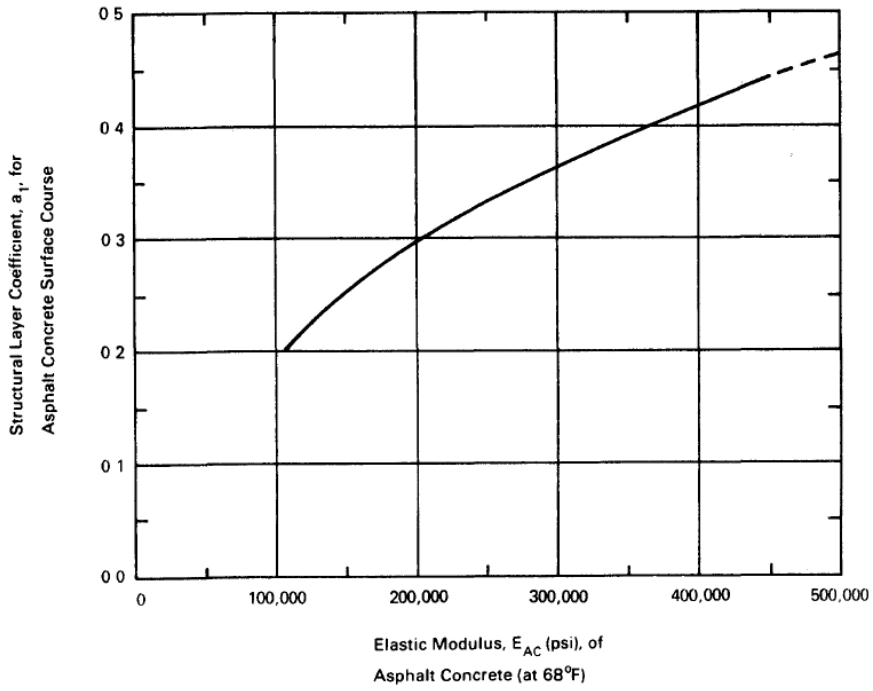

Figure 2.4 Chart for estimating structural layer coefficient of dense-graded asphalt concrete based on the elastic (resilient) modulus (AASHTO, 1993)

The structural layer coefficient of a granular untreated aggregate base material can be calculated based on its elastic modulus with the following equation (AASHTO, 1993):

$$a_2 = 0.249(\log_{10} E_{BS}) - 0.977 \tag{2.10}$$

where E_{BS} is the elastic (resilient) modulus of the granular base material in pound per square inches. For bituminous-treated and cement-treated base materials, the structural number can no longer be calculated with Equation (2.10). Huang (1993) provided the structural layer coefficients for the treated-base material based on moduli, as shown in Figure 2.5.

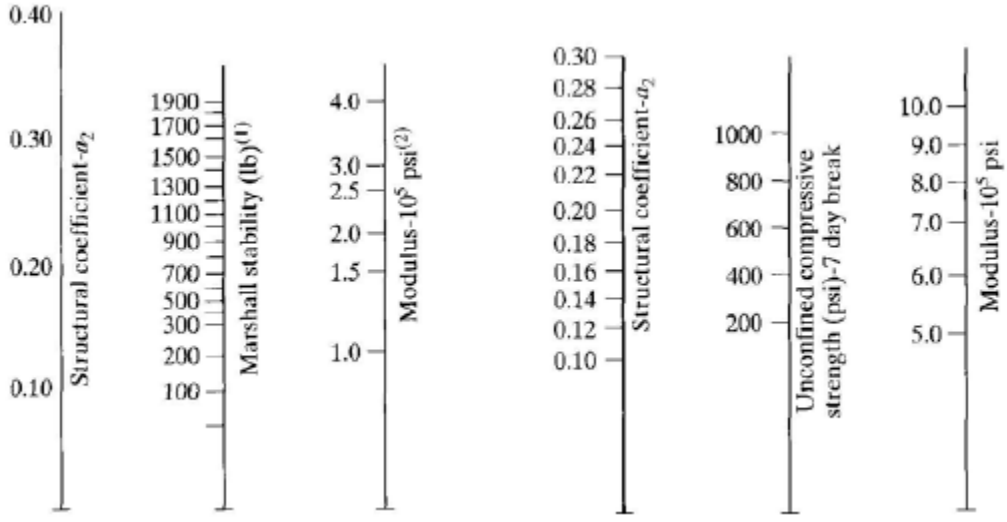

(a) Bituminous treated (b) Cement Treated

Figure 2.5 Correlation charts for estimating resilient modulus of bases. (After Huang, 1993)

The elastic modulus of untreated aggregate base material is under the influence of moisture and stress state (θ) (AASHTO, 1993):

$$E_{BS} = k_1 \theta k_2 \tag{2.11}$$

where θ is the stress state or the sum of principal stresses (σ_{1+} σ_{2+} σ_3); k_1 and k_2 are regression constants which are a function of material type. For base material, the value of k_1 typically ranges from 3000 to 8000, and the value of k_2 typically ranges from 0.5 to 0.7.

The structural layer coefficient of aggregate subbase can be calculated with the following equation:

$$a_2 = 0.227(\log_{10} E_{SB}) - 0.839 \quad (2.12)$$

where E_{BS} is the elastic (resilient) modulus of the granular base material in pound per square inches. For the subbase material, the elastic modulus can be calculated with Equation 12. However, for subbase material, the typical value for k_1 ranges from 1500 to 6000 and the typical value for k_2 ranges from 0.4 to 0.6. The suggested values for k_1 and k_2 are presented in Table 2.3.

Table 2.3 Typical values for k_1 and k_2 for unbound base and subbase material (AASHTO, 1993)

Moisture Condition	k1	k2
	Base	
Dry	6000-10000	0.5-0.7
Damp	4000-6000	0.5-0.7
Wet	2000-4000	0.5-0.7
	Subbase	
Dry	6000-8000	0.4-0.6
Damp	4000-6000	0.4-0.6
Wet	1500-4000	0.4-0.6

The 1993 AASHTO guide evaluates the effect of drainage quality (or moisture in the base) on the properties of the pavement layer and the structural capacity of the pavement by modifying the structural layer coefficient (a_i) of the untreated base or subbase layer as shown in Equation (10). Two effects of drainage on the pavement structures are considered: (1) The quality of the drainage (i.e., the time required for the pavement to drain) and (2) Percent of time the pavement structure is exposed to the moisture level approaching saturation. The quality of drainage is classified in five levels by calculating the time required to drain the base layer to 50 percent saturation (Seed and Hicks, 1991). If the excess water in the pavement structure is removed within 2 hours, the drainage quality is considered excellent. If the excess water is removed within one day, the drainage quality is considered good. If the excess water is removed within one week, the drainage quality is considered fair. A pavement structure with poor drainage quality would remove the excess water from the pavement structure within one month. If water does not drain, the drainage quality is considered very poor. In the development of drainage coefficient, the effect of drainage was expressed by adjusting the base modulus. Seed and Hicks (1991) suggested a modulus of 50000 psi for the excellent drained base and 10000 psi for the very poorly drained base. The deflections of pavement structures with adjusted base moduli were calculated mechanically with the same pavement layer configuration as the AASHTO road test. The calculated deflections were then compared with the measured AASHTO road test deflections to yield the drainage coefficient (m_i). Note: The AASHTO road test condition was assumed to have an aggregate base modulus of 30000 psi and a road bed soil modulus of 3000 psi. The quality of drainage is reflected by adjusting the structural layer coefficient (a_i) with the drainage coefficient (m_i) as shown in Equation 10. Table 2.4 presents the recommended m_i value based on the quality of drainage and the percentage

of time during a year that the pavement structure would be exposed to approaching saturation moisture.

Table 2.4 Recommended m_i value for calculating structural number of untreated base and subbase material in flexible pavements (AASHTO, 1993)

Quality of drainage	Percent of time pavement structure is exposed to moisture levels approaching saturation			
	Less than 1%	1-5%	5-25%	Greater than 25%
Excellent	1.40-1.35	1.35-1.30	1.30-1.20	1.20
Good	1.35-1.25	1.25-1.15	1.15-1.00	1.00
Fair	1.25-1.15	1.15-1.05	1.00-0.80	0.80
Poor	1.15-1.05	1.05-0.80	0.80-0.60	0.60
Very poor	1.05-0.95	0.95-0.75	0.75-0.40	0.40

Another environmental factor considered by the 1993 AASHTO design guide is the roadbed soil resilient modulus change due to seasonal moisture conditions. The 1993 AASHTO design guide points out the resilient modulus of roadbed soil in a climate which is not subjected to extended sub-freezing temperatures should be tested for the difference between the wet and dry seasons. The concept of effective roadbed soil resilient modulus is introduced in the design guide to represent the seasonal moisture condition. The effective roadbed soil modulus is a weighted value that gives the equivalent annual damage obtained by treating each seasonal time period independently in the performance equation and combining the damage (AASHTO, 1993). Three steps are needed to obtain the effective soil modulus. The first step is to enter the seasonal moduli in their respective time periods. The time periods should be in equal length. Then the relative

damage (u_f) value is estimated based on each modulus. The relationship between soil modulus (M_R) and relative damage (u_f) is as follows (AASHTO, 1993):

$$u_f = 1.18 \times 10^8 \times M_R^{-2.32} \tag{2.13}$$

Next, the average relative damage ($\overline{u_f}$) is determined by summing the u_f values then dividing the sum by the number of seasonal period in a year as shown in Equation 15 (AASHTO, 1993):

$$\overline{u_f} = \frac{\sum u_f}{n} \tag{2.14}$$

where n is the number seasonal periods in a year. The effective roadbed soil resilient modulus M_R can then be calculated using Equation 14.

2.4 Mechanistic-empirical pavement design guide

The AASHTO pavement design guides have been widely adopted by transportation agencies in the past serval decades. Overall, the 1993 AASHTO design guide served well as a design guide. The empirical relationships in the 1993 AASHTO design guide were established by the AASHTO road test conducted in the 1950s. In the past more than half a century, many limitations were found in the AASHTO pavement design guide. The AASHTO road test was conducted at one specific geographic location, on one type hot mix asphalt over two types of unbound dense granular based materials, over one type of subgrade soil. The test duration of the AASHTO road test was over two years, however, the pavements designed nowadays are to remain in service for 20 to 50 years. Thus it is believed that the 1993 AASHTO design guide is insufficient to predict the long-term performance of pavement structures. On the other hand, the heavy truck traffic volume today has increased about 10 to 20 times since the 1960s. The sub-drainage, which is common nowadays, was not considered in the development of the 1993 AASHTO design

method. The primary parameter to evaluate the performance of pavement in the AASHTO design guide, i.e., present serviceability index, was affected dominantly by longitudinal profile. However, other distress factors, such as cracking, rutting, and joint faulting were found to influence the pavement performance as well, thus should be considered as factors to influence pavement performance. As a result of the changes in traffic volume, materials, and construction techniques, the AASHTO design method can no longer keep up with the current design demand. A new and more comprehensive design method is required. During the development of the AASHTO design guide, it was recognized that a design method based on mechanistic-empirical principles would be necessary. However, the capability of computers in the late 1900s limited development of such a design guide. The amount of computing power from a personal computer nowadays makes a mechanistic approach to pavement design possible. The mechanistic-empirical pavement design guide (MEPDG) was developed by the National Cooperative Highway Research Program (NCHRP) in 2004.

Pavement responses to traffic and environmental loads can be stress, strain, and deflection of the structure. The relationships between the loads and response of the pavement can be described with mathematical models. The "Mechanistic" in the MPEDG refers to the utilization of the generalized multi-layered elastic system. The empirical parts of the MEPDG relate to the characterization of materials or to traffic, environment, and field performance data used to correlate to accumulated damage (NCHRP, 2004).

The MEPDG evaluates the performance of a pavement based on its smoothness. The indicator used to measure the smoothness of a pavement is the International Roughness Index (IRI). During the service of a pavement, the IRI of the pavement will increase over time due to distresses. Similar to the present serviceability index (PSI) in the 1993 AASHTO design method, the initial

smoothness (IRI_i) and the terminal smoothness (IRI_t) are provided by the MEPDG. If the smoothness of the pavement reaches the terminal smoothness (IRI_t), rehabilitation is required. The typical initial smoothness (IRI_i) ranges from 50 to 100 inches/mile. The typical terminal smoothness (IRI_t) ranges from 150 to 200 inches/mile. The major factors contributing to the increase of IRI are distresses, such as cracking, rutting, faulting, and punch-outs. These distresses are influenced by the design, material, subgrade, traffic, age, and environment.

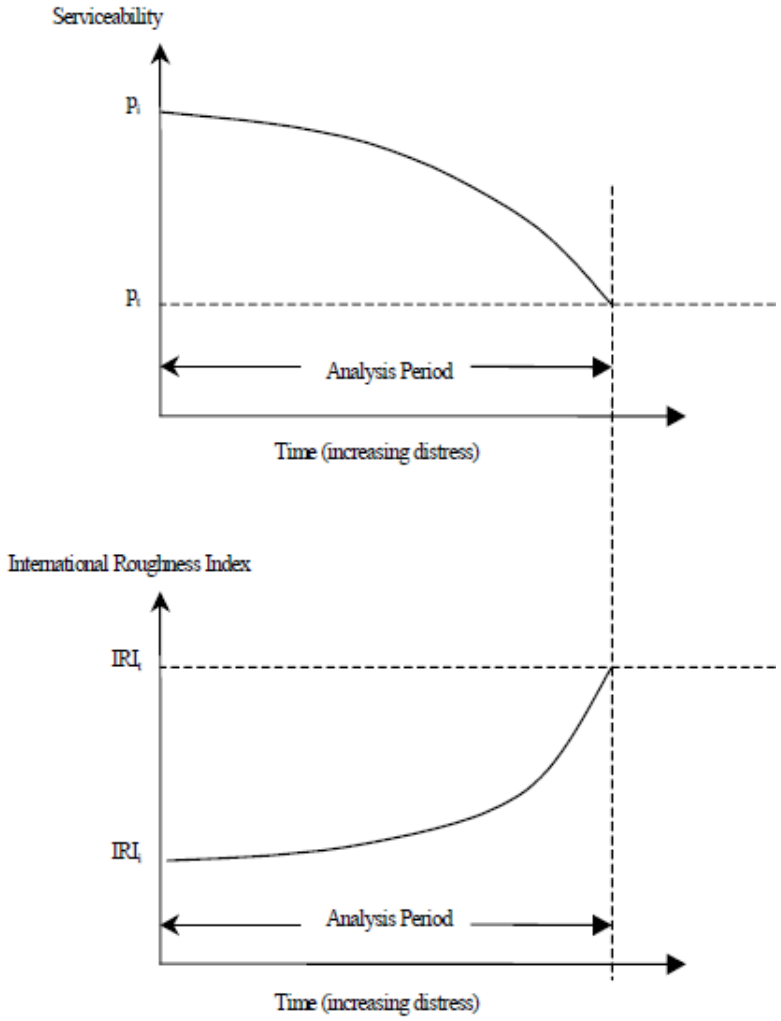

Figure 2.6 Pavement performance trends illustrated using serviceability and IRI values (NCHRP, 2004)

Yoder and Witczak (1975) proposed the following assumptions for the multi-layered elastic system: (1) The material properties of each layer are homogeneous; (2) Each layer, except for the lowest layer, has a finite thickness and is infinite in the lateral directions; (3) Each layer is isotropic; (4) Full friction is developed between layers; (5) Surface shearing forces are not present; and (6) The stress solution is characterized by Poisson's ratio (μ) and the elastic modulus (E) of the of the material in each layer. Figure 2.7 illustrates the multi-layered elastic system.

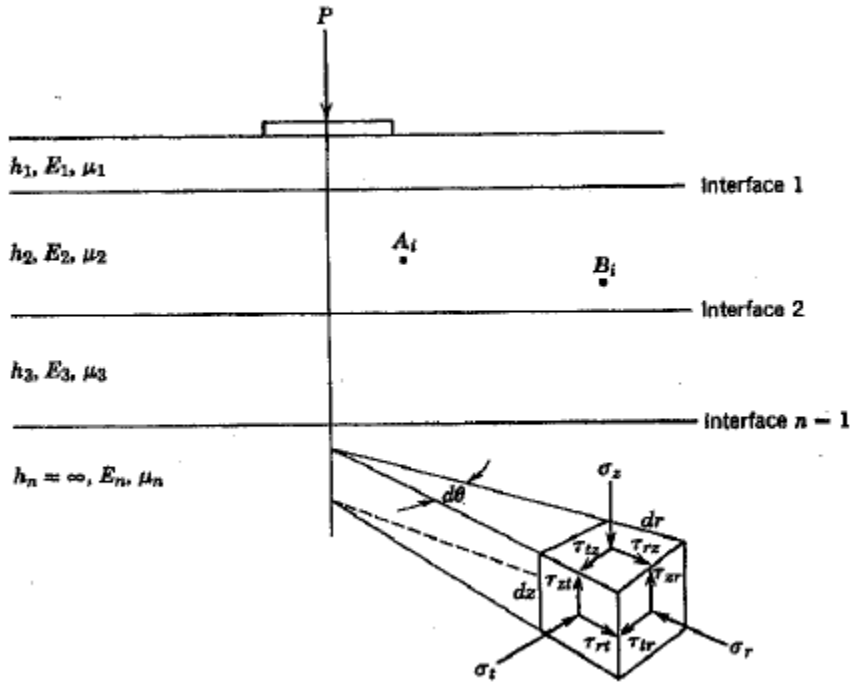

Figure 2.7 Generalized multi-layered elastic system (after Yoder and Witczak, 1975)

The multi-layered system is analyzed in a polar coordinate system. The stresses in the system act on vertical (z), radial (r), and tangential (t) planes. Based on the principal stresses, the vertical strain can be determined by the following equation:

$$\varepsilon_z = (1/E)[\sigma_z - \mu(\sigma_r + \sigma_t)] \quad (2.15)$$

Based on the theory, the relationship between stress and strain, the time dependency of strain under a constant stress, and the rebound strain after removal of the stress can be established.

The equation used to predict the permanent deformation in unbounded base materials was developed by Tseng and Lytton (1989). The basic formula to estimate the permanent deformation of granular materials is presented in Equation 2.16:

$$\left.\begin{aligned} &\delta_a = \beta_1 \left(\frac{\varepsilon_0}{\varepsilon_r}\right) e^{\left(\frac{\rho}{N}\right)^{\beta}} \varepsilon_v h \\ &\log\left(\frac{\varepsilon_0}{\varepsilon_v}\right) = 0.80978 - 0.06626W_c - 0.003077\sigma_\theta + 0.000003E_r \\ &\log(\beta) = -0.919 + 0.03105W_c + 0.001806\sigma_\theta + 0.0000015E_r \\ &\log(\rho) = -1.78667 + 1.45062W_c + 0.0003784\sigma_\theta^2 - 0.002074W_c^2\sigma_\theta - 0.0000105E_r \end{aligned}\right\} \quad (2.16)$$

where δ_a is the permanent deformation for the layer/sublayer (in); N is the number of traffic repetitions; $\varepsilon_0, \beta \; and \; \rho$ are material properties; ε_r is the resilient strain imposed in laboratory test to obtain the material properties $\varepsilon_0, \beta \; and \; \rho$ (in/in); ε_v is the average vertical resilient strain in the layer/sublayer as obtained from the primary response model (in/in); h is the thickness of the layer/sublayer (in), β_1 is the calibration factor for the unbound granular and subgrade material; W_c is the water content (%); E_r is the resilient modulus of the layer/sublayer (psi); and σ_θ is the bulk stress (psi). In the calculation of permanent deformation with Equation (2.16), water content, deviator stress, bulk stress, and resilient modulus of the layer/sublayer are required. Some researchers found the Tseng and Lytton equation, in many cases, yielded wrong trends for the predicted rut depth. Ayres (2002) later modified Equation (2.16) so that the bulk and deviator stresses are no longer needed for the calculation of permanent deformation for the base and subgrade. However, the predictions made by Aryes' model resulted in high degree of scatter and

large rutting in subgrade. Finally, El-Basyouny and Witczak (NCHRP, 2004) developed a model based on Tseng and Lytton as well as Ayres models, which is used in the MEPDG. The model in the MEPDG eliminated the stress terms. The equations to calculate "β" and "ρ" are also simplified. The MEPDG predicts the permanent deformation of unbound material with the following equations:

$$\begin{cases} PD = k \cdot h_{soil} \cdot \varepsilon_v \cdot (\frac{\varepsilon_0}{\varepsilon_r}) \cdot e^{-\left(\frac{\rho}{N_L}\right)^{\beta}} \\ log\beta = -0.61119 - 0.017638W_c \\ \rho = 10^9 \cdot \left(\frac{-4.89285}{1-(10^9)\beta}\right)^{\frac{1}{\beta}} \\ \frac{\varepsilon_0}{\varepsilon_r} = \frac{0.15 \cdot e^{\rho^{\beta}} + 20 \cdot e^{\left(\frac{\rho}{10^9}\right)^{\beta}}}{2} \end{cases} \quad (2.17)$$

where *PD* is permanent deformation of the soil layer; h_{soil} is the thickness of the soil layer; *(ε0/εr)*, β, and ρ is parameters of the unbound material of the soil layer; *k* is the calibration factor, 1.67 for base course and 1.35 for subgrade; ε_v is the average vertical resilient strain of the soil layer; W_c is the water content; and *N* is the number so load cycles.

The MEPDG also considered the influence of moisture on unbound base material. The influence of moisture on the unbound material is primarily considered in the term of resilient modulus. The MEPDG proposed to estimate the unbound material resilient modulus based on its resilient modulus at optimal water content ($M_{R\ opt}$) and the difference between the investigated water content and optimal water content ($w-w_{opt}$). Based on numerous models, a linear relationship is proposed for modulus ratio in a log scale (NCHRP, 2004):

$$\log\left(\frac{M_R}{M_{r\ opt}}\right) = k_w(w - w_{opt}) \quad (2.18)$$

$$\log\left(\frac{M_R}{M_{r\,opt}}\right) = k_s(S - S_{opt}) \tag{2.19}$$

where M_R is the resilient modulus at water content w (%); $M_{R\ opt}$ is the resilient modulus at maximum dry density and optimum water content w_{opt} (%); and k_w is the gradient of log resilient modulus ratio ($\log(M_R/M_{R\ opt})$) with respect to the variation in percent water content (w-w_{opt}). Regression analysis was performed on test results from seven investigators on 49 soils. The MEPDG proposed k_w = -0.0602 for fine-grained materials and k_w = -0.0463 for coarse-grained materials. Similar approach can also be applied to the degree of saturation of the unbound material, which yields Equation (2.19), where S is the degree of saturation; S_{opt} is the optimum degree of saturation; and k_S is the gradient of log resilient modulus ratio with respect to variation in the degree of saturation. The regression analysis suggested k_S = -0.0128 for fine-grained materials and k_S = -0.0463 for coarse-grained materials. The regression lines of coarse-grained materials are presented in Figure 2.8.

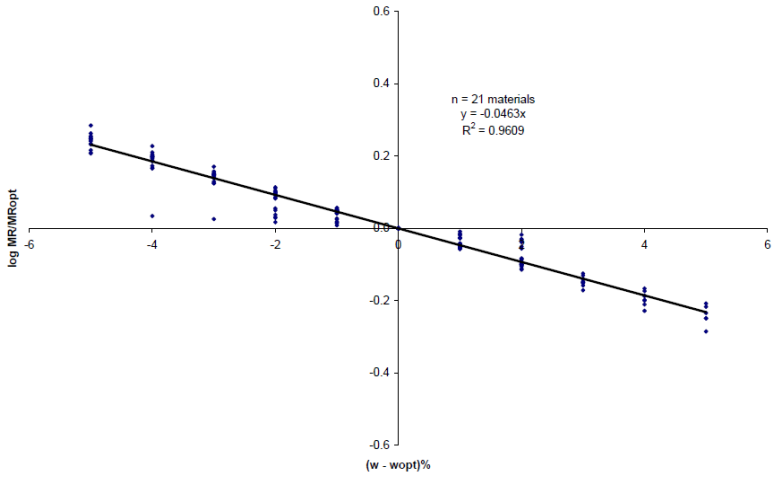

(a) Regression for k_w

(b) Figure 2.8 Linear regression in the semi-log space for coarse-grained materials (NCHRP, 2004)

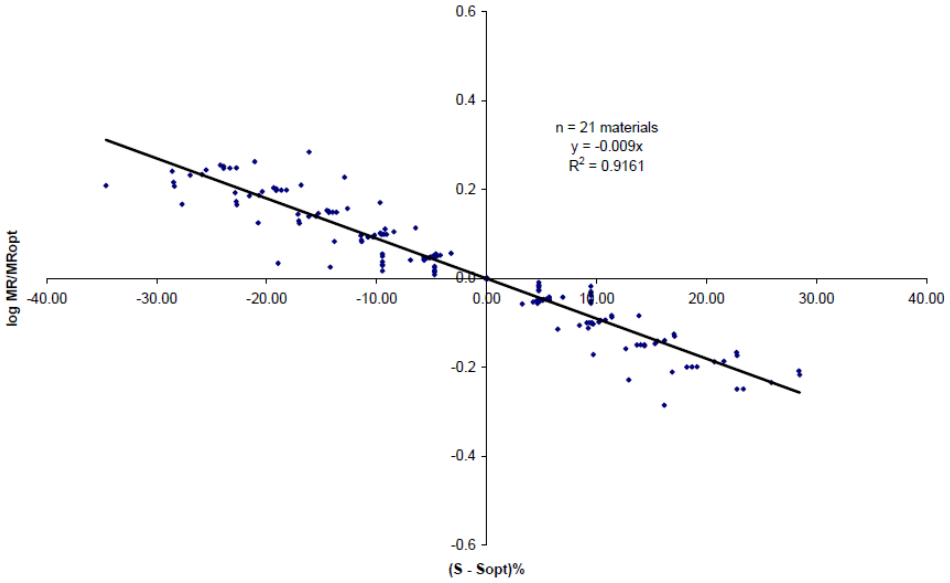

(c) Regression for k_s

Figure 2.8 Linear regression in the semi-log space for coarse-grained materials (NCHRP, 2004) (continued)

The linear regression, although providing a good interpretation, presents a limitation for extrapolation. It was found that most of base and subbase materials are usually at a low degree of saturation between 3% and 10%, which is more than 50% below the degree of saturation corresponding to optimum water contents. The data used to develop the linear regression consisted of test results ranging within ± 30% of the optimum degree of saturation. The MEPDG proposed a maximum modulus ratio of 2.5 for fine-grained materials and 2.0 for coarse-grained materials. The linear regression would overestimate the resilient modulus of a material if the degree of saturation is 30% less than the optimum degree of saturation. A revised model was developed to maintain the estimation conservative. The original linear regression was replaced by an S-curve that approaches the linear relationship observed within 30% of the optimum degree of saturation

but flattens out for the degrees of saturation of 30% lower than the optimum degree of saturation (NCHRP, 2004):

$$\log\left(\frac{M_R}{M_{r\,opt}}\right) = a + \frac{b-a}{1+EXP(\beta+k_s(S-S_{opt}))} \tag{2.20}$$

where a is the minimum of $\log(M_R/M_{R\ opt})$; b is the maximum of $\log(M_R/M_{R\ opt})$; β = ln(-b/a), location parameter to impose the condition of zero intercept; k_S = regression parameter; and (S – S_{opt}) = the variation in degree of saturation expressed in decimal.

The suggested values for the above parameters by MEPDG are presented in Table 2.5. Figure 2.9 presents the revised model.

Table 2.5 Coefficients for the moisture-resilient modulus model (after NCHRP, 2004)

Parameter	*Coarse-grained materials*	*fine-grained materials*
a	-0.3123	-0.5934
b	0.3	0.4
β	-0.0401	-0.3944
kS	6.8157	6.1324

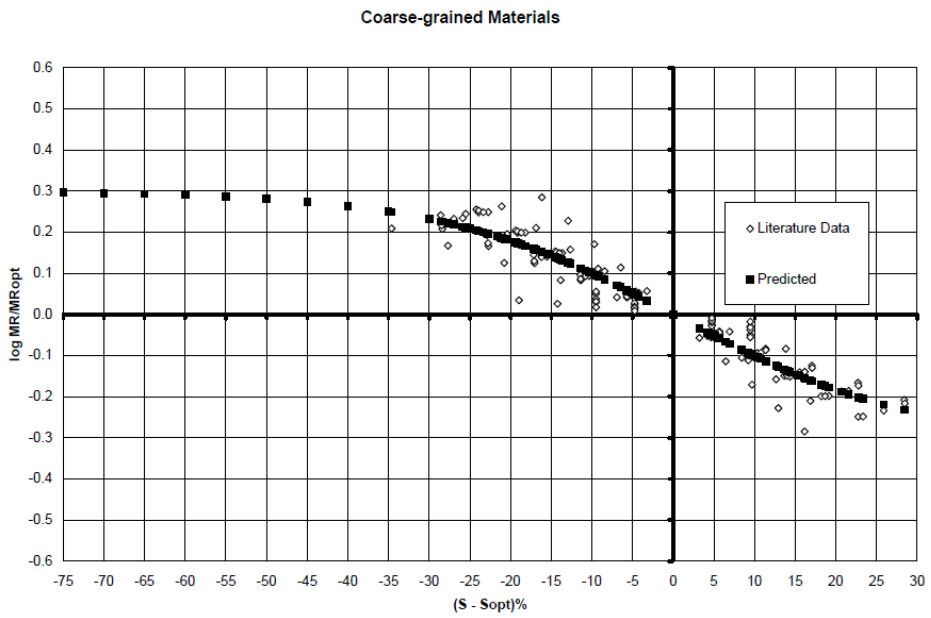

Figure 2.9 Revised model for coarse-grained material in semi-log scale (NCHRP, 2004)

2.5 Summary

This chapter first reviewed the mass transfer-based methods to estimate the evaporation rate of water. The mass transfer-based methods are empirical relationships between the environmental factors, such as temperature, relative humidity, the difference between saturated and partial vapor pressures, and the rate of water evaporation. These methods were proven to be able to estimate the water evaporation rate to a reasonable accuracy.

This chapter also reviewed the application of geotextile in pavement structures and the problem of geotextile in unsaturated soil. Geotextiles are installed in pavement structures often for its drainage function, however, in unsaturated soil the effectiveness of conventional geotextiles is reduced. The wicking geotextile aims to continue removing water from roadway structures even when the geomaterial becomes unsaturated. Based on case studies, the wicking geotextile showed promising ability to improve the performance of roadway structures.

The final part of this chapter briefly reviewed the 1993 AASHTO pavement design method and MEPDG. The review on the design guides focused on the effect of moisture on the pavement structure design. In both design guides, the major effect of moisture is on the unbound base/subbase materials.

CHAPTER 3 Qualitative experiments and evaporation estimation

This chapter presents the laboratory tests aiming to: (1) demonstrate the difference between the wicking geotextile and the conventional geotextile; (2) investigate the boundary effect on the wicking geotextile through vertical hanging tests; and (3) estimate the evaporation from the wicking geotextile under control temperature and relative humidity.

3.1 Material

Two geotextiles were tested in the laboratory tests reported in this chapter, one conventional woven geotextile and one wicking geotextile. Both geotextiles were fabricated and provided by the TenCate Geosynthetics.

The conventional woven geotextile was HP570 as the commercial name and its properties are listed in Table 3.1.

Table 3.1 Properties of conventional woven geotextile No. 1

Properties	**Unit**	**Minimum average roll value**	
		MD	CD
Tensile strength (2% strain)	kN/m	14	19.3
Tensile strength (5% strain)	kN/m	35	39.4
Flow rate	l/min/m^2	1222	
Permeability	cm/sec	0.5	
Permittivity	sec^{-1}	0.4	

Note: MD = machine direction and CD = cross-machine direction.

Table 3.2 Properties of wicking geotextile

Properties	Unit	Minimum average roll value	
		MD	CD
Tensile strength (2% strain)	kN/m	7	15.8
Flow rate	$l/min/m^2$	1222	
Permittivity	sec^{-1}	0.4	

3.2 Demonstration tests

Although the wicking geotextile has been successfully applied in the field, the behavior of the wicking geotextile has not been fully understood. The demonstration tests were performed to provide some understanding of the behavior of the wicking geotextile as compared with a conventional woven geotextile in their siphon behavior.

3.2.1 Test setup

In the first demonstration test, two 700 ml beakers were used as water containers. Geotextile specimens were 45 mm wide by 260 mm long. The geotextile specimens were placed over the edges of the beakers with half of their length inside the beaker. The beakers were filled with water to the 700 ml mark. Glass plates were placed over the beaker to limit evaporation from the water surface. The setup of the first test is shown in Figure 3.1 (a). The amount of water change in the beakers was measured by the water level change using a ruler.

Larger containers and specimens were used in the second test. In the second test, 4 liter water containers were used. The geotextile specimens were 120 mm wide and 335 mm long. The specimens were placed over the edges of the containers with 120 mm of the specimen outside of the container. Both containers were filled with 4 liters of water. The containers were covered with

plastic sheets to prevent evaporation from the water surface. The amount of water change in the containers was measure by a scale. The setup of the second test is shown in Figure 3.1 (b). In both tests, the geotextile specimens before placed in the water containers were dry.

(a)

(b)

Figure 3.1 Demonstration test setup

3.2.2 Test results and discussion

During the first test, the air temperature ranged from 21℃ to 25℃ and the relative humidity ranged from 27% to 47%. During the second test, the air temperature ranged from 21℃ to 24℃ and the relative humidity ranged from 16% to 30%.

In both tests, the volume changes of water in the water containers were measured over time. At the beginning of Test 1, water drops were observed at the ends of the exposed geotextile specimens. As the test progressed, water drops disappeared from the conventional geotextile specimens. Test 1 was terminated at 113 hours into the test as the water level in the wicking geotextile container approached to the end of the wicking geotextile specimen as shown in Figure 3.2.

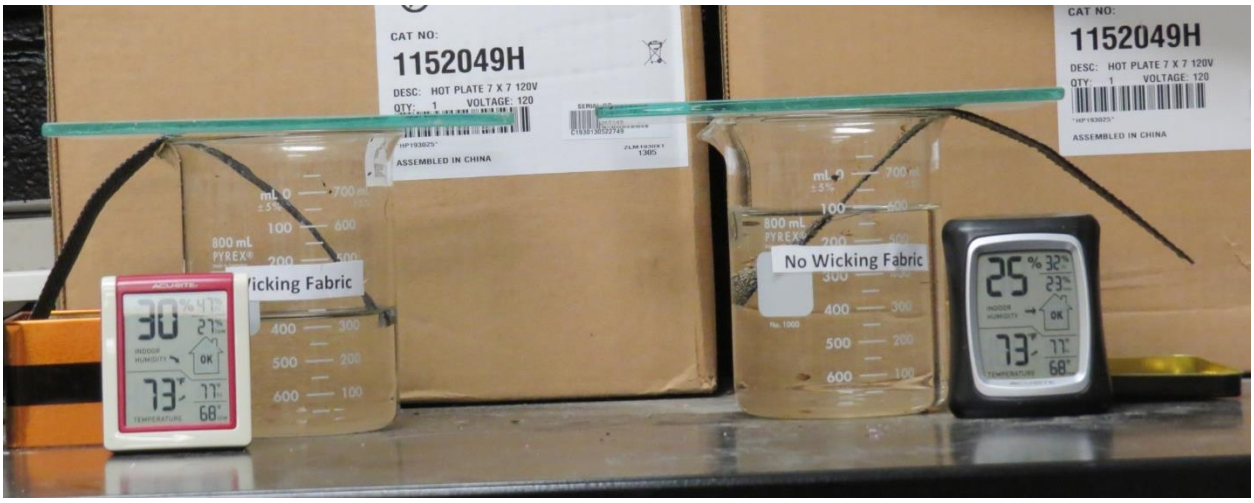

Figure 3.2 Water level at the end of 1st demonstration test

In the second test, no water drop was observed at the end of the conventional geotextile. The exposed part of the conventional geotextile specimen was adjusted to steepen the gradient of

the exposed portion of the specimen. The adjustment did not result in water drop at the end of the conventional geotextile. Water drops were observed on both wicking geotextiles at the ends of the exposed parts. In the early stage of both tests water dropped from the wicking geotextile specimens frequently. The frequency of water drop decreased as the test progressed. Eventually no water drop was observed at the end of the wicking geotextile specimens; however, the exposed portion of the wicking geotextile specimen remained wet.

Two different specimen widths were used in these two demonstration tests, to compare their results. The parameter of water volume change in the container to the width of the geotextile specimen (i.e., ml/mm) is adopted herein to present the test results as shown in Figure 3.3.

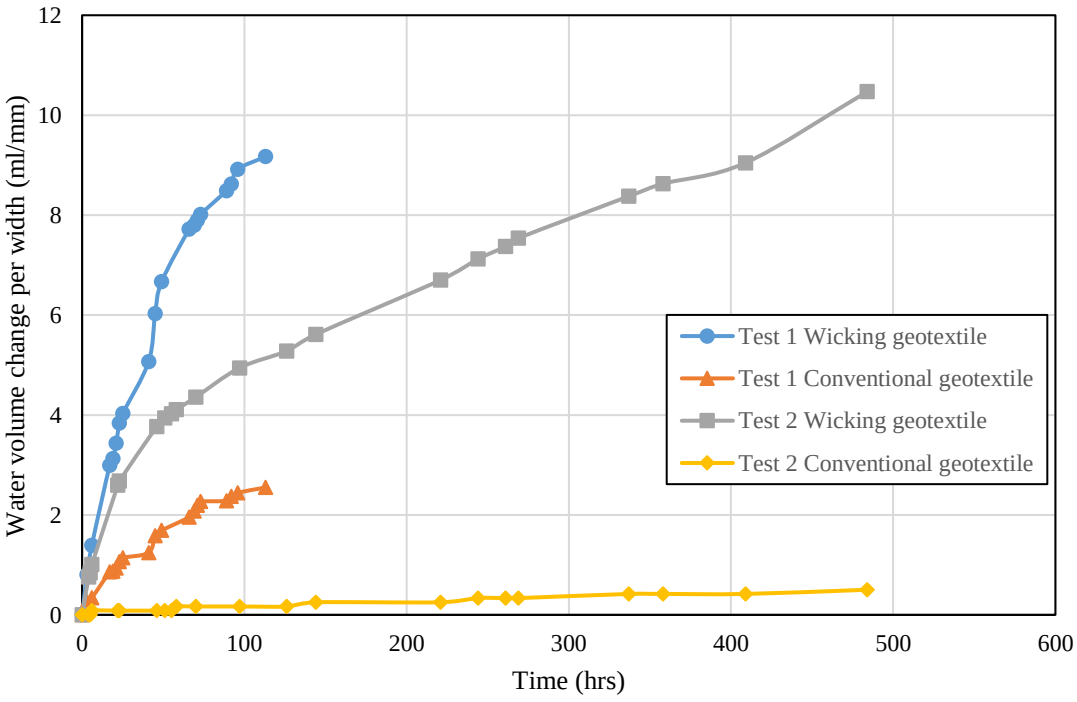

Figure 3.3 Water volume change in the container per width of geotextile specimen with time

From Figure 3.3, in the second test, the water volume changed insignificantly in the water container with the conventional geotextile. This result is consistent with no observed water drop from the conventional geotextile specimen. The evaporation from the water surface is likely the cause for the volume change of water in the container with the conventional geotextile in the second test. The conventional geotextile in the first test did remove water from the container. For the geotextile specimen to transport water from the container, the water in the container needed to travel upwards against the gravity to the edge of the container with in the geotextile specimen. After passing over the edge of the container, the water within the geotextile specimen traveled along the gradient of the geotextile in a downward direction under the action of gravity thus forming a siphon. The action of water traveling against gravity in an initially dry porous medium, such as geotextile, requires capillary force. It is believed that the conventional geotextile specimen in the second test could not provide sufficient capillary force for the water to reach the edge of the container. Both wicking geotextile specimens showed exceptional ability to remove water compared to the conventional geotextile specimens. The ability of the wicking geotextile to generate capillary force to form a siphon should attribute to the wicking fibers.

The water volume changes from the first test demonstrates the difference in the water removal ability between conventional and wicking geotextiles. A simple, linear regression was used to estimate the rate of water removal from the containers, as shown in Figure 3.4. Based on the slope of the regression line, the water removal rate by the wicking geotextile is approximately 3.7 time of the water removal rate by the conventional geotextile. As the conventional geotextile did not result in significant water volume change in the second test, such a comparison based on the second test results is not appropriate.

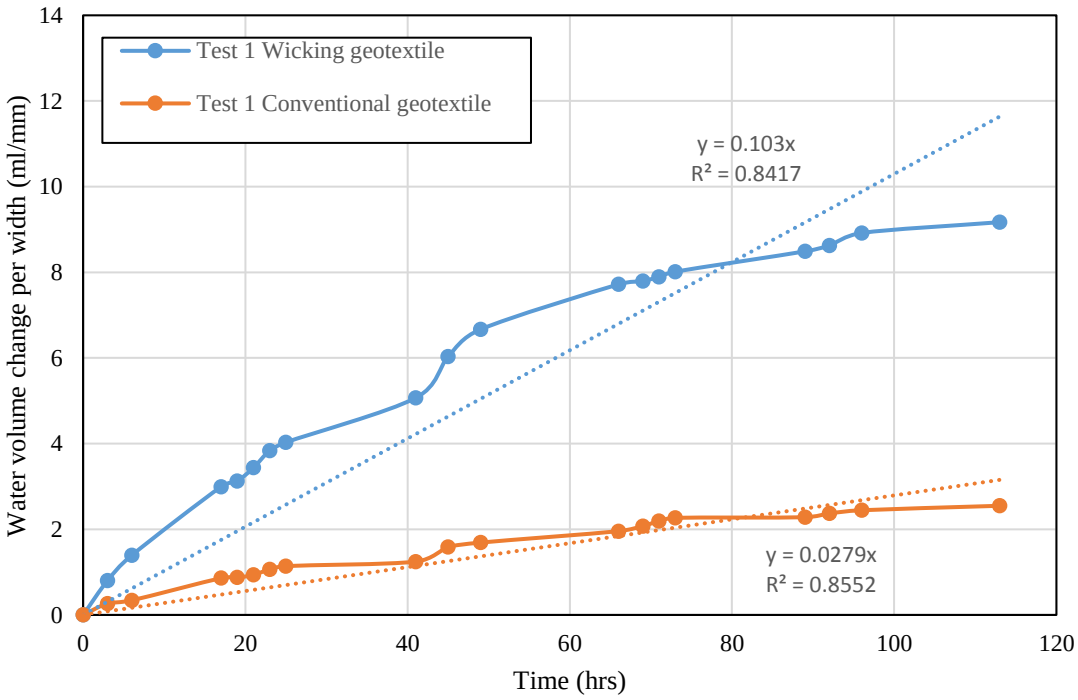

Figure 3.4 Comparison of water removal rates from conventional and wicking geotextiles

The water volume changes in the containers with wicking geotextiles in both tests are presented in Figure 3.5. Figure 3.5 indicates the water volume change in the container or water removal by the wicking geotextile specimens can be divided into two portions: an initial portion with higher water removal rate and a later portion with a reduced removal rate. The trend of water removal consists of the observed water drops at the ends of the wicking geotextiles specimens. The initial higher rate of water removal resulted from rapid water dropping from the exposed geotextile specimens. The later lower water removal rate could result from water evaporation from the exposed geotextile surface into the air. It is deducted that the capillary force generated by the wicking geotextile at the beginning of the tests was able to transport a relatively large quantity of water to supply the formation of the water drop. As the amount of water decreased in the container,

the distance from the water surface to the edge of the container increased. Thus water passed over the edge of the containers in a much smaller quantity. Although the reduced amount of water was not able to form water drops, it was able to maintain the exposed portion of the wicking geotextile specimens relatively wet for evaporation. Thus evaporation became a major parameter for evaluation of the water removal ability of the wicking geotextile.

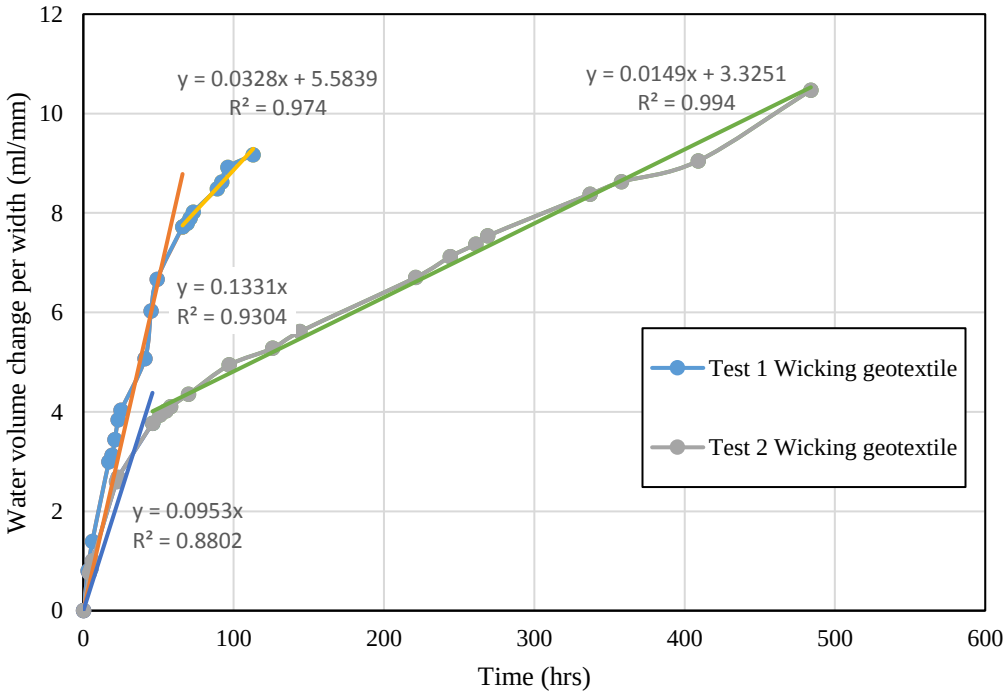

Figure 3.5 Comparison of water removal rates from the wicking geotextiles

3.2.3 Conclusion

The demonstration tests showed the ability of the wicking geotextile to generate capillary force to remove water from a container. One of the conventional geotextile specimens failed to remove water from its container. The water was removed by the wicking geotextile through water flow in the geotextile and evaporation from the geotextile surface. The evaporation on the wicking

geotextile surface continued removing water from the container even after the water stopped dropping from the end of the exposed wicking geotextiles specimen. Evaporation action was identified as a factor describing the ability of wicking geotextile to remove water.

3.3 Vertical hanging test

Geotextiles in the practice are usually continuous in the machine direction. Such a condition cannot be achieved in a laboratory due to limited space. Thus geotextile specimens are usually cut in the cross-machine direction. The cutting process not only breaks the continuity of the yarns but also distorts the arrangement of the yarns near the cut. Water moves through a geotextile in the void between the yarns; therefore, a distortion in the yarn arrangement will influence the hydraulic properties of a geotextile. Boundary effect thus became a major concern for the design of wicking geotextile experiment. The geotextile specimens should have sufficient width so that the distortion at the boundary does not influence the overall hydraulic properties of the specimens. The demonstration tests in the previous section showed the ability of the wicking geotextile to generate capillary force, which is an important aspect to the water removal efficiency of the wicking geotextile. Thus the effect of specimen width on its ability to generate capillary force was investigated and the suitable width of specimen without a boundary effect was identified and used in later tests. The vertical hanging test is one way to measure the capillary force generated by a textile. The textile specimens are hung from a beam and the lower end of the specimen is submerged in water. If a textile is able to generate capillary force, water will be driven by the capillary force to move upwards along the textile. The vertical distance between the wet front and the water reservoir surface is an indicator of the capillary force: the larger the distance, the higher the capillary force. In the vertical hanging test, wet front movement in geotextile specimens with

different widths were measured to determine whether the width of a specimen influenced its ability to generate capillary force.

3.3.1 Test setup

Figure 3.6 presents pictures of the test setup. This test was conducted in a room where the air temperature was approximately 15℃ and the relative humidity of the room was approximately 30%. A water reservoir of 1.6 m × 1 m (L × W) was constructed with timber and lined with 6 mil plastic sheet. The beam was approximately 1 m above the reservoir water surface. Specimens were cut in the cross-machine direction (i.e., the wicking yarns were in the vertical direction). All specimens were 1.1 m long and fixed to the beam with clamps. The lower ends of the specimens were fixed to a small PVD tube and put in water simultaneously, as shown in Figure 3.6. A video camera facing the specimens was used to record the movement of wet front in time. Two rulers were also hanged from the beam to measure the rise of water front. Markings were also made on geotextile specimens in 5-inch (125 mm) intervals. The distances between the wet fronts and the water surface (i.e., the wet front height) were observed based on the color change of the geotextile specimen. In Figure 3.7, the wet fronts were marked by yellow lines. Figure 3.7 shows that the wet fronts in wider specimens were not straight. The average height of the water front was used to represent the water rise in the specimen.

(a)

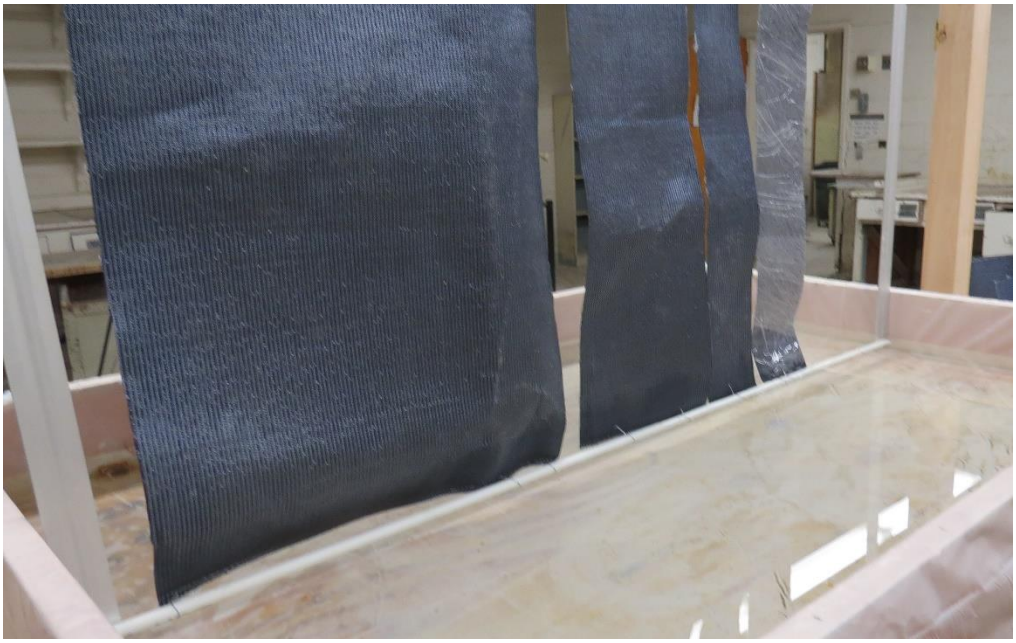

(b)

Figure 3.6 Pictures of the vertical hanging test.

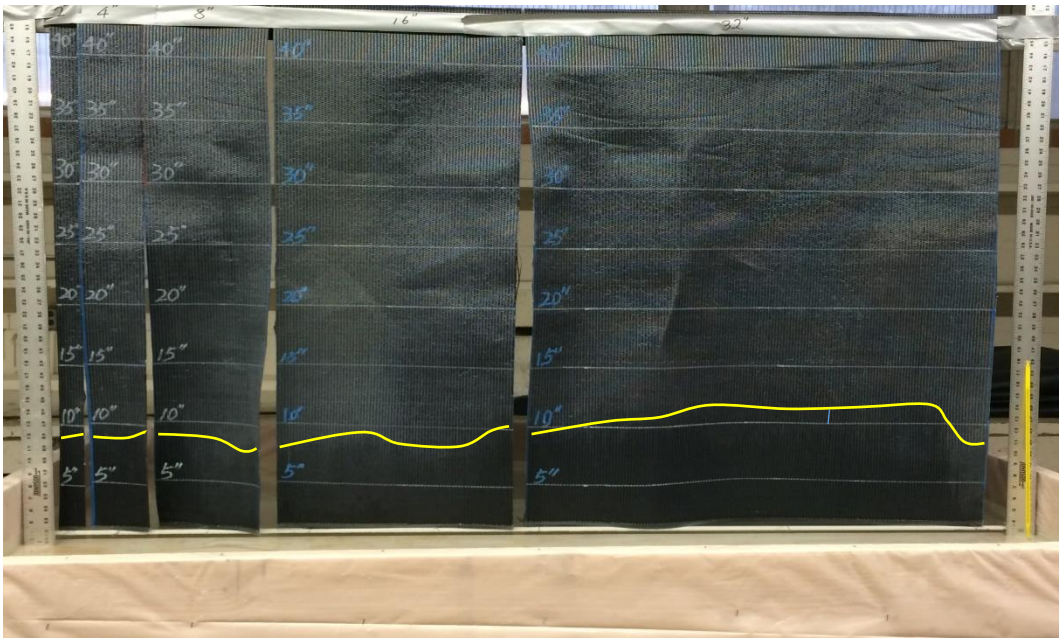

Figure 3.7 Locations of wet fronts on the wicking geotextile specimens at 120 min into the test

3.3.2 Test results and discussion

The tested specimens had widths of 50, 100, 200, 300, 400, 600, 800, and 1600 mm. The wet fronts stopped rising at approximately 120 min after the specimens were placed in contact with water. Figure 3.8 presents the wet front heights on the wicking geotextiles with time. The wet fronts rose rapidly within the first 40 min. Then the movement of wet fronts slowed down between 40 to 120 min. Little increase in the heights of wet fronts was observed between 90 min and 120 min. The heights of the wet fronts on the specimens of different widths at each observation time were relatively similar except for the specimen of 600 mm. Later inspection found a large amount of dust was the surface of the specimen of 600 mm. The dust might have obstructed the observation of wet fronts. At 120 min, the wet fronts in most specimens were over 200 mm above the water surface. The scatter of the data points within the first 50 min of the test were very narrow.

The scatter of data points became wider with the progress of the test; however, the heights of most wet fronts were within 50 mm from each other.

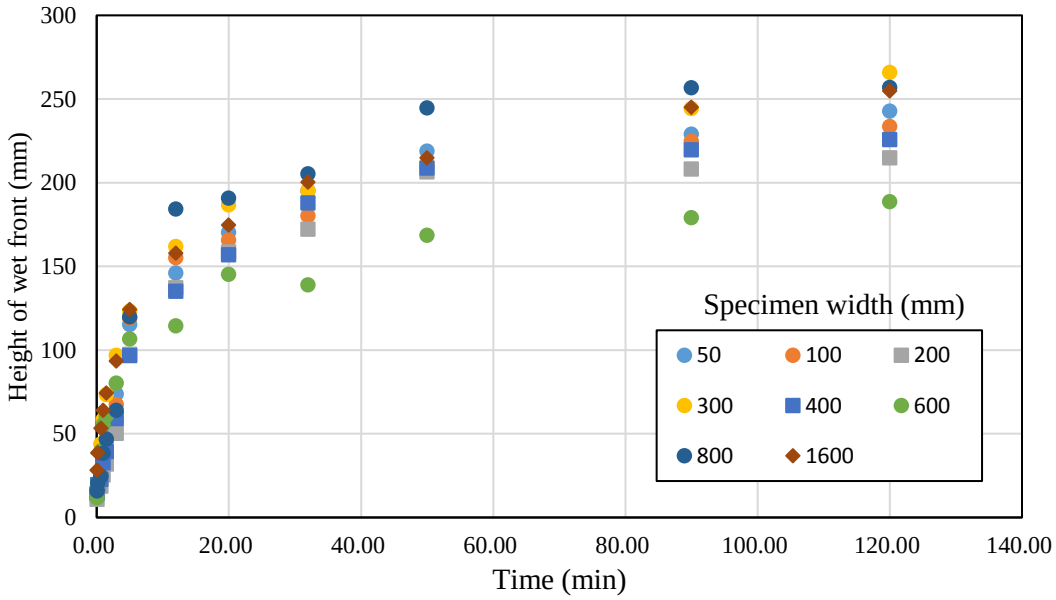

Figure 3.8 Heights of wet fronts on geotextiles with time

Figure 3.9 presents the distance from the wet front to the water surface versus the width of the specimen at 120 min after the specimen was in contact with water. At 120 min, the heights of the wet fronts on the specimens of 300, 800, and 1600 mm wide were over 250 mm. However, the heights of wet fronts of the narrower specimens (i.e., 50, 100, and 200 mm wide) were between 200 and 250 mm. No definitive evidence of boundary effect was found based on the heights of wet fronts. Therefore, it is concluded that the width of the specimen did not affect the ability of the wicking geotextile to generate capillary force. The yellow lines in Figure 3.7 present the wet fronts on the wicking geotextile specimens of 50, 100, 200, 400, and 800 mm wide. It was observed that the wet fronts on wider (i.e., 400 and 800 mm) specimens were not even. The uneven

distribution of wet fronts on large specimens might result from the variation in the production of wicking geotextile. The unevenly distributed wet fronts might complicate analysis of test results in further tests. It was concluded that geotextiles with an intermediate width should be chosen for the specimens in later tests so that they were not too wide for uneven wet fronts. It was also concluded that later tests should use specimens with a sufficient number and width to minimize the variability of test results for the wicking geotextiles.

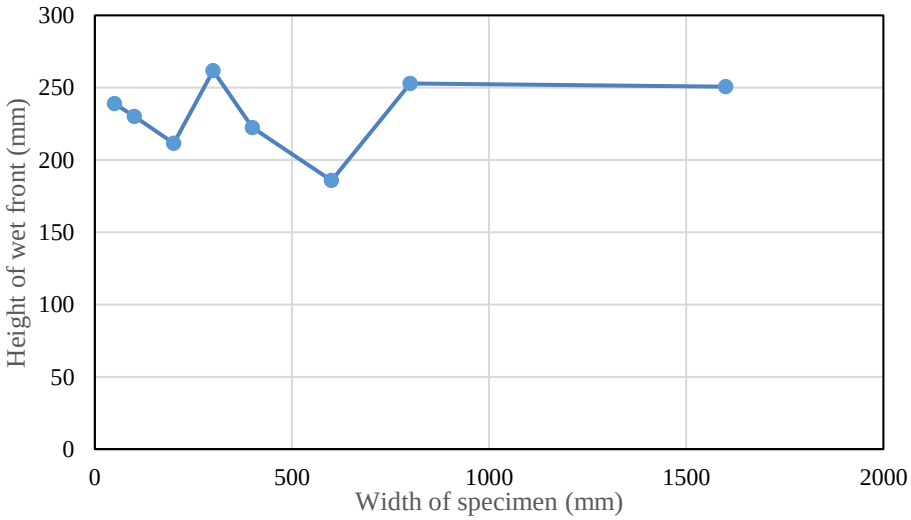

Figure 3.9 Height of wet front versus width of specimen

The vertical hanging test showed that the geotextile was capable of transporting water against gravity. When a local concave is present at the interface between base and subgrade, free water entering a roadway structure tends to accumulate at the concave location due to hydraulic gradient (such a phenomenon is called ponding). The excess moisture at the concave weakens both base and subgrade materials. The weakened base and subgrade material deform more under traffic loading result in the increase of the concave size. Conventional drainage systems which

rely on hydraulic gradient to remove water are not effective in removing water from ponding as the hydraulic gradient drives the water into the ponding location. The ability of wicking geotextile to transport water against gravity can reduce the water accumulation due to ponding.

3.4 Horizontal wicking test

Geotextiles are usually placed in roadway structures in the horizontal direction. Therefore, the location of wet front in a wicking geotextile specimen placed in a horizontal plane should be investigated.

3.4.1 Test setup

A schematic of the test setup for a horizontal wicking test is presented in Figure 3.10. The horizontal wicking test was conducted in a temperature-controlled room. The room temperature could be controlled between 0℃ to 10℃. A water tank of 250 mm x 500 mm x 300 mm (L×W×D) was used as a water reservoir. The water tank was placed next to a long table on a lower table so that the top of the water tank was approximately at the same level with the long table. A 1.3-m long wicking geotextile specimen was placed on the long table. Based on the vertical hanging test, a geotextile specimen of 300 mm wide was selected. One end of the specimen was placed in the water tank, which was then filled with tap water to 20 mm below the top of the tank. Each specimen was let on the table for 48 hours so that the wet front could be stabilized. A dehumidifier was used to control the relative humidity in the test room. As previously stated, visual inspection of the sample could not accurately determine the location of the wet front. Therefore, the water content of the wicking geotextile specimen by weight was used to determine the location of the wet front. At the end of each test, the geotextile specimen was cut into 50 mm or 100 mm long segments. Each section was weighted right after the cut was made. After the entire specimen was

cut and weighted, the geotextile segments were transported into an oven and dried at 105℃ for 24 hours. The dried segments were then weighted again to determine their dry weights. The water content of the wicking geotextile specimen was determined in the same way as the determination of soil water content. The location of wet front can be determined based on the distribution of water content along the distance from the source of water.

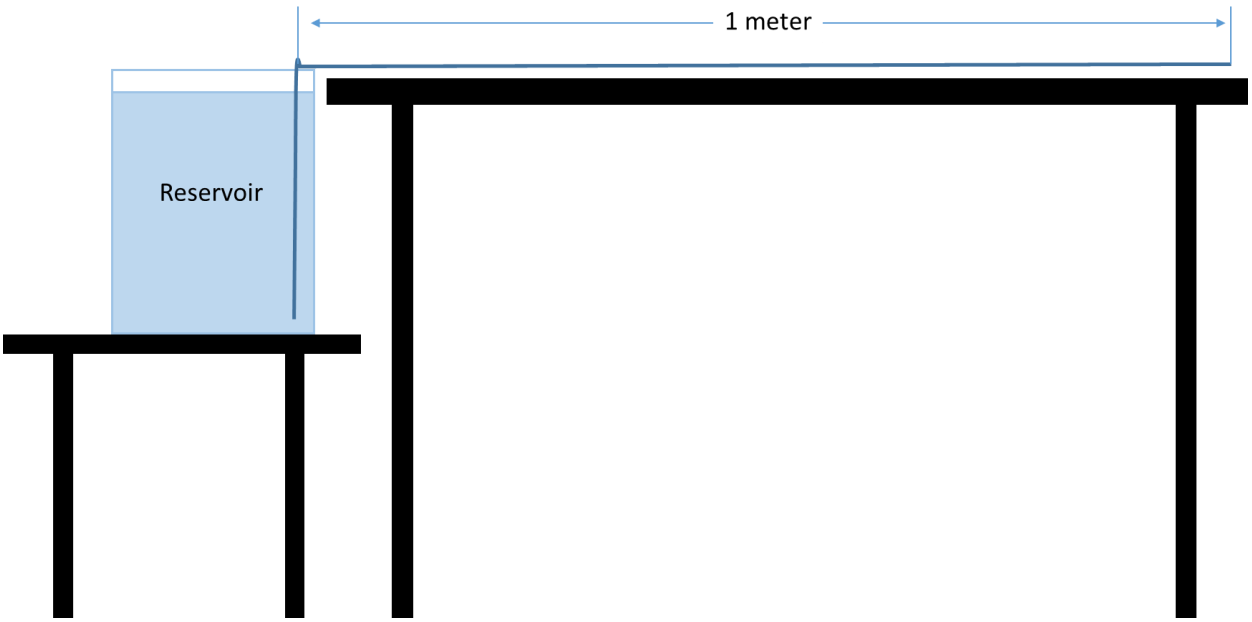

Figure 3.10 Schematic of horizontal wicking test setup

3.4.2 Test results and discussion

Figure 3.11 presents the distribution of water content of the wicking geotextile specimen with the distance to the water source under different air temperature and relative humidity. The legend in Figure 3.11 represents the test conditions: the number following the letter "T" indicates the test air temperature in degree Celsius while the number following the letters "RH" indicates the relative humidity in percentage. The horizontal wicking test was conducted under five

combinations of temperature and relative humidity. No gravitational drainage was observed during the test. Under all the conditions, the distance from the wet front to the water source was over 0.6 m, significantly longer than the wetted height recorded in the vertical hanging test. The maximum distance between the wet front and the water source was over 1 m when the air temperature was 8.2℃ and the relative humidity was 96.3%. The minimum wetted length was slightly over 0.6 m when the air temperature was 7.3℃ and the relative humidity was 65.3%. The wetted length of the wicking geotextile was longer under higher relative humidity or lower evaporation potential. The water content gradient indicates the amount of water within the geotextile specimen decreased as the distance from the water source increased. The relationship between the water content and the distance to the water source appears to be linear. The water contents close to the water source varied significantly between 30% and 60%, which might result from material variation.

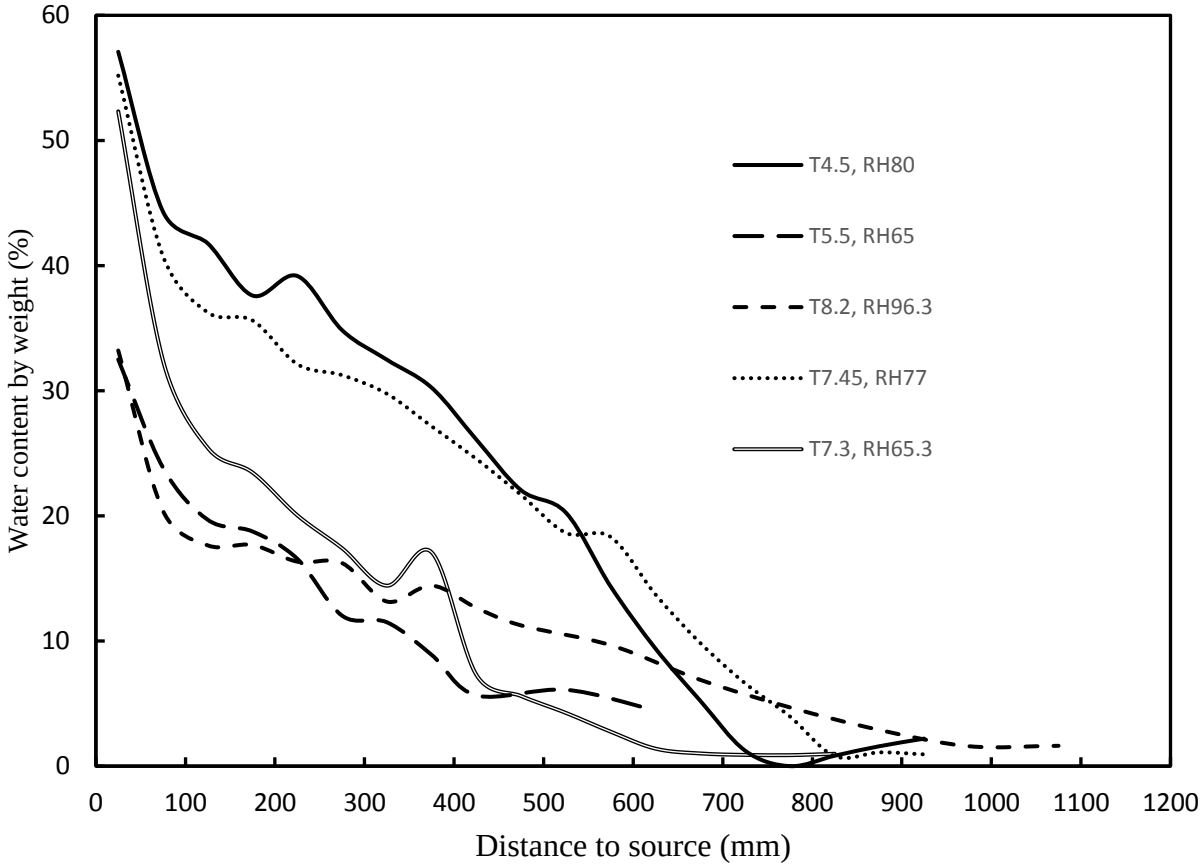

Figure 3.11 Variation of water content in the horizontal wicking test

The wetted lengths under different evaporation conditions indicate the effect of evaporation. When the evaporation potential was low, less water evaporated from the wicking geotextile into the air thus the wetted length was longer. The wetted length varying with evaporation potential presents a conundrum in estimating the evaporation from the wicking geotextile. The total amount of water removed by a geotextile via evaporation is the product of evaporation rate and evaporation area (or wetted length). Contrary to the relationship between wetted length and evaporation potential, the evaporation rate increased with the increase in evaporation potential. The following

section provides more detailed discussion regarding the influence of evaporation potential on the total evaporation from the wicking geotextile.

3.5 Quantitative evaporation test

3.5.1. Gravitational and evaporation drainage

As discussed earlier in this chapter, wicking geotextile specimens could remove water from containers by forming water drops at the exposed ends of the specimens and evaporate water from the surface of the specimens. These two mechanisms of wicking geotextile to remove water should be considered separately. The movement of water in an initially dry geotextile specimen can be described as a wetting process, in which the wetting front is formed as shown in Figure 3.12. Note that the portion of the geotextile between the wet front and the water source is not necessarily saturated. The water in the wetted portion of a geotextile evaporates due to the relative humidity difference between the geotextile and air. The total amount of water evaporating from a geotextile surface (E_g) is the product of the wetted area of the geotextile and the evaporation rate from the wetted geotextile surface. The wetted area of a wicking geotextile specimen is the product of the width of the specimen and the wetted length (L_w). The rate of evaporation depends on parameters, such as temperature, relative humidity, and vapor pressure. When the amount of water entering the geotextile (E_w) equals to the total amount of water evaporating from the geotextile surface (E_g), the wet front is stationary, as shown in Figure 3.13(b). When the amount of water entering the geotextile is less than the total amount of water evaporating from geotextile surface, the wetting front moves toward the water source and the wicking geotextile is under a drying process, as shown in Figure 3.13(c). If the amount of water entering the geotextile is more than the total amount of water evaporating from the geotextile surface, the wet front moves away from the water source and eventually stops at the exposed end of the geotextile. When the wet front is at the end of the

geotextile, the capillary force or suction of the wicking geotextile prevents the water from leaving the geotextile and moisture starts to accumulate. Water drops start to form when enough hydraulic gradient is achieved to overcome the suction by the wicking fibers in the geotextile, as illustrated in Figure 3.13(a). Gravitational drainage is achieved as water drops from the wicking geotextile.

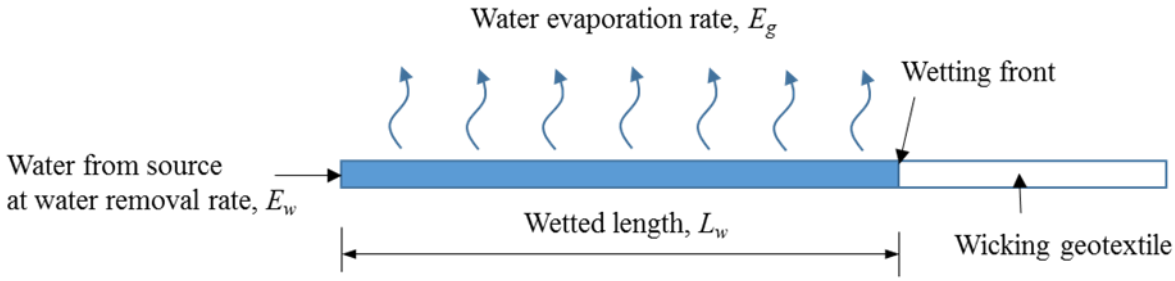

Figure 3.12 Schematic of water transport and evaporation in the wicking geotextile (Guo et al., 2016)

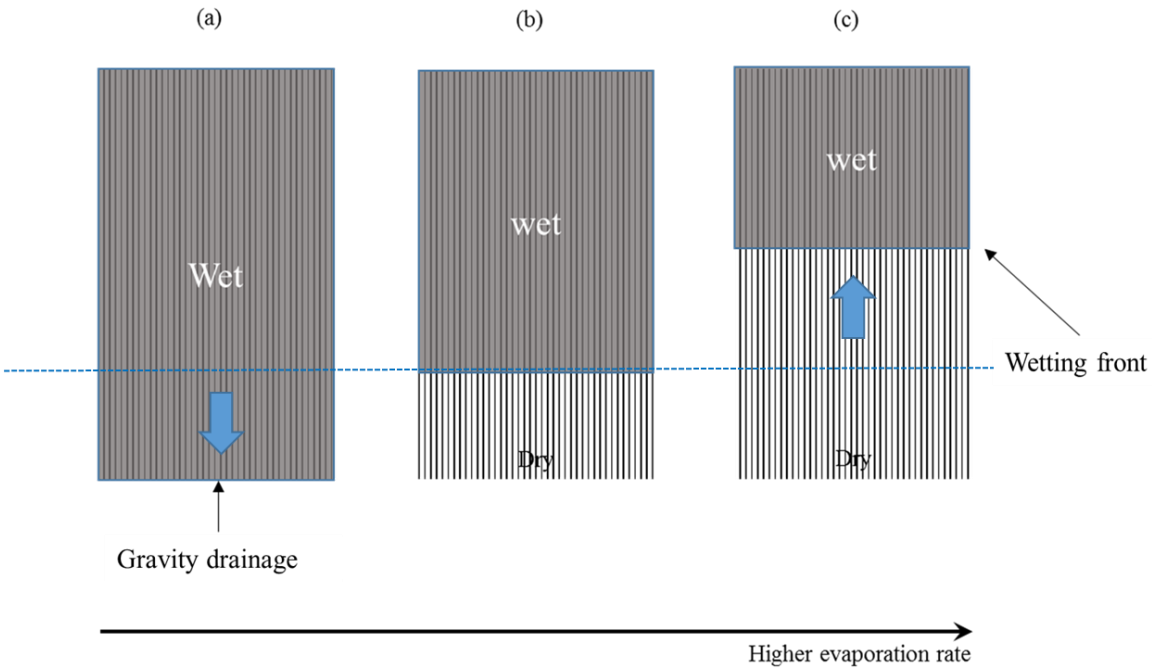

Figure 3.13 Schematic of the movement of wet front under different conditions (Guo et al., 2016)

3.5.2 Method for water removal via evaporation by wicking geotextile

The exposed length of the wicking geotextile should be equal to or greater than the wetted length of the wicking geotextile to have the maximum water removal via evaporation. The location of the wet front depends on the capillary force of the geotextile, the rate of water flow in the geotextile, and the water evaporation rate from the geotextile surface. However, a theoretical solution to calculate the wetted length remain elusive. The difficulty in developing such a solution results from the incomplete saturation of the geotextile. In other words, the movement of water in the geotextile is in the form of two immiscible fluids (i.e., air and water) moving through a porous media. The unsaturated flow in the wicking geotextile follows the generalized Darcy law (Bear, 1972; Helmig, 1997; and Szymkiewicz, 2007), which requires the water pressure, water viscosity, absolute permeability of the geotextile, and relative permeability with respect to water. The relative permeability with respect to water depends on the degree of saturation of a porous medium (the wicking geotextile in this case). As shown in Section 3.3, the water content of the wicking geotextile varied with the distance and is difficult to determine. This situation makes the generalized Darcy law impractical to calculate the wetted length. Experimental determination of the wetted length is also difficult. Based on the experience from the previous vertical hanging test, visual inspection and measurements cannot determine the wetted length accurately during the test. The test method used in the horizontal wicking test is applicable to specimens placed horizontally. Due to the high transmissivity of the wicking geotextile, as any gradient in the geotextile specimen would cause the water within the geotextile flow towards the lower gradient rapidly which result in errors of water content measurements.

Even though the wetted length cannot be accurately measured or theoretically calculated, it may be obtained based on the equivalence of water mass change due to the wicking geotextile

specimen if gravitational drainage does not occur. In other words, the amount of water removed from a reservoir by a wicking geotextile specimen should be equal to the amount of water evaporated from the wicking geotextile specimen. Considering Figure 3.12 represents a cross-section of a unit width of a geotextile specimen. The water removal rate by a unit width of a wicking geotextile, E_w, equals to the average water evaporation rate from the geotextile of a unit area, E_g, multiplied by the wetted length of the geotextile, L_w, i.e.,

$$E_w = E_g L_w \tag{3.1}$$

Dividing the average water evaporation rate from a free water surface, E, at both sides of equation 21:

$$\frac{E_w}{E} = \frac{E_g L_w}{E} = L_{we} \tag{3.2}$$

where L_{we} is the equivalent water surface evaporation length.

3.5.3 Test setup

Figure 3.14 presents the test setup of a laboratory study. Nine water tanks with the dimension of 250 mm wide, 500 mm long, and 300 mm deep each were used as water reservoirs for wicking geotextile specimens. A ruler with accuracy of 1 mm was attached on one side wall of each tank to measure the water level change during the test. These tanks were placed in a temperature-controlled room. A dehumidifier was used to automatically adjust the relative humidity in the room to a desired value. When the relative humidity in the room was higher than the desired value, the dehumidifier was automatically turned on. Before each test, all of these nine tanks were filled with regular tap water. Temperature of the room was set to a target temperature.

One day was allowed for the room to reach the desired temperature. At the same time, the dehumidifier was turned on to adjust the room relative humidity to the desired value. After the room air condition (i.e., the temperature and relative humidity) reached the desired values, the wicking geotextile specimens were placed into the tanks. Geotextile specimens were placed in seven water tanks while the other two tanks without any geotextile were used as the control tanks. Each wicking geotextile specimen had a dimension of 600 mm long and 300 mm wide with wicking fibers oriented in the longitudinal direction. Each specimen was folded over the 500-mm long edge of the tank. A half length of each specimen was submerged into water and the other half was hung outside of the tank, which was exposed to the air as shown in Figure 3.14. A pair of small circular magnets with a diameter of 15 mm were used to fix a specimen both inside and outside the tank. Each test was conducted for one week. During this period, the water temperature was also measured, which was approximately the same as the desired air temperature. Therefore, the air temperature reported in this paper is also the water temperature. After each test was finished, water in the tanks was replaced and the tested specimens were discarded. The room temperature and relative humidity were recorded by the Dickson TM 320 thermometer every hour. The water temperature and the water level in each tank were measured every 24 hours. It should be noted that the reading of the water level was taken starting from the second day of the test, which excluded the amount of water absorbed into the geotextile after a dry specimen was placed into a water tank (i.e., the amount of water in the wetted area of each geotextile specimen). In other words, the water level change was calculated after the wet front in the geotextile became stable.

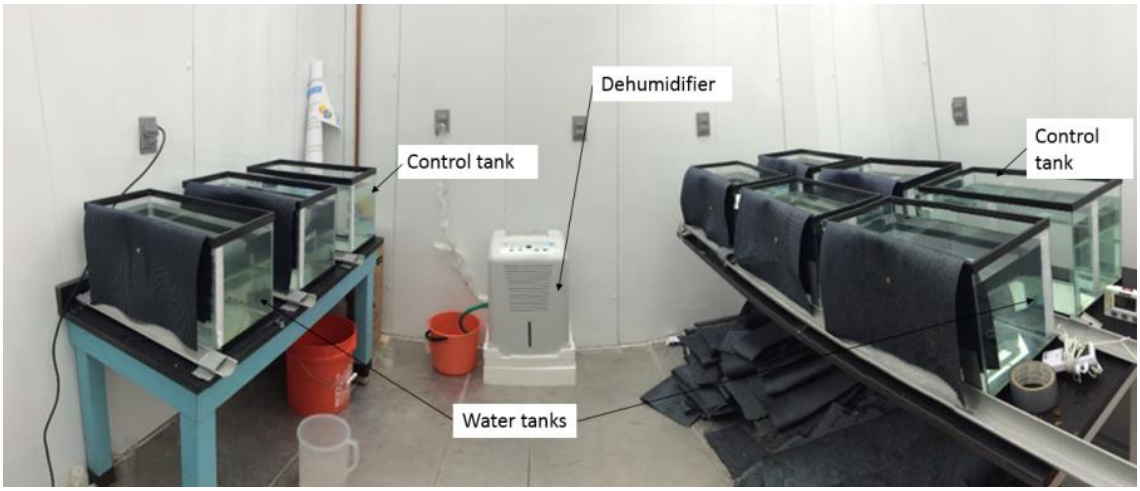

Figure 3.14 A picture of evaporation test setup

Table 3.3 provides the information on the test conditions for 12 tests conducted in this study. The temperature varied from 4.0°C to 30°C while the relative humidity changed from 51.2% to 86.8%. The temperature and relative humidity provided in the table are average values during the test duration. The water removal rate was calculated using the total amount of water removed from each water tank divided by the test duration. Visual inspection on the specimens was carried out every 24 hours to examine any possible liquid water drop at the exposed end. If water drop was observed in a test, the test was marked as "GD" (i.e., Gravitational Drainage) in Table 3.3. Among 12 tests, three tests had gravitational drainage. In other words, the water loss in the reservoirs in these tests was not fully removed by evaporation. These test data were excluded from the following data analysis to evaluate the water removal rate by the wicking geotextile through evaporation. The water removal rate by the wicking geotextile reported in Table 3.3 is the average value from seven water tanks containing wicking geotextiles under each test condition while the water evaporation rate without a wicking geotextile is the average value from two control tanks.

Table 3.3 Test conditions and water removal rates of all tests

	Test condition			Total water removal rate		Note
Test No.	Temperature	RH	Duration	W/O	W/	
	^{o}C	%	hours	x10^3 mm^3/hr	x10^3 mm^3/hr	
1	25	61.7	170	5.3	11.9	
2	20	86.8	165	2.1	9.2	GD
3	25	65.2	211	4.5	11.1	GD
4	30	58.7	144	8.7	15.8	
5	10	51.2	172	7.3	14.0	
6	10	56.6	168	7.1	13.9	
7	10	58.7	169	6.5	13.0	
8	10	62.0	166	4.8	10.7	
9	10	72.9	169	4.1	8.4	
10	10	77.7	168	4.8	7.8	GD
11	4	71.7	174	3.7	5.5	
12	8	71.7	143	3.5	6.3	

Note: RH = relative humidity; W/ = tank with a wicking geotextile; W/O = tank without a wicking geotextile; GD = Gravitational Drainage.

3.5.4 Test results and analysis

Table 3.3 shows that the total water removal rate of the water tank with a wicking geotextile was much larger than that without a wicking geotextile. The water removal rate by the wicking geotextile can be calculated as the water removal rate from the water tank with the wicking geotextile subtracting the water removal rate (i.e., the water evaporation rate) from the control tank without a geotextile under the same test condition. Table 3.4 provides the water removal rates by

wicking geotextiles in all the tests in this laboratory study. The test results show that the increase of the relative humidity reduced the water removal rate. The increase of the temperature increased the water removal rate. These test results were also analyzed using the three methods mentioned in the previous chapter. In the analysis, the water evaporation rate from the water tank was calculated based on the tank unit surface area while the water removal rate by the wicking geotextile was calculated based on the specimen unit width.

Table 3.4 Water removal rates by wicking geotextiles in the tests

Test No.	Temperature ^{o}C	Relative Humidity %	WR_w $x10^3\ mm^3/hr$
1	25	61.7	6.6
2	20	86.8	7.1
3	25	65.2	6.6
4	30	58.7	7.1
5	10	51.2	6.7
6	10	56.6	6.8
7	10	58.7	6.5
8	10	62.0	5.9
9	10	72.9	4.3
10	10	77.7	3.0
11	4	71.7	1.8
12	8	71.7	2.8

Note: WR_w = water removal rate by the wicking geotextile.

The Romanenko (1961) equation can be used to calculate the water evaporation rate of the control water tank based on the temperature and the relative humidity. From the Romanenko (1961) equation no water evaporation could occur when the relative humidity was equal to 100%. Based

on the test data, constants *A* and *B* could be back-calculated as 1.46×10^{-4} and 75, respectively. Therefore, the Romanenko (1961) equation can be rewritten as follows:

$$E = 1.46 \times 10^{-4} \left(T + 75\right)^2 \left(100 - RH\right) \qquad (3.3)$$

Figure 3.15 presents the comparison of the average water evaporation rate of the control water tanks calculated by Equation (23) with the experimental data. In Figure 3.13, the y-axis presents the measured water removal from control water tanks while the x-axis presents the calculated water removal based on the Romanenko (1961) equation.

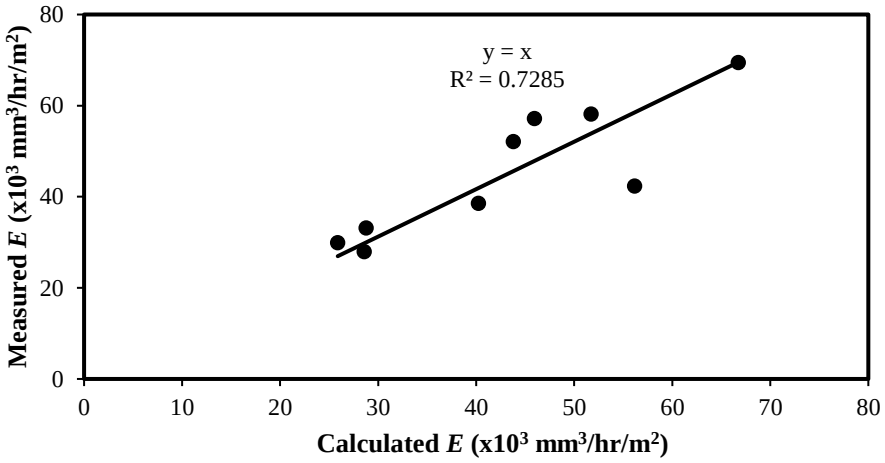

Figure 3.15 Water evaporation rates of the control tanks measured and calculated using the Romanenko (1961) equation

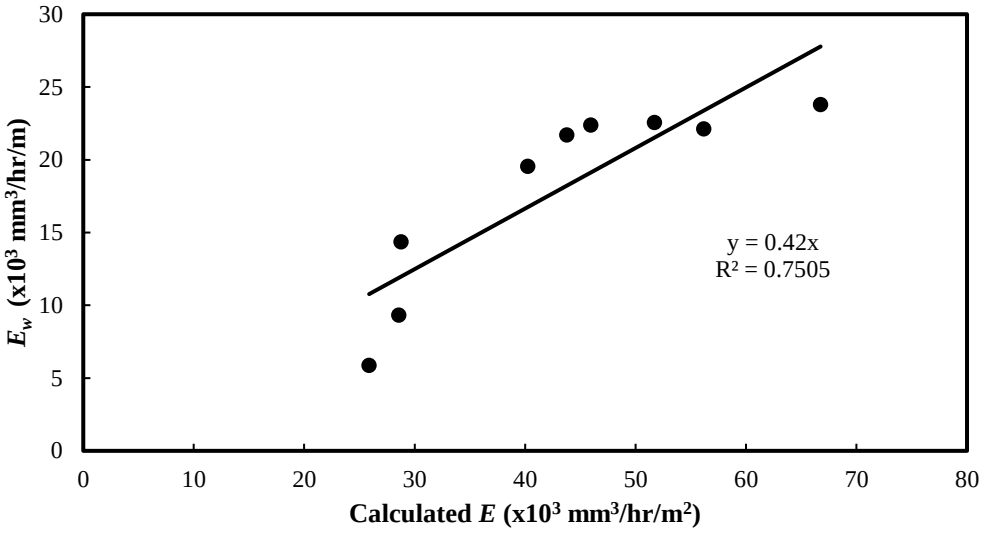

Figure 3.16 Relationship between the water removal rate by the wicking geotextile and the water evaporation rate calculated using the Romanenko (1961) equation

Figure 3.16 shows the relationship between the water evaporation rates from the control water tanks calculated using Equation (23) and the measured water removal rates by the wicking geotextile. This relationship can be expressed as follows:

$$E_w = 0.42E \tag{3.4}$$

where E_w is the water removal rate per unit width by the wicking geotextile (x10^3 mm^3/hr/m) and E is the water evaporation rate per unit area calculated using Equation (23) (x10^3 mm^3/hr/m^2). Based on Equation (22), the equivalent water surface evaporation length, $L_{we} = E_w/E = 0.42$ m, which is longer than the exposed length (0.3 m). This is because the water evaporation from the geotextile happened on both sides but the equivalent water surface evaporation is only possible on one side.

Figure 3.17 presents the average evaporation rate E of the two control tanks changed with the difference between the saturation vapor pressure and the actual vapor pressure. Based on Singh and Xu (1997), the relationship between the water evaporation rate and the vapor pressure difference should be linear. Therefore, the following relationship can be obtained to estimate the water evaporation rate from the control water tanks:

$$E = 12.69(e_s - e) \tag{3.5}$$

where E is the water evaporation rate per unit area (x10^3 $mm^3/hr/m^2$) and e_s-e is the difference between the saturated vapor pressure and the actual vapor pressure (kPa).

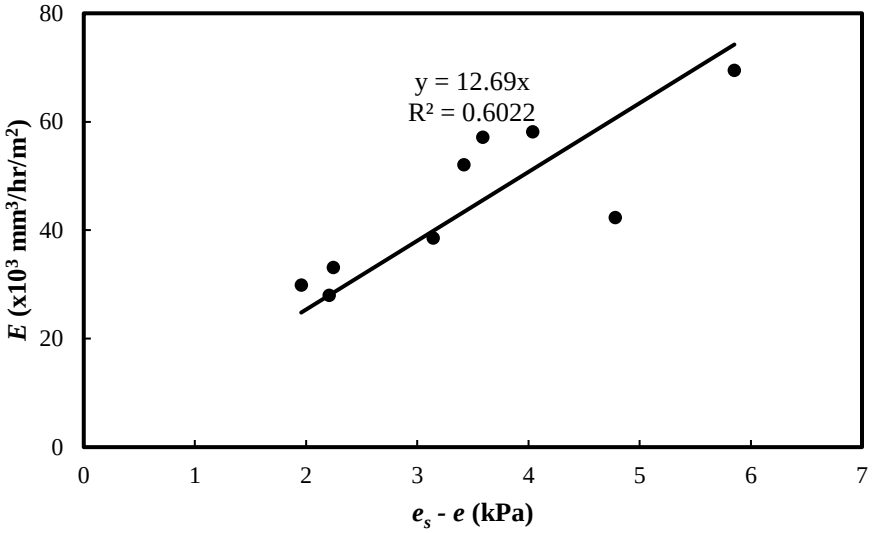

Figure 3.17 Relationship between the evaporation rate of the two water tanks and the difference of the saturated vapor pressure and the actual vapor pressure

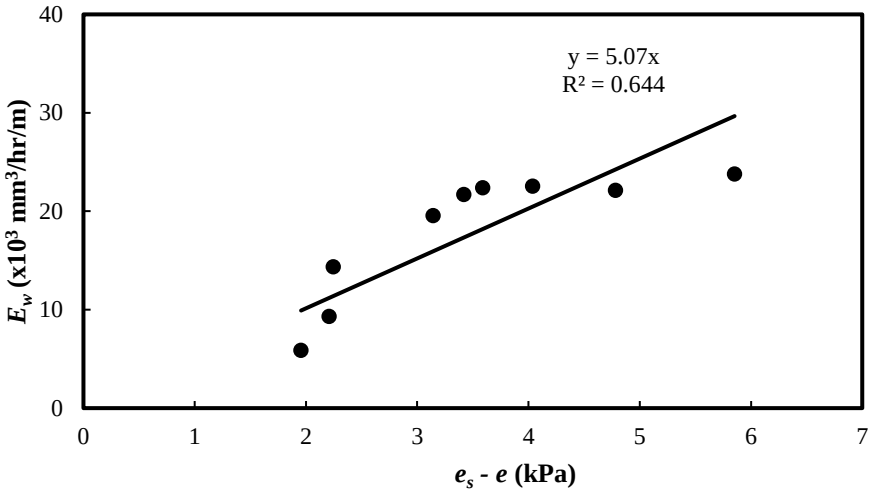

Figure 3.18 Relationship between of the water removal rate by the wicking geotextile and the difference of the saturated vapor pressure with the actual vapor pressure

The water removal rate by the wicking geotextile is presented in Figure 3.18. The water removal rate by the geotextile has a similar trend as the average evaporation rate from the control tanks in Figure 3.17. Therefore, the water removal rate by the wicking geotextile can be calculated as follows:

$$E_w = 5.07(e_s - e) \tag{3.6}$$

where E_w is the water removal rate per unit width by the wicking geotextile (x10^3 mm^3/hr/m), e_s-e is difference of the saturated vapor pressure with the actual vapor pressure (kPa). The ratio of E_w from Equation (26) to E from Equation (25) is 0.40 m, which is close to the equivalent water surface evaporation length, L_{we} = 0.42 m as presented earlier.

Based on the Bosen (1960) method, Figure 3.19 presents the relationship of the average water evaporation rate of the control tanks versus the difference between the dew point temperature and the air temperature (i.e., $T - T_{dp}$). The following empirical correlation can be obtained from the test data as shown in Figure 3.17:

$$E = 5.69\left(T - T_{dp}\right) \tag{3.7}$$

where E is the water evaporation rate per unit area from the control tanks (x10^3 mm^3/hr/m).

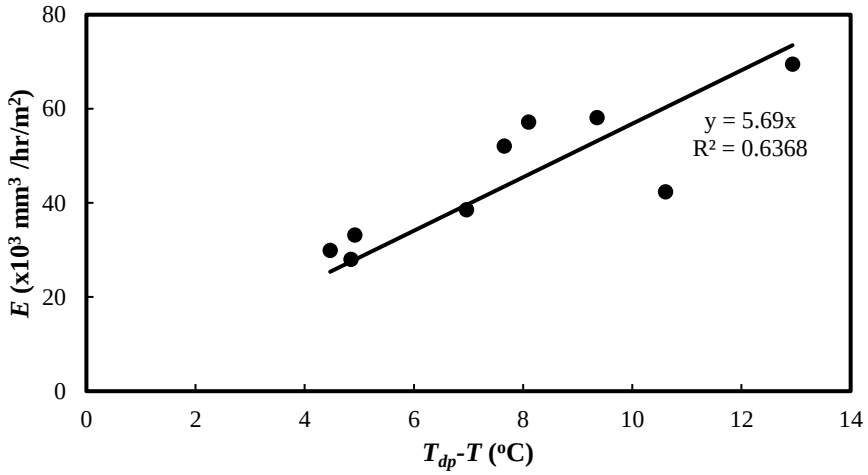

Figure 3.19 Relationship between the water evaporation rate in control tanks and the difference of the air temperature and the dew point temperature

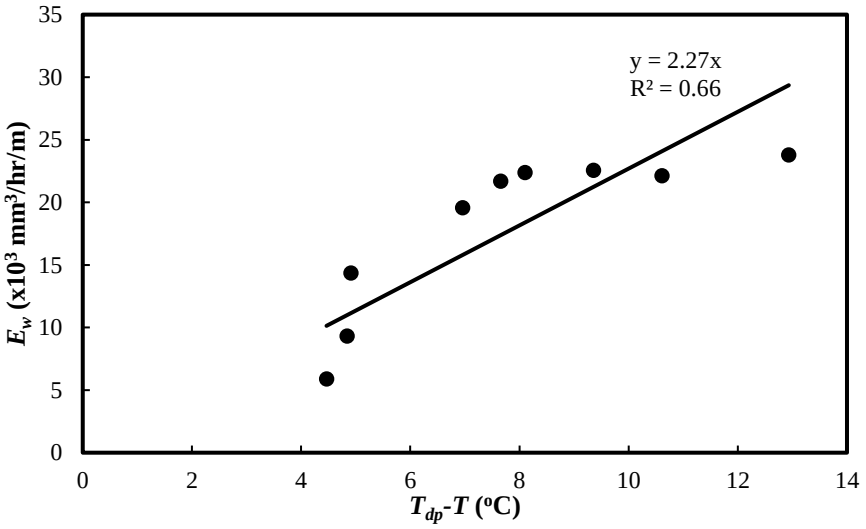

Figure 3.20 Relationship between the water removal rate by the wicking geotextile and the difference of the air temperature and the dew point temperature

The water removal rate by the wicking geotextile can also be correlated with T_{dp}-T as follows based on the test data as shown in Figure 3.20:

$$E_w = 2.27\left(T - T_{dp}\right) \tag{3.8}$$

where E_w is the water removal rate per unit width by the wicking geotextile (x10^3 mm^3/hr/m). Again, the E_w/E ratio from equations (27) and (28) is 0.40 m.

3.6 Conclusion

In the first stage of the study of wicking geotextile, a series of small-scale demonstration and quantitative tests were conducted. In the demonstration test, wicking geotextile and conventional geotextile specimens were placed in beakers with near one half of length submerged

in water and the rest of length exposed to air. The demonstration test showed the wicking geotextile was more effective in removing water from the beaker. Different rates of water removed from the beaker and the observation of water drops at the exposed end of the wicking geotextile specimen lead to the conclusion that the wicking geotextile can remove water via both gravitational drainage and evaporation.

In the vertical hanging test, geotextile specimens of different widths were suspended over a water reservoir with the lower end of the specimens dipping in water. The wicking geotextile specimens were able to "wick" water over 200 mm above the water surface. The vertical hanging test confirmed the capillary force generated by the wicking geotextile could transport water against gravity. No clear evidence of boundary effect was found in the vertical hanging test. However, unevenly distributed wet fronts present on wider specimens suggest the variability of the hydraulic properties of the wicking geotextile.

In the horizontal wicking test, wicking geotextile specimens of 1.3 m by 0.3 m were placed with zero gradient over a table. Water contents at different distances of the specimen to the water source were used to identify the location of wet front. The horizontal wicking test showed that the wicking geotextile specimens were able to transport water as far as 1.0 m. The wetted length of the wicking geotextile depended on the evaporation condition.

In the quantitative evaporation test, 12 laboratory tests were conducted in a controlled room to investigate the water removal rates by the wicking geotextiles under different temperature and relative humidity conditions. Wicking geotextile specimens of 600 mm long and 300 mm wide each were submerged into water tanks by half length and the other half was hung outside of the tanks. Under different temperature and relative humidity conditions, seven geotextile specimens were tested in seven water tanks for one week while the other two tanks without any geotextile

specimen were used as the control tanks. The rates of evaporation from the wicking geotextile specimens were compared with those from free water surface in the control tanks. A new concept of the equivalent water evaporation length for a wicking geotextile specimen was proposed based on mass-transfer methods.

The following conclusions can be drawn from the tests completed in the first stage:

(1) Based on the amount of water was supplied to the wicking geotextile and the evaporation potential of the air, wicking geotextile could remove water through gravitational drainage and evaporation.

(2) The capillary force generated by the wicking yarns in the wicking geotextile could overcome the gravity of water. Thus the wicking geotextile was capable of wicking water over 200 mm above the water surface or transporting water as far as 1 m under zero gradient.

(3) In the process of removing water via evaporation, the wicking yarns suck water into the geotextile to create a wetted area and the water on the wetted area evaporated into the air due to the difference of relative humidity between the geotextile surface and the air. This process continued with time at a certain water removal rate.

(4) The wicking geotextile significantly enhanced the water removal ability. The water removal rate of the wicking geotextile increased with an increase of the temperature and a decrease of the relative humidity.

(5) The mass transfer-based methods could be used to estimate the water removal rate of the wicking geotextile based on vapor pressures, temperature, and relative humidity.

(6) Based on this study, the newly proposed equivalent water evaporation length of a wicking geotextile sample was constant for this product and equal to 0.4 m. Thus an exposed length of 0.4 m is suggested for the application of the wicking geotextile.

CHAPTER 4 Small-scale drainage tests

The previous chapter demonstrated the water removal ability of wicking geotextile directly in contact with water. The wicking geotextile can remove water via two mechanisms, i.e., gravitational drainage and evaporation, from water reservoirs. In actual applications, however, the geotextile is always in contact with soil. This chapter presents the second stage of tests aiming to evaluate the benefits of the wicking geotextile in removing water in soil by conducting two small-scale laboratory tests.

4.1 Materials and instrumentation

4.1.1 Subgrade material

The subgrade material was a mixture of 75% Kansas River sand and 25% Kaolinite by weight. The compaction curve of the subgrade material is presented in Figure 4.1. The permeability of the subgrade was determined using a rigid-wall permeability test with a falling head method as 2.3×10^{-9} m/s.

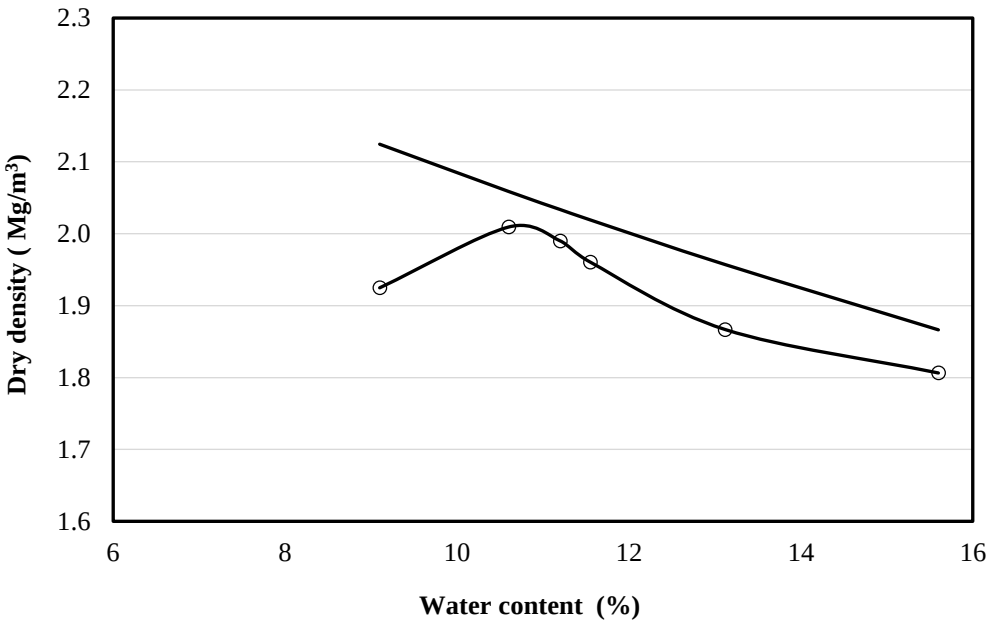

Figure 4.1 Compaction curve of the subgrade material

In the test, the volumetric water content of the subgrade was measured with sensors. However, in most applications, gravimetric water content rather than volumetric water content is used. The relationship between the volumetric and gravimetric water contents for the subgrade was determined experimentally in this study. The subgrade sample of different water content was compacted in a container with a pneumatic compactor. The gravimetric water content of the compacted subgrade sample was determined by a scale while the volumetric water content was determined by a Campbell HS2 hand-held moisture sensor. The relationship between the gravimetric and volumetric water contents of the subgrade is presented in Figure 4.2, which shows a linear relationship as follows:

$$W_{gravitational} = 0.43W_{volumetric} + 3.5 \quad (4.1)$$

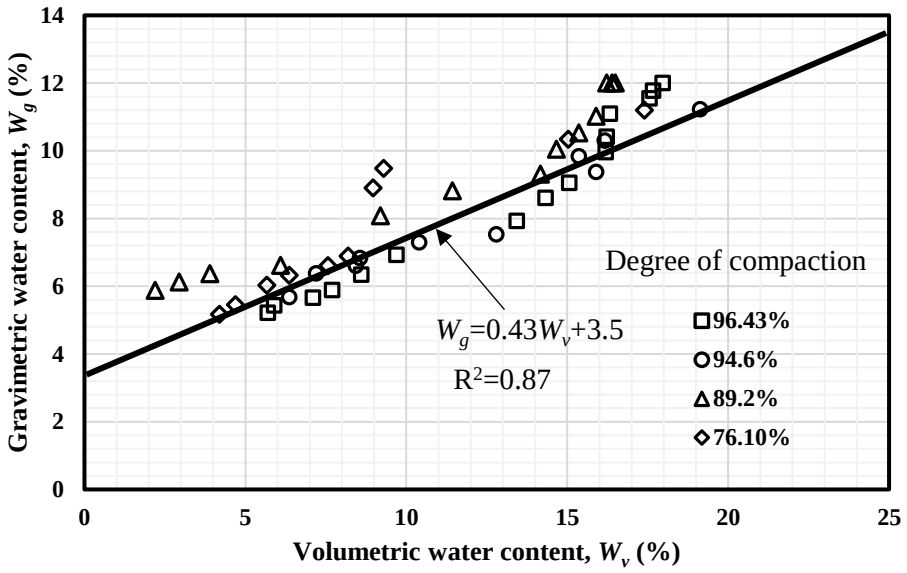

Figure 4.2 Relationship between volumetric and gravimetric water contents of subgrade

4.1.2 Base material

The AB-3 aggregate, commonly used by the Kansa Department of Transportation as a base material, was selected as the base material in this study. Figures 4.3 and 4.4 presents the gradation and the compaction curves of the AB-3 aggregate. The specific gravity of the material was 2.7. The uniformity coefficient and the coefficient of gradation of the AB3 aggregate were calculated as 50 and 2.88, respectively. The fine content of the AB3 aggregate was approximately 10%. The liquid limit of the fine particles in the AB3 aggregate was 20% while the plasticity index was 7; therefore, the fine particles in the AB3 aggregate can be classified as CL-ML using the Unified Soil Classification System (USCS). According to the USCS, this sand is classified as poorly-graded sand (SP) while the AB3 aggregate is classified as well-graded gravel (GW-GC). The permeability of the base course was determined as 9.5×10^{-7} m/s through a flexible-wall permeability test with a falling head method.

Similar to the subgrade material, the volumetric water contents of the base material during the test were measured with sensors. Due to high stiffness of the base material after compaction, the hand-held moisture sensor was not able to be used to measure volumetric water contents. The relationship between gravimetric and volumetric water contents could not be obtained via the experimental method. However, at a given gravimetric water content, if the bulk dry density of soil is known, the volumetric water content can be calculated by:

$$W_v = \frac{V_{water}}{V_{total}} = \frac{m_{water}/\rho_{water}}{m_{soil}/\rho_{soil}} = W_g \times \frac{\rho_{soil}}{\rho_{water}} = W_g \times \frac{G_s}{1+e} \quad (4.2)$$

where W_v is the volumetric water content, W_g is the gravimetric water content, ρ_{soil} is the bulk dry density of soil, G_s is the specific gravity, and e is the void ratio.

Figure 4.5 presents the relationship between the gravimetric and volumetric water contents of the AB-3 base course material. The gravimetric water contents were obtained from direct measurements during the compaction tests while the corresponding volumetric water contents were calculated with Equation (30) based on the measured bulk dry densities. The linear relationship between these two parameters can be expressed as follows:

$$W_{gravitational} = 0.45 W_{volumetric} + 0.746 \quad (4.3)$$

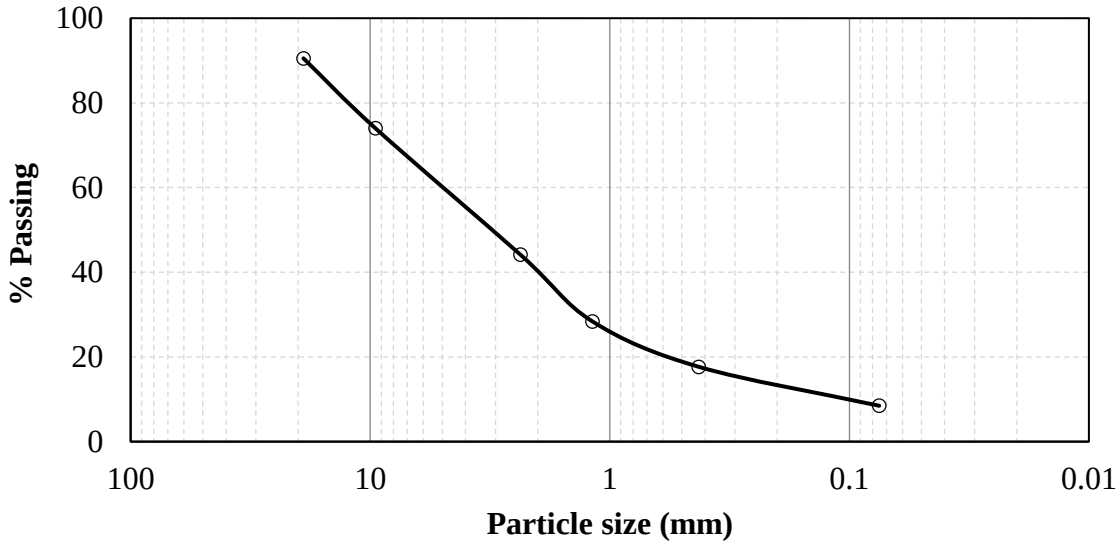

Figure 4.3 Gradation curve of the AB-3 aggregate

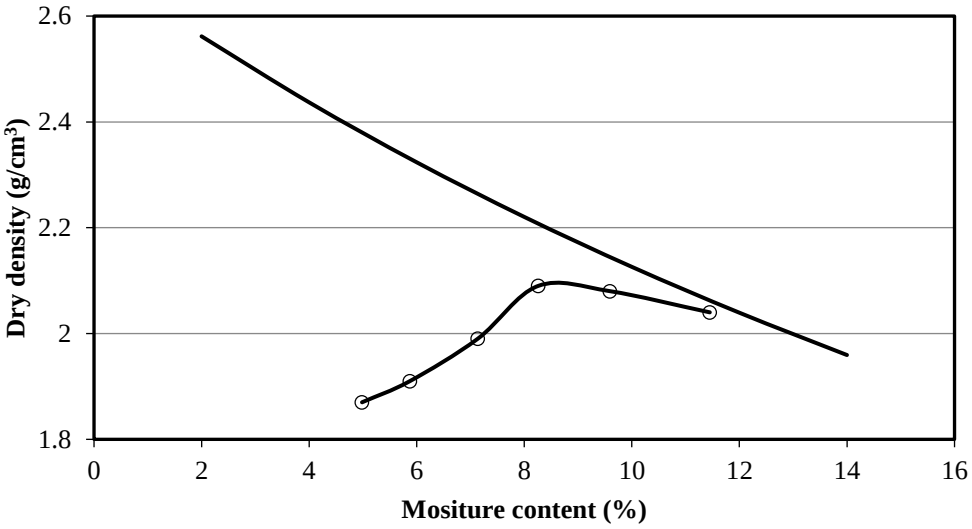

Figure 4.4 Compaction curve of the AB-3 aggregate

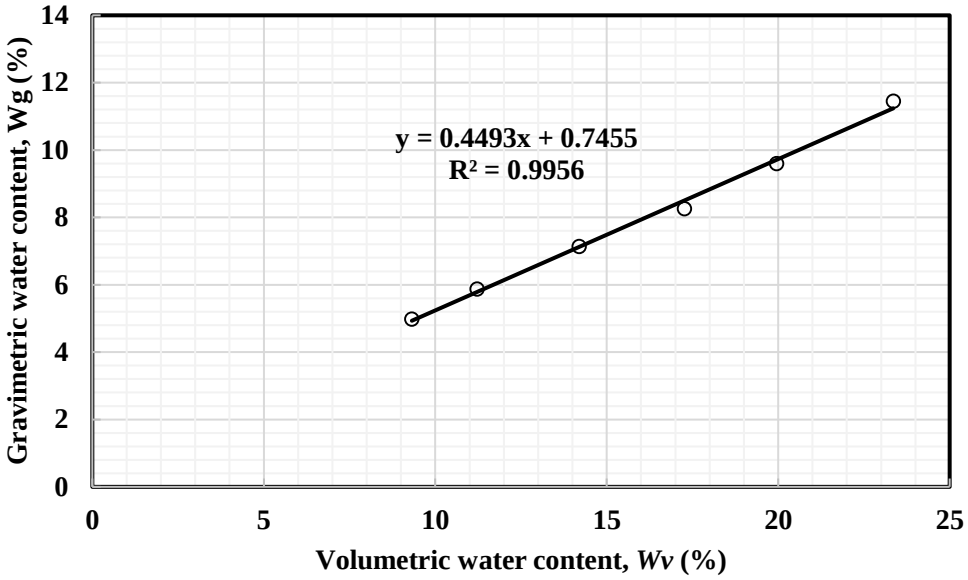

Figure 4.5 Relationship between volumetric and gravimetric water contents of AB-3 aggregate

\4.1.3 Conventional woven geotextile

A new conventional woven geotextile (referred to as the conventional No. 2) was used in some of the tests presented in the chapter for comparison with the wicking geotextile. The woven geotextile was also fabricated and provided by the TenCate Geosynthetics. The properties of the conventional woven geotextile are listed in Table 4.1. The conventional woven geotextile No. 2 has similar mechanical properties as the wicking geotextile and can be considered as wicking geotextile without the wicking yarns, while the mechanical properties of the conventional woven geotextile No. 1 is weaker compared to the wicking geotextile. As this study focused on the effect of wicking function, it is preferred that the mechanical properties of the wicking geotextile and the conventional geotextile are similar.

Table 4.1 Properties of conventional woven geotextile No. 2

Properties	**Unit**	**Minimum average roll value**	
		MD	CD
Tensile strength (2% strain)	kN/m	7	26.3
Tensile strength (5% strain)	kN/m	21	69.3
Flow rate	$l/min/m^2$	3056	
Permittivity	sec^{-1}	1	

4.1.4 Volumetric water content sensor

The Decagon EC-5 soil moisture sensors were used in the tests presented in this chapter to monitor the water content changes in geomaterials. The dimension of the EC-5 sensor was 89 mm long × 18 mm wide × 0.7 mm thick. The EC-5 sensors are able to measure soil volumetric water content from 0 to 100%. The sensor measures soil water content within a volume of 240 ml in the soil surrounding the sensor. The sensors were connected to a Campbell CR-1000 data logger. It should be noted that volumetric water content is defined as the ratio of the volume of water to the total measured volume. Gravimetric water content, defined as percent of water mass to the mass of soil solids, is more commonly used in geotechnical and pavement practice. The relationship between the gravimetric water content and the volumetric water content for each geomaterial used in the tests will be introduced in the following section.

4.2 Small-scale box test

In the previous chapter, the wicking geotextile specimens were placed directly in contact with water. The test results from the previous chapter proved the efficiency of the wicking geotextile in removing water is superior to that of the conventional woven geotextile. Case studies (Zhang et al., 2014, TenCate, 2013) also showed the effectiveness of the wicking geotextile when installed in the soil. To further investigate the effectiveness of the wicking geotextile in removing water from soil, small-scale box tests were conducted with simulated rainfall. In a test box, a scaled roadway structure was constructed with a subgrade layer, a base course layer, and a geotextile specimen at the interface. One test section included a conventional woven geotextile and another one included a wicking geotextile specimen. Soil water content sensors were placed in the model to monitor the water content change under different intensity of simulated rainfall.

4.2.1 Test setup and procedure

Figure 4.6 presents a schematic of the setup for a small-scale box test. High-strength plastic boxes with a dimension of 1041 mm long × 686 mm wide × 584 mm high was used as test boxes. Two pieces of 13-mm thick HDPE plastic panels were used to separate the box into two compartments. The larger compartment of the test box was filled with compacted subgrade and base course. A dehumidifier was placed in the smaller compartment to provide a stable evaporation condition and collect water removed from the soil by the geotextile. The geotextile specimen was placed at the interface between the subgrade and the base course.

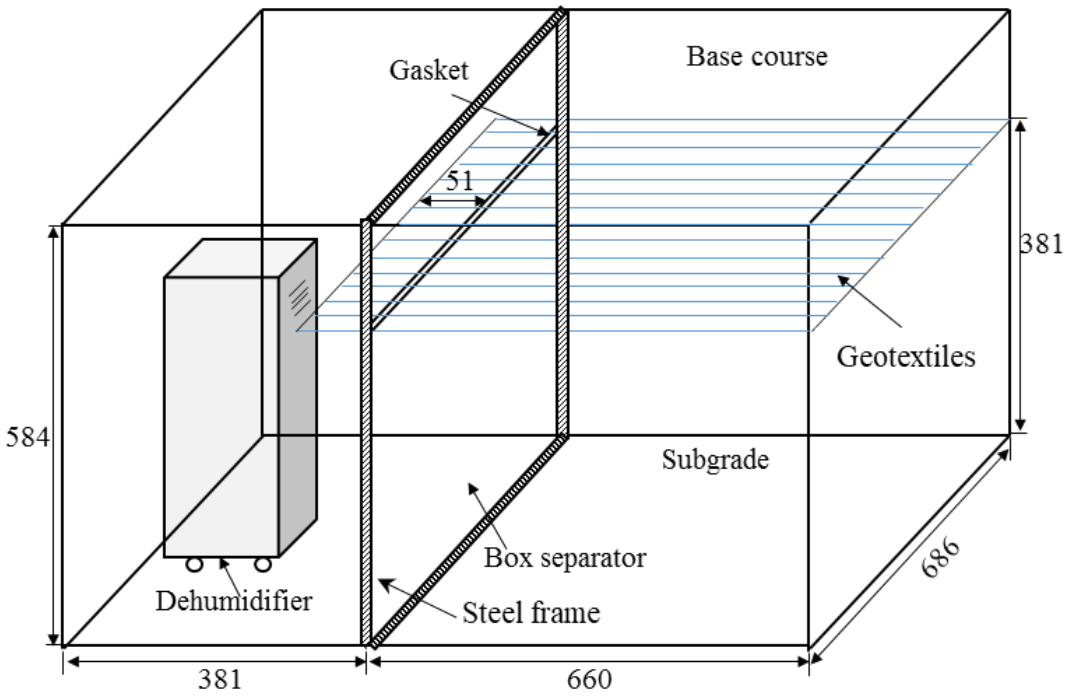

Figure 4.6 Test setup for the small box test

In the preparation of the test, the first piece of HDPE plastic panel was first installed. The HDPE panel was placed against a steel frame which was bolted to the wall of the box. After the placement of the first panel, silicon seal was placed between the panel edges and the wall of the box for water proofing. A pair of door gaskets were glued to the top and bottom edges of the lower and upper panels, respectively, to limit water leakage. Then the subgrade material was placed and compacted in the larger compartment of the box in three lifts to achieve a total thickness of 381 mm. Before the placement of subgrade, the material was adjusted to a water content of 10.6%, which was close to the optimum water content of 11%. The weight of each lift was measured to control the degree of compaction to the target value of 95%. Each lift of subgrade material was compacted with a hand-held pneumatic compactor. The diameter of the compactor plate was 130

mm and the compactor was operated at a pressure of 550 kPa, as shown in Figure 4.7(a). After the subgrade was compacted to the thickness of 381 mm, a geotextile specimen with the dimension of 710 mm long and 570 mm wide was placed on the subgrade. In the small-scale test, the conventional geotextile No. 2 and the wicking geotextile were used. The geotextile specimens were cut from the roll in the way that the cross-machine direction was in the longitudinal direction of the specimen, as shown in Figure 4.7(b). A 51 mm long portion of the geotextile was extended to the smaller compartment. The upper panel was then placed against the steel frame. The AB-3 base course material was placed and compacted in two equal lifts. The thickness of the base course after compaction was 150 mm. The water content of the base course was approximately 8%, close to the optimum water content of 8.3%. After the construction of the section, the top surface of the base course was covered with a plastic sheet to limit water evaporation from the soil into the air.

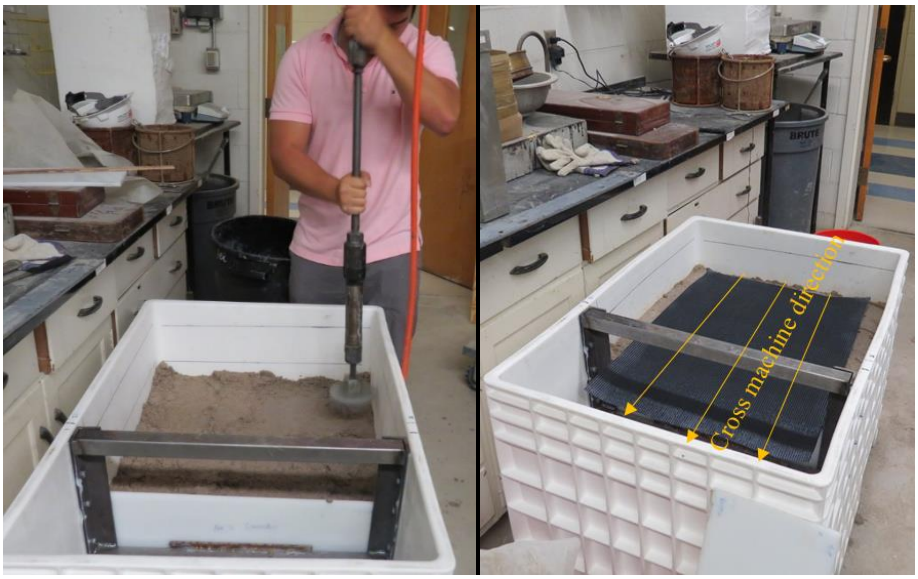

(a) (b)

Figure 4.7 Small box test preparation: (a) compaction of subgrade material and (b) placement of geotextile

After compaction of each lift of subgrade, three EC-5 moisture sensors were placed along the longitudinal center line of the box. To place the EC-5 sensor in the subgrade, a small hole was dug on the compacted subgrade surface to the desired depth, then the sensor was pushed into the subgrade material in the horizontal direction, as shown in Figure 4.8. The hole was filled and compacted by hand after the installation of the sensor. Three layers, a total of nine EC-5 moisture sensors were placed in the subgrade. The sensors placed in the subgrade were labeled as Number 1 through 9. One layer of three EC-5 sensors was placed at the mid-depth of the base course. The AB-3 base course material contained large particles thus the sensors could not be inserted in the base course with the same technique used in the subgrade. The moisture sensors in the base course were placed on the surface of the first lift after the compaction. Then, the second lift of AB-3 base course material was placed directly over the sensors and compacted. The sensors in the base course were labeled Number 10 through 12. Figure 4.9 presents a schematic of moisture sensor locations.

Figure 4.8 Placement of a moisture sensor in subgrade

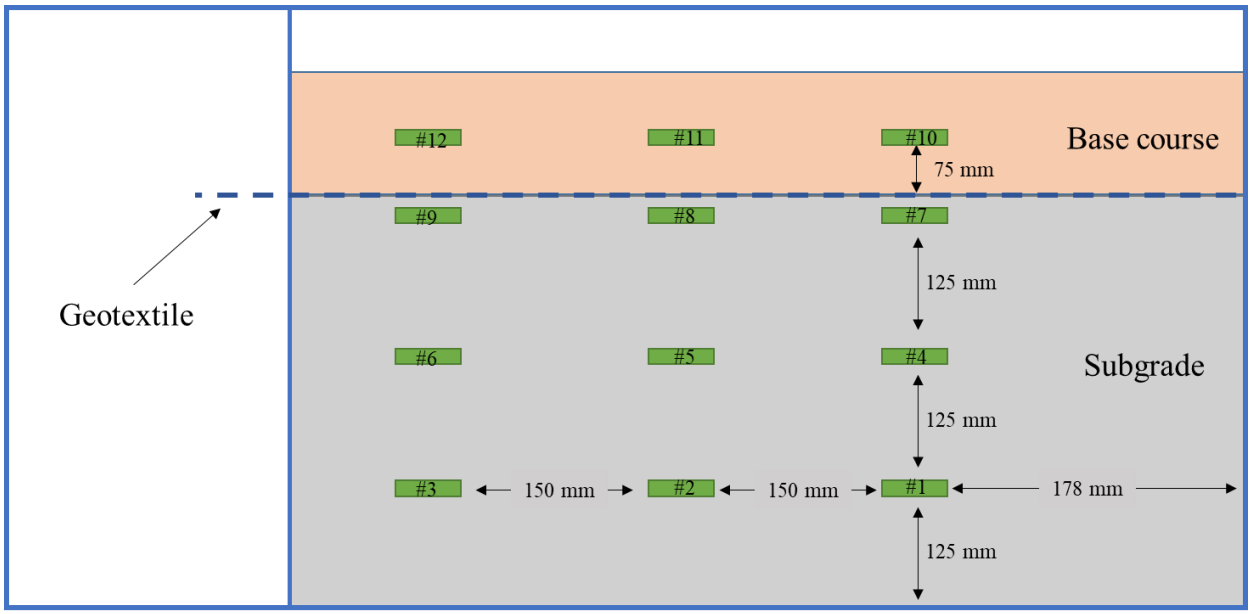

Figure 4.9 Locations of moisture sensors

A reference box with the same dimension and also separated by a HDPE panel into two compartments as the test box was placed adjacent to the test box. However, the larger compartment of the reference box was left empty. Two dehumidifiers were placed in the smaller compartments of both the reference and test box. The dehumidifiers were set to adjust the relative humidity to 30%, which was close to the room relative humidity. The dehumidifier would turn on automatically when the relative humidity of air in the smaller compartments was higher than 30%.

Three rainfall simulations were conducted on each test section. During the first rainfall, 2.26 liter of water was sprayed over the base course surface in 20 minutes. The surface area of the base course was approximately 0.4 m^2. Thus the rainfall intensity was approximately 1.7 cm/hour. In the second rainfall, 4.52 liter of water was sprayed over the base course surface in 20 minutes.

The rainfall intensity was 3.4 cm/hour. The last rainfall has an intensity of 6.78 cm/hour. Approximately 9 liter of water was sprayed over the base course surface in 20 minutes. The amounts of water collected by dehumidifiers both in the reference box and test box were used as an indicator to start the subsequent rainfall simulation. The water collected by both dehumidifiers was weighted periodically. When these two dehumidifiers collected the same amount of water, it is considered that the geotextile could no longer remove water from the test section and the current rainfall simulation test was complete. Then the next rainfall simulation test could begin.

4.2.2 Test results

The moisture sensors measured the volumetric water content, which were converted to gravimetric water contents using Equations (29) and (30). The sensors in each layer, although placed at the same depth, measured different water contents, especially in the base course layer. Figure 4.10 presents the gravimetric water contents in the base course of the wicking geotextile-improved section during the test period. The initial water contents measured by Sensors #10 and #12 were 7.3% and 7.8% respectively, which were close. However, the initial water contents recorded by Sensor #11 was approximately 9.6%, which was significantly higher than the value recorded by Sensors #10 and #12. The difference in the values recorded by sensors was likely caused by the difference in the density of the geomaterial around the sensors. Particle arrangement, installation of the sensor, and the difference in water content during compaction contributed to the difference in the soil density. Although the initial values recorded by sensors were different, the trends of water content change measured by sensors were consistent. From Figure 4.10, three significant increments of water content can be observed at the beginning of the test, approximately

19,000 minutes to 34,000 minutes into the test. The observed increase in water content corresponded to the simulate rainfall. For the sake of comparison, the water content changes, i.e., the difference between water content at any given moment and initial water content, are presented in Figure 4.10. The initial gravimetric water contents are presented in Table 4.2.

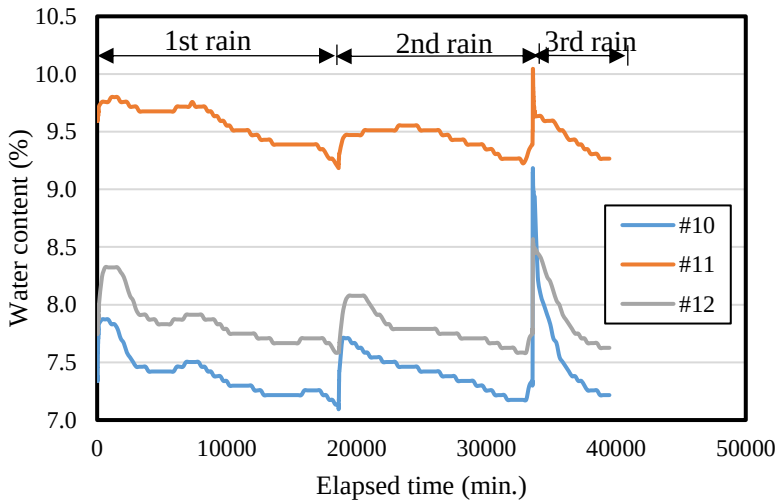

Figure 4.10 Gravimetric water contents in the base course of wicking geotextile section

Table 4.2 Initial gravimetric water contents of small-scale tests

Sensor	Initial water content (%)	
	Conventional geotextile	Wicking geotextile
#1	11.30	11.66
#2	10.96	10.85
#3	10.10	10.85
#4	10.44	9.62
#5	10.53	10.23
#6	11.13	11.76
#7	11.22	10.62
#8	10.79	10.79
#9	10.79	9.50
#10	8.84	7.34
#11	9.15	9.59
#12	9.15	7.75

Figure 4.11 presents the water content change of the conventional woven geotextile-improved section. The gravimetric water content changes measured by sensors in the same layer were similar. The water contents in the subgrade showed similar trend in all three layers: a significant water content increase at the beginning of the test, then the water content decreased until the third rainfall simulation at approximately 35,000 minutes into the test. The second rainfall simulation did not influence the water content in the subgrade. By the end of the test, the subgrade water content was approximately 0.1% lower than the initial water content. Overall, simulated rainfalls did not impact the water content of the subgrade significantly. Over the test period, the

water content change in the subgrade were within 0.3%. The permeability of the clayey subgrade material was low. Water was more likely to enter the subgrade material through the crack around the sensors created during the installation of the sensors. The water content change in the base course was much more pronounced when compared with the subgrade. The first rainfall increased the gravimetric water content of 0.4% in the base course. Over the drying period following the first rainfall, the water content of the base course returned to the initial value. The second rainfall increased the gravimetric water content in the base course by approximately 0.6%. The water content returned to the initial value again at the end of the drying period. The third rainfall increased the gravimetric water content in the base course by approximately 1.4%. The increase of water content after each rainfall was consistent with the amount of water sprayed over the base course.

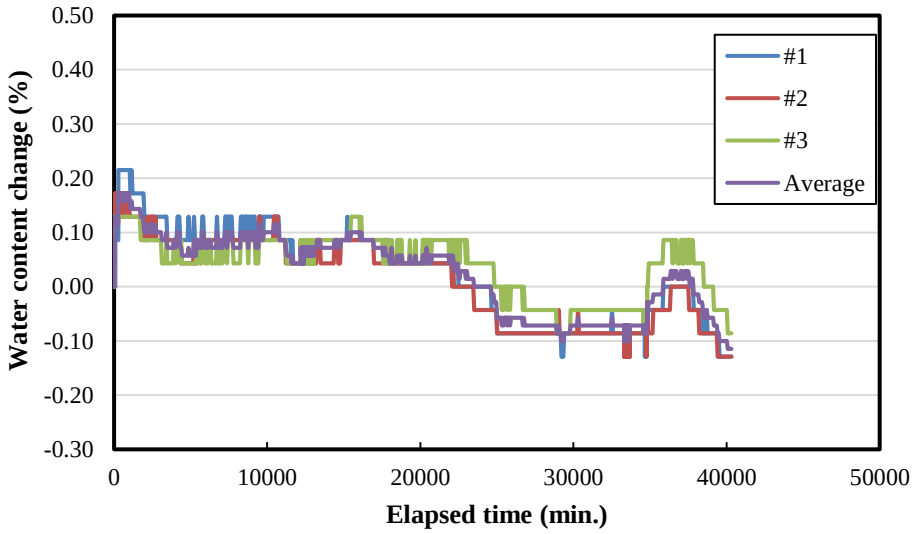

(a) Subgrade lower layer

Figure 4.11 Water content changes in the conventional woven geotextile-improved section

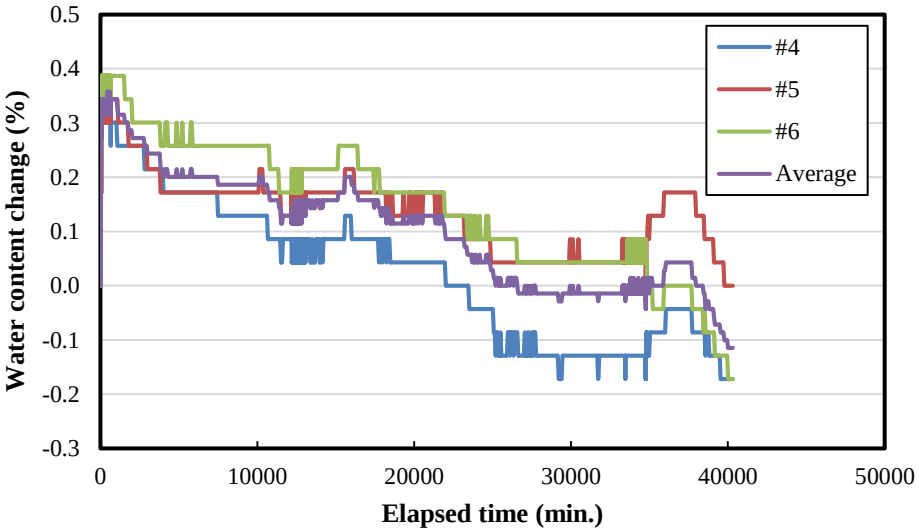

(b) Subgrade middle layer

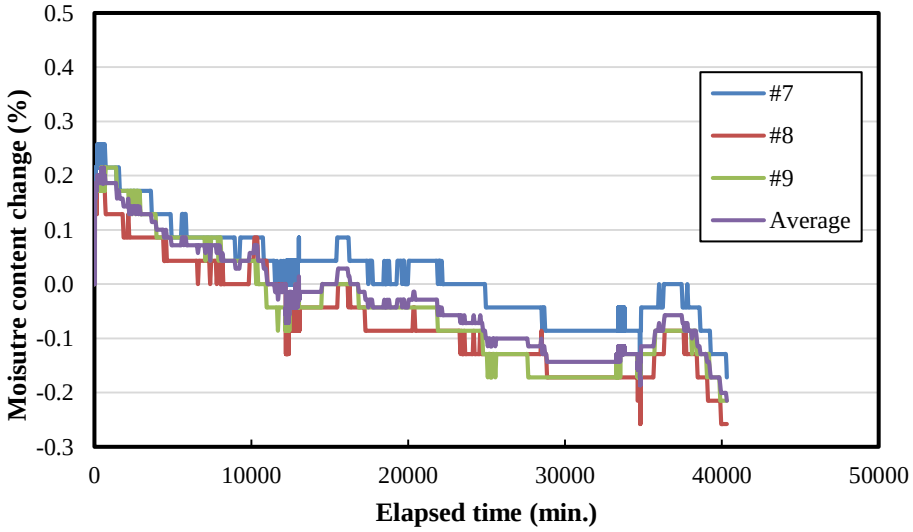

(c) Subgrade upper layer

Figure 4.11 Water content changes in the conventional woven geotextile-improved section

(continued)

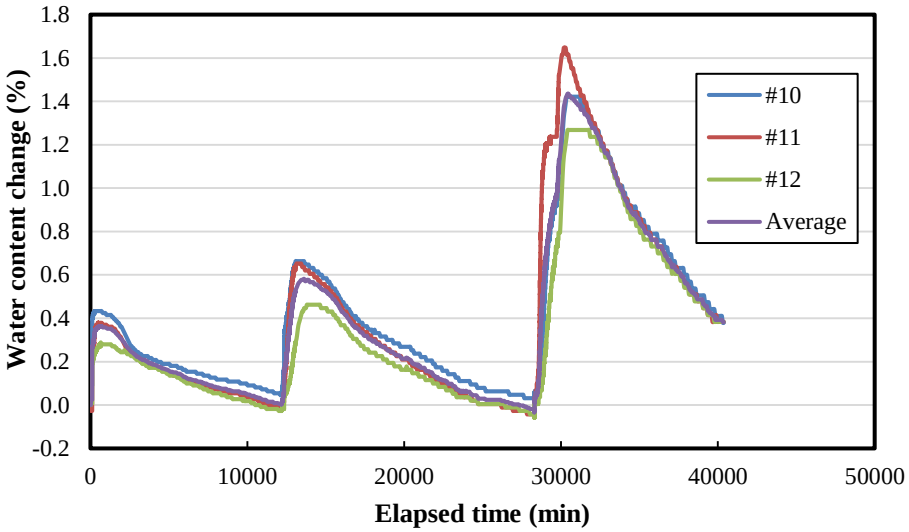

(d) Base course layer

Figure 4.11 Water content changes in the conventional woven geotextile-improved section (continued)

Figure 4.12 presents the water content changes in the wicking geotextile-improved section, which show different trends. The lower subgrade layer showed an increase in water content as the progress of the test. The water content increase in the lower layer can be divided into three stages: from the beginning of the test to 19,000 minutes, from 19,000 minutes to 33,500 minutes, and from 33,500 minutes to the end. Each stage of water content increase corresponded to a rainfall simulation. Overall the water content in the lower subgrade layer increased. The increased water content was a result of rainfall water accumulation at the bottom of the section. At the end of the test, the water content in the lower subgrade layer increased approximately by 0.35%. The water

content changes in the middle and upper subgrade layers were similar. The water content increased rapidly after the third rainfall (33,500 minutes into the test). The rapid increase of water content was most likely caused by water entering the soil surrounding the sensors through the cracks generated during the installation of sensors. In each stage, the water content in the subgrade then decreased in the drying period.

The water content change in the base course of the wicking geotextile-improved section was similar to that of the conventional woven geotextile-improved section. A rapid increase in water content was observed after each rainfall simulation. The water content decreased in the drying period. At the end of the first and second drying periods, the water content in the base course was lower than the initial value. The first rainfall increased the water content in the base course by 0.4%. At the end of the first drying period, the water content was 0.25% lower than the initial water content. The second rainfall raised the average water content in the base course by approximately 0.5%. At the end of the second drying period, the average water was 0.22% lower than the initial water content.

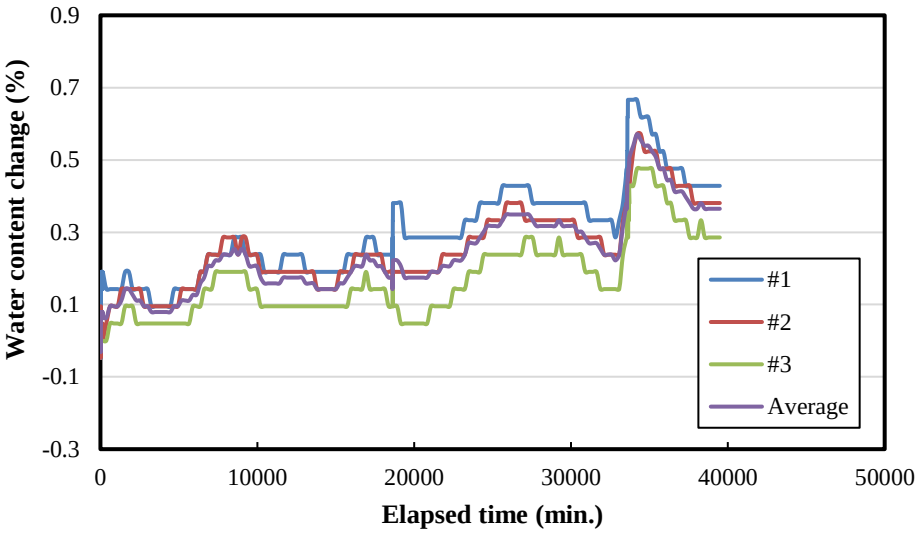

(a) Lower subgrade layer

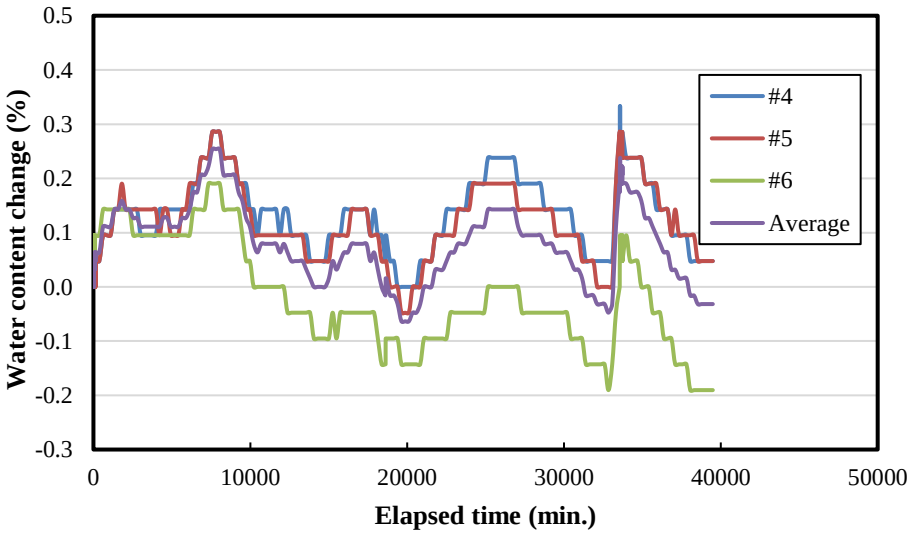

(b) Middle subgrade layer

Figure 4.12 Water content changes in the wicking geotextile-improved test section

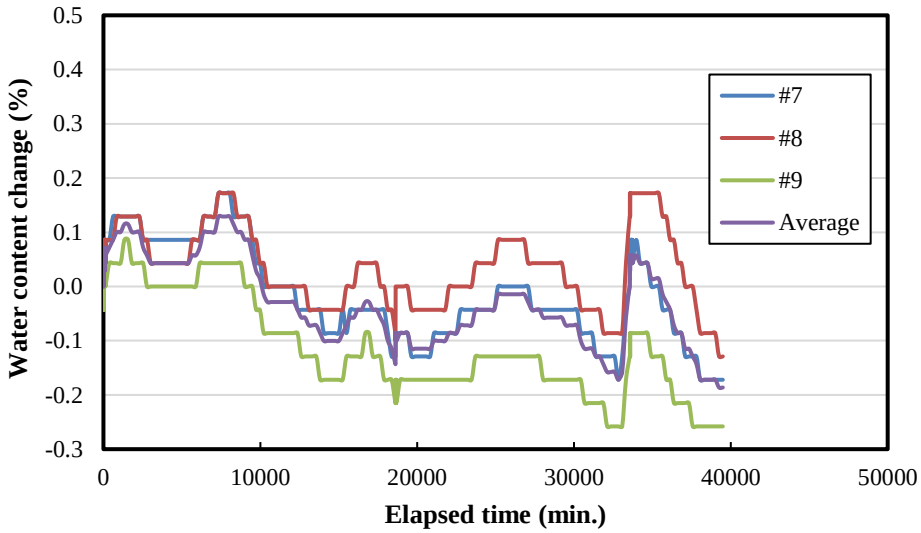

(c) Upper subgrade layer

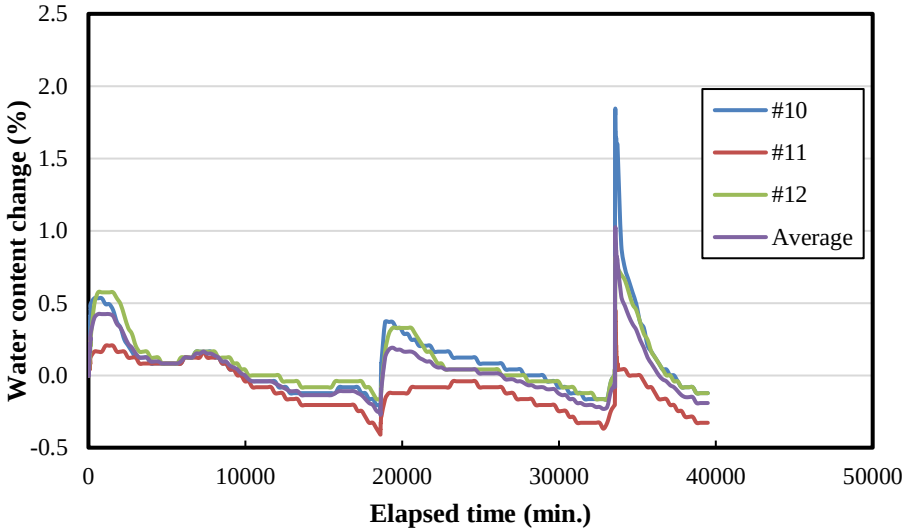

(d) Base course layer

Figure 4.12 Water content changes in the wicking geotextile-improved test section (continued)

The difference in the trends of water content change in the subgrade between the conventional and wicking geotextile-improved sections was likely due to the cracks in the subgrade material around the sensors. In the conventional woven geotextile-improved section, the

subgrade material surrounding the sensors was better compacted after the installation of the sensor, thus there was less crack in the subgrade near the sensor. As a result, the water contents recorded by the sensors in the subgrade of the conventional geotextile-improved section fluctuated less. Although a direct comparison could not be made, the magnitudes of water content change indicate the wicking geotextile did not impact the water content in the subgrade significantly. The water content changes in the subgrade were less than 0.3% in most layers of both the conventional and wicking geotextile-improved sections.

Figure 4.13 presents a comparison of the average water content change in the base course of the conventional woven geotextile and wicking geotextile-improved sections. The water content increases induced by the first rainfall simulation were similar. Based on the water collected by the dehumidifiers, the conventional geotextile stopped removing water from the base course at approximately 12,000 minutes after the rainfall. The wicking geotextile stopped removing water from the base course at approximately 18,000 minutes after the rainfall. At the end of the first drying period, the conventional geotextile maintained the base course water content at the initial value. At the end of the drying period, the wicking geotextile reduced the water content in the base course to 0.25% below the initial value or 0.65% lower than its optimum water content. The water content changes in the second simulation rainfall and drying period were similar to those of the first simulation rainfall and drying period. At the end of the second drying period, the conventional woven geotextile maintained the water content to the initial value. By the end of the second drying period, the water content in the base course of the wicking geotextile-improved section was similar to that at the end of the first drying period. Based on the comparison, the conventional woven geotextile was only able to remove the excess water, while the wicking

geotextile continued removing moisture in the base course as the water content was lower than its initial water content.

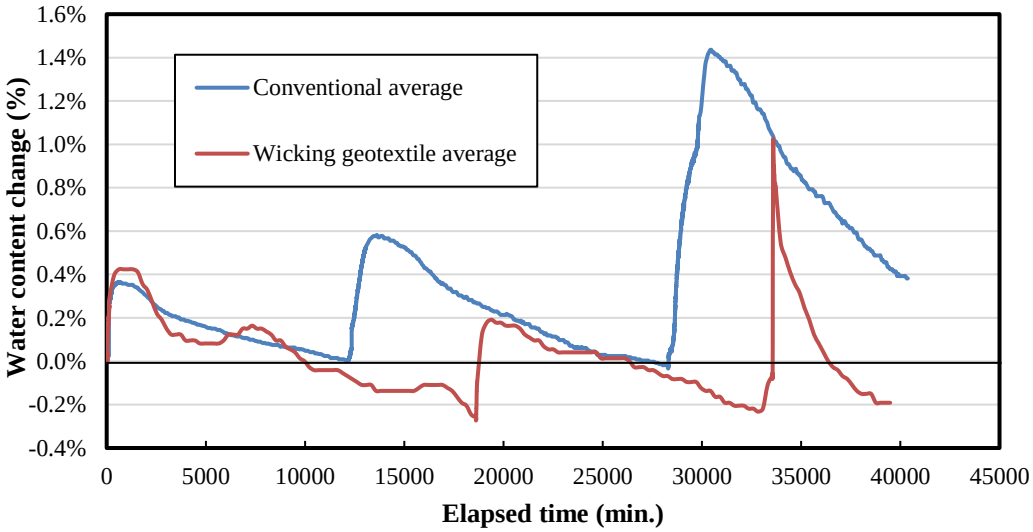

Figure 4.13 Comparison of average water content change in the base course

4.3 Soil column test

The small scale rainfall test proved the wicking geotextile not only removed the excess water from induced by the rainfall but also continued to lower the water content in the base course material. However, only one layer of sensors was installed at the mid-depth in the 150-mm-thick base course in the small scale rainfall test. The soil column test was thus designed to investigate the water content change at different depths of base course due to the water removing action of the wicking geotextile. Similar to the small scale rainfall test, the conventional woven geotextile was used as a comparison.

4.3.1 Test setup

Figure 4.14 presents a schematic of the test device. The soil columns were constructed with 4-gallon buckets. The dimension of the column was 254 mm × 254 mm × 335 mm (L×W×H). A 2.5-mm-high, 220-mm-wide opening was cut on one side of the bucket close to the bottom for the placement of the geotextile. In the preparation of the test, the geotextile specimen with a dimension of 200 mm wide and 1.3 m long was inserted into the soil column through the opening. The geotextile specimen was cut in the way that the cross-machine direction was in the longitudinal direction of the specimen. The end of the geotextile specimen was in contact with the column wall opposite to the wall with the opening. It is to be noted that the geotextile specimen placed in the soil column was dry. Door gaskets were placed at the opening as the geotextile specimen was installed to prevent water and soil from coming out. Then the soil column was filled with AB-3 base course material in multiple lifts. Each lift of the AB-3 aggregate was compacted with 56 blows using a standard Proctor rammer, i.e., 2.5 kg weight falling from a height of 305 mm. The number of lifts was determined by the number of moisture sensors to be installed in the soil column. The water content sensor was placed over the compacted AB-3 surface; then the next lift was added to cover the sensor. The sensors were placed over the longitudinal center line of the geotextile specimen. Each sensor was also placed with a minimum 50 mm offset in the horizontal direction from the adjacent sensor to avoid interference between the sensors. After the compaction of the last lift of AB-3 aggregate, the top of the soil column was covered with multiple layers of plastic wrap to prevent evaporation from the base course surface. After the preparation, soil columns were transferred to the temperature-controlled room as described in Chapter 3. The soil columns and the geotextile specimens were placed on a long table so that the exposed portions of the geotextile specimens could be extended.

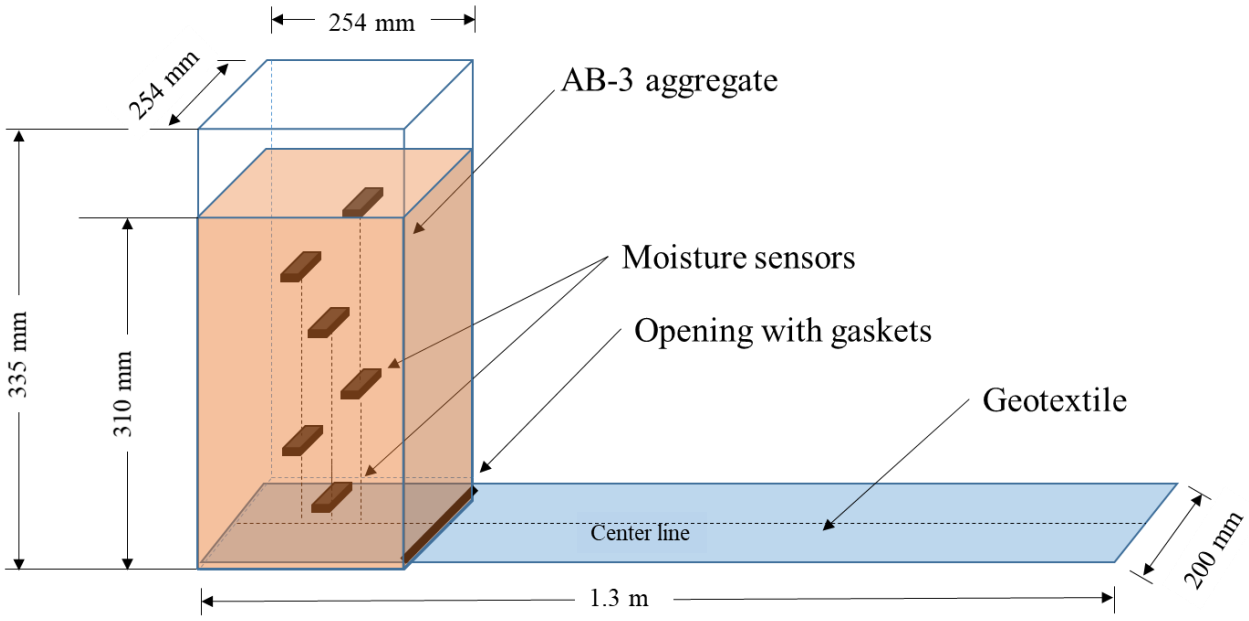

Figure 4.14 Schematic of soil column

Three comparison tests were conducted. Two soil columns were prepared for each test: one with conventional woven geotextile and one with wicking geotextile. Table 4.3 presents the test room condition, the gravimetric water content at the beginning of the test, and the bulk dry density of the compacted AB-3 aggregate in the soil column. In the first test, eight moisture sensors were installed in the soil column. Thus the soil column was filled by ten lifts of AB-3 aggregate. A couple of sensors were damaged during the excavation process of the first test. Thus only six sensors were installed in the soil column in the second test and the soil column was filled with AB-3 aggregate in eight lifts. In the last test, seven moisture sensors were installed in the soil column and the soil column was filled in nine lifts. The difference in the bulk dry densities of the aggregate in different tests likely resulted from different number of lifts used to fill the soil columns. As a result of different number of lifts to fill the soil column, the locations of sensors relative to

the geotextiles are different. Table 4.4 presents the vertical distances of the sensors to the geotextiles in each test. Figure 4.15 presents a picture of soil columns during a test.

Table 4.3 Soil column test room condition and aggregate properties

Test No.	Geotextile	Temperature (℃)	RH (%)	Water content (%)	Bulk density (kN/m^3)
#1	Conventional No. 1	7.3	60	11.1	18.5
#2	Conventional No. 2	8.6	60	9.8	18.3
#3	Conventional No. 2	10.1	40	8.6	17.3

Table 4.4 Vertical distance of sensor to geotextile

Sensor No.	Distance to geotextile (mm)		
	Test #1	Test #2	Test #3
8	280	N/A	N/A
7	245	N/A	280
6	210	270	240
5	175	225	200
4	140	180	160
3	105	135	120
2	70	90	80
1	35	45	40

Figure 4.15 Picture of soil columns during the third test

4.3.2 Test results and analysis

The results of the soil column tests are presented based on gravimetric water content changes in the aggregate. The initial water contents were measured by the moisture sensors two to four hours after the preparation of the soil column. The gravimetric water contents were calculated with Equation (30). The changes of water content was calculated by subtracting the initial gravimetric water content from the gravimetric water content during the test period.

In the first test, the two soil columns were installed with conventional woven geotextile No. 1 and the wicking geotextile. The AB-3 base course was compacted at the water content of 11.1%, which is higher than the optimum water content of 8.6%. The average air temperature and relative humidity in the room were 7.6℃ and 60%, respectively, during the test. Figure 4.16 presents the base course water content change in Test 1. The "C" in the figure represents the water content change in the conventional woven geotextile soil column. The "W" in the figure represents the water content change in the wicking geotextile soil column. The number following the letter represents the vertical distance from the sensor to the geotextile.

The water content at each measurement depth decreased more significantly in the wicking geotextile soil column than in the conventional woven geotextile soil column. A 0.2% water content increase in the base course of 35 mm above the geotextile specimen was observed in the conventional geotextile No.1 soil column, as shown in Figure 4.16(a). This was likely due to the water movement under the influence of gravity and accumulating at the bottom of the soil column. The accumulated water did not generate any hydraulic head to push water into the conventional woven geotextile specimen, thus the accumulated water was not removed. In the wicking geotextile soil column, the water content decreased by 0.8% rapidly within the first 48 hours of the test, then remained stable. Figure 4.16(g) shows that at a distance of 245 mm above the geotextile specimens, the water content changes in both soil columns were similar. It is believed the wicking geotextile could only remove water from the surrounding geomaterial within a distance via suction. The water content change in an unsaturated geomaterial beyond this distance was contributed little by the wicking geotextile. Thus the influence distance of the wicking geotextile in Test 1 was between 210 mm and 245 mm. One week (168 hours) after the beginning of the test, the average water content of the AB-3 aggregate within the influence distance (i.e., 35

mm to 210 mm above the geotextile specimen) in the wicking geotextile soil column was 0.7% lower than that of the conventional geotextile No. 1 soil column.

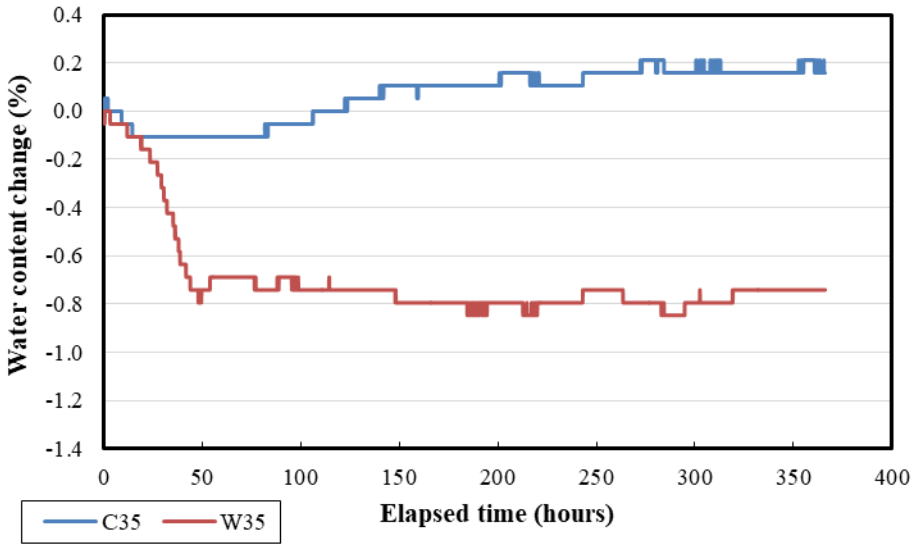

(a)

Figure 4.16 Water content changes at different depths in the soil column in Test 1

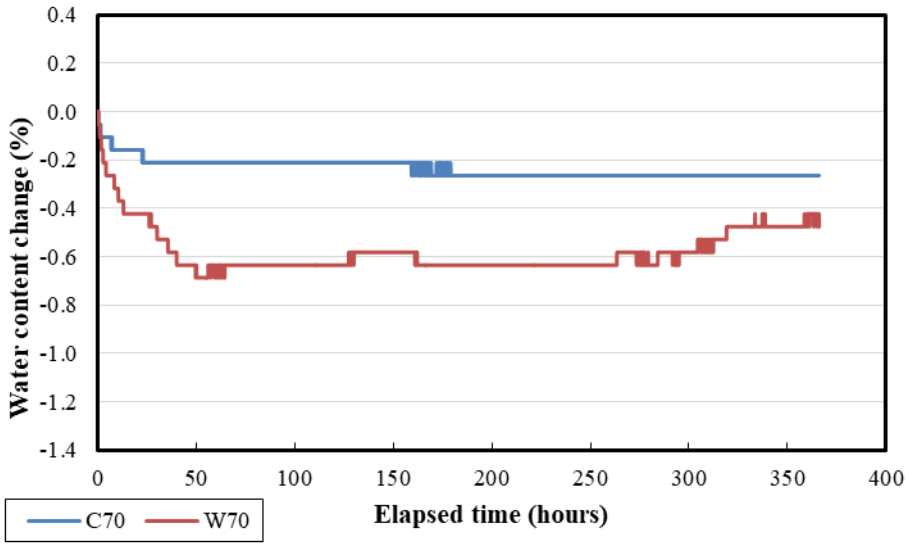

(b)

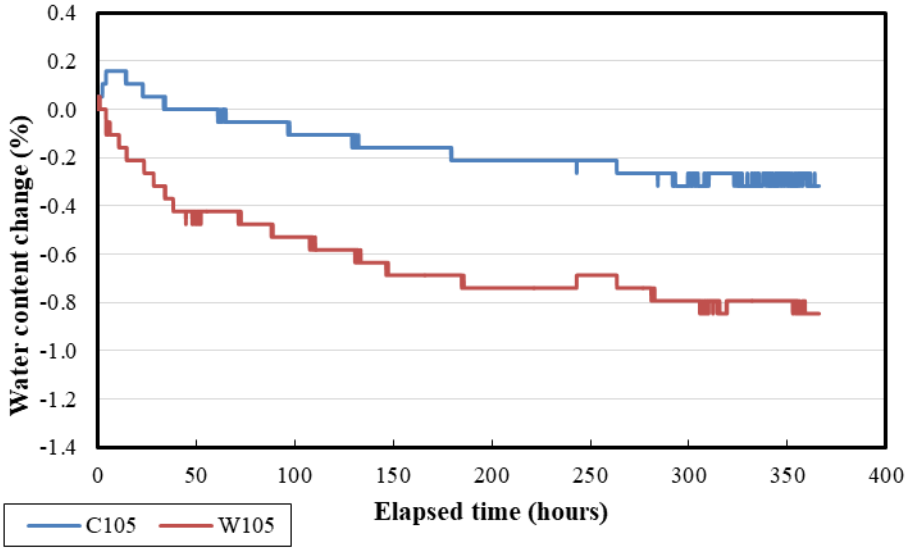

(c)

Figure 4.16 Water content changes at different depths in the soil column in Test 1 (continued)

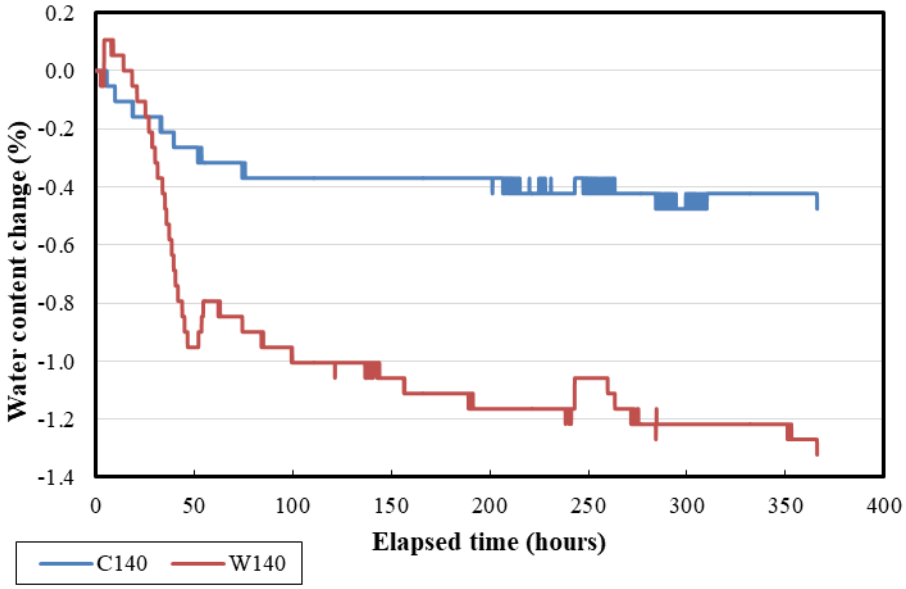

(d)

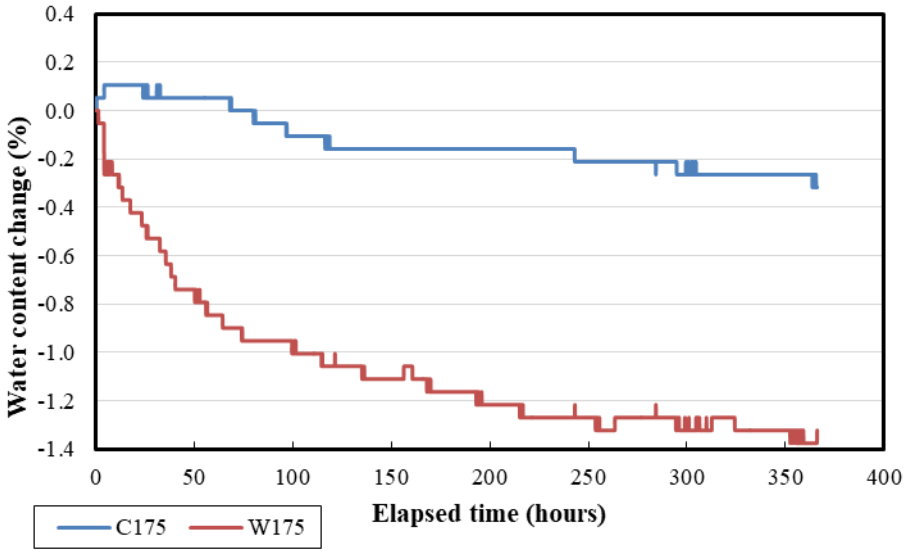

(e)

Figure 4.16 Water content changes at different depths in the soil column in Test 1 (continued)

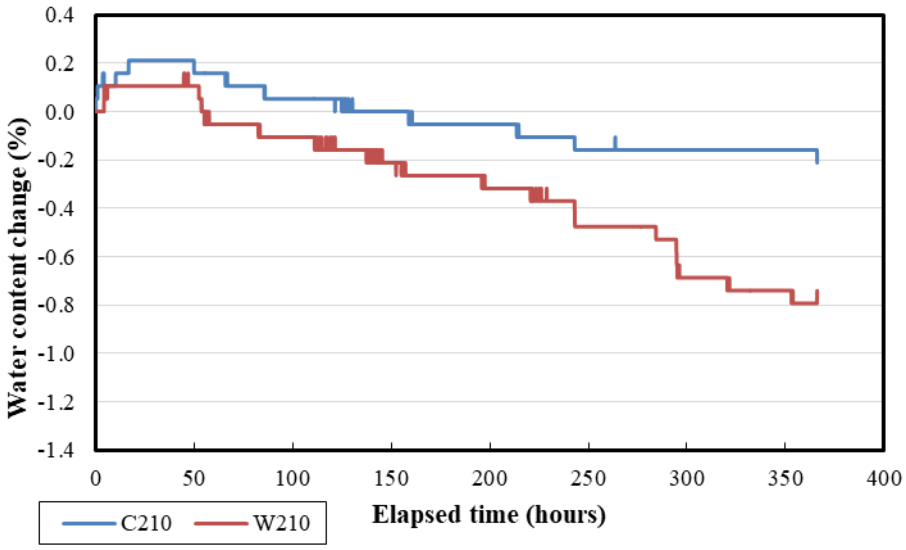

(f)

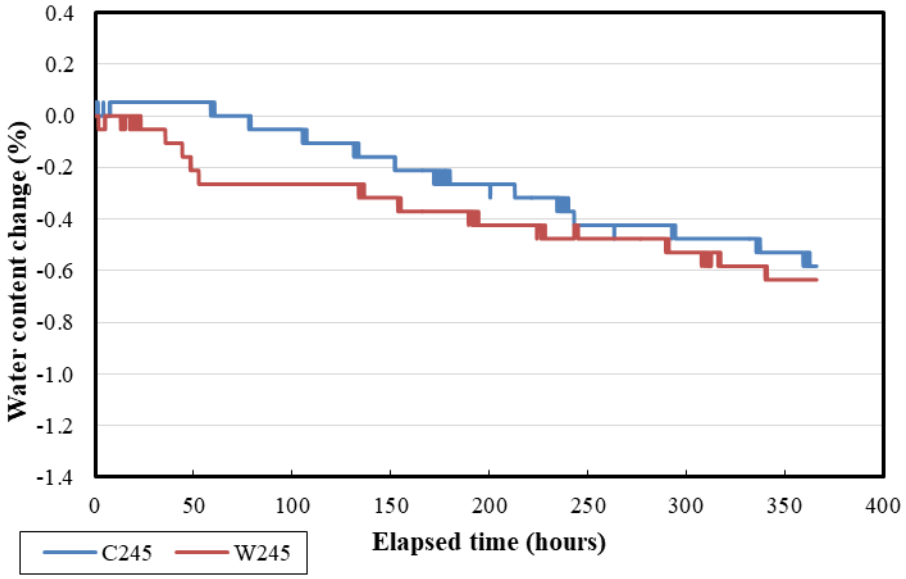

(g)

Figure 4.16 Water content changes at different depths in the soil column in Test 1 (continued)

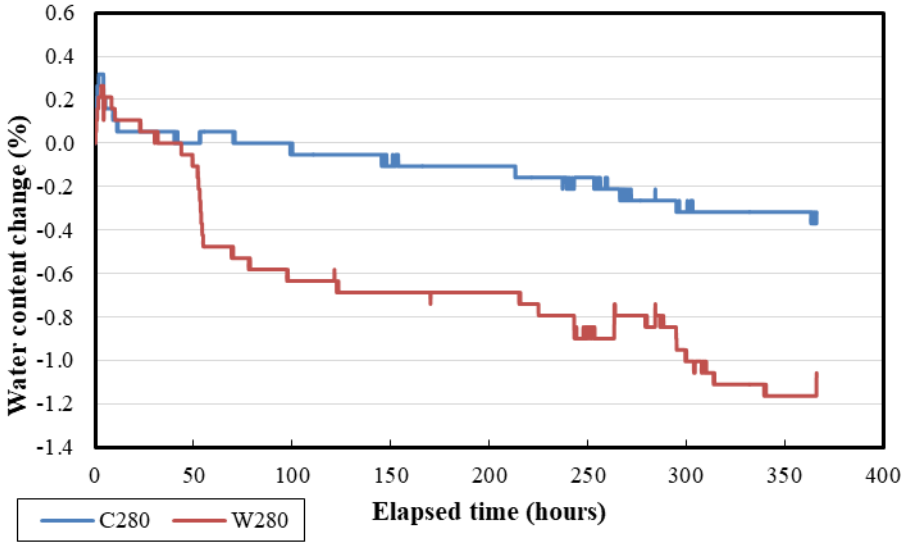

(h)

Figure 4.16 Water content changes at different depths in the soil column in Test 1 (continued)

Figure 4.17 presents the water content changes at various depths in the second soil column test. The second soil column test included a conventional geotextile No. 2 soil column and a wicking geotextile soil column. Six moisture sensors were installed in each soil column. The AB-3 aggregate was compacted at 9.8% water content. The average room temperature and relative humidity were 8.6℃ and 60%, respectively.

Similar to Test 1, the water content changes in both conventional and wicking geotextile soil columns were similar at a distance from the geotextiles. Figure 4.17(d) shows that at a distance of 180 mm above the geotextile specimens, the water content changes from both soil columns were

similar. Thus the effective distance of the wicking geotextile as compared to the conventional woven geotextile No. 2 was 180 mm. Based on the observation from both Tests 1 and 2, the concept of the effective wicking zone is proposed. The effective wicking zone is the portion of the geomaterial surrounding the wicking geotextile that benefits from the ability of the wicking geotextile to remove moisture from an unsaturated geomaterial. From Figures 4.17(a) through (c), in the first 40 hours, the water content changes within both soil columns were similar. However, the conventional woven geotextile No.2 stopped removing water from the soil column after 50 hours while the wicking geotextile continued reducing the water content within the effective zone. By the end of the first week (168 hours), the average water content in the effective wicking zone of the wicking geotextile soil column was 0.2% lower than the average water content in the same zone in the conventional geotextile soil column. By the end of 20 days, the wicking geotextile reduced 0.4% more average water content in the effective wicking zone than the conventional woven geotextile.

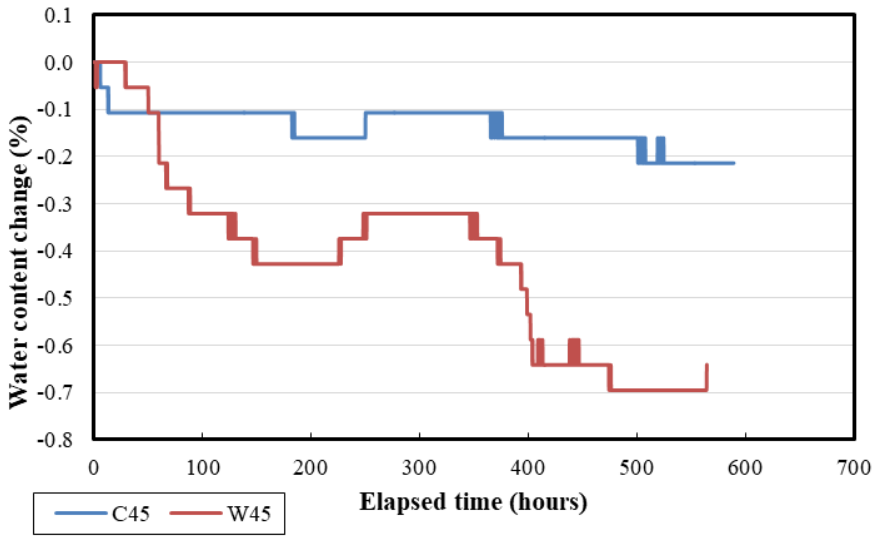

(a)

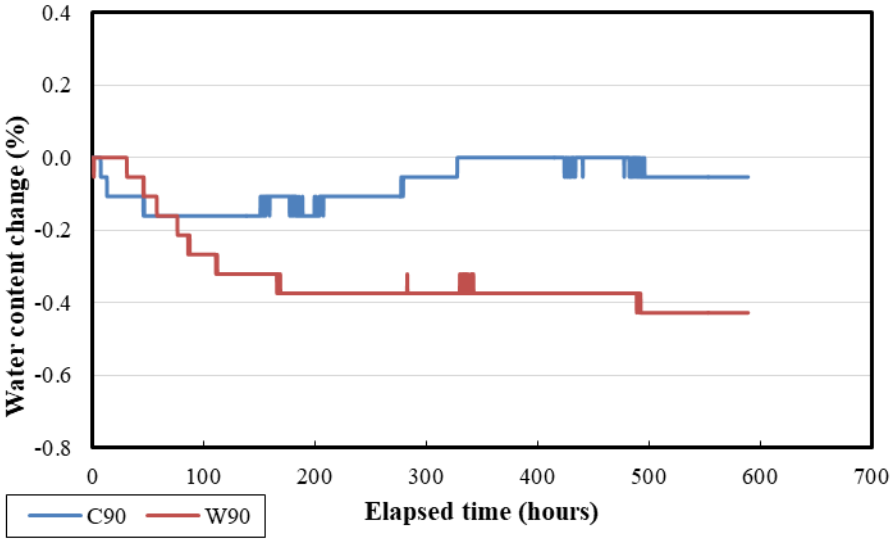

(b)

Figure 4.17 Water content changes at different depths in the soil column in Test 2

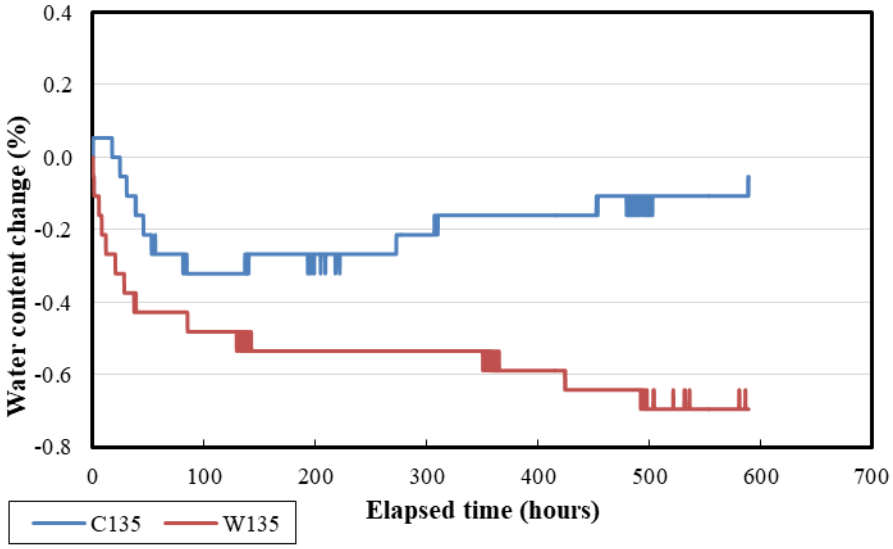

(c)

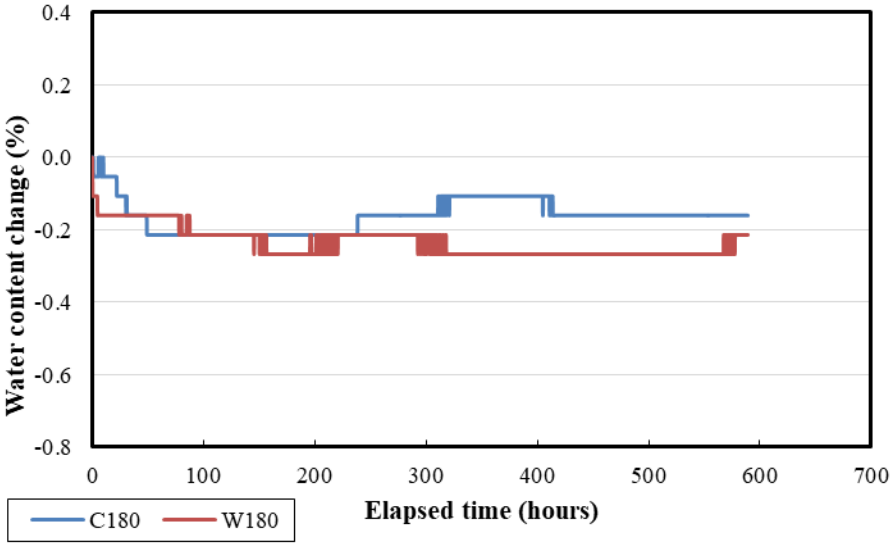

(d)

Figure 4.17 Water content changes at different depths in the soil column in Test 2 (continued)

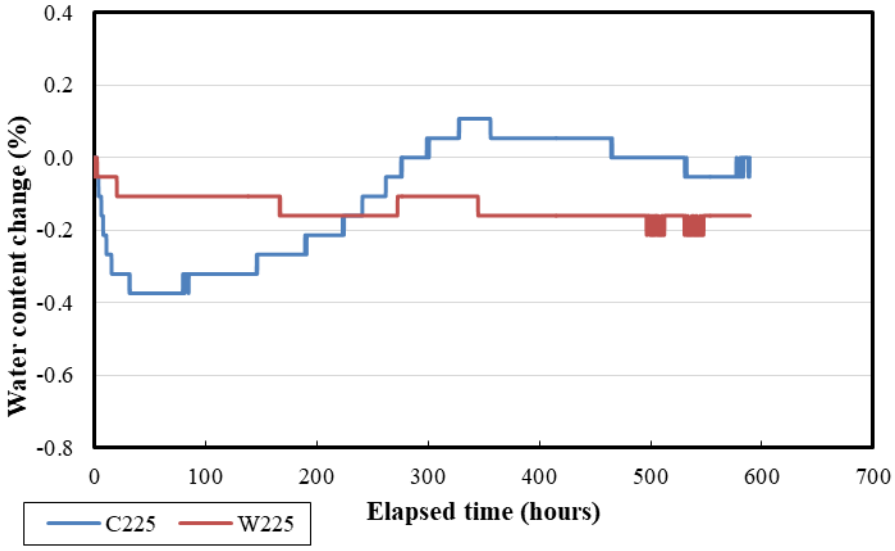

(e)

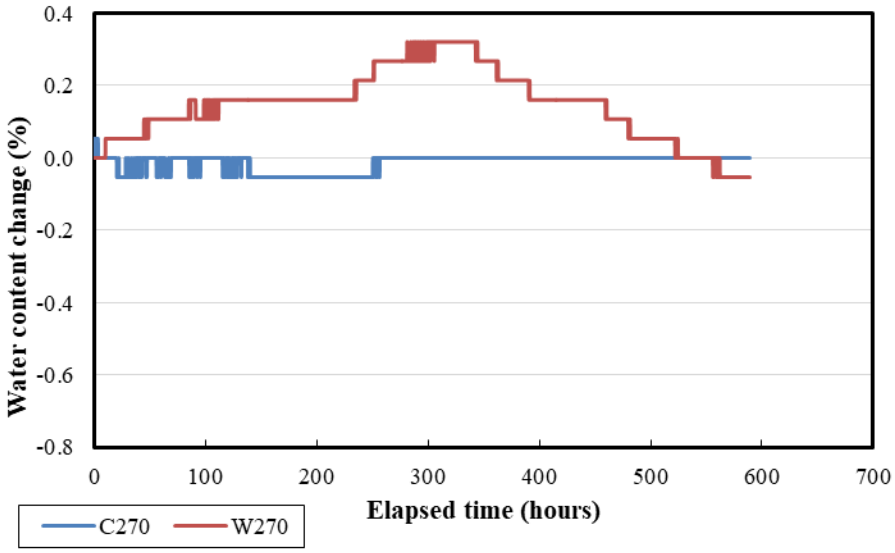

(f)

Figure 4.17 Water content changes at different depths in the soil column in Test 2 (continued)

The third soil column test procedure was slightly different from that of the previous two tests. The third test included a conventional geotextile No. 2 soil column and a wicking geotextile soil column. Seven moisture sensors were installed in each soil column. The AB-3 aggregate was compacted at the optimum water content, 8.6%. The average room temperature and relative humidity were 10.1℃ and 40%, respectively. The third test consisted of two stages. The first stage was similar to that in the previous two tests, the soil columns were placed in the temperature-controlled room and the soil water content changes were monitored. After approximately 20 days, the plastic sheets covering the top of soil columns were removed and the soil columns were submerged into two large water tanks for 50 hours. The submerging process allowed the AB-3 aggregate to absorb soil and reach a condition close to saturation. Then, the soil columns were removed from the water tanks and placed on the table. The top of the soil columns were then covered again with plastic sheets.

The test results of the third soil column test are presented in two figures. Figure 4.18 presents the water content changes from the beginning of the test to the end of the first stage (0 to 500 hours). Figure 4.19 presents the water content changes starting from the soil columns were removed from the water tank. The water content changes in both figures were calculated based on the initial water content after the preparation of the soil columns.

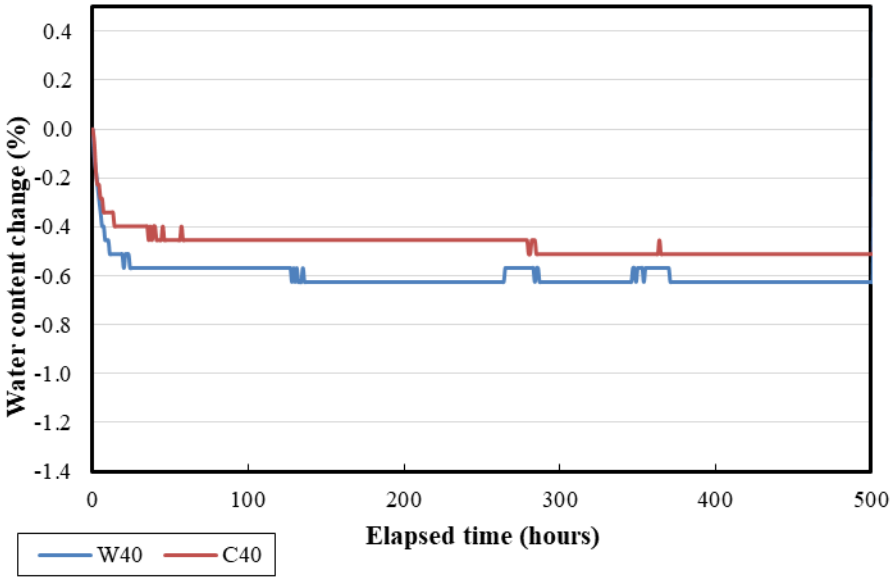

(a)

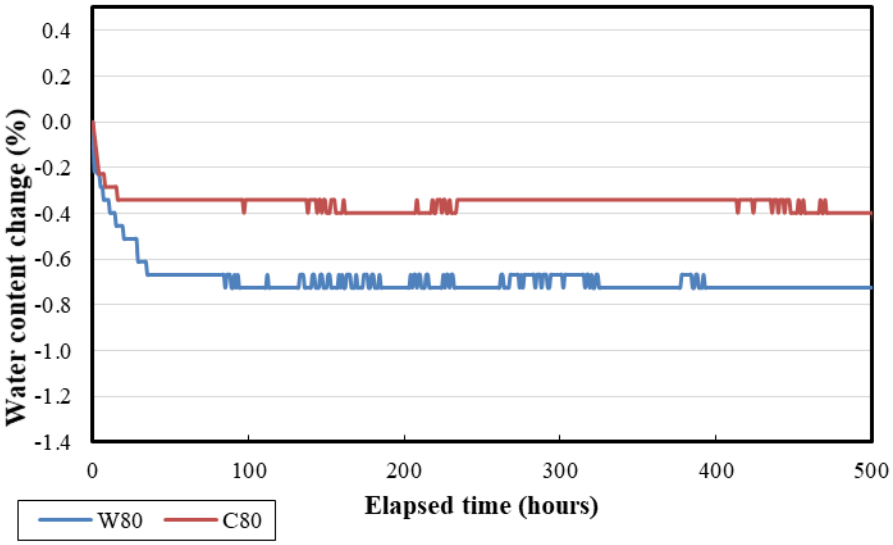

(b)

Figure 4.18 Water content changes at different depths in the soil column of the first stage in Test 3

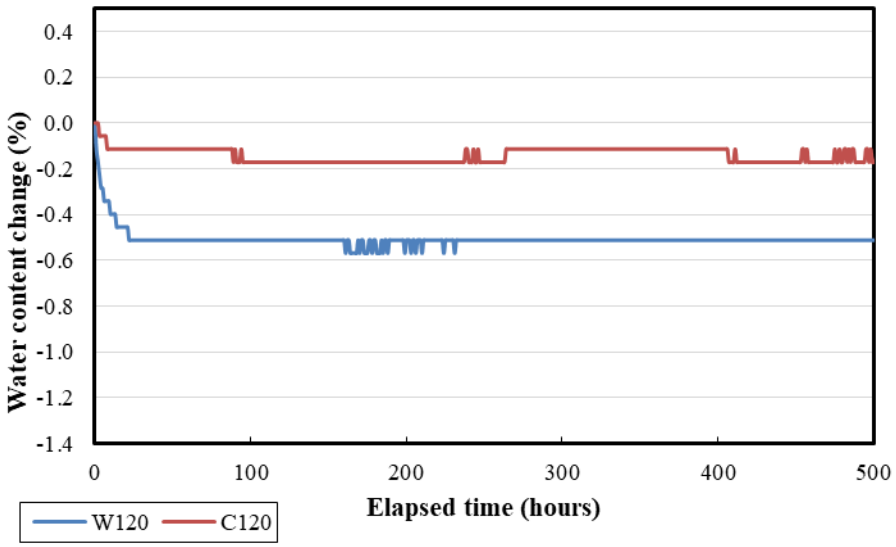

(c)

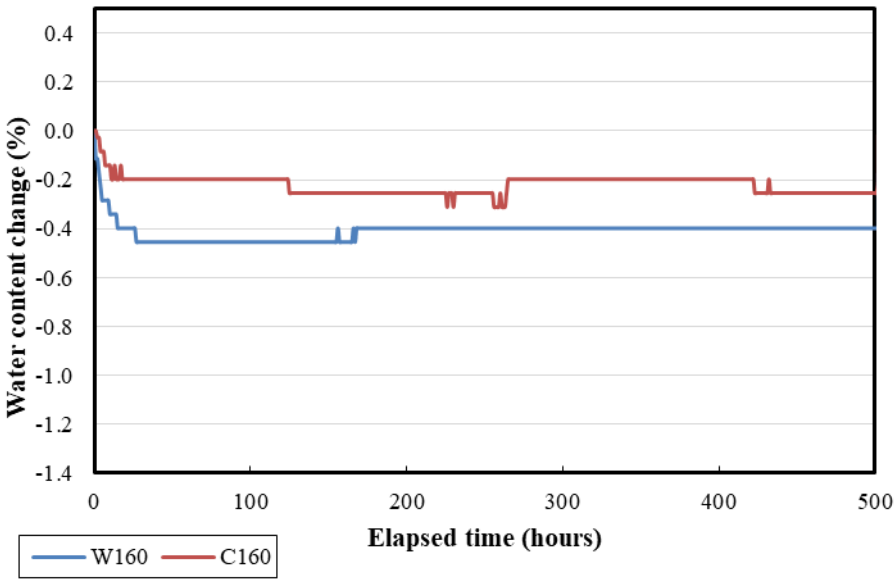

(d)

Figure 4.18 Water content changes at different depths in the soil column of the first stage in Test 3 (continued)

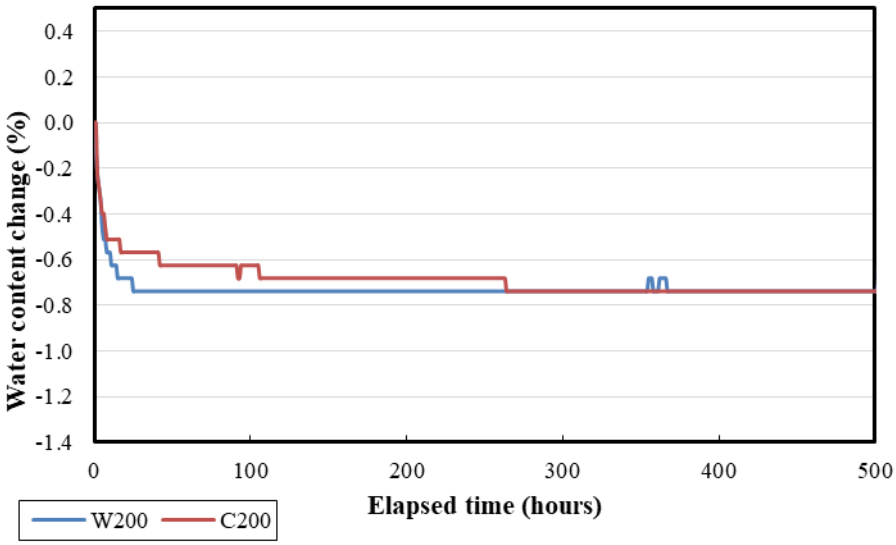

(e)

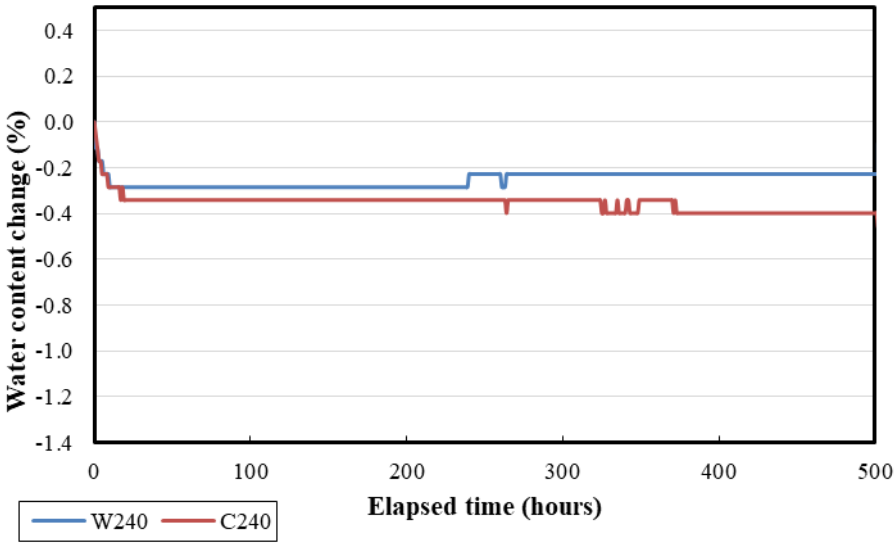

(d)

Figure 4.18 Water content changes at different depths in the soil column of the first stage in Test 3 (continued)

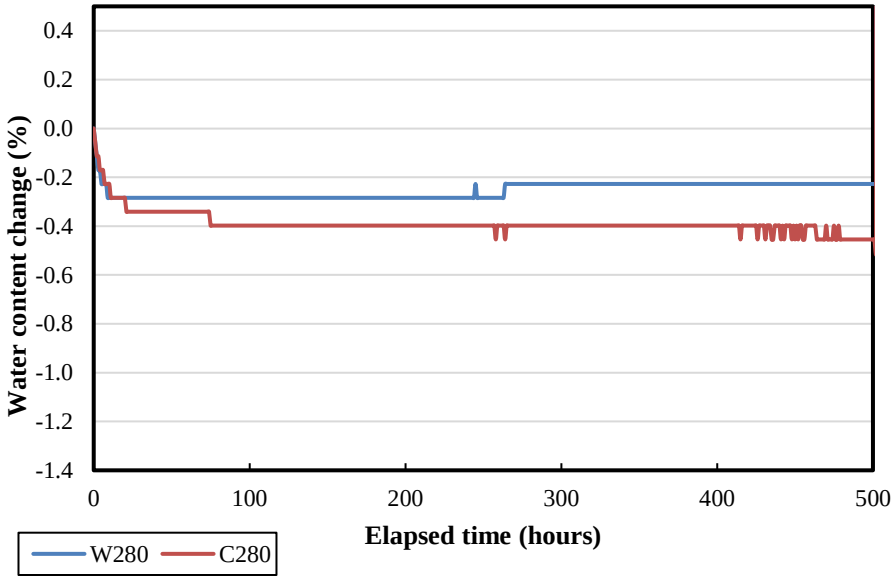

(e)

Figure 4.18 Water content changes at different depths in the soil column of the first stage in Test 3 (continued)

Since the AB-3 aggregate was compacted at the optimum water content, the water content changes in the first stage of the test were less as compared to those in the previous two tests. However, the effective wicking zone could still be observed. At the distance of 200 mm from the geotextiles, the water content changes of the two soil columns were almost exactly the same. The water content changes within the effective wicking zone showed that the wicking geotextile was slightly more effective in removing moisture from the soil column than the conventional geotextile. At the end of the first week, the wicking geotextile reduced 0.2% more water content in the effective wicking zone as compared to the conventional geotextile.

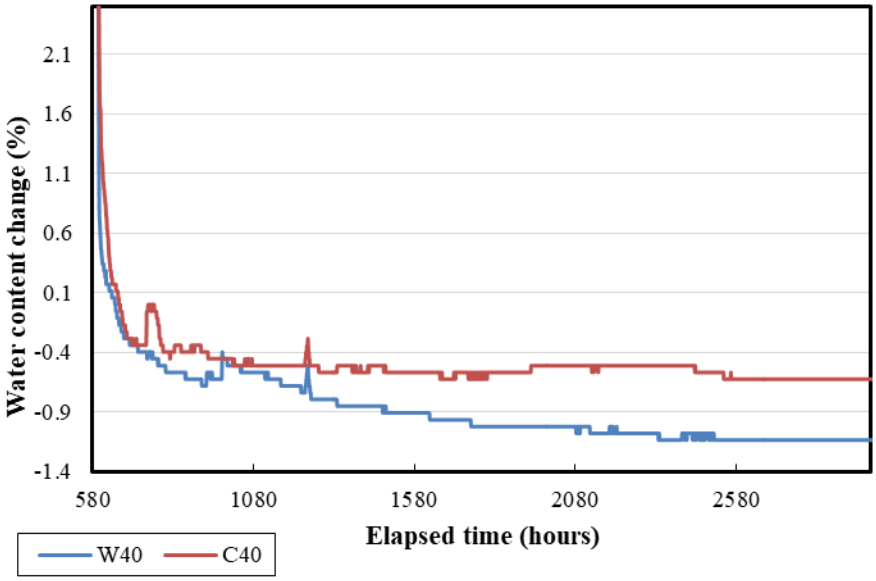

(a)

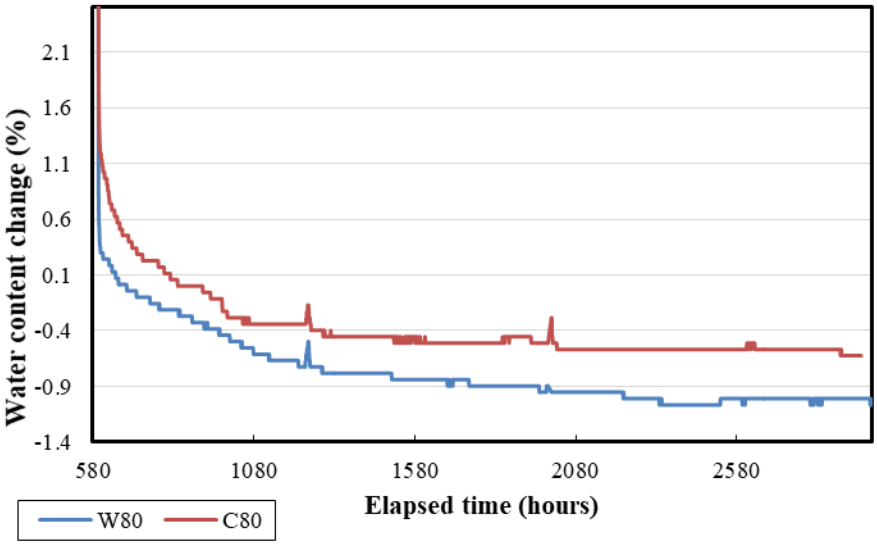

(b)

Figure 4.18 Water content changes at different depths in the soil column of the second stage in Test 3

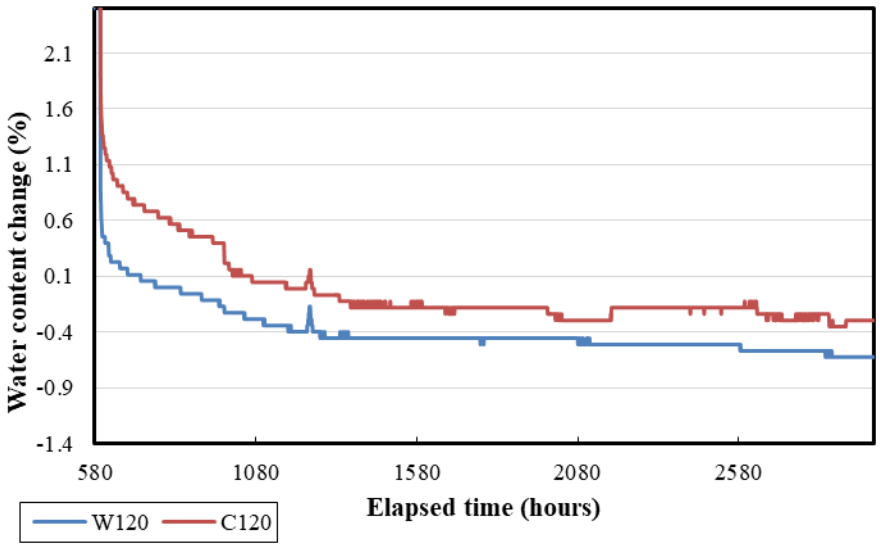

(c)

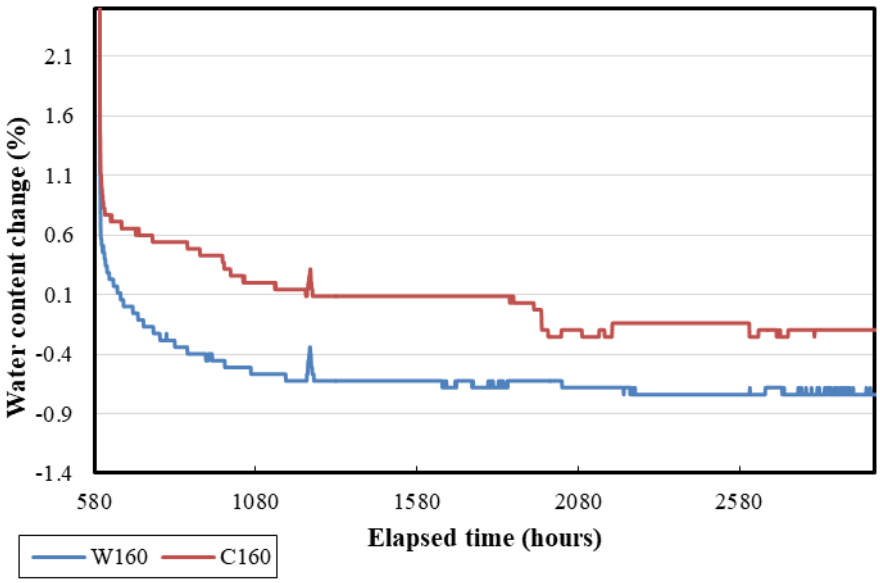

(d)

Figure 4.18 Water content changes at different depths in the soil column of the second stage in Test 3 (continued)

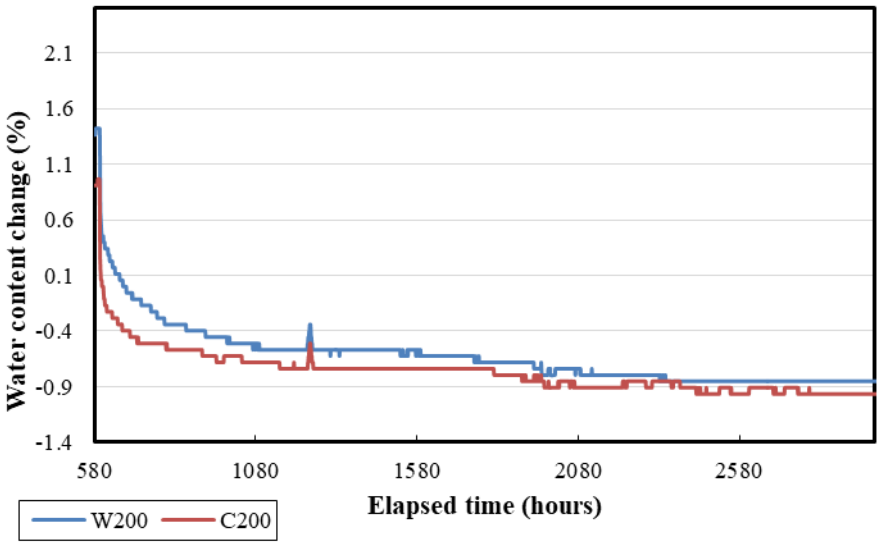

(e)

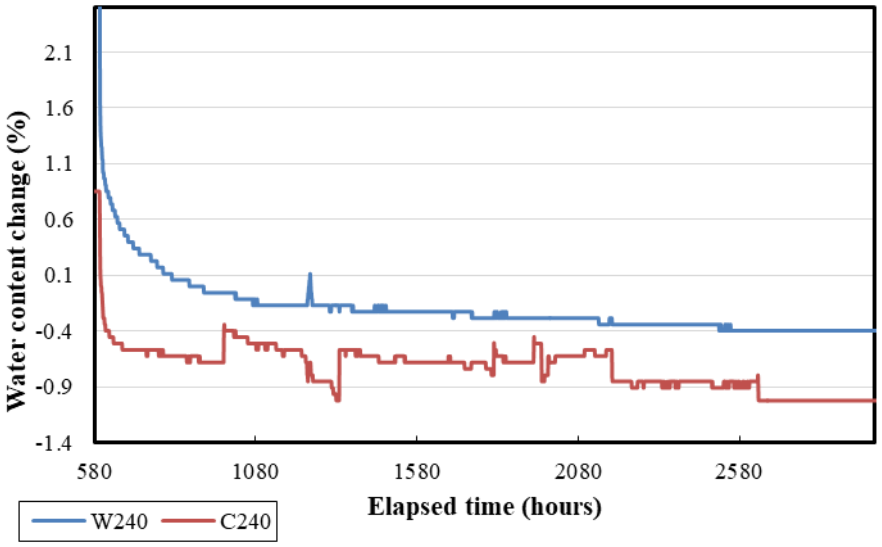

(f)

Figure 4.18 Water content changes at different depths in the soil column of the second stage in Test 3 (continued)

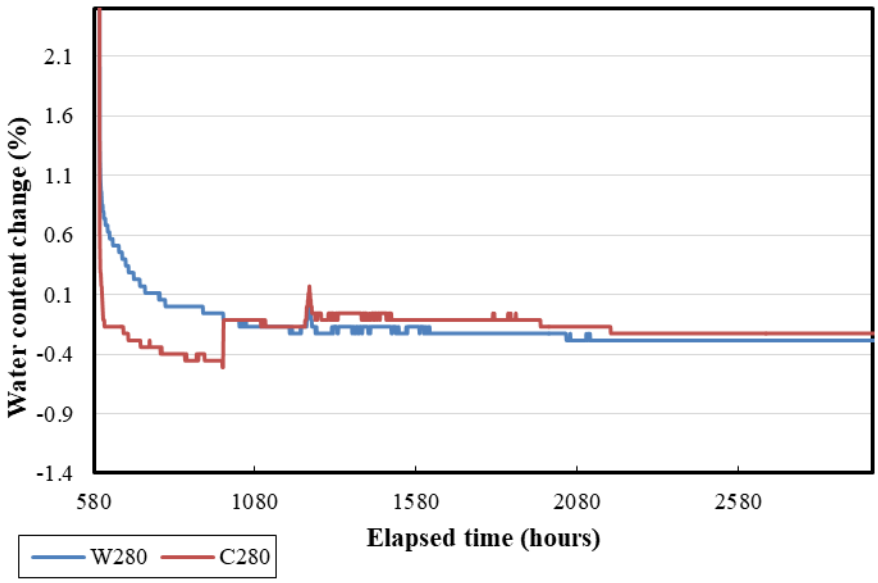

(g)

Figure 4.18 Water content changes at different depths in the soil column of the second stage in Test 3 (continued)

A rapid decrease in water content was observed within the first two hours after the soil columns were removed from the water tank. This potion of water content decrease can be considered as gravitation drainage. The rates of water content decrease in the conventional and wicking geotextile soil columns were very similar. Then the rate of water content decrease became slow. At approximately 600 hours after the soil columns were removed from the water tank, the water contents in the soil columns were similar to those at the end of stage one. The effective wicking zone for the second stage of the third soil column test was the same as the first

stage. From Figure 4.18(e), the effective wicking zone of the second stage was from the geotextile to 200 mm above the geotextile, which was the same as the location of the effective wicking zone from the first stage of the test.

Table 4.5 presents the duration of time from the soil columns removed from the water tank to the soil water content decreasing to the optimum water content (i.e., water content at the beginning of the test) at different depths. The water contents in the conventional geotextile soil column close to the base course surface (i.e., 280, 240, and 200 mm from the geotextile) returned to the optimum water content very quickly. This phenomenon was likely caused by the soil disturbance during the process of moving the soil column from the water tank. By comparing the time needed for the water content of the AB-3 aggregate within the effective wicking zone to return to the optimum water content, it is found that the wicking geotextile accelerated the drainage more effectively than the conventional woven geotextile.

Table 4.5 Time needed for the soil column to return to the optimum water content

Distance to geotextile (mm)	Time to return to optimum water content (hr.)	
	Wicking geotextile	Conventional woven geotextile No.2
280	206	11
240	279	5
200	73	8
160	75	1347
120	191	580
80	92	248
40	53	66

The soil column tests demonstrated the effectiveness of the wicking geotextile in removing water from the surrounding geomaterial. The effective zone of the wicking geotextile in the AB-3 aggregate was from the geotextile to 180 to 210 mm above the geotextile. Figure 4.19 presents the average water content changes in the effective zone in the three soil column tests. In the first soil column test, the conventional woven geotextile No. 1 had a lower flow rate that was approximately one-third of the conventional woven geotextile No. 2. Consequently, the water content reduction rate from the conventional geotextile No. 1 was slower than that of the conventional geotextile No. 2. At the end of the first 48 hours of the tests, the wicking geotextile reduced more water content within the effective wicking zone than the conventional geotextile No. 1 by a margin of 0.5%. At the same duration into the test, the water content changes in the effective wicking zone in both soil columns of Test 2 were approximately the same. The effectiveness of the wicking geotextile in removing moisture from the AB-3 aggregate became more significant

with the progress of the test. From Figure 4.10(b), the conventional woven geotextile No. 2 could reduce the water content to a certain extent. However, when the water content of the surrounding geomaterial decreased, the conventional woven geotextile No. 2 stopped removing water. The wicking geotextile, on the other hand, could continue removing water at a lower rate. The wicking geotextile would eventually stop removing moisture from the geomaterial as the water content decreased to a certain value. Based on Figure 4.19(c), the initial dry wicking geotextile could remain functioning in the AB-3 aggregate of water content as low as 8%. The wicking geotextile was more effective in removing water from the nearly saturated AB-3 aggregate. It took 278 hours for the conventional woven geotextile No. 2 to reduce the average AB-3 water content in the effective wicking zone to the optimum water content from the near saturation condition. The wicking geotextile took 75 hours to reduce the water content of the AB-3 from the near saturation condition to the optimum water content. It took 1400 hours for the conventional woven geotextile No. 2 to reduce the average water content of the AB-3 aggregate to 8.2% (i.e., the average water content of AB-3 in the effective wicking zone at the end of the first stage of Test 3). It took 625 hours for the wicking geotextile to reduce the water content of the AB-3 in the effective wicking zone to the previous lowest value.

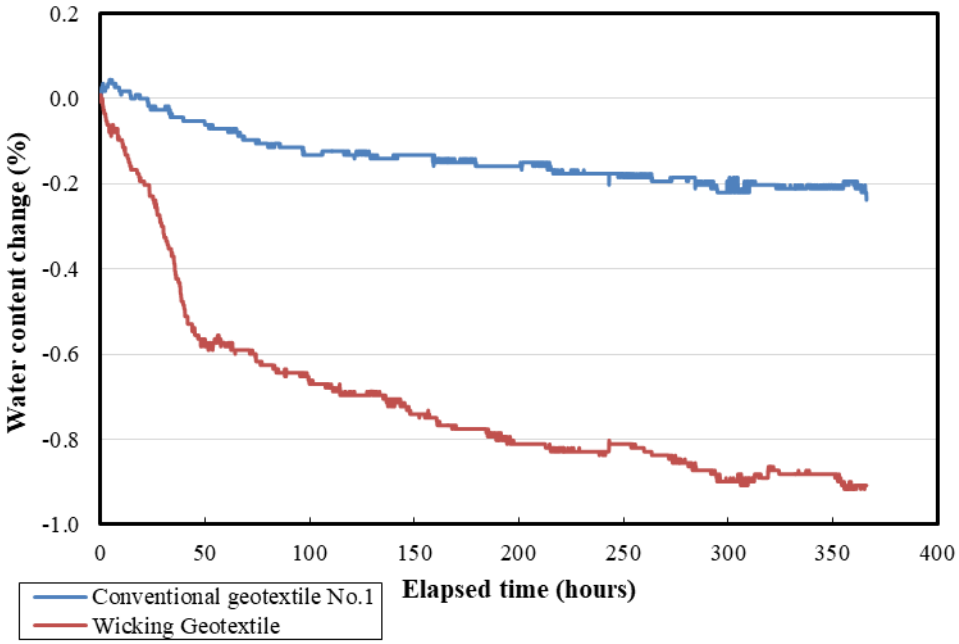

(a) Test 1

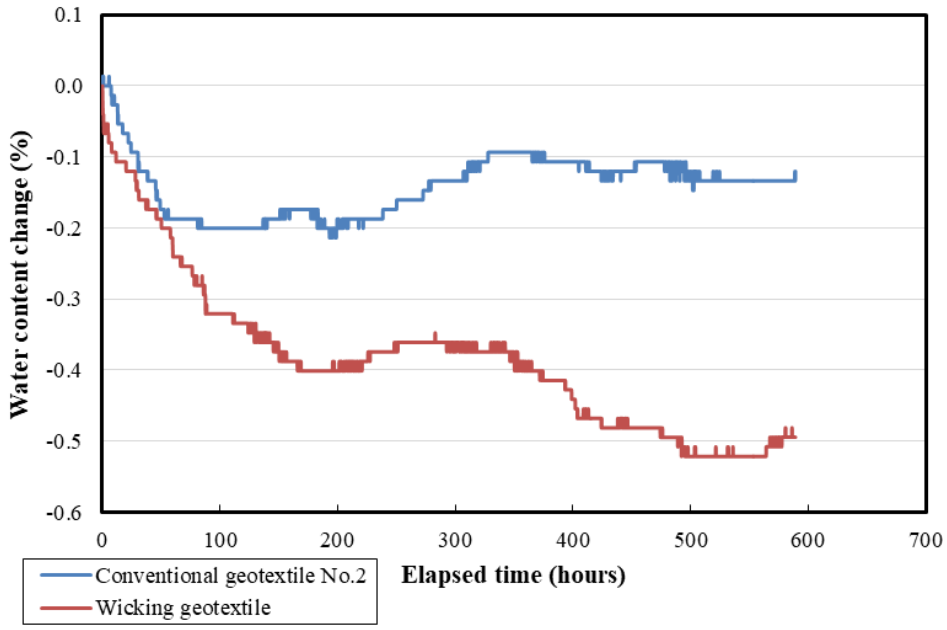

(b) Test 2

Figure 4.19 Average water content changes in effective wicking zones of soil column tests

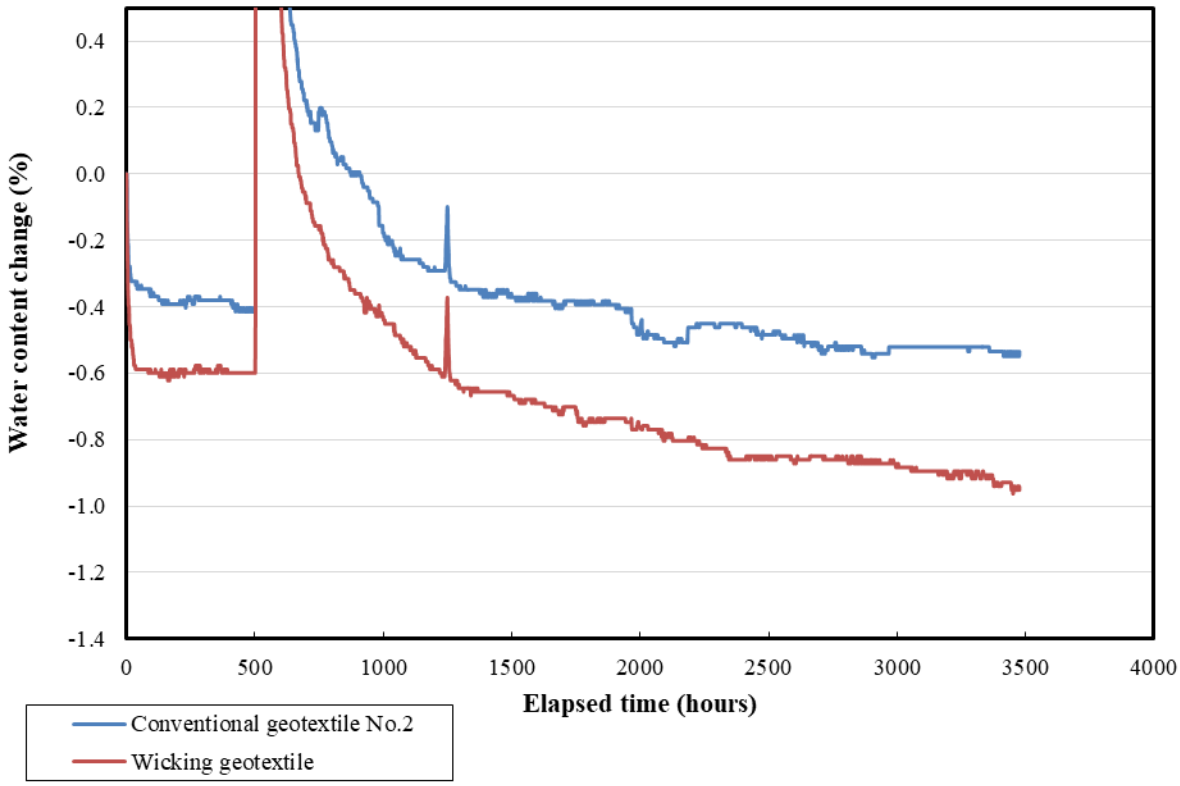

(c) Test 3

Figure 4.19 Average water content changes in effective wicking zones of soil column tests (continued)

4.4 Conclusions

The small-scale box tests and the soil column tests demonstrated the ability of wicking geotextile in removing water from geomaterials. Based on the test results and analysis, the following can be concluded:

(1) The conventional woven geotextile was effective in removing excess water from the AB-3. However, the conventional woven geotextile could not remove water from the AB-3 aggregate when the water content was close or slightly above the optimum water content. The wicking geotextile was able to continue removing water from the AB-3 at a lower water content.

(2) The wicking geotextile had little effect on the water content of the compacted subgrade material below the geotextile.

(3) The effective wicking zone of the wicking geotextile ranged from the geotextile to approximately 200 mm above the geotextile. The water content of geomaterial within the effective wicking zone was significantly affected by the wicking geotextile.

(4) When compared to a conventional woven geotextile, the effectiveness of the wicking geotextile in reducing the water content in the AB-3 aggregate was more pronounced as more time was allowed.

(5) The wicking geotextile removed water from the nearly-saturated AB-3 aggregate much faster than the conventional woven geotextile. The time required for the wicking geotextile to reduce the water content of AB-3 aggregate from a near saturation condition to the optimum water content was approximately one-fourth of time required for the conventional geotextile.

CHAPTER 5 Large-scale cyclic plate loading tests

The small-scale box tests and the soil column tests demonstrated the effectiveness of the wicking geotextile in removing moisture from base courses. In addition to its drainage function, the geotextile serves the functions of separation, filtration, and mechanical stabilization. To further investigate the benefits of the wicking geotextile close to a field condition, six large-scale cyclic plate loading tests with simulated rainfall were conducted to evaluate the combined effect of the wicking geotextile on limiting permanent deformations of base courses. The large-scale cyclic plate loading tests were conducted on test sections with 3% or 5% CBR subgrades. Under each subgrade CBR condition, an unreinforced, a conventional woven geotextile-improved, and a wicking geotextile-improved section were tested. Each test section underwent three rainfall and drying cycles: 7 days, 2 days, and 2 hours. At the end of each rainfall and drying cycle, a cyclic plate loading test was conducted.

5.1 Test setup

The cyclic plate loading tests with simulated rainfall were conducted in a large test box in a dimension of 2 m × 2.2 m × 2 m (W×L×H). Each test section consisted of a 0.9 m thick subgrade layer and a 0.3 m thick base course layer. Geotextile was placed at the interface between the subgrade and the base course. Figure 5.1 presents a schematic of one test section. The loading plate of 300 mm in diameter was attached to an actuator located above the center of the test box. Four layers of EC-5 volumetric moisture sensors were installed in each section: three layers in the base course at depths of 75, 150, and 225 mm; as well as another layer at 75 mm beneath the base course-subgrade interface as presented in Figure 5.1(a). Each layer consisted of six individual

volumetric moisture sensors with relative distances to each other as shown in Figure 5.1(b). These four layers of sensors were placed along a longitudinal line at 0.3 m from the center of the loading plate to avoid damaging sensors during loading. A telltale was placed at 10 cm from the center of the loading plate with the base plate placed at the interface between the base course and the subgrade. It is to be noted that in the improved sections, a base plate for the telltale was placed over the geotextile. A displacement transducer was used to measure the deflection of the base course and subgrade interface indicated by the telltale. Four earth pressure cells were placed on the subgrade surface at the center of the loading plate and, 150 mm, 300 mm, and 600 mm from the center of the loading plate.

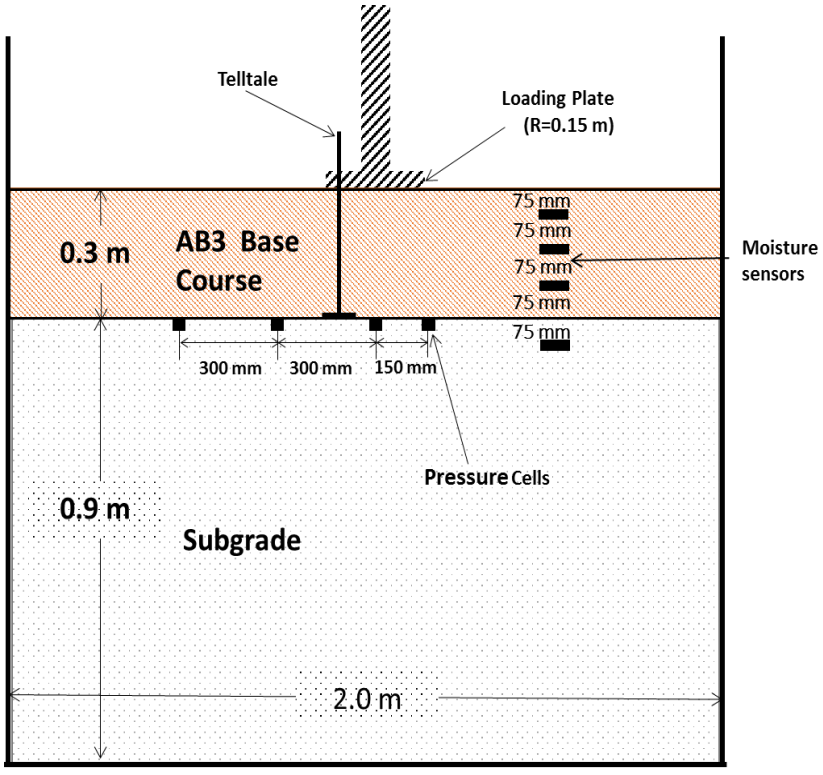

(a) Cross-section view of test section

Figure 5.1 Schematic of the large-scale cyclic plate loading test

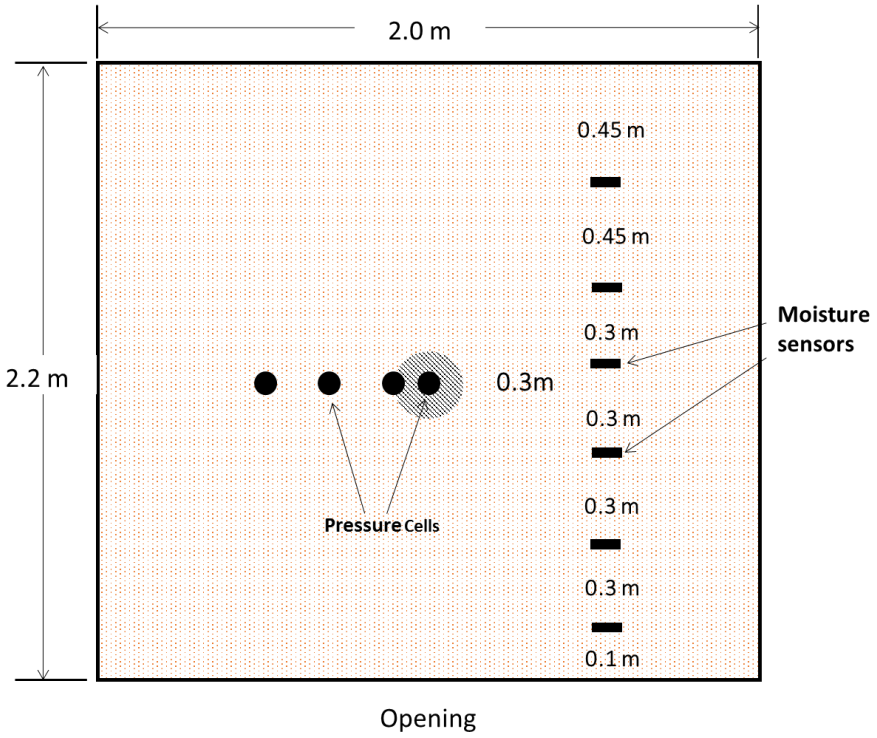

(b) Top view with sensor locations

Figure 5.1 Schematic of the large-scale cyclic plate loading test (continued)

As demonstrated in the previous chapters, the water removal rate of the wicking geotextile depended on air temperature and relative humidity. To control the temperature and relative humidity during the drying periods, an environmental chamber was constructed with a fiber-reinforced plastic sheet and isolation material to enclose the entire testing box as shown in Figure 5.2. The inner layer of the plastic sheet was glued to the edge of the box for sealing. The front opening of the inner layer could be sealed by strip-loop. During the test, the bottom of the inner layer in the front was taped to the floor for sealing. Outside of the inner layer, on three sides and the top, a layer of fiberglass isolation was placed to reduce heat transfer. An outer layer of the fiber-reinforced plastic sheet was installed over the insulation layer. Since the tests were conducted in the summer, the main challenge was to maintain the temperature inside the chamber.

An air conditioner was used to cool the air between the outer and inner layers to limit the effect of outside air temperature fluctuation on the temperature within the chamber.

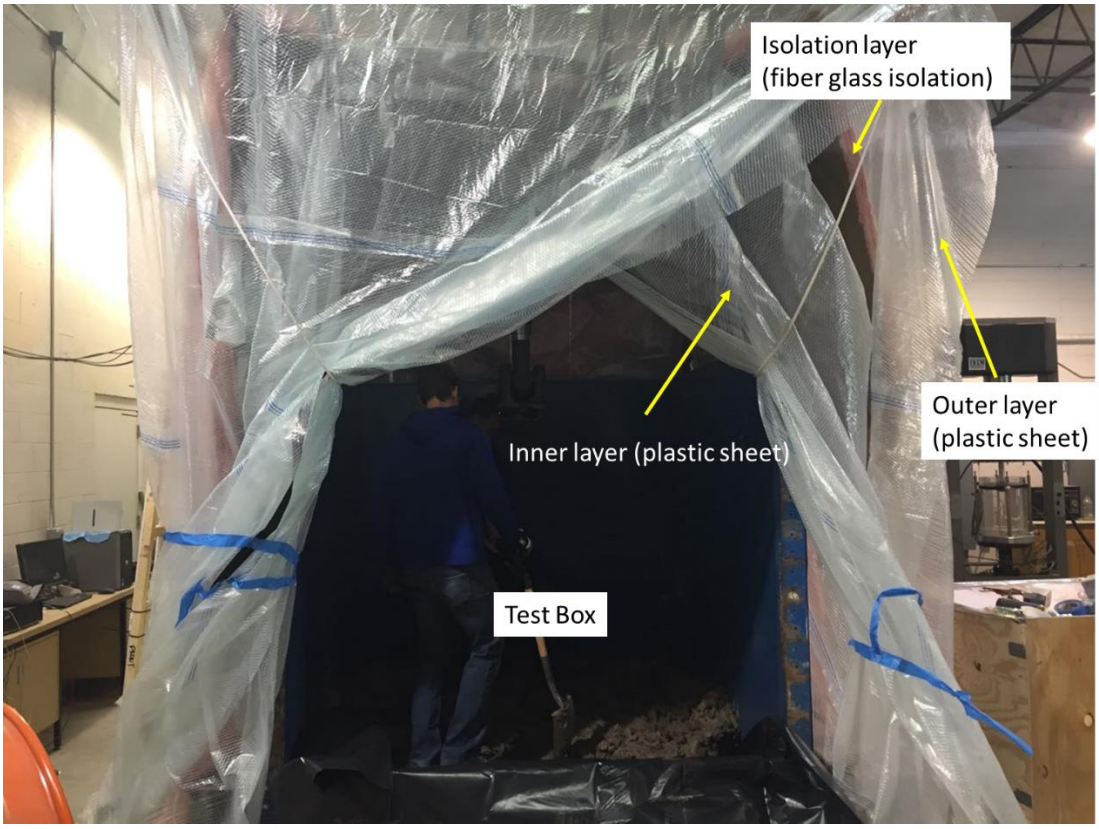

Figure 5.2 Environmental chamber

To maintain the relative humidity and temperature in the environmental chamber, the air inside the chamber was cycled through an air regulating system that consisted of a dehumidifier and an air conditioner. A schematic of the air regulating system is shown in Figure 5.3. The dehumidifier was placed in the environmental chamber. The operation of the dehumidifier was expected to generate a substantial amount of heat. Thus an air cooling process was necessary before

the dried air was released back into the environmental chamber. A 150 mm diameter aluminum air duct was attached to the exhauster to the dehumidifier which directed the dried air to the cooling chamber. The cooling chamber was constructed with plywood and painted with water resistant paint. A window air conditioner was fitted to the side of the cooling chamber. When the air in the cooling chamber was warmed to the preset temperature, the air conditioner was turned on automatically. The cooled air was then pumped back to the environmental chamber via a fan. Another air duct connecting the environmental chamber to the cooling chamber allowed air withdrawn directly from the environmental chamber to the cooling chamber directly, so that when the air within the environmental chamber was cooled without going through the dehumidifier.

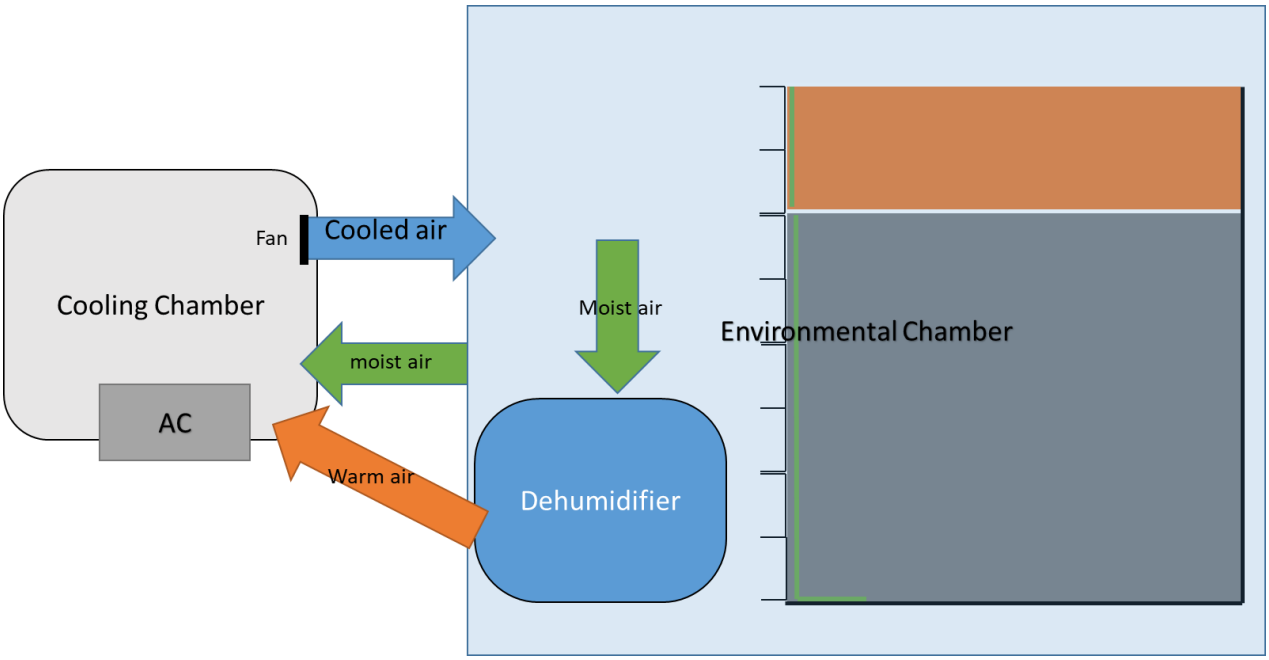

Figure 5.3 Schematic of the air regulating system

A rainfall simulator was constructed with 19 mm diameter PVC pipes to evenly distribute precipitation over the surface of a test section as shown in Figure 5.4. The rainfall simulator had an overall dimension of 2 m × 2.2 m. The PVC pipes were fixed onto a wood frame in a parallel pattern with 150 mm spacing. Each end of the PVC pipes was connected with PVC pipes of the same diameter. At the mid-span of the top and bottom PVC pipes, T-shape adaptors were fitted as water inlets. Two 20 mm diameter garden hoses were fitted to the water inlets while the open ends of both hoses were joined together to a high precision flowmeter. Holes of 0.8 mm in diameter were drilled along each PVC pipe between the top and bottom pipes at 150 mm spacing as shown in Figure 3.6. The two PVC pipes near the center were cut and capped due to the loading apparatus. During the test, the rainfall simulator was placed over the top of the testing box at approximately 0.7 m from the test section surface.

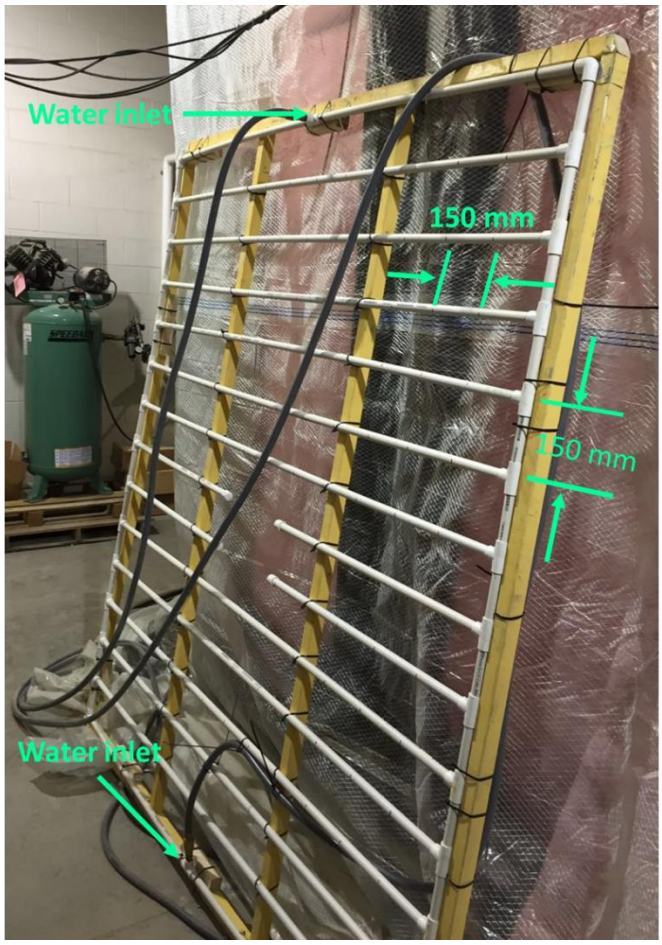

Figure 5.4 The rainfall simulator

The subgrade of each test section was compacted in six 150 mm lifts using an electric vibratory compactor. The subgrade material was the same as the subgrade material used in the small-scale box tests, i.e., 25% kaolin and 75% Kansas River sand by weight. The CBR value of the compacted subgrade was achieved by adjusting the water content of the subgrade material. After each lift, five vane shear tests were conducted to verify the CBR of the subgrade. Due to size limitation and shape of the compactor plate, the subgrade material at the edge and corner of the box did not receive the same degree of compaction as the central region. Hand compaction

was utilized to compact the soil at the edges and corners. After the construction of the subgrade, trenches were dug for the installation of pressure cells and volumetric water content sensors. The volumetric water content sensors were installed in the similar fashion as those in the small-scale box test. After the preparation of the subgrade, for the geotextile-improved sections, a 2 m × 3.2 m (machine direction × cross-machine direction) geotextile was placed over the subgrade surface with the cross-machine direction perpendicular to the front facing of the test box. Rebars were used to fix the geotextile at the corners. The geotextile was allowed to extend 1 m beyond the edge from the opening side of the testing box. For the control test sections, a 2 m × 1.2 m (W × L) plastic sheet was placed at the interface over the front edge with 1 m extended beyond the box. Approximately 0.2 m of the plastic sheet would be placed at the interface between the base course and the subgrade along the opening. The part of the plastic sheet between the base course and the subgrade would intercept the water flowing along the interface which otherwise would flow along the front facing and could not be accounted for. The front facing of the testing box was assembled by bolting eight 150 mm – wide "C" channel facing bars in the horizontal direction. The "C" channel at the base course – subgrade interface level was ground off by approximately 1.5 mm to accommodate the exiting of the geotextile or plastic sheet from the testing box. The base course was constructed with AB-3 aggregate, same as that used in the small box tests. The AB-3 aggregate was adjusted to its optimum water content (i.e., 8.6%) before compaction. The base course was compacted in two 150 mm lifts with the same electric vibratory compactor. After the compaction of the first base course lift, trenches were dug for volumetric water content sensors corresponding to the depth of 225 mm. The volumetric water content sensors corresponding to the depth of 150 mm were placed over the first lift of base course. The second lift of base course was then compacted. The volumetric water content sensors corresponding to the depth of 75 mm

were placed in the second lift of base course with the same technique as those at the depth of 225 mm. Due to small particle sizes, the volumetric water content sensors could be inserted into the subgrade soil directly. However, direct insertion could not be achieved in the aggregate base course due to the larger particle sizes of the AB-3 aggregate. Thus the volumetric water content sensors were buried in the trench first. Then hand compaction was conducted over the sensors to compact the aggregate.

After the preparation of the test section, the rainfall simulator was placed over the testing box. A 2 m × 1 m (W × L) water container was placed on the floor in front of the box to collect water exiting the box from the front facing gaps below the interface. A table was placed on the water container to support the geotextile or plastic sheet to a 1:5 (V:H) slope as shown in Figure 5.5. A PVC pipe at the lower end of the table was used to collect the water exiting from the interface. The rainfall simulator was then connected to the flowmeter and water supply.

Figure 5.5 Test setup for rainfall simulation

5.2 Test procedure

Each test section underwent three rainfall and drying cycles and cyclic plate loading tests. After the preparation of the test section, the 1st rainfall simulation was conducted. At the end of the rainfall simulation, the section was covered with a layer of plastic sheet to limit evaporation from the base course surface. During and after the rainfall simulation, water exiting from the interface and front facing was collected and weighted. The water collection process lasted around 12 hours after the completion of simulated rainfall. After the water exiting from the interface and the front facing had been weighted on the second day, the table and water container were removed. The plastic sheet or geotextile was hung from the testing box vertically. The air ducts from the air regulating system were then installed into the environmental chamber. The environmental

chamber was then sealed. The air conditioners and dehumidifier were then turned on. The environmental chamber was sealed for six days and the water extracted from the dehumidifier and the air conditioner from the air regulating system was measured. On the 7th day after the 1st rainfall simulation, the environmental chamber was opened. The loading plate and LVDT for the telltale were installed. The 1st cyclic plate loading test was then conducted. One day after the 1st cyclic loading test, the water container and the table were then placed at the same location and the 2nd rainfall was conducted. After the 2nd rainfall, the same plastic sheet was used to cover the test section. There was a two-day drying period after the second rainfall test during which the amount of water exiting from the interface and front facing was measured. The 2nd cyclic loading test was then conducted for two days after the 2nd rainfall simulation. Immediately after the 2nd cyclic plate loading test, the 3rd rainfall simulation was conducted. The 3rd cyclic plate loading test was conducted for two hours after the completion of the 3rd rainfall test. Due to the short interval between the 3rd rainfall and cyclic loading, the amount of water exiting from the box could not be measured accurately. Figure 5.6 presents a flow chart for the test procedure.

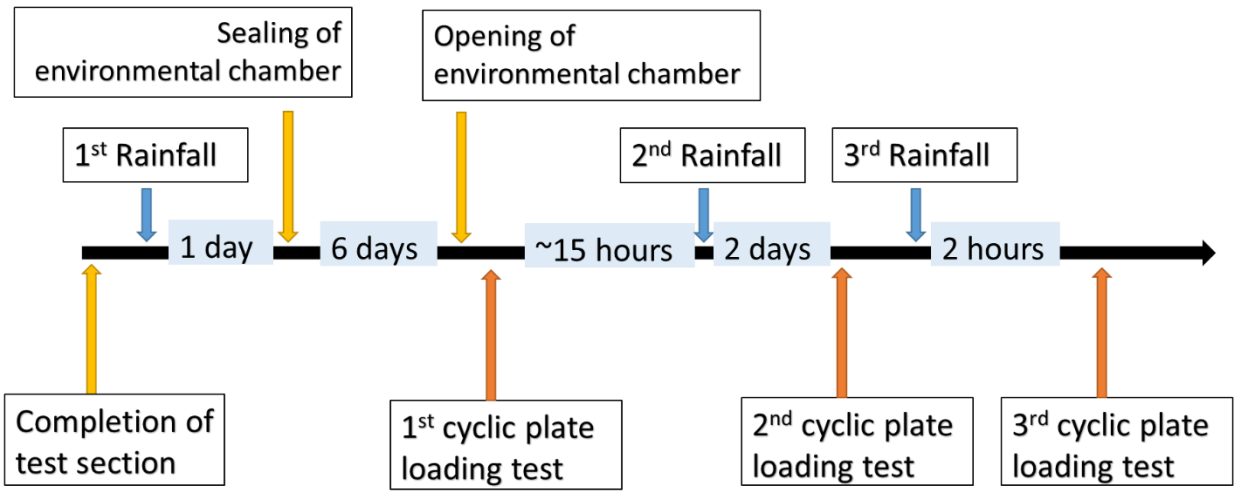

Figure 5.6 Large-scale rainfall and cyclic plate loading test procedure

Cyclic loading was applied on the loading plate. To distribute the load onto the base course surface evenly, a 20 mm - thick rubber layer was attached to the bottom of the loading plate. The loading plate was attached to the actuator at the end of each rainfall and drying cycle and was removed from the test box after the completion of the cyclic loading test. The load was applied by an actuator in a trapezoidal waveform as presented in Figure 5.7. The peak loading had a duration of 0.2 second with a magnitude of 10 kN. The contact pressure between the loading plate and the base course surface at the peak load was 151.5 kPa. Each cyclic loading test at the end of a rainfall and drying cycle consisted of 1000 cycles of loading.

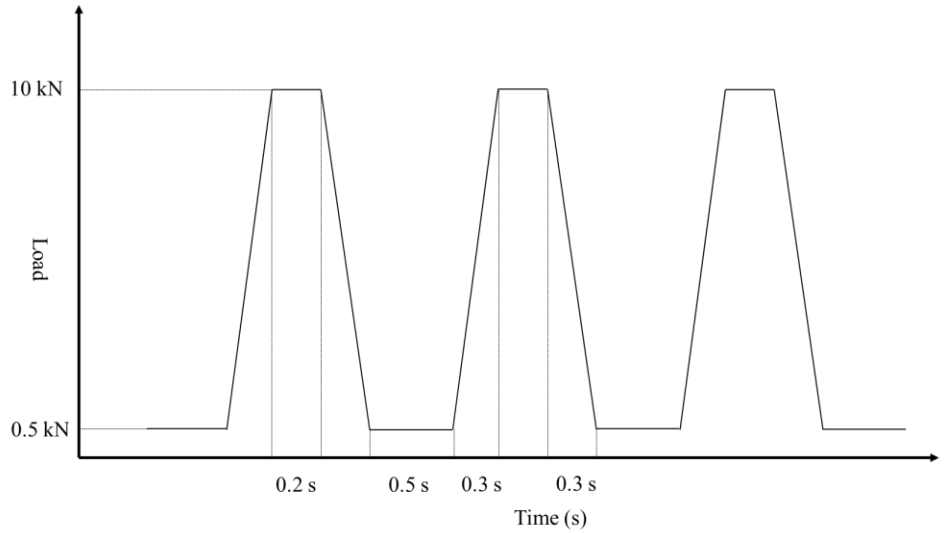

Figure 5.7 Cyclic loading pattern

5.3 Test results

The following parameters were measured during the tests:

1. Amount of water of rainfall, water exiting from the interface of base course and subgrade, and water exiting from the front surface;

2. Volumetric water content in the base course;
3. Permanent deformations and elastic deformations of the base course surface and the base course – subgrade interface;
4. Pressure at the base course – subgrade interface.

Two types of geotextile were used: the conventional woven geotextile No. 2 and the wicking geotextile. For the ease of presenting test results, the unimproved sections are noted as "Control", the conventional woven geotextile No. 2-improved sections are noted as "Conventional", and the wicking geotextile-improved sections are noted as "Wicking". Table 5.1 presents the test conditions. The CBR value presented in Table 5.1 was obtained by vane shear tests during compaction of the subgrade layers.

Table 5.1 Test section subgrade conditions and use of geosynthetic

Test No.	Subgrade CBR	Geosynthetic
1	3.3%	N/A
2	2.9%	Conventional woven geotextile No. 2
3	3.1%	Wicking geotextile
4	4.7%	N/A
5	4.8%	Conventional woven geotextile No. 2
6	5.0%	Wicking geotextile

5.3.1 Amount of rainfall water and water retained in test sections

In each rainfall simulation, approximately 300 liters of water was distributed to the base course surface through the rainfall simulator over a 1.5 hour period. During the rainfall simulation, water exited the testing box from (1) the base course – subgrade interface and (2) the gap between

the bottom "C" channel facing bar and the bottom of the testing box. The total amount of water for the rainfall simulation was recorded by a high precision flowmeter. The water exited from the bottom of the bottom of the box was collected within 15 hours after the completion of rainfall simulation. Due to the low permeability of the subgrade material, the water collected at the bottom of the box within 15 hours after the completion of rainfall simulation could not flow through the subgrade. The water collected at the bottom of the box most likely flowed through the gap between the subgrade material and the wall of the testing box. Thus this portion of water can be considered as runoff. The water exited from the interface was collected by the table placed at the interface level. The amount of water retained in the test section was calculated by subtracting the amount of water exited from the bottom of the testing box and the base course – subgrade interface from the total rainfall amount. The water collection at the interface after the third rainfall was weighted after the third cyclic loading test was finished (i.e., approximately 5 hours after the completion of third rainfall). Thus the collected amount of runoff water might be less than the actual amount. Figure 5.8 presents the amounts of water runoff, exiting from the interface, and retained in the base course in the test section with 3% CBR subgrade. Figure 5.9 presents the amounts of water runoff, exiting from the interface, and retained in the base course over 5% CBR subgrade.

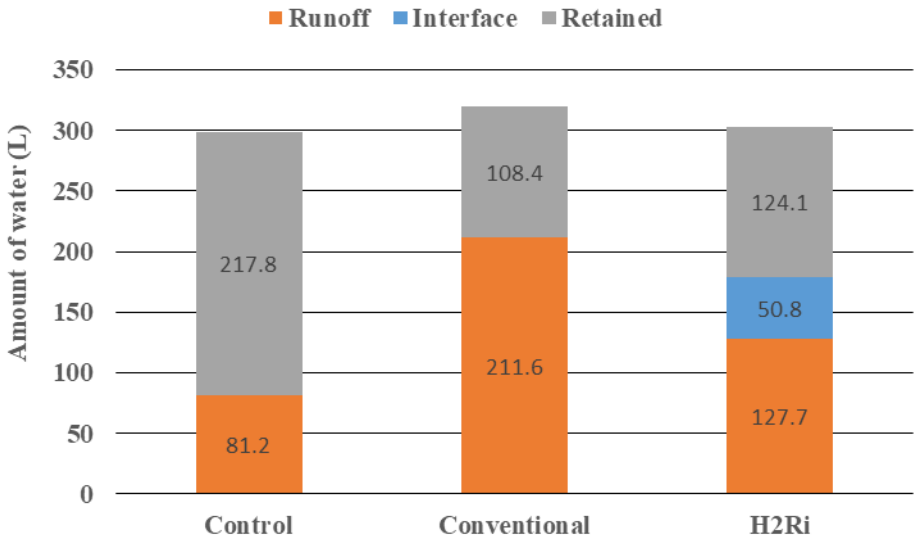

(a) 1st rainfall

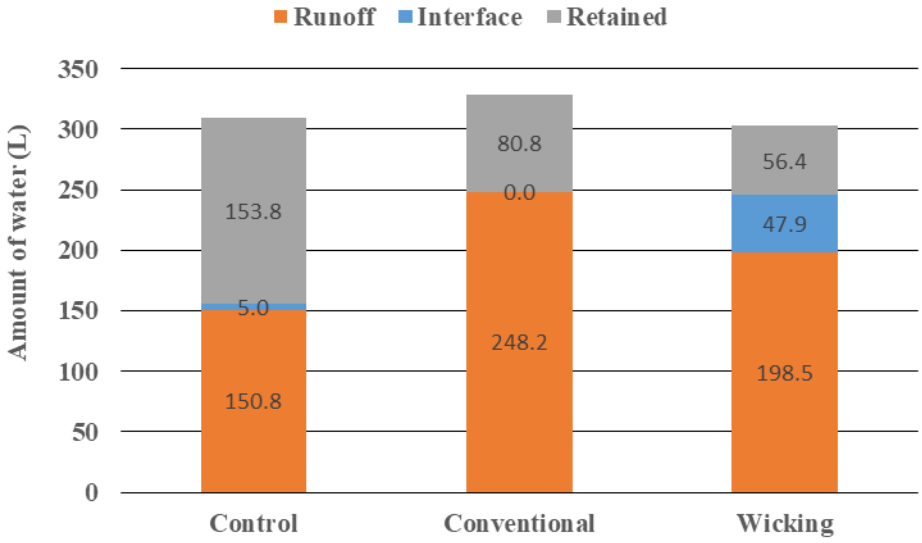

(b) 2nd rainfall

Figure 5.8 Total amounts of rainfall, water exiting the interface, and runoff from test sections with 3% CBR subgrade

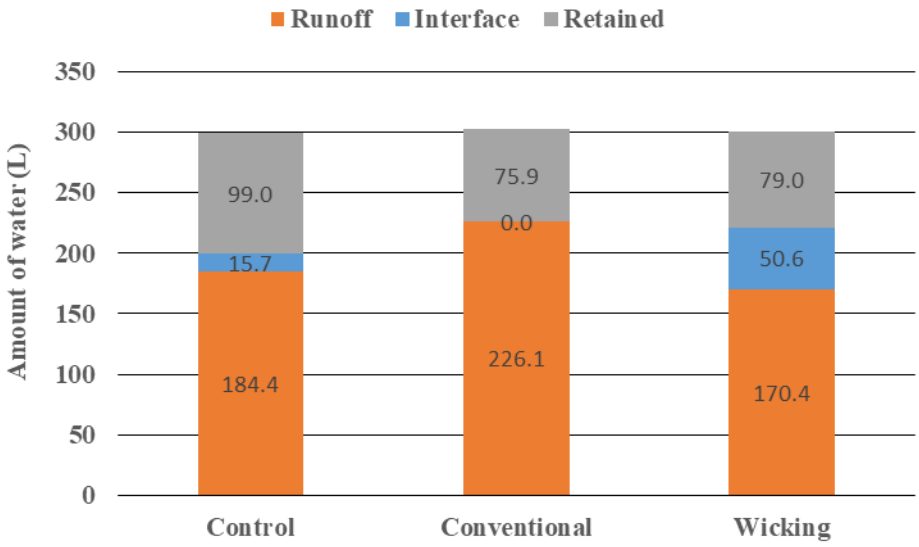

(b) 3rd rainfall

Figure 5.8 Total amounts of rainfall, water exiting the interface, and runoff from test sections with 3% CBR subgrade (continued)

During the rainfall, water flowed through the relatively permeable base course and accumulated at the base course – subgrade interface. The water head generated by the accumulated water at the interface would cause the water flow to the least resisting flow path. In actual roadways with geotextile, the least resisting flow path would be along the geotextile. Figure 5.8 shows a high percentage of runoff and no water exiting from the interface from the conventional geotextile, which indicates that the majority of the rainfall flowed through the gap between the subgrade and test box walls. The flow of water between the box wall and subgrade resulted in a low water head in the base course, and the water head was not sufficient to generate water flow in the conventional geotextile. In all three test sections, the runoff amount from the 2nd rainfall simulation was larger than that from the 1st rainfall simulation. This result suggested two

possibilities: First, as the water flew through the gap; fine particles were washed from the subgrade thus increasing the size of the gap between the subgrade and the wall of the test box. And second, the water absorbed into the base course during the first rainfall simulation was not fully dissipated which resulted in the amount of water absorbed by the base course in the second and third rainfall were smaller. The amounts of runoff from the control section and the wicking geotextile section were similar. Therefore a reasonable comparison can be made between the wicking geotextile section and the control specimen. In all three rainfall simulations, the amounts of water exiting from the interface through the wicking geotextile were approximately 15% of the total rainfall. While in the control section, no water exited from the interface in the first rainfall simulation and 1.5% of the total rainfall existed from the interface in the second rainfall. The comparison indicated that the wicking geotextile was effective in transferring water during and immediately after rainfall.

After the tests on 3% CBR subgrade were completed, modifications were made to the test sections. For the control section with 5% CBR subgrade, after the compaction of subgrade, a 150 – mm wide tape was fixed along the edges of the subgrade surface with half width of the tape on the box wall and half of the tape width on the subgrade surface. For the geotextile-improved sections, the tape was installed after the placement of the geotextile. The function of additional tape was to increase the length of the flow path from the base course to the edge of the subgrade surface thus limiting the amount of water flow through the gap between the subgrade and the testing box wall.

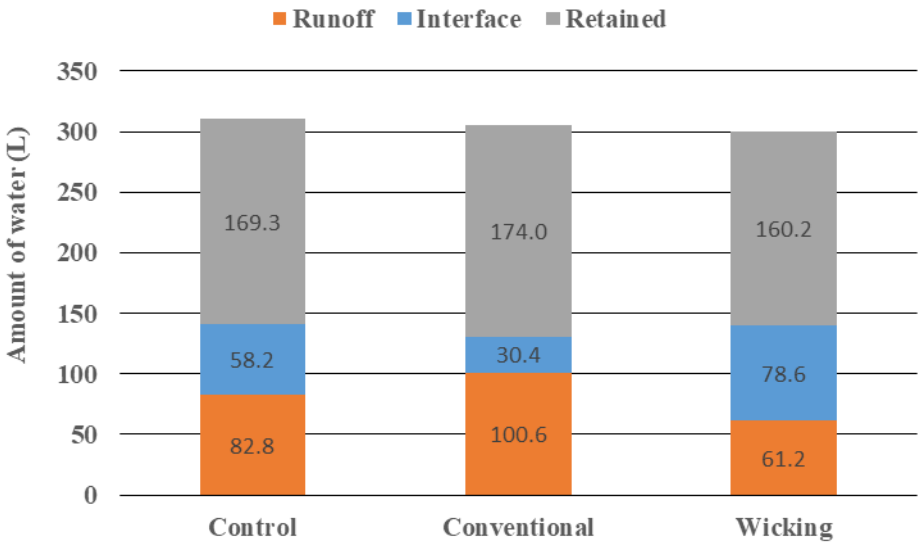

(a) 1st rainfall

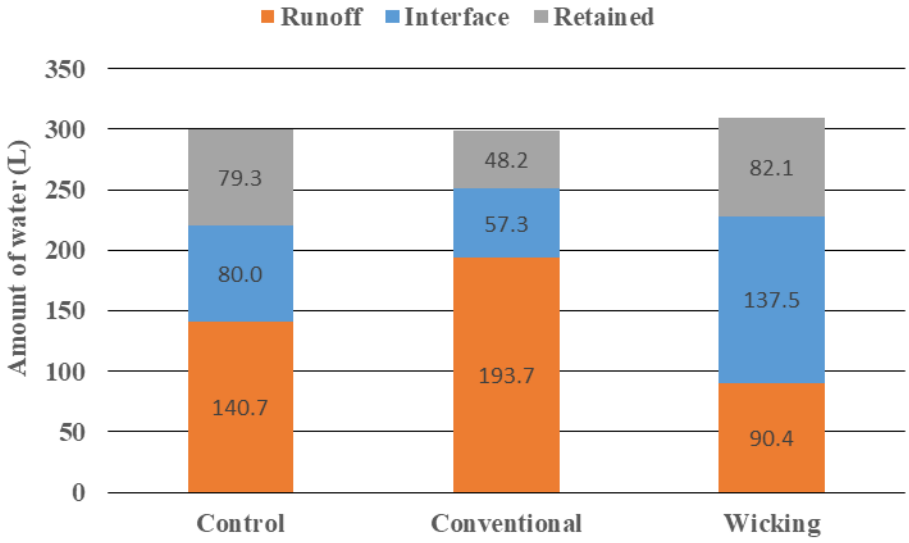

(b) 2nd rainfall

Figure 5.9 Total amounts of rainfall, water exiting the interface, and runoff from test sections with 5% CBR subgrade

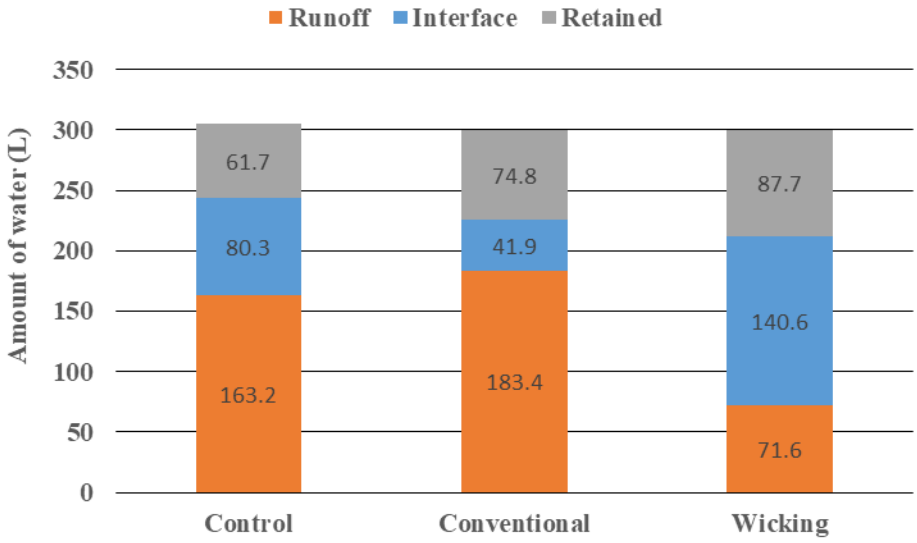

(b) 3rd rainfall

Figure 5.9 Total amounts of rainfall, water exiting the interface, and runoff from test sections with 5% CBR subgrade (continued)

Figure 5.9 shows additional tape did limit the amount of runoff. In the first rainfall simulation, 26% of the total rainfall was removed by the wicking geotextile from the test section. The effectiveness of the wicking geotextile increased in the 2nd rainfall simulation: 44% of the total rainfall was removed by the wicking geotextile. In the third rainfall, 47% of the total rainfall was removed by the wicking geotextile. In comparison, 19%, 26%, and 36% of the total rainfall exited from the interface of the control section in the 1st, 2nd, and 3rd rainfall simulations, respectively. The amounts of water removed in the conventional geotextile test section were less than those of the control section, while the amounts of runoff of the conventional geotextile test section were more than those of the control test section. The limited water removal by the conventional geotextile can be contributed to two reasons. First, the transmissivity of the conventional geotextile in the cross-machine direction was similar to that of the machine direction. As the base course – subgrade interface had no slope, the water within the conventional geotextile

was not directed towards the opening of the box. As a result, the water would tend to flow towards the edge of the conventional geotextile, reached the gap between the subgrade and testing box wall, and exited from the test section in the form of runoff. Such an effect was not observed in the wicking geotextile-improved section because the transmissivity of the wicking geotextile in the wicking yarn direction was greater than that of the machine direction. Thus the water within the wicking geotextile flowed in the wicking yarn direction (i.e., the cross-machine direction) and exited the test section. Secondly, the air bubbles might exist in the conventional geotextile during the rainfall thus reducing the transmissivity of the conventional geotextile.

In conclusion, the wicking geotextile was very effective in removing water during and shortly after the simulated rainfall.

5.3.2 Water content change in the base course

The water contents of the base course were monitored by three layers of EC-5 water content sensors placed in the base course. These sensors were placed at 75 mm, 150 mm, and 225 mm below the surface of the base course. Each layer consisted of six EC-5 water content sensors that measured the volumetric water contents of the surrounding base course. The locations of the EC-5 sensors are presented in Figure 5.1. The layer of sensors that were at 75 mm above the subgrade – base course interface is referred to as "Layer 1". The middle layer of sensors is referred to as "Layer 2". The layer of sensors that was at 75 mm below the base course surface is referred to as "Layer 3".

The EC-5 sensors measured the volumetric water contents of the surrounding base course. As stated in the previous chapter, the measurements made by the volumetric water content sensors

are under the influence of the density of the surrounding material. The sensor installation process could result in different densities in the base course material surrounding the sensors. As a result, the volumetric water content measurements varied between sensors. Figure 5.10 presents the volumetric water contents of Layer 2 in the wicking geotextile test section with 5% CBR subgrade. The average volumetric water content change of each layer is presented in this chapter to minimize the variability of test sections. Figure 5.11 presents the volumetric water content changes in test sections with 3% CBR subgrade.

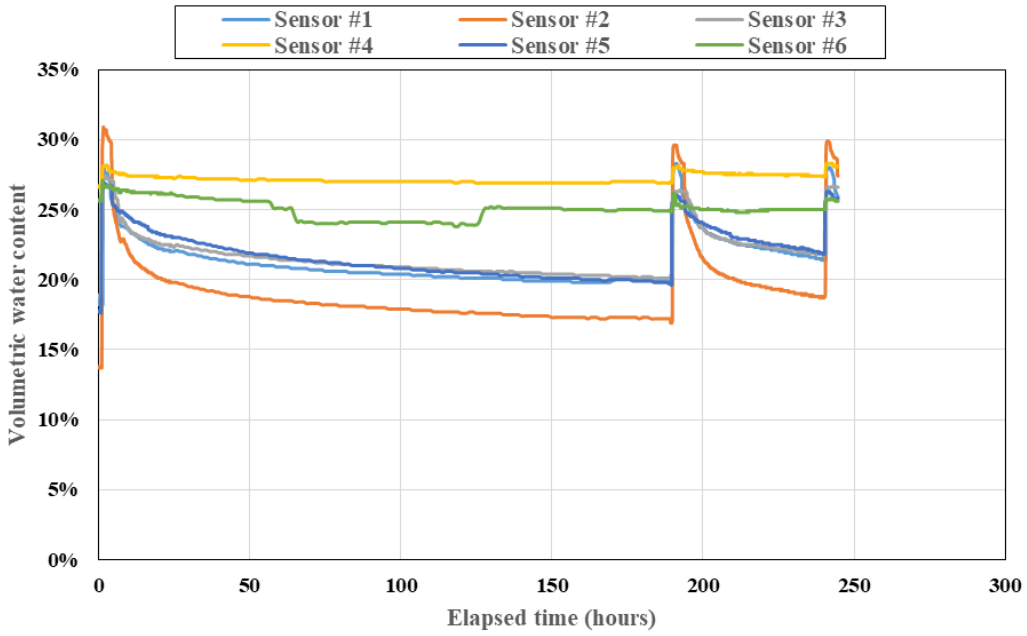

Figure 5.10 Volumetric water contents in the middle of the base course of the control test on 5% CBR subgrade

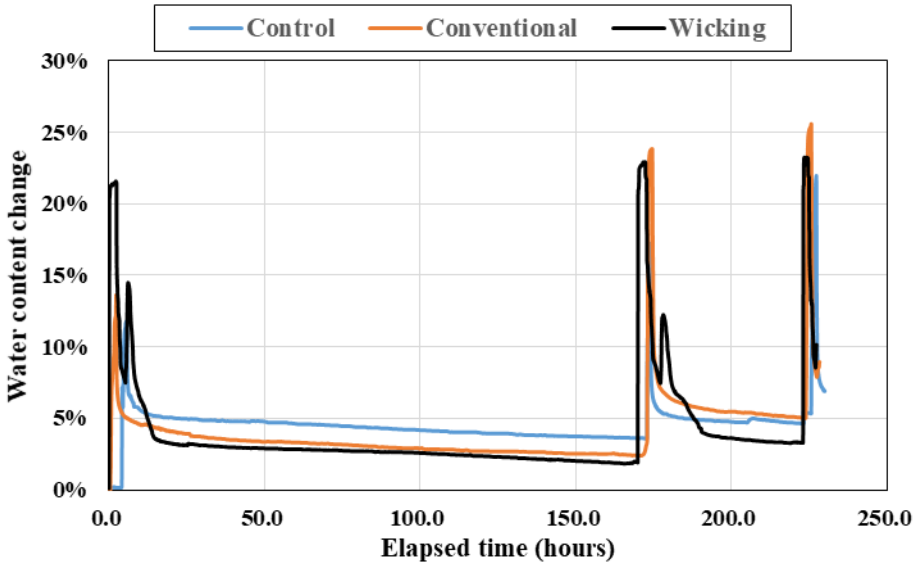

(a) Layer 1

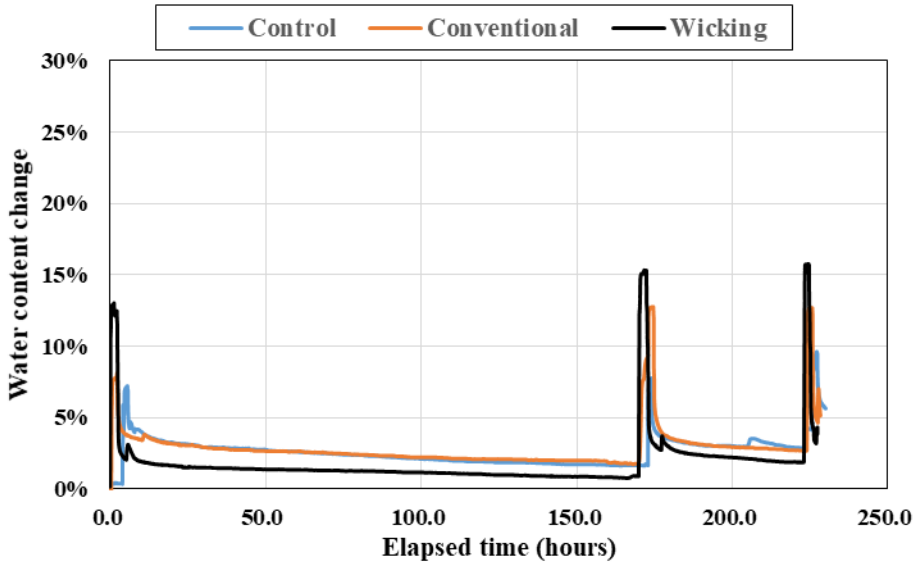

(b) Layer 2

Figure 5.11 Volumetric water content changes of the test sections with 3% CBR subgrade

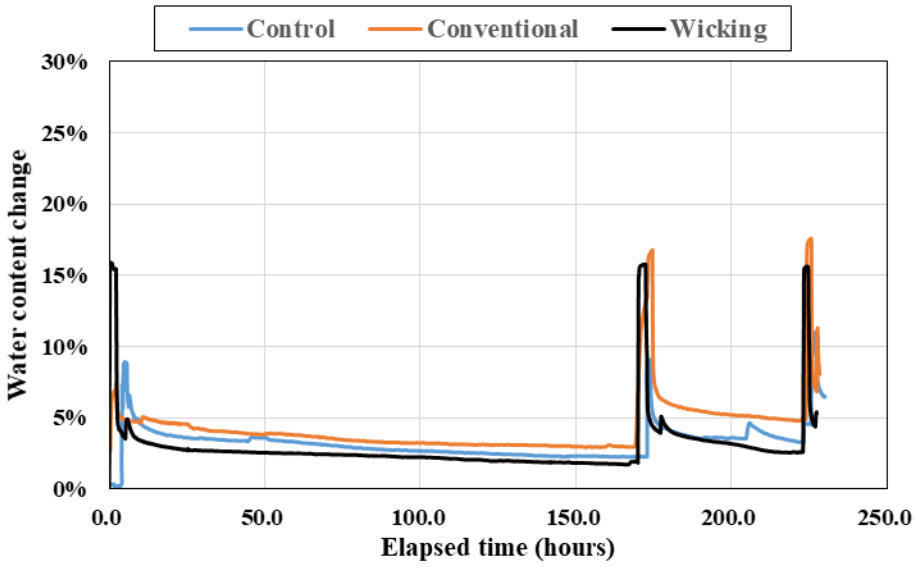

(c) Layer 3

Figure 5.11 Volumetric water content changes of the test sections with 3% CBR subgrade (continued)

Overall, the water content changes in all test sections and layers were similar. The volumetric water content increased rapidly after each rainfall simulation, then decreased rapidly for a short period. After that, the volumetric water content decreased at a much slower rate. At one week (168 hours) after the first rainfall simulation, the volumetric water contents at Layer 1 increased 3.6%, 2.4%, and 1.9% in the control, conventional woven geotextile-improved, and wicking geotextile-improved sections, respectively. At the same time, the volumetric water contents at Layer 2 increased 1.7%, 1.7%, and 0.9% in the control, conventional woven geotextile-improved, and wicking geotextile-improved sections, respectively. At Layer 3, the volumetric water contents increased 2.3%, 3.0%, and 1.9% in the control, conventional woven geotextile-improved, and wicking geotextile-improved sections, respectively. Based on the increase in the

volumetric water content at one week after the first rainfall simulation, the wicking geotextile effectively reduced the water content at all three measurement depths in the base course. The water reduction effect of the wicking geotextile was more pronounced within the effective wicking zone (i.e., 75 mm and 150 mm above the subgrade – base course interface). The conventional geotextile showed an effect in reducing the volumetric water content at Layer 1. However, in the middle of the base course, the volumetric water content changes of the control specimen and conventional woven geotextile-improved sections were very similar.

Figure 5.11 presents the volumetric water content changes in the test sections consisting of 5% CBR subgrade.

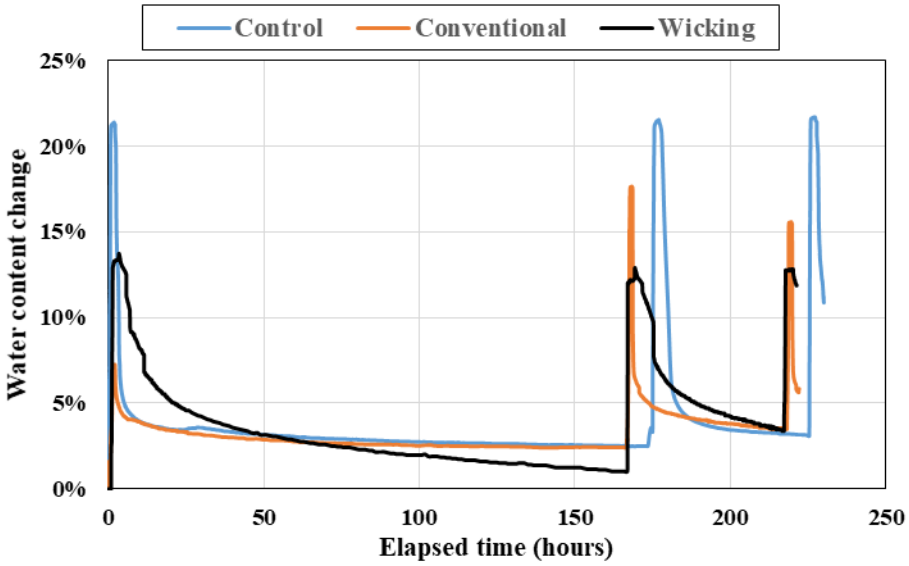

(a) Layer 1

Figure 5.12 Volumetric water content changes in base courses over 5% CBR subgrade

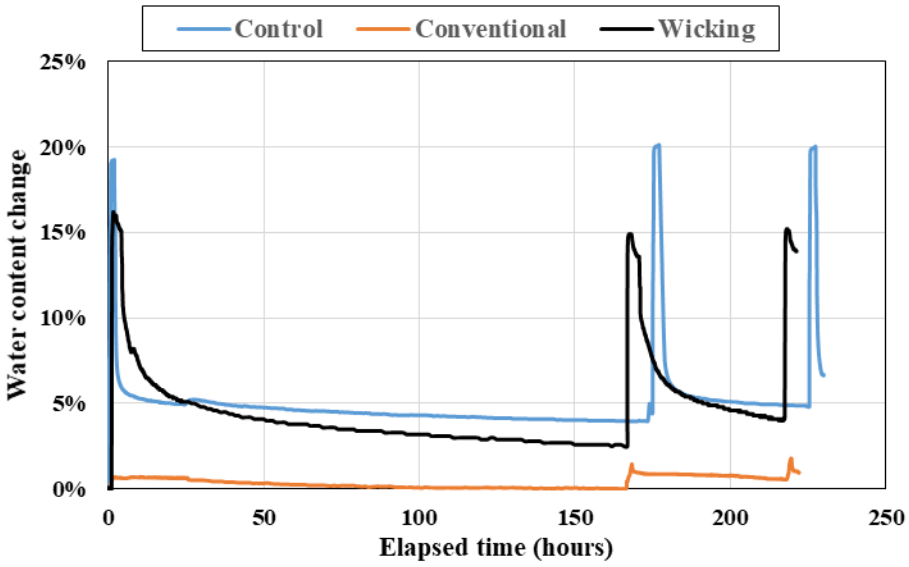

(b) Layer 2

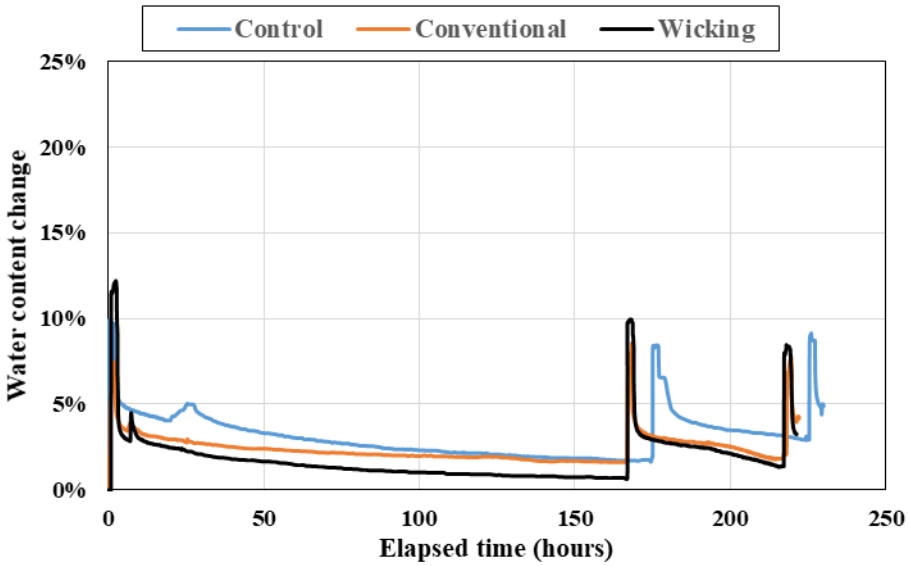

(C) Layer 3

Figure 5.12 Volumetric water content changes in base courses over 5% CBR subgrade (continued)

The water content change in the test section with 5% CBR subgrade had the similar trend as that with 3% CBR subgrade. Unfortunately, the channels of the data acquisition system to record Layer 2 volumetric water content sensors were damaged during the test on conventional woven-improved sections. As a result of the damage, the volumetric water content changes at Layer 2 in the conventional woven geotextile section was significantly less than the other sections. At Layer 1, the water content changes in the control and conventional woven geotextile-improved sections were very similar after the first and second rainfall simulations. The wicking geotextile showed a slower reduction in water content after the rainfall. The slow drainage was most likely caused by the difference in compaction after the installation of the sensors. Approximately 48 hours after the first and second rainfall simulations, the water content changes in the geotextile-improved specimens were similar to those in the control specimens. In the drying periods following the rainfall, at Layers 1 and 2, the volumetric water contents in the wicking geotextile test sections decreased at a faster rate as compared to the control and conventional woven geotextile-improved sections. In the tests with 5% CBR subgrade, the water content changes in the conventional woven geotextile-improved sections were similar to the control section at Layers 1 and 3. The water content increased in the wicking geotextile reinforced section as all measured depths were lower than the control and conventional woven geotextile-improved section.

The first and second cyclic plate loading tests were conducted at approximately one week after the first rainfall simulation and two days after the second rainfall simulation, respectively. The water content changes at the time of the cyclic plate loading test were important. Table 5.2 presents the water content changes at each layer at one week after the first rainfall simulation. Table 5.3 presents the water content change at each layer at two days after the second rainfall simulation. It is to be noted that due to the damaged data acquisition system, the measurements

from Layer 2 of the conventional woven geotextile reinforced section with 5% CBR subgrade were not representative of the actual condition. Thus the water content change from Layer 2 of 5% CBR conventional geotextile specimen was not included in the calculation of the average base course water content.

Table 5.2 Volumetric water content changes in the base course at one week after the first rainfall simulation.

	Volumetric water content change							
Specimen	3% CBR subgrade				5% CBR subgrade			
	Layer 1	Layer 2	Layer 3	Average	Layer 1	Layer 2	Layer 3	Average
Control	3.6%	1.7%	2.3%	2.5%	2.5%	4.0%	1.7%	2.7%
Conventional	2.4%	1.7%	3.0%	2.4%	2.4%	0.1%*	1.6%	2.0%
Wicking	1.9%	0.9%	1.9%	1.6%	1.0%	2.6%	0.7%	1.4%

Table 5.3 Volumetric water content change in the base course at two days after the second rainfall simulation.

	Volumetric water content change							
Specimen	3% CBR subgrade				5% CBR subgrade			
	Layer 1	Layer 2	Layer 3	Average	Layer 1	Layer 2	Layer 3	Average
Control	5.4%	4.2%	4.6%	4.7%	3.2%	4.9%	3.0%	3.7%
Conventional	5.2%	2.8%	5.0%	4.3%	3.5%	0.6%*	1.8%	2.65%
Wicking	3.3%	1.9%	2.6%	2.6%	3.5%	4.1%	1.4%	3.0%

5.3.3 Surface permanent deformations

The surface deformation under the loading plate during cyclic loading was measured by the displacement transducer in the actuator. The loading plate was placed on the surface of the

base course at the end of each rainfall and drying cycle. During the installation of the loading plate, disturbance of the base course surface was inevitable and the plate might not be in full contact with the base course; therefore, the first loading cycle in each loading test was considered as preconditioning of the test section and its corresponding data was not included in the result. Under each loading cycle, the total surface deformation included a permanent deformation and an elastic rebound (also called elastic deformation). Figure 5.12 presents the surface permanent deformation due to cyclic loading on the test section at seven days after the rainfall simulation. It is to be noted that the cyclic loading test conducted at seven days after the rainfall simulation is referred to as the first cyclic loading test.

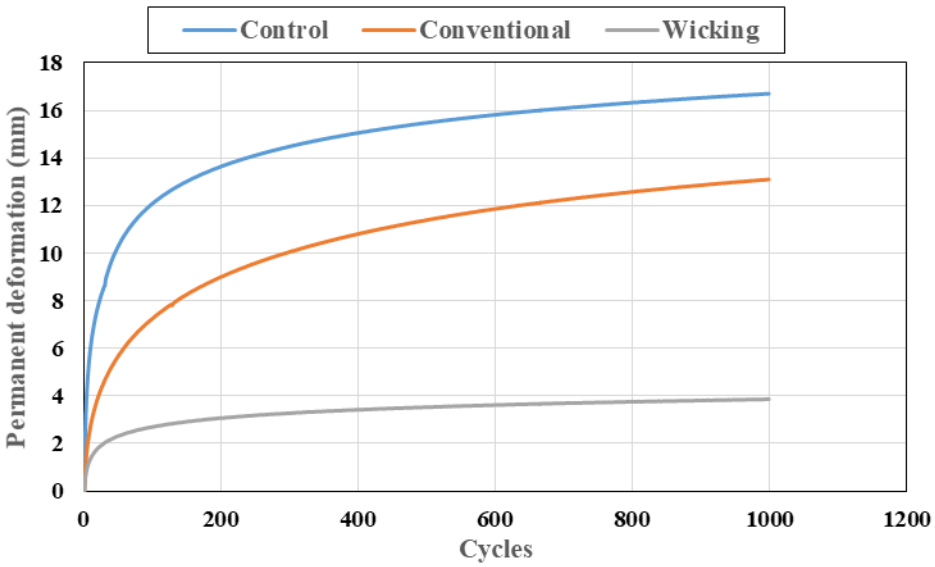

(a) 3% CBR subgrade

Figure 5.13 Surface permanent deformation at seven days after the first rainfall simulation

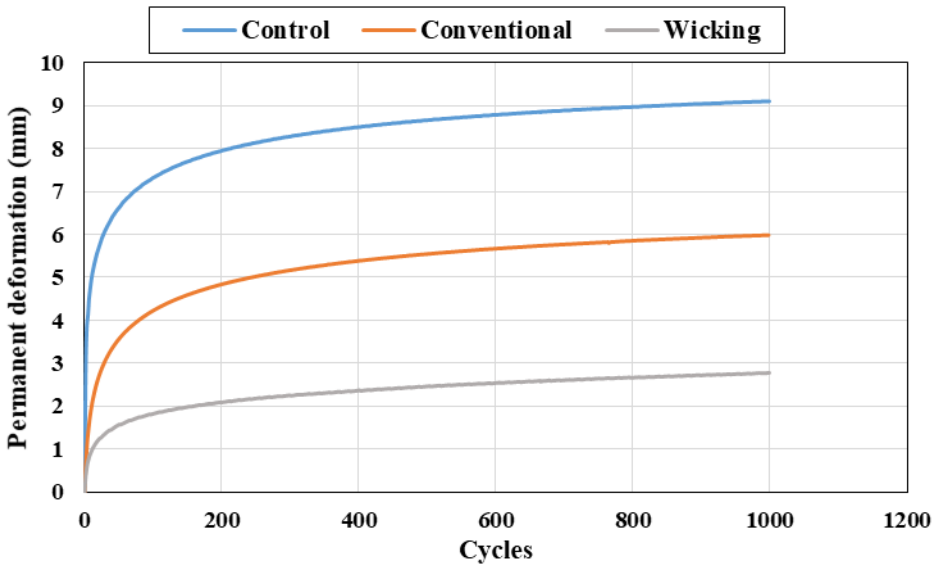

(b) 5% CBR subgrade

Figure 5.13 Surface permanent deformation at seven days after the first rainfall simulation (continued)

At the end of the first cyclic loading test, the permanent deformations from the control, conventional geotextile-improved, and wicking geotextile-improved test sections with 3% CBR subgrade were 16.7, 13.1, and 3.9 mm, respectively. The permanent deformations from the control, conventional geotextile-improved, and wicking geotextile-improved test sections with 5% CBR subgrade were 9.1, 6.0, and 2.7 mm, respectively. The permanent deformations of the test sections on the 5% CBR subgrade were smaller than those on the 3% CBR subgrade. The permanent deformations of the test sections on both 3% and 5% CBR subgrade showed similar comparisons among the control, conventional geotextile-improved, and wicking geotextile-improved sections. The control sections had the largest permanent deformations, followed by the conventional geotextile-improved and wicking geotextile-improved sections. The permanent deformations of

the conventional geotextile-improved sections with 3% CBR and 5% CBR subgrade were 78% and 67% those of the control sections, respectively. The permanent deformations of the wicking geotextile-improved sections were significantly smaller than the control and conventional geotextile-improved sections. The significant differences in the permanent deformations between the wicking geotextile-improved sections and other sections on both 3% CBR and 5% CBR subgrade should be largely attributed to the water content reduction of the base course by the wicking geotextile. As demonstrated in Table 5.2, at the time of the first cyclic loading test, the volumetric water contents in the base course of the wicking geotextile-improved section were 0.9% and 1.3% lower than those of the control sections on 3% CBR and 5% CBR subgrade, respectively. The effect of the water content reduction in the base course on the surface permanent deformation will be further analyzed in the following chapter when it is considered in the development of design methods.

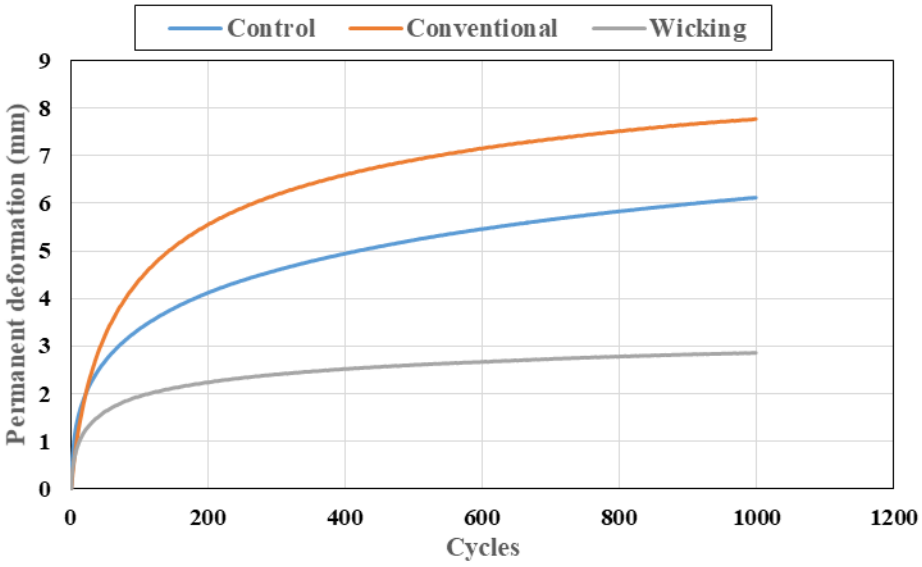

(a) 3% CBR subgrade

Figure 5.14 Surface permanent deformation at two days after the second rainfall simulation

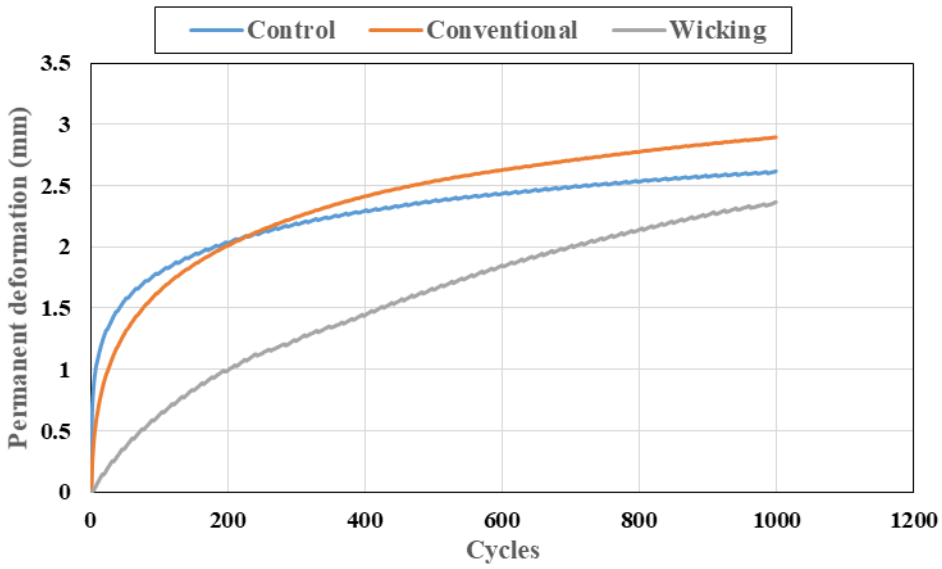

(b) 5% CBR subgrade

Figure 5.14 Surface permanent deformation at two days after the second rainfall simulation (continued)

Figure 5.14 presents the surface permanent deformations due to the second cyclic loading test conducted at 2 days after the second rainfall simulation. It is shown that by the end of the second cyclic loading, the conventional geotextile-improved sections had the largest permanent deformations, followed by the control and wicking geotextile-improved sections. By the end of the second cyclic loading test, the surface permanent deformations of the control, conventional geotextile-improved, and wicking geotextile-improved sections on 3% CBR subgrade were 6.1, 7.8, and 2.9 mm, respectively. The surface permanent deformations of the control, conventional geotextile-improved, and wicking geotextile-improved sections on 5% CBR subgrade were 2.6, 2.9, and 2.4 mm, respectively. Again, the wicking geotextile demonstrated its effectiveness in reducing the permanent deformations of the test sections. The permanent deformation results

corresponded to the volumetric water contents of base courses for different test sections at the moment of the loading test. As demonstrated in Table 5.3, the volumetric water content increases of base courses in the control, conventional geotextile-improved, and wicking geotextile-improved sections on 3% CBR subgrade were 4.7%, 4.3%, and 2.6%, respectively. The volumetric water content increases in the control and conventional geotextile-improved sections were similar while the water content change in the wicking geotextile-improved section was lower than other sections by a margin of 2%. In the 5% CBR subgrade tests, the volumetric water content changes were similar in all three sections. As a result, the surface permanent deformations in these three sections were similar.

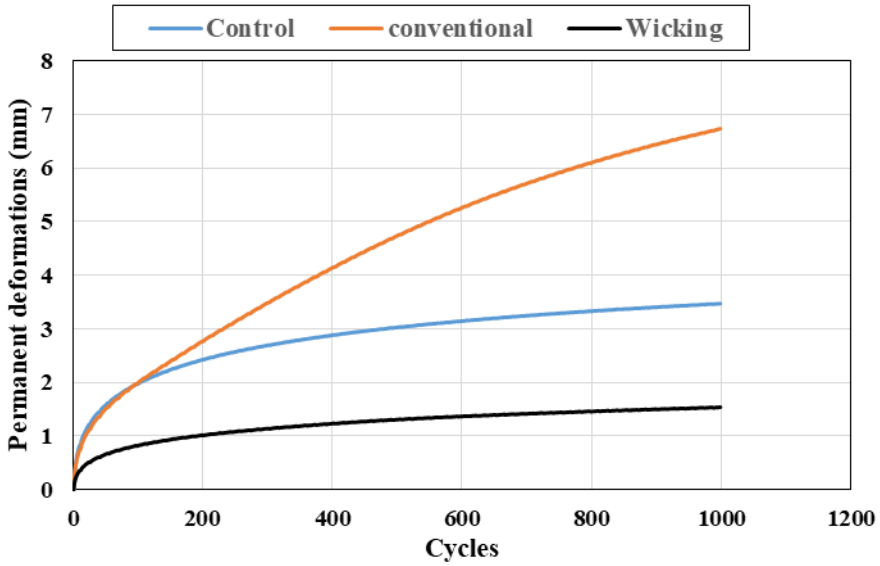

(a) 3% CBR subgrade

Figure 5.15 Surface permanent deformations at two hours after the third rainfall simulation

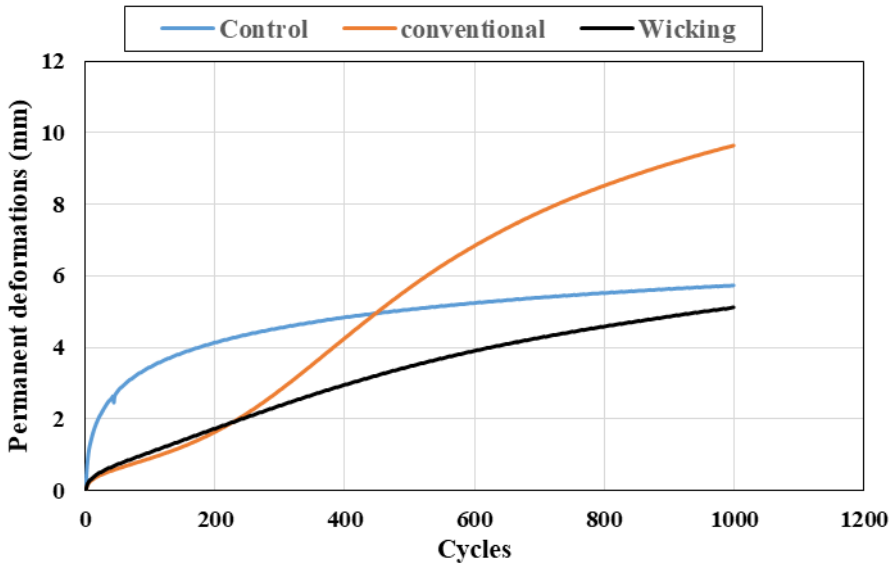

(b) 5% CBR subgrade

Figure 5.15 Surface permanent deformations at two hours after the third rainfall simulation (continued)

Figure 5.15 presents the surface permanent deformations during the third cyclic loading tests. In both tests on the 3% CBR and 5% CBR subgrade, the least permanent deformations were observed in the wicking geotextile-improved sections, while the largest surface permanent deformations were observed in the conventional geotextile-improved sections. The large surface permanent deformations in the conventional woven geotextile-improved section could result from the water accumulation at the subgrade – base course interface due to the concave deflections below the loading plate from the previous tests as shown in Figure 5.15. During the simulated rainfall, the water flowed through the base course under the action gravity and accumulated at the subgrade – base course interface. In the sections with a geotextile, water was intercepted by the geotextile and flowed towards and trapped at the deflected concave area. Since the permeability of the AB-3 base course was much lower than the conventional woven geotextile, the amount of

water accumulated at the concave area in a control section would be less than that in the conventional woven geotextile-improved section. In other words, the conventional woven geotextile collected more water and transported a portion of the water into the concave area. The water accumulated at the concave area softened the AB-3 base course and reduced the friction between the base course and the geotextile. As a result of the high water content in the base course and possible slippage between the geotextile and the base course, the permanent deformations of the conventional woven geotextile-improved sections in the second and third cyclic loading tests were larger than those in the control sections. The permeability of the wicking geotextile in the direction of the wicking yarns is significantly higher than the permeability of the conventional woven geotextile. During the rainfall simulation, a large amount of water was drained from the base course into the geotextile by gravity. Since the wicking geotextile had the ability to transport water by suction, the water accumulated in the concave area in the wicking geotextile-improved section was removed via the capillary action and evaporation into the air. Thirdly, the permanent deformations of the wicking geotextile-improved sections after the first cyclic loading was significantly smaller than those of the control and conventional geotextile-improved sections. Therefore, in the subsequent rainfall simulations, water less likely accumulated in the base course directly below the loading plate. As a result of the previously stated reasons, the permanent deformations in the wicking geotextile-improved sections were significantly smaller than the control and conventional geotextile-improved sections.

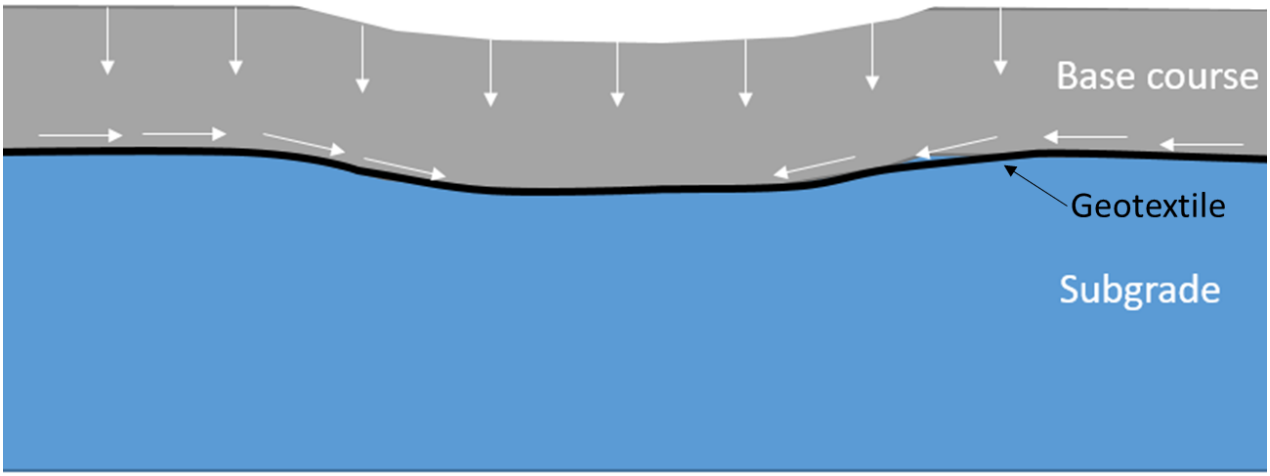

Figure 5.16 Schematic of water accumulation in the base course within the concave area

5.3.4 Interface vertical stresses

The vertical stresses at the interface of base course and subgrade were measured by the earth pressure cells installed in the subgrade close to the interface. During the cyclic loading tests, the earth pressure cells measured the vertical stresses at the interface at the frequency of 10 Hz. Figures 5.17 and 5.18 present the maximum interface vertical stresses at the center of the loading plate at each loading cycle.

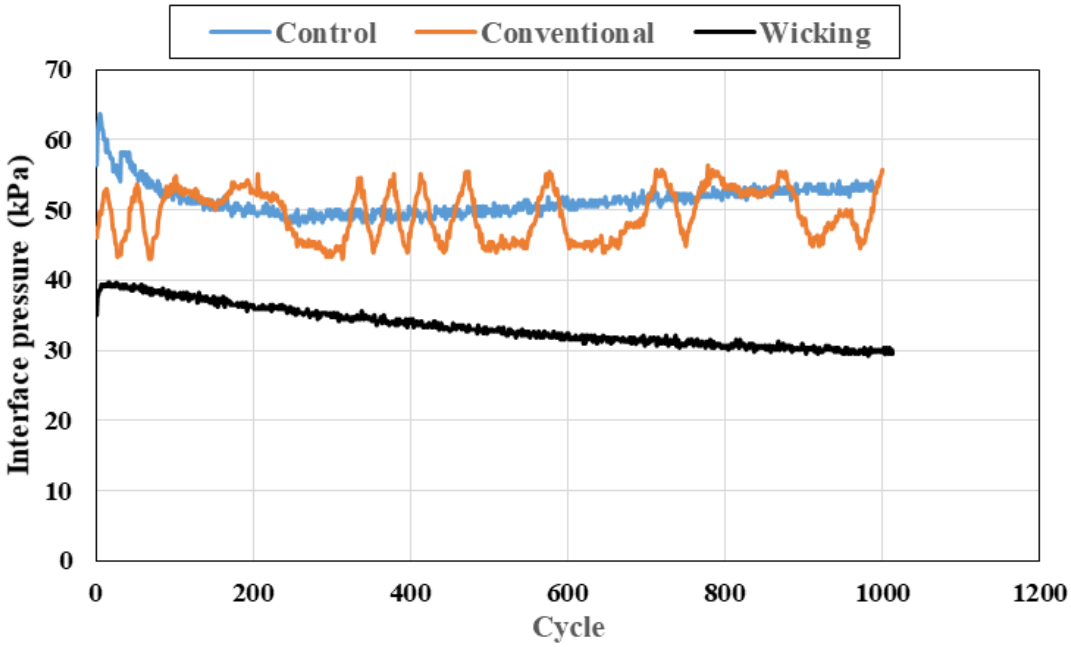

(a) First loading

Figure 5.17 Measured maximum interface vertical stresses at the center of the loading plate on the test sections with 3% CBR subgrade

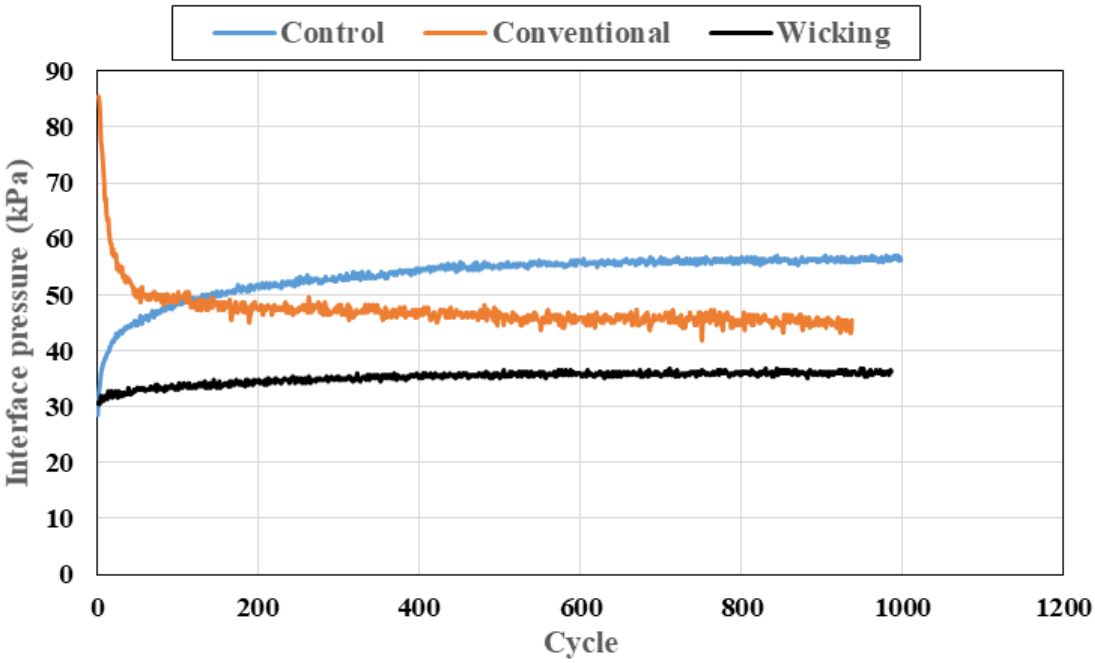

(b) Second loading

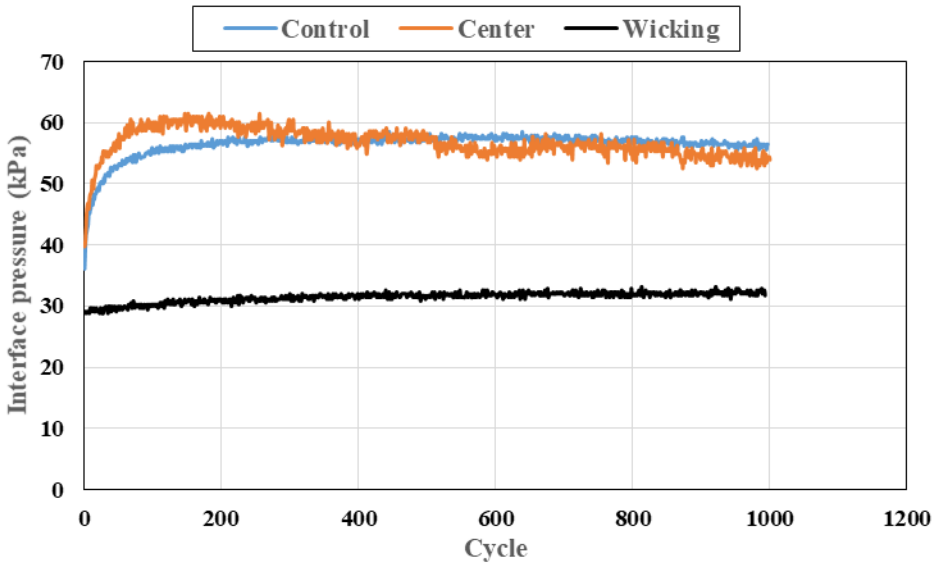

(c) Third Loading

Figure 5.17 Measured maximum interface vertical stresses at the center of the loading plate on the test sections with 3% CBR subgrade (continued)

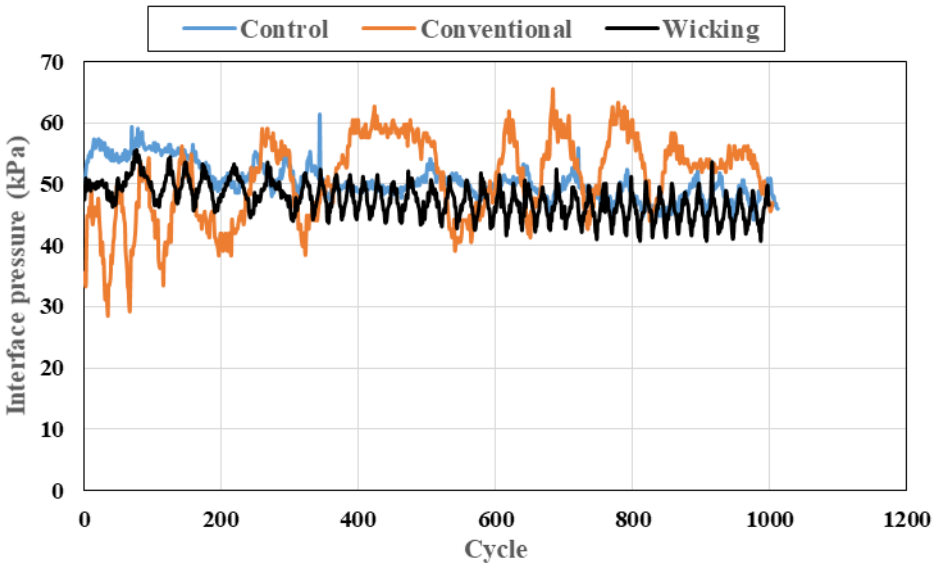

(a) First loading

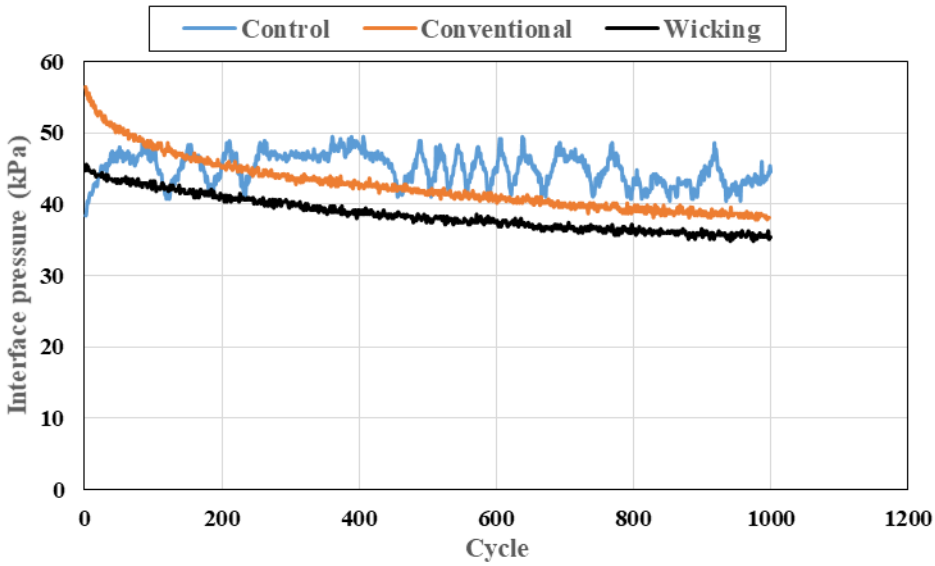

(b) Second loading

Figure 5.18 Measured maximum interface vertical stresses at the center of the loading plate on the test sections with 5% CBR subgrade

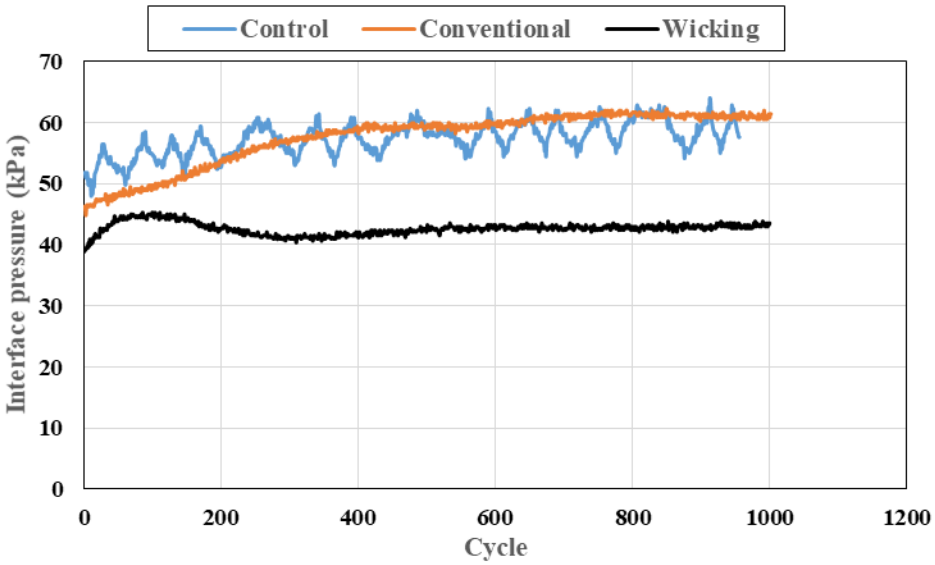

(c) Third loading

Figure 5.18 Measured maximum interface vertical stresses at the center of the loading plate on the test sections with 5% CBR subgrade (continued)

The measured maximum vertical stresses at the interface had clear trends with respect to the loading cycles even though there were some variations for certain earth pressure cells. In all the cyclic plate loading tests, the maximum interface vertical stresses tended to stabilize after the first 200 loading cycles. For the ease of analysis, the average values of the maximum interface vertical stresses from 200 loading cycles to the end of each test (1000 cycles) were calculated and are presented in Table 5.4. Figures 5.15 and 5.16 and Table 5.4 show that the wicking geotextile-improved sections had lowest maximum interface vertical stresses, followed by the conventional geotextile-improved section and the control section, especially for the sections with 3% CBR subgrade. This result indicates that the wicking geotextile-improved sections had the highest moduli of the base courses. Table 5.4 also shows the difference in the measured vertical stresses became less when the test sections were on 5% CBR subgrade.

Table 5.4 Average maximum interface vertical stresses between 200 and 1000 loading cycles for all cyclic plate loading tests

Time after rainfall simulation	Specimen	Average interface stress at center (kPa)	
		3% CBR subgrade	5% CBR subgrade
7 days	Control	50.85	49.38
2 days		55.08	45.07
2 hours		57.09	58.11
7 days	Conventional	49.00	52.98
2 days		46.09	41.12
2 hours		56.38	59.37
7 days	Wicking	32.33	46.85
2 days		35.66	37.49
2 hours		31.79	52.4

5.4 Conclusions

Based on the large-scale cyclic plate loading tests with rainfall simulation, the following conclusions can be drawn:

(1) Based on the amount of water exited from the interface of the test section during the rainfall simulation, the inclusion of the wicking geotextile at the interface significantly increased the gravitational drainage;

(2) The inclusion of the wicking geotextile increased the rate of water content reduction in the base course during the drying period following the rainfall simulation. The water content

reduction in the base course was especially noticeable in the wicking zone, i.e., within 200 mm above the wicking geotextile.

(3) The wicking geotextile significantly reduced the permanent deformation of the test section, especially in the first loading test at seven days after the first rainfall simulation.

(4) The wicking geotextile-improved sections had the lowest measured maximum vertical stresses at the interface of base course and subgrade, indicating the highest moduli of the base courses in the wicking geotextile-improved sections.

(5) The reduction of the permanent deformations and interface vertical stresses was more pronounced with a weaker subgrade when the wicking geotextile was used.

CHAPTER 6 Design with wicking geotextile

This chapter documents the development of guidelines for designing of wicking geotextile for pavement applications with the 1993 AASHTO Pavement Design Guide and the AASHTO Mechanistic-Empirical Pavement Design Guide (MEPDG). The effects of wicking geotextile on the improved performance of base course are represented by two improvement factors for the resilient modulus of the base course: hydraulic improvement factor (F_h) and mechanical improvement factor (F_m). The hydraulic improvement factor adjusts the resilient modulus of the base course as a result of wicking geotextile reducing the base course water content and increasing the base course resilient modulus. The mechanical improvement factor adjusts the resilient modulus of the base course for the mechanical stabilization (i.e., lateral confinement) of wicking geotextile.

6.1 Resilient modulus and water content of AB-3 Aggregate

The relationship between the resilient modulus and water content of the AB-3 aggregate under different confining pressures are presented in Figure 6.1. The resilient modulus tests on the AB-3 aggregate were conducted at different confining pressures and water contents. The confining pressure of 34.5 kPa was selected for the following analysis to simulate the base course condition under traffic loading. Under the confining pressure of 34.5 kPa, the relationship between water content and resilient modulus of the AB-3 aggregate can be expressed in the following equations (Lin et al., 2015)

$$M_R = -22.105w + 294.74 \qquad \text{for } 8.9\% \leq w < 11\% \tag{6.1}$$

$$M_R = -132.5w + 1277.2 \qquad \text{for } 7\% < w < 8.9\% \tag{6.2}$$

where M_R is the resilient modulus of the AB-3 aggregate in MPa and w is the gravimetric water content of the AB-3 aggregate in percentage. The AB-3 aggregate had an optimum water content of 8.6%. The saturation water content of the AB-3 aggregate varied with the degree of compaction. At 95% degree of compaction, the saturation water content of the AB-3 aggregate was approximately 13%. The water content of the base course in a roadway structure typically varies between saturation and optimum water contents, thus the range of water content in Equations (6.1) and (6.2) is wide enough to represent the AB-3 base course under a field condition. Figure 6.1 also demonstrates that at lower confining pressures (i.e., 20.7 and 34.5 kPa), the reduction in the water content of AB-3 aggregate below 8.9% significantly increases the resilient modulus of the material.

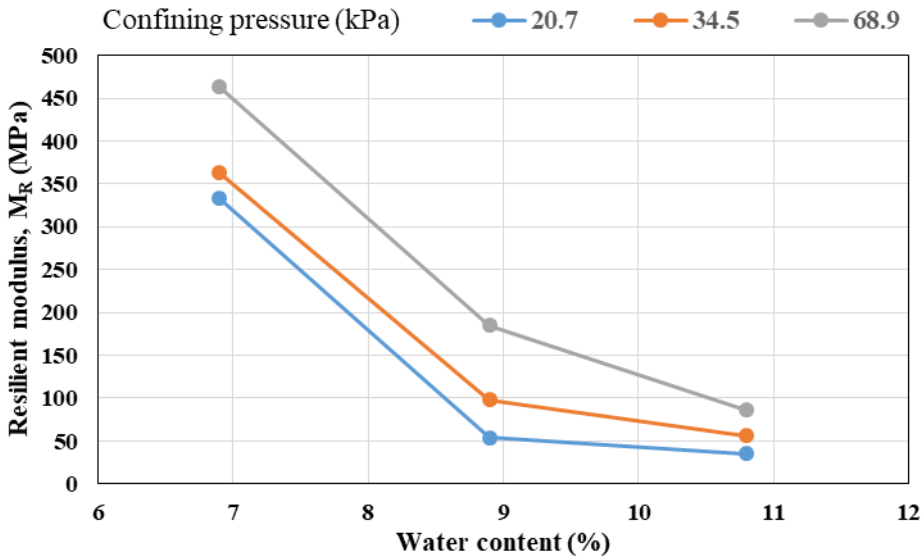

Figure 6.1 Relationship between resilient modulus and water content of the AB-3 aggregate under different confining pressures (Lin et al., 2016)

With Equations (6.1) and (6.2), the resilient moduli of the AB-3 base course in the small-scale box tests and the soil column tests could be back-calculated as a function of the measured water content of the base course. In the small-scale box test with simulated rainfall, the measurements showed that the average initial base course water content in the conventional woven geotextile No. 2-improved section was approximately 9.0% while the average initial water content in the wicking geotextile-improved section was approximately 8.2%. Based on the small-scale box test, the conventional woven geotextile No. 2-improved base course returned to the initial water content after the first rainfall. The wicking geotextile, on the other hand, continued reducing the water content in the base course below the optimum water content. As a result, the wicking geotextile-improved base course had a higher resilient modulus than the conventional geotextile-improved section. Figure 6.2 presents the resilient moduli of the conventional geotextile-improved and wicking geotextile improved base courses calculated based on the water content changes.

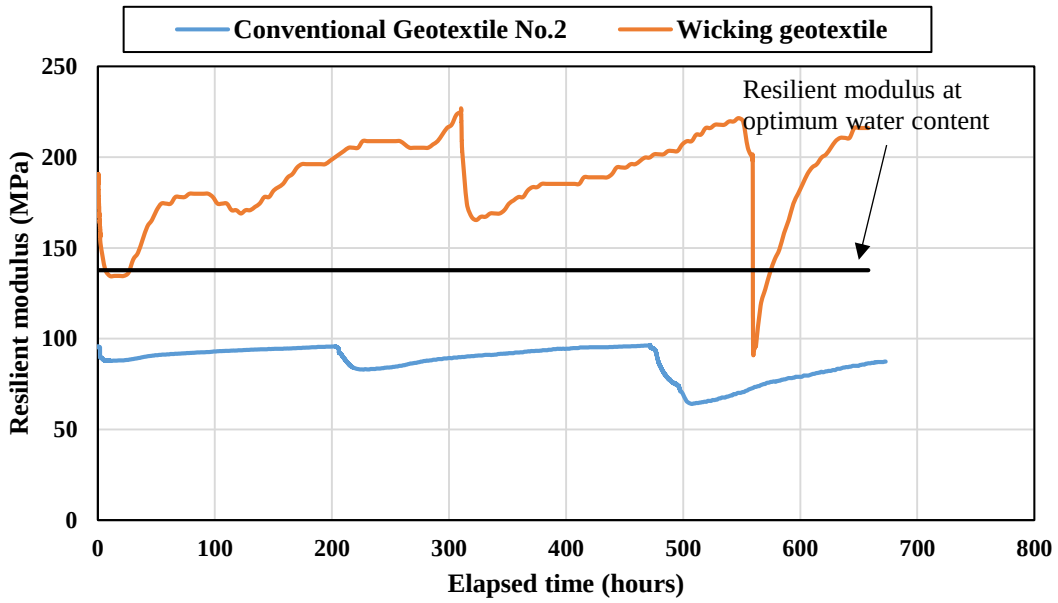

Figure 6.2 Base course resilient moduli in small-scale box tests

The effect of the wicking geotextile on the AB-3 aggregate water contents at different depths was investigated in the soil column tests. A noticeable water content reduction in the AB-3 base course as a result of the wicking geotextile was observed. Based on the soil column tests, the wicking geotextile had an effective wicking zone of 200 mm in the AB-3 aggregate. The water contents of the wicking geotextile-improved base course within the effective wicking zone were significantly lower than those in the conventional geotextile-improved base course. Figure 4.19 presents the average water content change of the AB-3 base course within the effective wicking zone of the soil column test. The resilient moduli of the base material in the soil column tests were based on the initial water content presented in Table 4.3 and the water content change in Figure 4.19.

Figure 6.3 presents the resilient modulus of the AB-3 base course in the effective wicking zone in the first soil column test. The first set of soil column test consisted of a conventional geotextile No.1-improved and a wicking geotextile-improved soil column. Based on the test results of the large-scale cyclic plate loading tests, the water content change in the control section was almost the same as that in the conventional geotextile-improved section. The improvement factor is defined as the ratio of the resilient modulus of the base material in the wicking geotextile-improved section to that in the conventional geotextile-improved section. Figure 6.3 shows that the improvement factor increased the time of the test. The wicking geotextile increased the resilient modulus of the AB-3 base course within the effective wicking zone by 20% in 50 hours as compared to the conventional geotextile-improved base course. The improvement factor increased gradually from 1.23 to 1.27 from 50 to 350 hours, respectively.

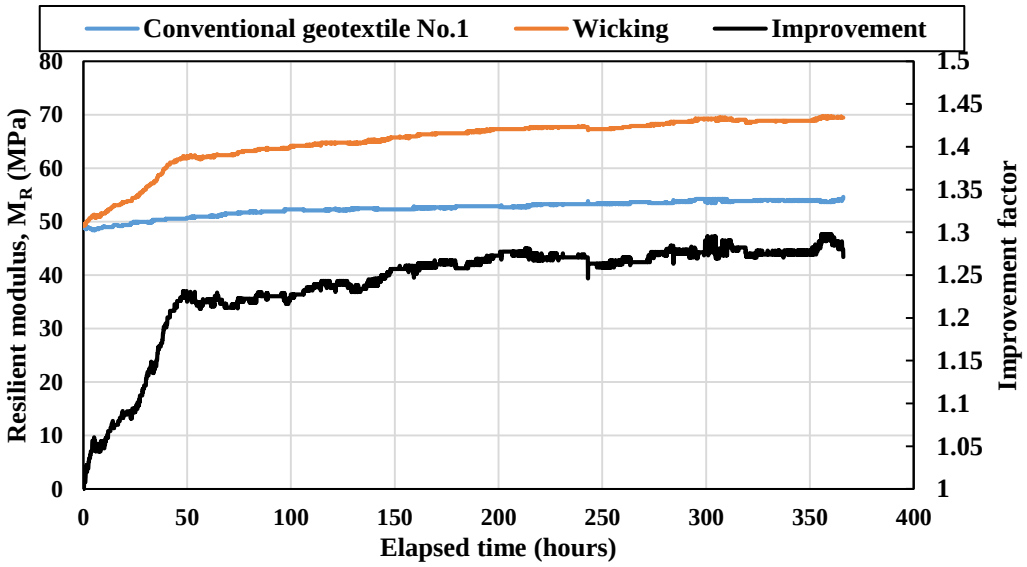

Figure 6.3 Resilient modulus change within the effective wicking zone in the 1st set of soil column tests

The similar calculation was performed based on the water content changes in the second and third soil column tests. It should be noted that the second and third sets of soil column tests consisted of a conventional woven geotextile No. 2-improved base material and a wicking geotextile-improved base material. Figure 6.4 presents the resilient modulus change within the effective wicking zone of the second set of soil column tests. In this set, the AB-3 aggregate was compacted at 9.8% water content. The resilient moduli of the AB-3 aggregate within the effective wicking zone were similar in both specimens in the first 60 hours. Then, as the wicking geotextile continued to remove water from the base course, the improvement factor for resilient modulus started to increase. At one week after the beginning of the test, the wicking geotextile increased the resilient modulus within the effective wicking zone 6% more than the resilient modulus of the conventional woven geotextile-improved base course. The improvement in the resilient modulus continued to increase as the progress of the test.

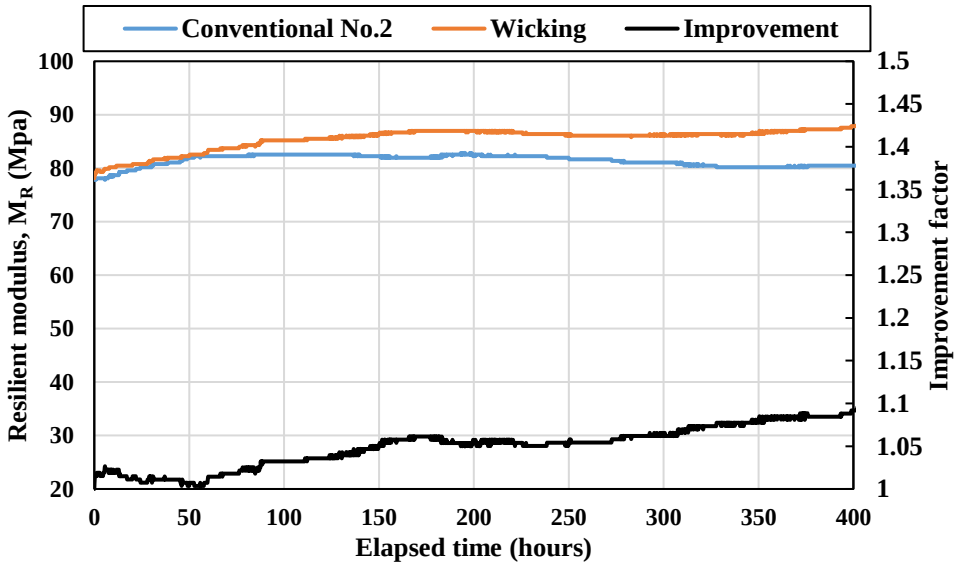

Figure 6.4 Resilient modulus change within the effective wicking zone of the 2nd set of soil column tests

The base course resilient moduli within the effective wicking zone of the third set of soil column tests are presented in two parts. Figure 6.5 (a) presents the resilient modulus after the AB-3 aggregate was compacted at a moisture content of 8.6% while Figure 6.5 (b) presents the resilient modulus of the base course after the soil columns were removed from the water tank. At 36 hours after the AB-3 aggregates were compacted at the optimum water content, the wicking geotextile increased the resilient modulus by over 30 MPa more than the conventional geotextile, which yielded an improvement factor of 1.2. The resilient modulus of the wicking geotextile-improved base remained stable 36 hours after the compaction of the base course. The resilient modulus of the conventional geotextile-improved base showed a slight increase 36 hours after the compaction. Figure 6.5 (b) presents the change of the resilient moduli of the base course from a saturated condition. The improvement factor at 36 hours after the compaction was around 1.2. The resilient moduli of both conventional geotextile-improved and wicking geotextile-improved base materials

increased rapidly within the first 200 hours after the soil columns were removed from the water reservoirs. At 48 hours after the soil columns were removed from the water reservoirs, the wicking geotextile-improved base showed a resilient modulus of 6.9 MPa higher than the conventional geotextile-improved base and the improvement factor at this moment was 1.08. One week after the soil columns were removed from the water reservoirs, the wicking geotextile-improved base course resilient modulus was 40 MPa higher than the conventional geotextile-improved base course, which yielded an improvement factor of 1.4. In the longer time (i.e., over 200 hours after the soil columns were removed from the water reservoirs), the resilient modulus also increased approximately 40 MPa, which yielded an improvement factor of 1.4.

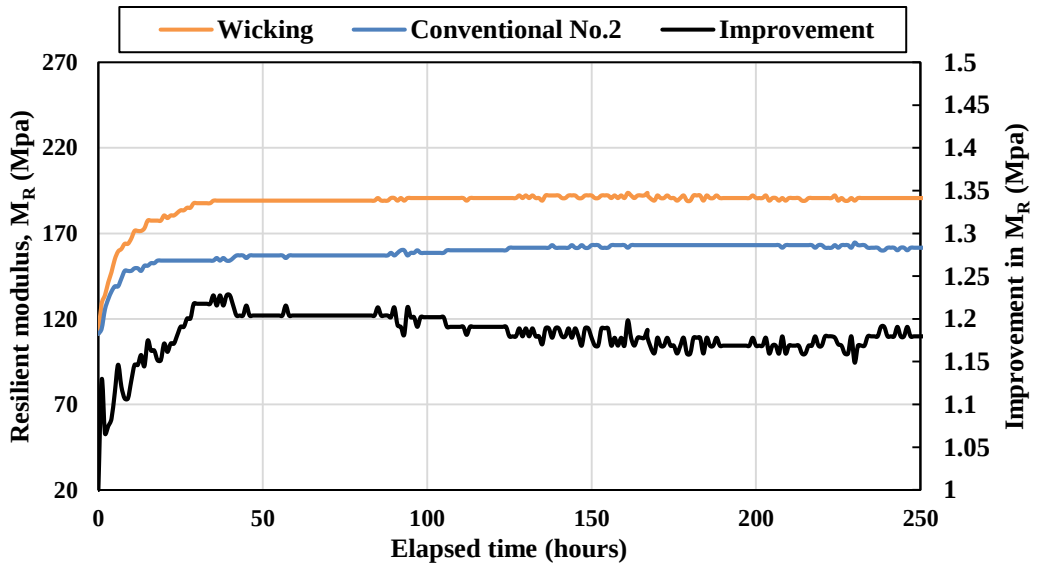

(a) After compaction

Figure 6.5 Resilient modulus change within the effective wicking zone of the 3rd set of soil column tests

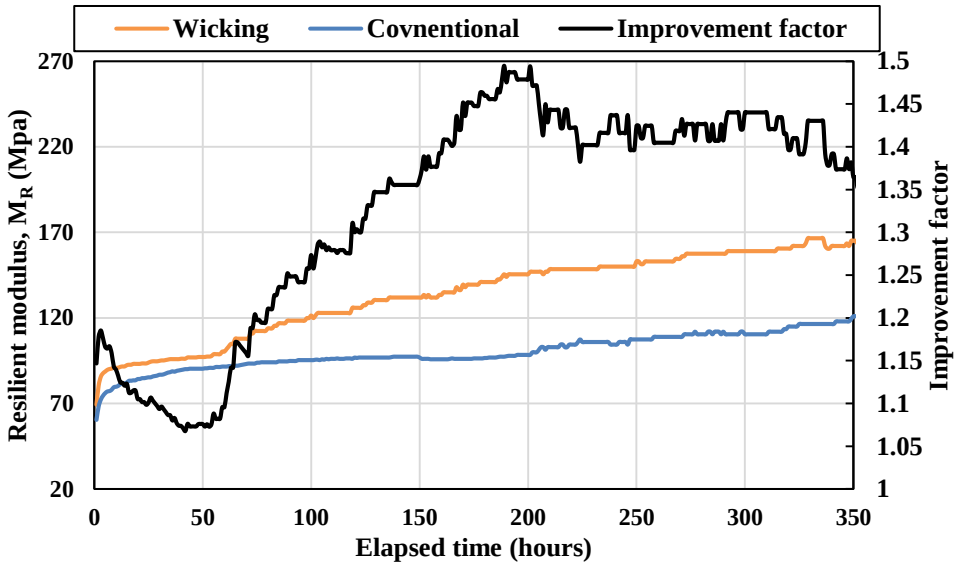

(b) After removed from the water tank

Figure 6.5 Resilient modulus change within the effective wicking zone of the 3rd set of soil column tests (continued)

Based on the soil column tests, it is concluded that the wicking geotextile-improved base showed a higher resilient modulus than the conventional geotextile-improved base. The improvement factor varied from 1.0 to 1.5. The value of the improvement factor varied with time. Generally, the improvement factor increased over a time period then remained stable. It is also found that the soil columns with saturated or near saturated initial water content (i.e., the 1st set of soil column tests and the second stage of the 3rd set of soil column tests) showed greater improvement factors. The suction in the base course decreased as the water content of the base course increased. The wicking geotextile removed water from the base course via the suction difference between the base course and the wicking geotextile. As the base course became drier, the suction difference between the wicking geotextile and the base course decreased. On the other

hand, the permeability of soil decreased with water content. Thus as the water content in the base course decreased, the water movement in the base course became more difficult. Consequently, the water removal rate of the wicking geotextile decreased as the water content of the base course decreased.

Table 6.1 summarizes the average daily improvement factors of base course resilient moduli within the effective wicking zone as a result of the water content reduction by the wicking geotextile. The water content reduction in the base course is the result of the special hydraulic properties of the wicking geotextile. Thus the improvement is named as the hydraulic improvement factor (F_h). The hydraulic improvement factor of the base course within the effective wicking zone is calculated with the following equation:

$$F_h = \frac{M_{R\ wicking}}{M_{R\ conventional}} \tag{6.3}$$

where $M_{R\ wicking}$ is the resilient modulus of the wicking geotextile-improved base course and $M_{R\ conventional}$ is the resilient modulus of the conventional geotextile-improved base course or unimproved base course.

The initial water contents of the base courses in the 1st set of soil column test and second stage of the 3rd set of soil column tests were close to the saturation water content, thus the hydraulic improvement factors from these tests were used to determine the value of hydraulic improvement factor for the base course resilient modulus within the effective wicking zone after a rainfall that saturated the base course. The values of the daily hydraulic improvement factor for the base course resilient modulus within the effective wicking zone after saturation are proposed in Table 6.2. The hydraulic improvement factor (F_h) increases from 1.12 to 1.32 in the first week after rainfall. The

hydraulic improvement factor (F_h) remains relatively stable in the second week. The improvement factor can also be expressed with the following equation:

$$F_h(N) = 0.1021 \ln(N) + 1.0938 \quad (6.4)$$

where N is the number of days after a major rainfall that saturates the base.

By assuming the resilient modulus of a wicking geotextile-improved base course is the same as that of an unimproved base course beyond the effective wicking zone, the hydraulic improvement factor for the resilient modulus of the entire thickness of the base course layer can be approximately calculated by:

$$F_{h\,eq} = F_h \times (H_{wicking}/H_{total}) \quad (6.5)$$

where $F_{h\,eq}$ is the average resilient modulus, $H_{wicking}$ is the thickness of the effective wicking zone, F_h is the improvement factor in the resilient modulus of the effective wicking zone, and H_{total} is the total thickness of the base course.

Table 6.1 Improvement factors of the resilient modulus within the effective wicking zone over time

Test	Reinforcement	Initial water content	Improvement factor on day							
			1	2	3	4	5	6	7	7+
Soil column #1	Conventional No. 1	11.10%	1.06	1.16	1.22	1.22	1.23	1.24	1.26	1.27
Soil column #2	Conventional No. 2	9.80%	1.02	1.01	1.01	1.03	1.03	1.04	1.06	1.08
Soil column #3 (stage 1)	Conventional No. 2	8.60%	1.13	1.21	1.20	1.20	1.19	1.18	1.18	1.17
Soil column #3 (stage 2)	Conventional No. 2	Saturated	1.21	1.08	1.12	1.22	1.28	1.34	1.38	1.32

Table 6.2 Proposed improvement factor for the resilient modulus of the AB-3 aggregate base

Days after rainfall	1	2	3	4	5	6	7
Improvement factor within effective wicking zone (F_h)	1.1	1.1	1.2	1.2	1.3	1.3	1.3
Days after rainfall	8	9	10	11	12	13	14
Improvement factor within effective wicking zone (F_h)	1.3	1.3	1.4	1.4	1.4	1.4	1.4

6.2 1993 AASHTO design method

6.2.1 Design consideration

Figure 6.1 shows that the resilient modulus of the AB-3 aggregate has an inverse relationship with the water content. Base course is typically compacted at its optimum water content. After the compaction, the base course water content would remain approximately constant. After a major rainfall, however, the water content in the base course increases to the saturation water content as water enters the roadway structure. As a result of the increased water content, the resilient modulus of the base course decreases. After the rainfall, as water starts to exit from the base course due to hydraulic gradient, the resilient modulus of the base course starts to recover and maybe return to the value before the rainfall. Figure 6.6 demonstrates the water content and resilient modulus changes of a base course before, during, and after a rainfall.

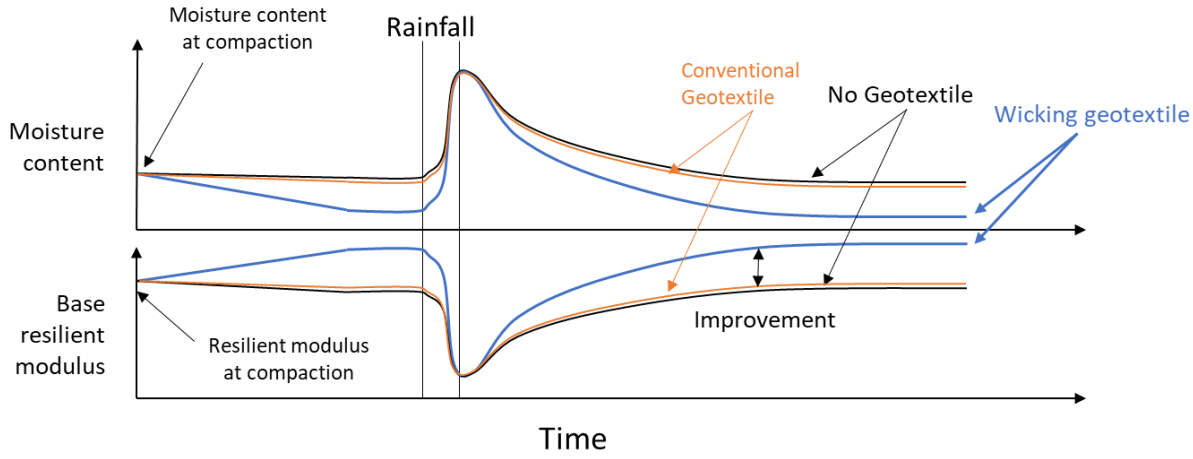

Figure 6.6 Water content and resilient modulus changes of the base course as a result of rainfall

The wicking geotextile shows the ability to reduce the base course moisture content to a value that is even lower than its optimum water content. After the wicking geotextile-improved

base course is compacted at its optimum water content, the water content of the base course decreases and the resilient modulus increases. During the rainfall, as the base course is saturated, the water content and resilient modulus of the wicking geotextile-improved base course are the same as those of an unimproved base course with no geotextile and the conventional geotextile-improved base course. After the rainfall, the wicking geotextile starts to remove water from the base course at a faster rate than the unimproved base course. As a result, the resilient modulus of the wicking geotextile-improved base recovers faster. The resilient modulus of the wicking geotextile-improved base eventually returns to the value before the rainfall, which is higher than that of the unimproved base. Based on the observation made in the big box tests, the water content change in the conventional geotextile-improved base was similar to that of the unimproved base. Thus in this analysis, the water content change of the conventional geotextile-improved base after a rainfall is assumed to be the same as that of the unimproved base. The relationship between resilient modulus increase as the result of water content reduction by the wicking geotextile and time after rainfall was investigated by the soil column tests and the suggested improvement factors were presented in Table 6.2.

6.2.2 Design concept

The 1993 AASHTO pavement design guide proposed a concept of relative damage (u_f) to consider the seasonal effect on roadbed resilient modulus. The equivalent roadbed modulus is a weighted value that gives equivalent accumulated annual damage caused by traffic on a road throughout one year with seasonal variations of the roadbed moduli (AASHTO, 1993). To calculate the equivalent modulus of the base course over a time period, the period of time was

divided into equal segments. Then the relative damage (u_f) of the segment of time can be calculated based on Equation (6.6):

$$u_f = 1.18 \times 10^8 \times M_R^{-2.32} \tag{6.6}$$

where u_f is the relative damage during a time segment and M_R is the resilient modulus of the respective time period.

After the relative damage of each time segment was determined, the average relative damage ($\overline{u_f}$) over the investigated time period is calculated by dividing the sum of all the relative damage during the period to the number of segments, *n*:

$$\overline{u_f} = \frac{\sum u_f}{n} \tag{6.7}$$

The final step is to back-calculate the equivalent resilient modulus ($\overline{M_R}$) over the investigated period using Equation (6.8):

$$\overline{M_R} = \left(\frac{1.18\times10^8}{\overline{u_f}}\right)^{\frac{1}{2.32}} \tag{6.8}$$

In this study, the relative damage concept was used to consider the effect of major rainfall on the base course resilient modulus. The resilient modulus of the wicking geotextile-improved base on a particular day after a rainfall can be calculated based on Equation (6.3) and Table 6.2:

$$M_{R\ wicking\ N} = M_{R\ convetional\ N} \times F_h(N) \tag{6.9}$$

where *N* is the number of days after rainfall. On the day of rainfall, both the wicking geotextile-improved and conventional geotextile-improved base courses are considered saturated, thus the resilient moduli of both base courses are equal, and the hydraulic improvement factor should equal to one.

Based on the resilient modulus, the relative damage of the N_{th} day after the rainfall (u_f) can be calculated with Equation (6.10):

$$u_{f\ wicking\ N} = 1.18 \times 10^8 \times M_{R\ wicking\ N}^{-2.32} \tag{6.10}$$

The average relative damage from the day of rainfall to the N_{th} day after the rainfall then is calculated as:

$$\overline{u_{f\ wicking}} = \frac{\sum u_{f\ wicking\ N}}{N} \tag{6.11}$$

The equivalent resilient modulus of a wicking geotextile-improved base over the N day period is calculated as:

$$\overline{M_{R\ wicking}} = \left(\frac{1.18\times10^8}{\overline{u_{f\ wicking}}}\right)^{\frac{1}{2.32}} \tag{6.12}$$

It should be noted that the equivalent resilient modulus of the wicking geotextile-improved base course represents the resilient modulus of the base over a period of time and is a function of the number of days after rainfall.

In practice, the engineers are often given the base course resilient modulus value that represents each month based on direct measurements made in that month. To simplify the design process, an improvement factor for the equivalent resilient modulus (F_{heq}) is proposed:

$$F_{h\,eq} = \frac{\overline{M_{R\,wicking}}}{\overline{M_{R\,convetional}}} \tag{6.13}$$

The equivalent resilient modulus improvement factor is defined as the ratio of the equivalent resilient modulus of the wicking geotextile-improved base to the equivalent resilient modulus of the conventional geotextile-improved base. Since the equivalent resilient modulus of the wicking geotextile-improved base depends on the number of days after rainfall, the equivalent resilient modulus improvement factor is also time-dependent. The equivalent resilient modulus of the conventional geotextile-improved base can be substituted by the resilient modulus that represents the monthly base course resilient modulus. Under this assumption that the equivalent resilient modulus of the conventional geotextile-improved base is independent of time, the improvement factor for the equivalent resilient modulus of the wicking geotextile-improved base is a function of the number of days after rainfall and can be expressed with Equation (6.14):

$$F_{h\,eq}(N) = 0.0743\ln(N) + 1.0741 \tag{6.14}$$

To illustrate the above concept, Figure 6.7 presents resilient moduli and equivalent resilient moduli of the wicking geotextile-improved base and the conventional geotextile-improved base. The resilient moduli of the conventional geotextile-improved base course were artificially generated between 210 and 190 MPa. The resilient moduli of the wicking geotextile-improved base were calculated based on the resilient moduli of the conventional geotextile-improved base

and Equation (6.4). Based on the resilient moduli of the conventional geotextile-improved base course, a value of 200 MPa was used to represent the equivalent resilient modulus of the base during the period of 14 days (i.e., N=14). The equivalent resilient modulus of the wicking geotextile-improved base was calculated based on the equivalent resilient modulus of the conventional geotextile-improved base (i.e., 200 MPa) and Equation (6.14).

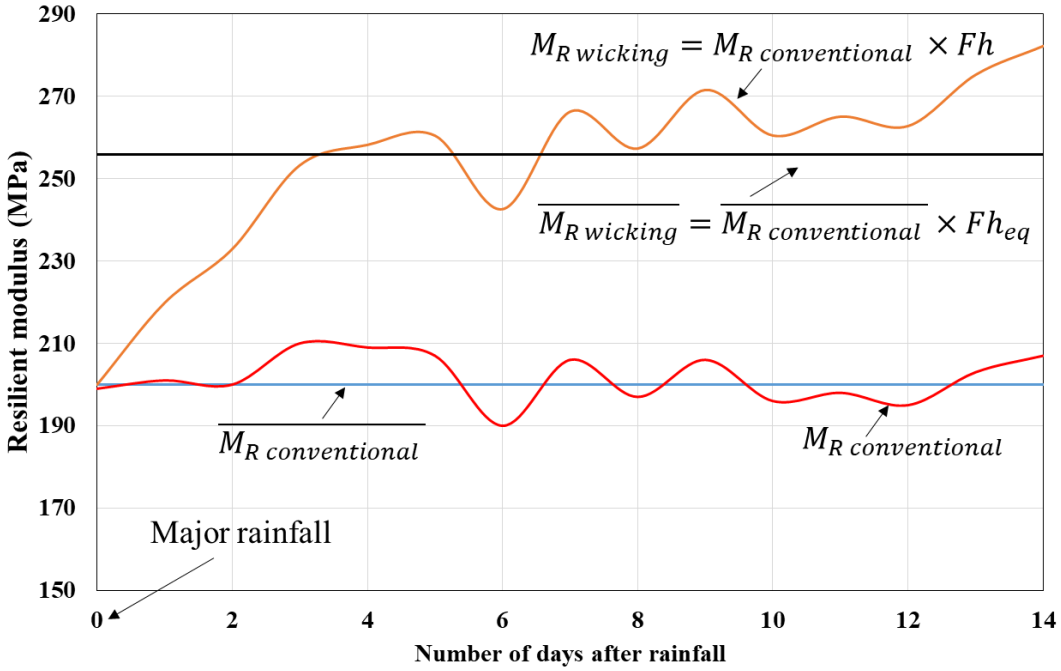

Figure 6.7 Demonstration of resilient moduli and equivalent resilient moduli of the wicking geotextile-improved base and the conventional geotextile-improved base

The calculation for the resilient modulus and the equivalent resilient modulus of the wicking geotextile-improved base course using Equations (6.9) to (6.14) is based on one major rainfall. To estimate the equivalent resilient modulus of a wicking geotextile-improved base using

the 1993 AASHTO pavement design guide, rainfall intensity and frequency of a project location are required. The National Oceanic and Atmospheric Administration website (www.ncdc.noaa.gov) offers daily precipitation data. After the precipitation data is obtained, it is necessary to determine the rainfall intensity that saturates the base course with Equation (6.45):

$$\begin{cases} n = 1 - \dfrac{\gamma_d}{G_s \times \gamma_w} \\ w_{sat} = \dfrac{n \times \gamma_w}{\gamma_d} \\ h_{rain} = h_{base} * (w_{sat} - w_{inital}) * \gamma_d / C_i \end{cases} \tag{6.15}$$

where n is the porosity of the base course, γ_d is the unit weight of the base course (i.e., 95% relative compaction in this study), G_s is the specific gravity of the base course, w_{sat} is the saturation water content, h_{base} is the thickness of the base, $w_{initial}$ is the initial water content, and C_i is the infiltration ratio. The infiltration ratio is defined as the portion of rainfall that enters the pavement through joints and cracks (FHWA, 1992). For asphalt concrete pavements the infiltration ratio is between 0.33 and 0.5 and for Portland cement concrete pavements the infiltration ratio is between 0.5 and 0.67. In this analysis, the worst case scenario (i.e., C_i = 0.67) is selected.

With the daily precipitation data and the calculated saturation rainfall intensity, the dates of major rainfalls and the number of days between major rainfalls (considered as a drying period) can be determined. The resilient modulus of the wicking geotextile-improved base course and the equivalent resilient modulus thus can be estimated based on Equations (6.9), (6.13), and (6.14) for each drying period. Based on the equivalent resilient modulus, the accumulated relative damage of each drying period can be calculated:

$$\sum u_{f\ j} = 1.18 \times 10^8 \times \left(\overline{M_{R\ wicking\ j}}\right)^{-2.32} \times N_j \quad (6.16)$$

where N_j is the length of the j_{th} dry period.

The average relative damage over the investigated period is calculated by dividing the sum of the accumulated relative damage of each drying period to the total number days of the drying period:

$$u_{f\ ave} = \frac{\sum u_{f\ j}}{\sum N_j} \quad (6.17)$$

Finally, the equivalent resilient modulus of the base course for the 1993 AASHTO pavement design can be calculated based on the average relative damage:

$$\overline{M_R{}'} = \left(\frac{1.18\times10^8}{\overline{u_{f\ ave}}}\right)^{\frac{1}{2.32}} \quad (6.18)$$

6.2.3 Sample calculation

A 200 mm thick base course was constructed in Lawrence, KS with an aggregate material of the following properties: specific gravity G_s = 2.65, dry unit weight γ_d =19.6 kN/m^3, and initial water content $w_{initial}$ = 9%. The equivalent resilient modulus of the conventional geotextile-improved base is 150 MPa for the investigation period. Based on Equation (6.15), the base course would be saturated if the precipitation exceeds 29 mm/day. Figure 6.8 presents the precipitation data of Lawrence from July 1^{st,} 2016.

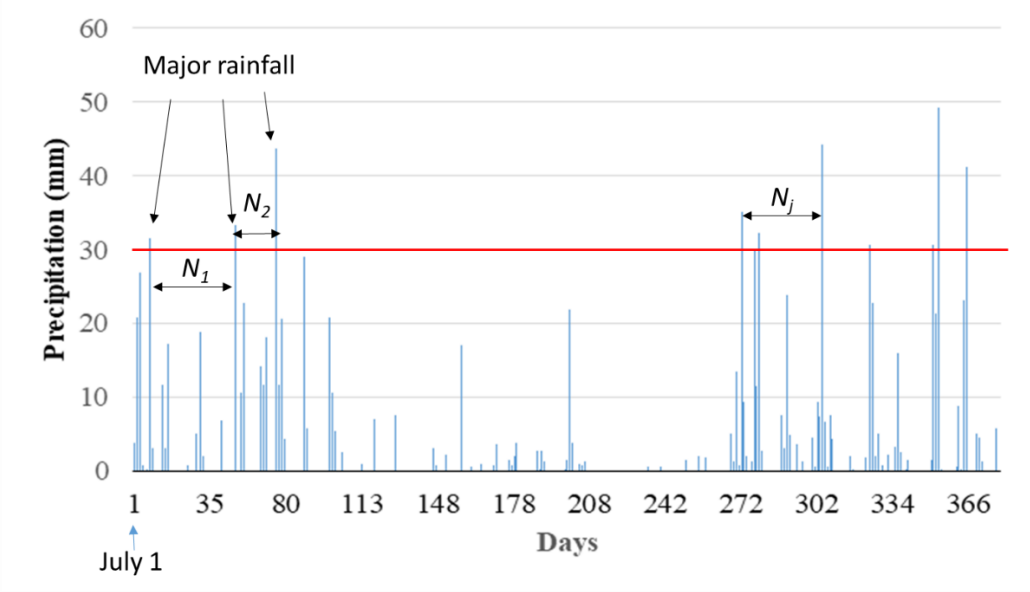

Figure 6.8 Daily precipitation of Lawrence, KS starting from July 1st, 2016.

Within the one year period starting from July 1st 2016, there were 10 days that Lawrence, KS received over 30 mm of precipitation in one day. The number of days between the days that received over 30 mm of precipitation was considered a drying period (N_j). The equivalent resilient modulus of the wicking geotextile-improved base course over the j_{th} drying period ($\overline{M_{R\ wicking\ j}}$) then can be adjusted based on Equation (6.14):

$$\overline{M_{R\ wicking\ j}} = \overline{M_{R\ con.}} \times Fh_{eq\ j} = \overline{M_{R\ con.j}} \times (0.0743 \ln(N) + 1.0741) \quad (6.19)$$

where $\overline{M_{R\ j}}$ is the equivalent resilient modulus of the unimproved or conventional geotextile-improved base course (MPa).

The daily relative damage ($u_{f\,j}$) then can be calculated based on the equivalent resilient modulus over the drying period:

$$u_{f\,j} = 1.18 \times 10^8 \times \overline{M_{Rw\,J}^{-2.32}} \tag{6.20}$$

The accumulated relative damage over a drying period equals to the product of length of the drying period (N_j) and the relative daily damage ($u_{f\,j}$). The equivalent resilient modulus of the wicking geotextile-improved base course over the year ($\overline{M_R{}'}$) thus can be calculated based on the total days of the drying period ($\sum N_j$) and the accumulated relative damage $\sum(u_{f\,j} \times N_j)$:

$$\overline{M_R'} = \left(\frac{1.18\times10^8}{\overline{uf}}\right)^{\frac{1}{2.32}} = \left(\frac{1.18\times10^8\times\sum N_j}{\sum(u_{f\,j}\times N_j)}\right)^{\frac{1}{2.32}} \tag{6.21}$$

Table 6.3 presents the calculation of equivalent annual resilient modulus of the wicking geotextile-improved base course.

Table 6.3 Calculation of the equivalent annual resilient modulus of the wicking geotextile-improved base course

Date	Precipitation	Length of Drying period, N_j	Equivalent resilient modulus improvement factor, F_{heq}	Adjusted equivalent resilient modulus, $\overline{M_{R\ wicking}}$	N_j*u_{fj}
	(mm)	(days)		(MPa)	
7/7/2016	31.5	7	1.22	182.8	0.0452
8/25/2016	33.3	52	1.37	205.2	0.2567
9/14/2016	43.7	15	1.28	191.3	0.0871
3/29/2017	35.1	195	1.47	219.9	0.8197
4/5/2017	32.3	6	1.21	181.1	0.0396
4/30/2017	44.2	24	1.31	196.5	0.1309
5/19/2017	30.7	18	1.29	193.3	0.1020
6/15/2017	30.7	26	1.32	197.4	0.1403
6/17/2017	49.3	3	1.16	173.4	0.0219
6/30/2017	41.1	10	1.25	186.8	0.0614
Rainfall		10	1	150	0.1021
Sum		356			1.8069
Average				$\overline{u_f}$	0.0049
			$M_{Rw}{}' =$	205.2 MPa	

Base on the calculation in Table 6.3, the equivalent resilient modulus for the wicking geotextile-improved base course is 205.2MPa. The inclusion of the wicking geotextile would increase the equivalent resilient modulus of the base course by 36.7% over the period between July 1st 2016 and July 1st 2017. It should be noted that the design guideline stated previously did not consider the increase in the resilient modulus due to the freezing of the base course. Over the

investigated period (i.e., one year starting from July 1st, 2016), there were only 19 days that the maximum air temperature was below 0 ℃. Among the 19 days, the number of the longest consecutive days was 8 days. Thus, the resilient modulus of the frozen base course should not have a significant impact on the overall equivalent resilient modulus. If the area that the wicking geotextile is to be utilized experiences a long period of sub-freezing temperature, the number of days of sub-freezing temperature should be excluded from the calculation.

The adjusted equivalent resilient modulus of the base course then can be used to calculate the base layer coefficient (a_2) with Equation (2.11):

$$a_2 = 0.249(\log_{10} E_{BS}) - 0.977 \quad (6.22)$$

Base on the equivalent resilient modulus calculated in Table 6.3, the layer coefficient for the wicking geotextile-improved base course is 0.137 while the layer coefficient for the conventional geotextile-improved base course without considering mechanical stabilization is 0.103. Based on this calculation, the layer coefficient ratio of the wicking geotextile to the conventional geotextile-improved base course considering the hydraulic improvement only is:

$$Layer\ coefficient\ ratio\ (LCR) = \frac{0.137}{0.103} = 1.33 \quad (6.23)$$

The above adjustment process for the equivalent resilient modulus for the base course and the layer coefficient based on daily rainfall can be used in the AASHTO 1993 pavement design.

6.3 MEPDG method

The current mechanistic-empirical pavement design guide (MEPDG) software includes an environmental effect model (EICM) to modify the representative resilient modulus of base course

for seasonal effects. Based on the water content change measured in the previous tests modification can be made to the environmental effect model in the MEPDG design software for the design of the wicking geotextile in roadway structures. However, the current MEPDG design software does not allow modification to the environmental effect component. The MEPDG design software allows input of base course resilient modulus of each month of the year. The base course resilient modulus of each moth can be calculated with the same procedure described in the previous section.

Another approach to incorporate the improvement of a pavement due to the increase in the base course resilient modulus by the wicking geotextile based on the permanent deformation measured from the large-scale cyclic plate loading tests. The damage model in the MEPDG is used to predict the permanent deformation of base course or subgrade, as expressed in Equation (6.23):

$$\begin{cases} PD = k \cdot h_{soil} \cdot \varepsilon_v \cdot \left(\frac{\varepsilon_0}{\varepsilon_r}\right) \cdot e^{-\left(\frac{\rho}{N_L}\right)^{\beta}} \\ log\beta = -0.61119 - 0.017638W_c \\ \rho = 10^9 \cdot \left(\frac{-4.89285}{1-(10^9)^{\beta}}\right)^{\frac{1}{\beta}} \\ \frac{\varepsilon_0}{\varepsilon_r} = \frac{0.15 \cdot e^{\rho^{\beta}} + 20 \cdot e^{\left(\frac{\rho}{10^9}\right)^{\beta}}}{2} \end{cases} \tag{6.23}$$

where *PD* is the permanent deformation of the soil layer; h_{soil} is the thickness of the soil layer; ($\varepsilon_0/\varepsilon_r$), β, and ρ are the parameters for the unbound material of the soil layer; *k* is the calibration factor (nationally 1.67 for base course and 1.35 for subgrade); ε_v is the average vertical resilient

strain of the soil layer; W_c is the water content; and N_L is the number of load cycles. In this equation, ε_v can be estimated by an elastic solution based on the moduli of base course and subgrade.

The damage model enables the estimation of the permanent deformation on the top of the base course surface under cyclic loading. In the calculation of the permanent deformation, the water contents and resilient moduli of both base course and subgrade are required. As this study focused on the effect of the wicking geotextile on the base course, the water content and CBR value of the subgrade were assumed to be constant over the investigated period. A correlation between subgrade CBR and resilient modulus was developed for the same subgrade material used in the previous study by Sun et al. (2016) as follows:

$$M_R = 25.9\ CBR^{0.39} \tag{6.24}$$

To simulate the large-scale cyclic loading test sections with the soil damage model, the 300 mm thick base course and the top 300 mm of the subgrade in the large scale test were divided into six 100 mm thick layers as presented in Figure 6.9. The stress at the mid-depth of each layer beneath the center of the loading plate was calculated based on the following equation:

$$\Delta\sigma_z = \left(1 - \left(\frac{1}{1+\left(\frac{B_f}{2Z_f}\right)^2}\right)^{1.5}\right) p_n \tag{6.25}$$

where $\Delta\sigma_z$ is the additional vertical stress at the mid-depth of soil layer, B_f is the diameter of the loading plate (i.e., 0.15 m), Z_f is the depth of the mid-depth to the base course surface, and p_n is the contact pressure of the loading plate (i.e., 138 kPa in this study).

The average vertical resilient strain of the soil layer (ε_v) is then calculated based on the vertical stress at the mid-depth of each soil layer and the resilient modulus of the base course or the subgrade:

$$\varepsilon_v = \Delta\sigma_z / M_R \tag{6.26}$$

where M_R is the resilient modulus of the soil layer.

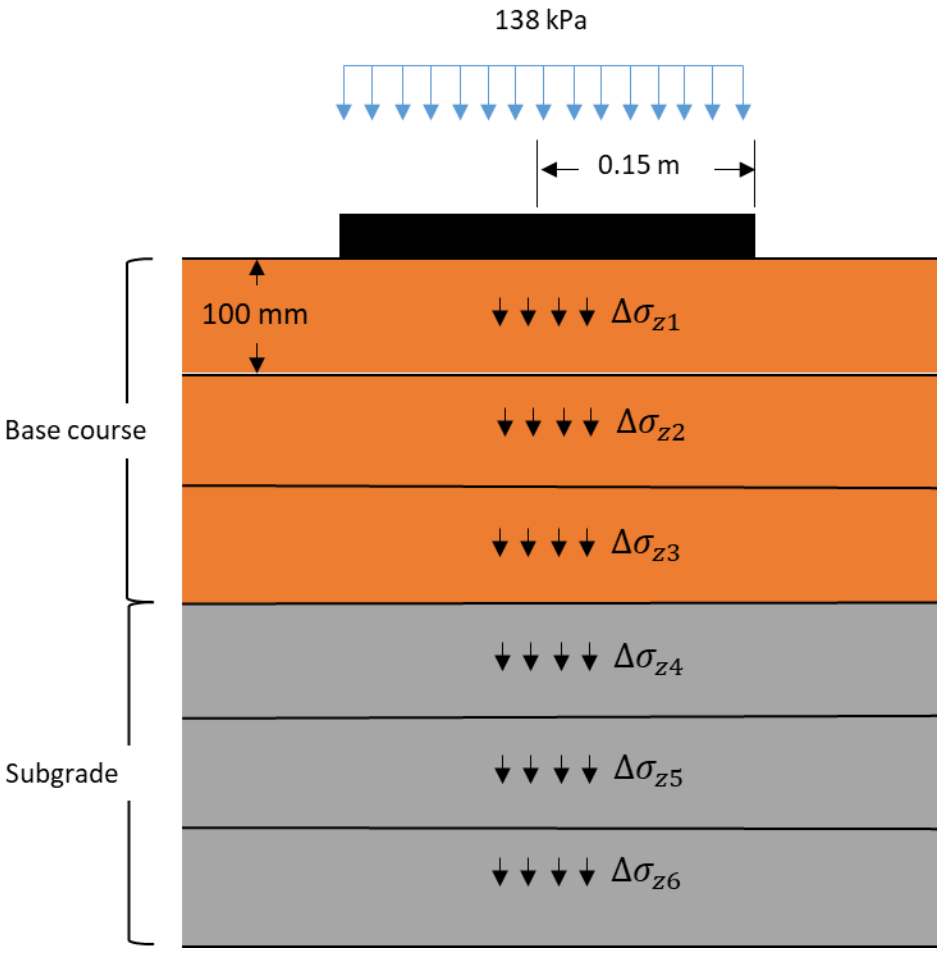

Figure 6.9 Division of soil layers

The permanent deformation of each soil layer of the control section then can be calculated with Equation (6.23). The water contents (W_c) in Equation (6.23) for the base course were estimated based on the measured volumetric water contents and the initial water contents of the base course. The base course was compacted at its optimum water content of 8.6%. The first rainfall simulation was conducted the next day, approximately 18 hours, after the compaction of base course. Based on the previous experience, water loss happened during compaction. Although the base course was covered with plastic sheet, the 18-hour delay after compaction of base course and before the first rainfall simulation would result in approximately 0.4% water content loss. Therefore, the initial water content of the base course was assumed to be 8.2%. The water contents (W_c) for the subgrade were 10.6% for the 5% CBR subgrade and 11.3% for the 3% CBR subgrade. The value of 1.0 was selected for the subgrade calibration factor *k* in Equation (6.23). The sum of the permanent deformations of the six layers was used to represent the permanent deformation of the base course surface.

The calibration factor *k* for the base course was determined by adjusting the value of k so that the soil damage model predicted the permanent deformation matching the permanent deformation measured from the control test section. In the soil damage model, the base course resilient modulus was calculated based on the water content changes measured by three layers of volumetric water content sensors and the initial water contents of the base course in the cyclic loading plate loading tests conducted at seven and two days after the simulated rainfall. The resilient modulus of the base course was difficult to determine in the cyclic plate loading tests conducted at two hours after rainfall because during the time of the test, the base course was still under gravitational drainage. Therefore, the base course water contents in the cyclic loading tests at two hours after the rainfall was assumed to be 11.3%, close to saturation. Based on the water

content, the resilient modulus of the base course was estimated as 45 MPa. It is also noticed that the first few cycles of the first cyclic loading test (i.e., 7 days after the rainfall) generated large permanent deformations due to seating problems of the loading plate and uneven base surface. Therefore, the first two loading cycles were considered as conditioning of the test section and were not included as part of permanent deformation measurements. Figure 6.10 presents the measured permanent deformations and the predicted permanent deformation of the cyclic loading tests on the control sections using the calibration factor for the base course.

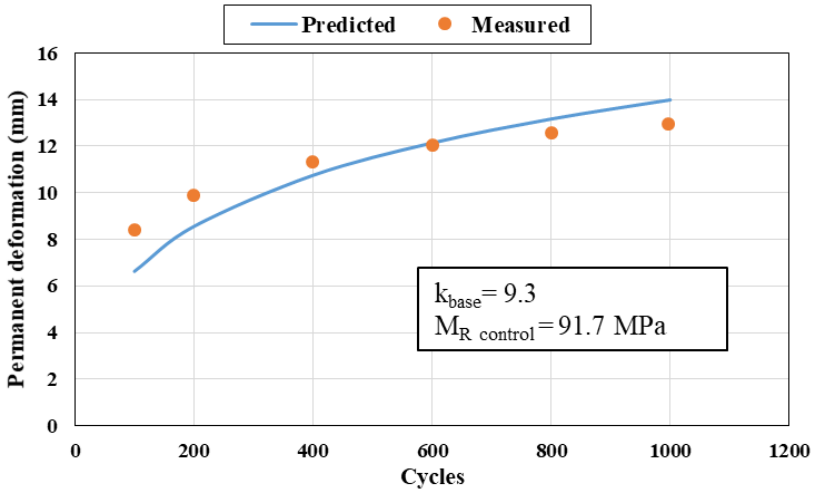

(a) 3% CBR subgrade at 7 days after rainfall

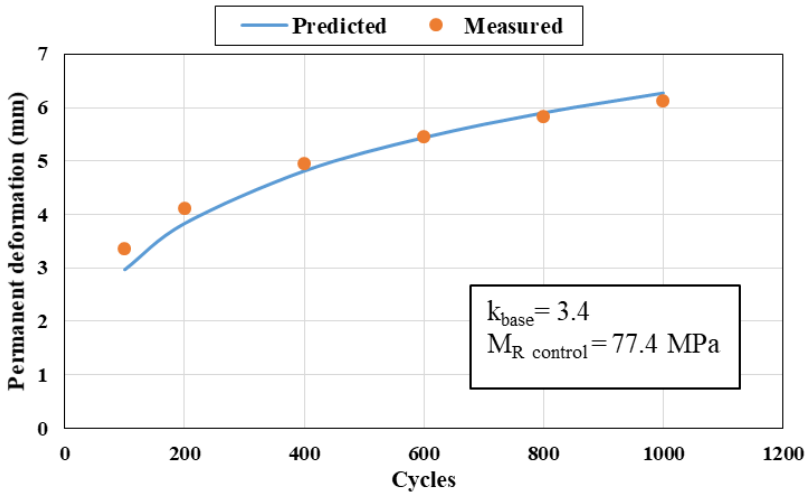

(b) 3% CBR subgrade at 2 days after rainfall

Figure 6.10 Calibration of the soil damage model based on the permanent deformations from the control sections

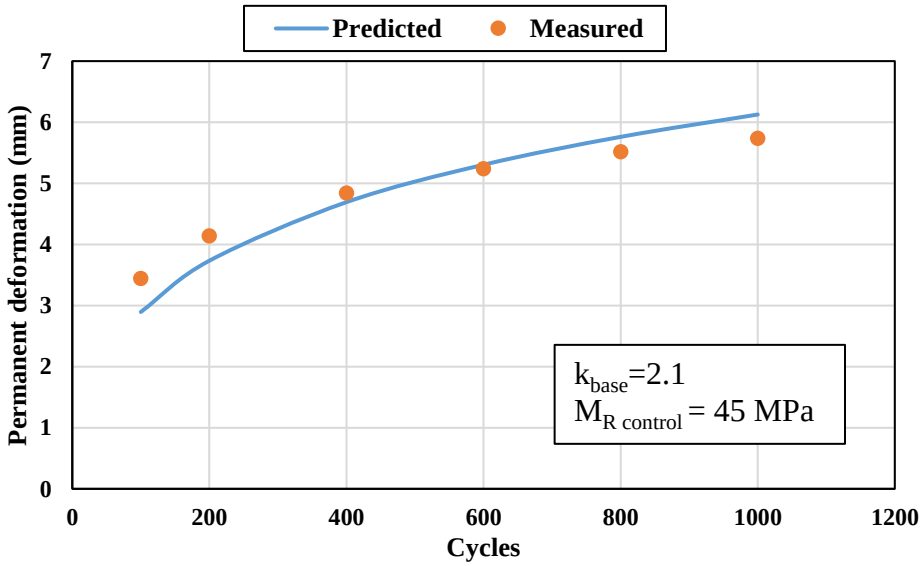

(c) 3% CBR subgrade at 2 hours after rainfall

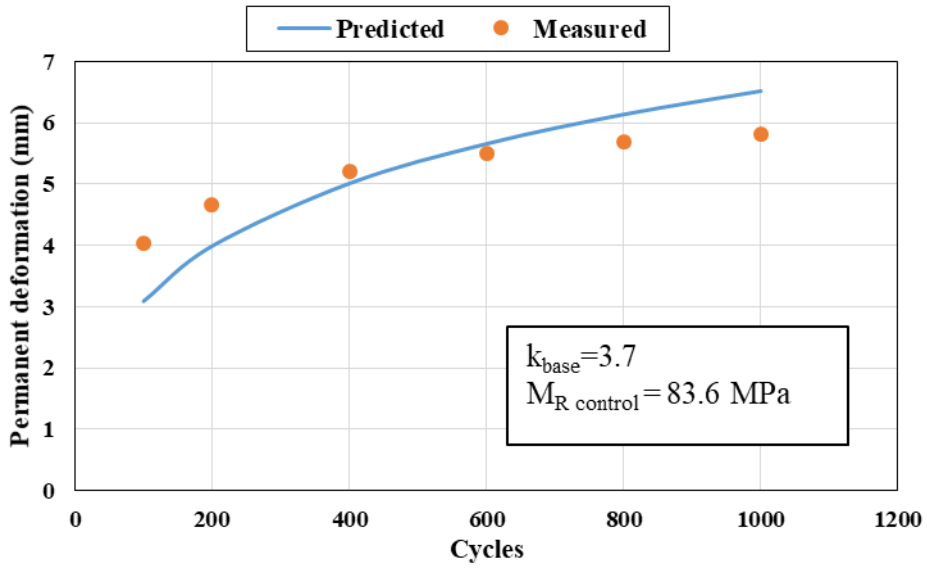

(d) 5% CBR subgrade at 7 days after rainfall

Figure 6.10 Calibration of the soil damage model based on the permanent deformations from the control sections (continued)

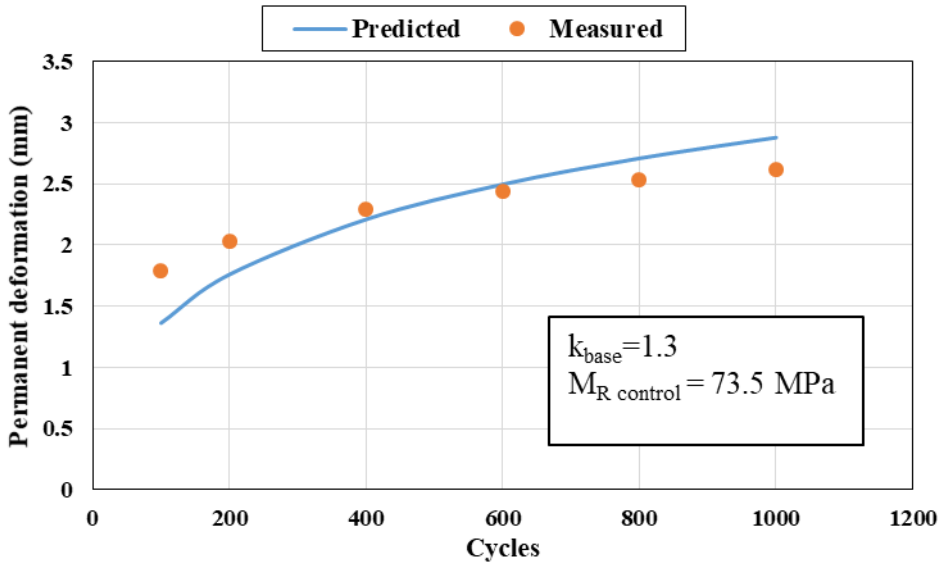

(e) 5% CBR subgrade at 2 days after rainfall

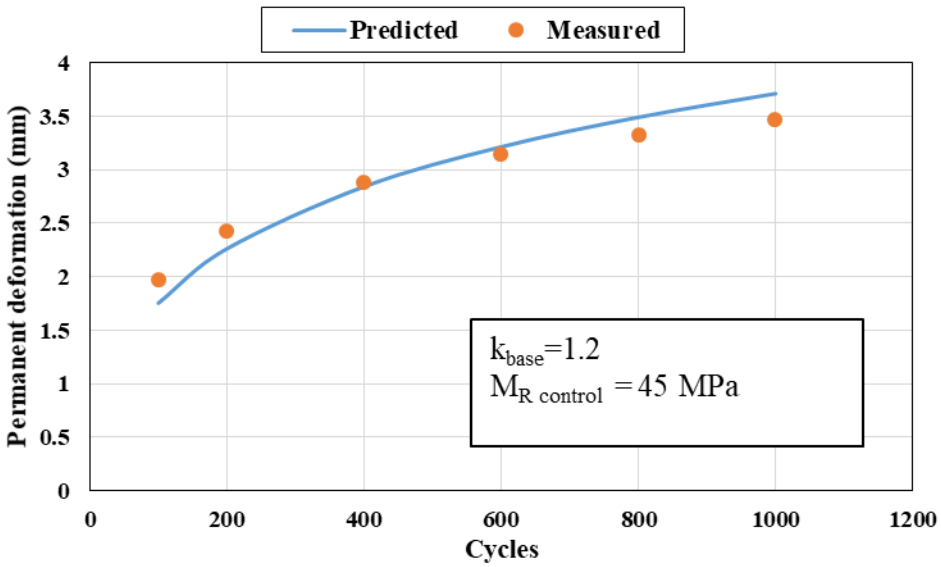

(f) 5% CBR subgrade at 2 hours after rainfall

Figure 6.10 Calibration of the soil damage model based on the permanent deformations from the control sections (continued)

Overall, the calibrated soil damage models predicted the permanent deformations in good agreement with the permanent deformations obtained from the large-scale cyclic plate loading tests. The values of the calibration factor k varied from 1.2 to 9.3. The calibrated soil damage model can be then used to estimate the permanent deformations of the geotextile-improved sections. As discussed previously, the wicking geotextile improves the base course resilient modulus through mechanical stabilization (lateral confinement) and hydraulic stabilization (drainage). The effect of mechanical stabilization can be estimated by the permanent deformation measured from the conventional geotextile-improved base course as compared to that of the control section in the large-scale cyclic plate loading tests. Since the wicking geotextile had similar mechanical

properties as the conventional geotextile, it is expected that the wicking geotextile should have a similar improvement factor for mechanical stabilization. The benefit of mechanical stabilization is represented by the mechanical improvement factor for the resilient modulus of the base course, F_m:

$$M_{R\ conventional} = F_m \times M_{R\ conventional} \tag{6.27}$$

where $M_{R\ conventional}$ is the resilient modulus of the conventional geotextile-improved base, which is estimated based on the initial water content and volumetric water content change measured by the soil water content sensors.

To determine the mechanical improvement factor (F_m), the average vertical resilient strain in Equation (6.23) was calculated by with the conventional geotextile-improved base course resilient modulus ($M_{R\ conventional}$):

$$\varepsilon_v = \Delta\sigma_z/(F_m \times M_{R\ conventional}) \tag{6.28}$$

The value of the mechanical improvement (F_m) factor was adjusted so that the model predicted the permanent deformations matching the measured permanent deformations. Figure 6.11 presents the measured and predicted permanent deformations of the conventional geotextile-improved sections.

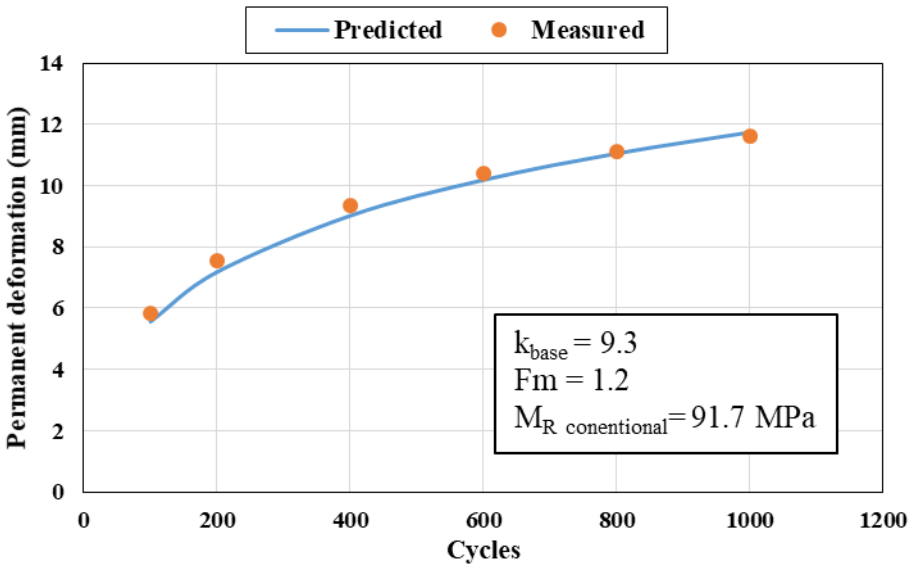

(a) 3% CBR subgrade at 7 days after rainfall

Figure 6.11 Measured and predicted permanent deformations of the conventional geotextile-improved sections

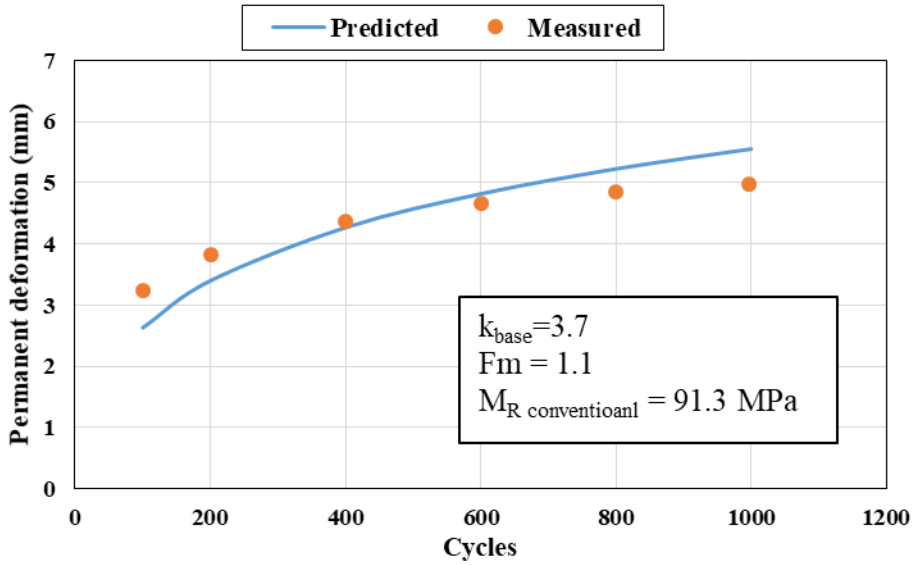

(b) 5% CBR subgrade at 7 days after rainfall

Figure 6.11 Measured and predicted permanent deformations of the conventional geotextile-improved sections (continued)

Based on Figure 6.11, the mechanical improvement factors are 1.1 and 1.2. As previously discussed in Chapter 5, the conventional geotextile-improved sections resulted in larger permanent deformations than the control sections in the cyclic plate loading tests at two days and two hours after rainfall. Thus the mechanical improvement factor could not be calculated based on the permanent deformations at two days and two hours after the rainfall. The mechanical improvement factors (F_m) for these four tests were assumed to be 1.1 and 1.2 for 3% CBR subgrade and 5% CBR subgrade, respectively.

Once the mechanical improvement factor was determined, comparisons could be made between the measured and predicted permanent deformations of the wicking geotextile-improved sections. The predicted permanent deformations of the geotextile-improved sections were calculated with the calibrated soil damage model. The average vertical resilient strain for the wicking geotextile-improved base course was calculated as:

$$\varepsilon_v = \Delta\sigma_z/(F_m \times M_{R\ wicking}) \tag{6.28}$$

where $M_{R\ wicking}$ was estimated based on the initial water content of the base course and the water content change measured by the volumetric water content sensor. Figure 6.12 presents the comparison between the measured and predicted permanent deformations of these test sections.

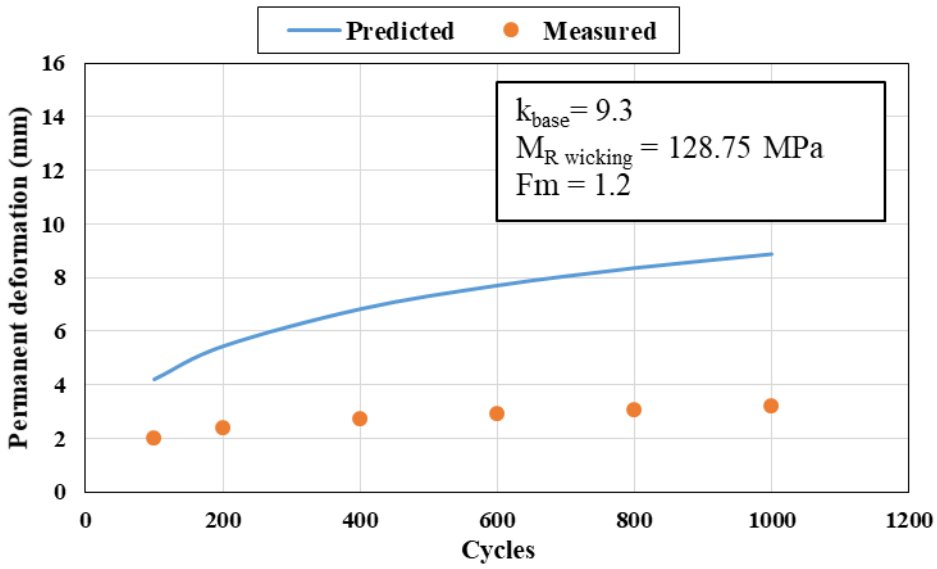

(a) 3% CBR subgrade at 7 days after rainfall

Figure 6.12 Measured and predicted permanent deformations of the wicking geotextile-improved sections

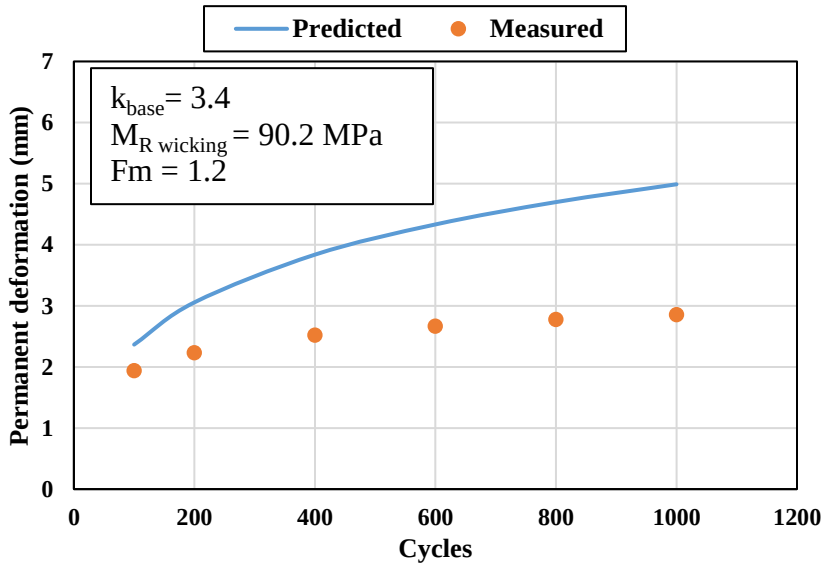

(b) 3% CBR subgrade at 2 days after rainfall

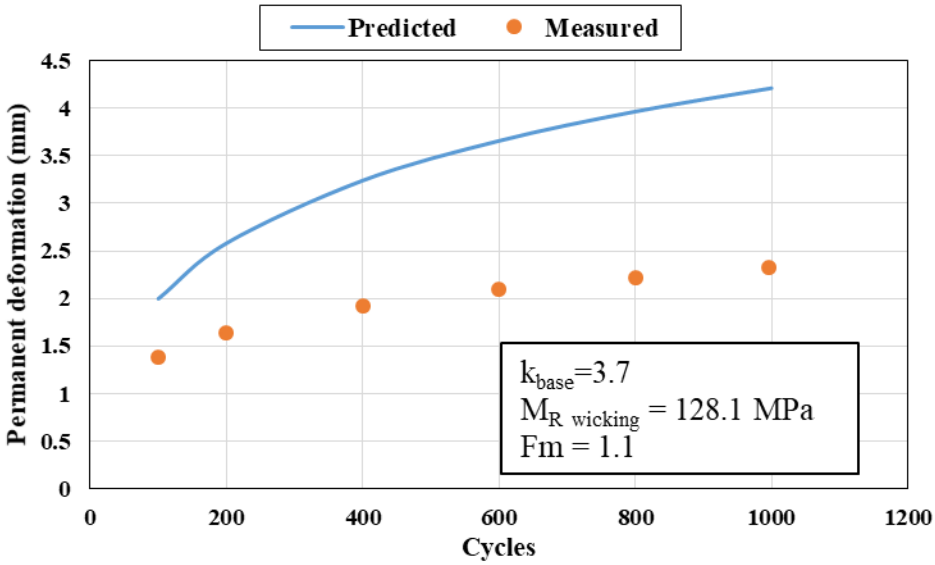

(d) 5% CBR subgrade at 7 days after rainfall

Figure 6.12 Measured and predicted permanent deformations of the wicking geotextile-improved sections (continued)

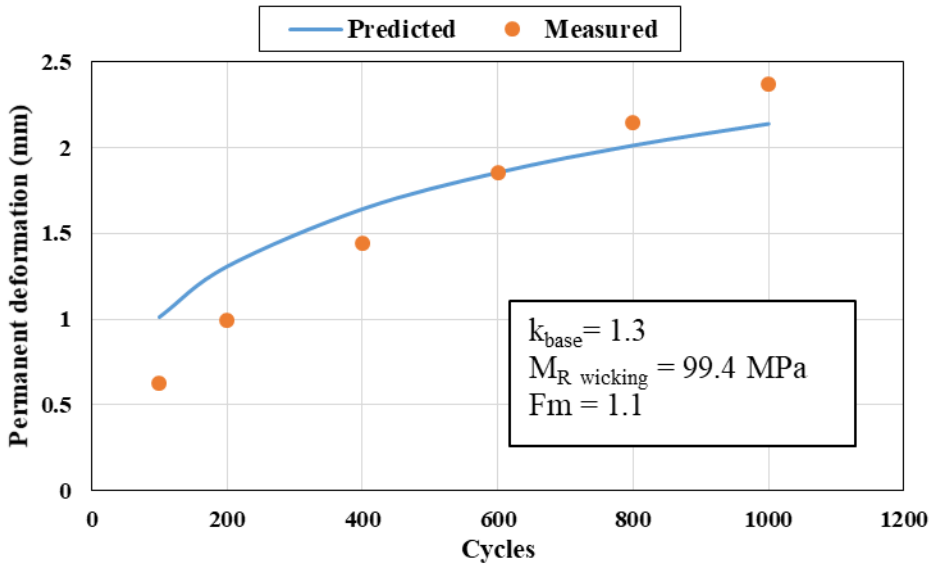

(e) 5% CBR subgrade at 2 days after rainfall

Figure 6.12 Measured and predicted permanent deformations of the wicking geotextile-improved sections (continued)

The predicted permanent deformations showed a good match with the measured permanent deformations in the cyclic plate loading tests on a 5% CBR subgrade at 2 days after rainfall. Overall, for the wicking geotextile-improved sections, the approach based on the mechanical improvement factors and the soil damage model using the measured water contents over-predicted the permanent deformations of the test sections. The over-prediction may be attributed to the following reasons: (a) the accuracy in the measurement of volumetric water content, (b) the variability of test sections, and (3) the accuracy of the soil damage model. The AB-3 aggregate consisted of large particles. During the installation of moisture sensors, the AB-3 aggregate around the sensors was hand -compacted. As a result, the degree of compaction around the sensors might

be different from the overall degree of compaction of the base course and resulted in possible errors and variability in the water content measurement. Each test section required a large amount of materials. It is possible that during the preparation of the sections the base course and the subgrade were not uniform. In addition, the soil damage model included in the MEPDG is empirical and it might not represent the behavior of the AB-3 aggregate well.

Due to the large difference between the measured and predicted permanent deformations of the wicking geotextile-improved sections, another approach was taken to back-calculate the hydraulic improvement factors based on the measured permanent deformations from the large-scale cyclic plate loading tests. In this approach, the resilient modulus of the wicking geotextile-improved base course is calculated as:

$$M_{R\ wicking} = F_m \times Fh \times M_{R\ control} \tag{6.29}$$

where $M_{R\ wicking}$ is the resilient modulus of the wicking geotextile-improved base course used for calculating its average vertical resilient strain (ε_v) in the soil damage model; F_m is the mechanical improvement factor determined previously; F_h is the hydraulic improvement factor to be determined; and $M_{R\ control}$ is the resilient modulus of the base course in the control section.

To determine the hydraulic improvement factor, the value of F_h was adjusted so that the soil damage model predicted the permanent deformations of the wicking geotextile-improved section close to those measured from the cyclic plate loading test. Figure 6.13 presents the value of the hydraulic improvement factor and the predicted and measured permanent deformations.

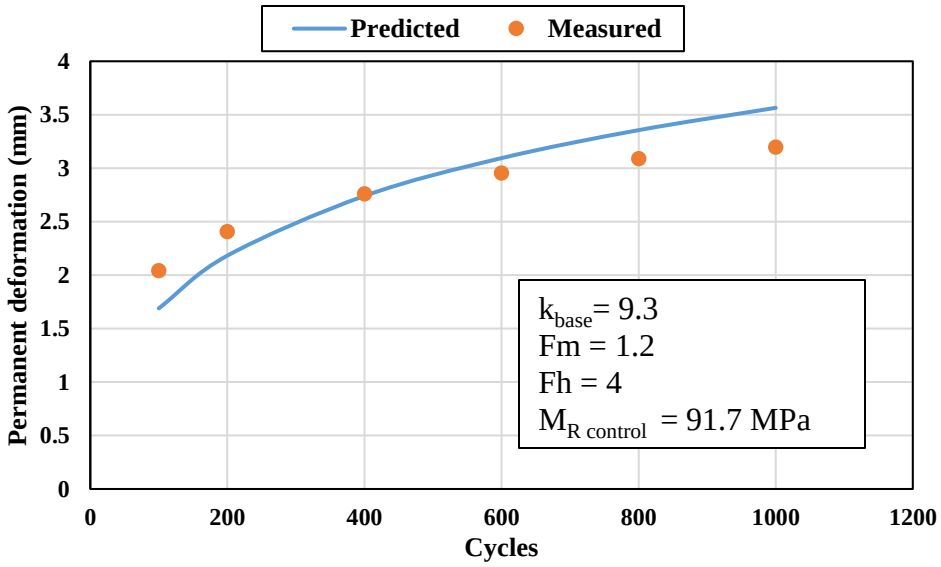

(a) 3% CBR subgrade at 7 days after rainfall

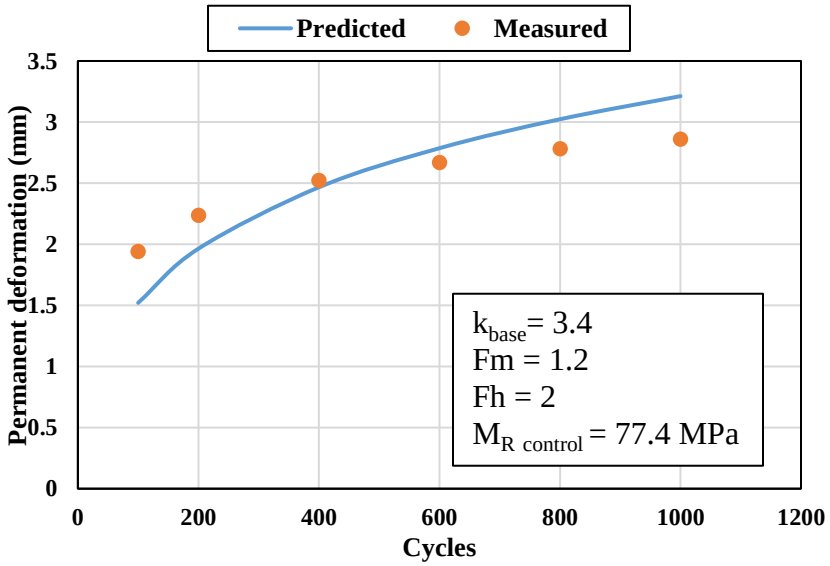

(b) 3% CBR subgrade at 2 days after rainfall

Figure 6.13 Measured and predicted permanent deformations of the wicking geotextile-improved sections with the back-calculated hydraulic improvement factor

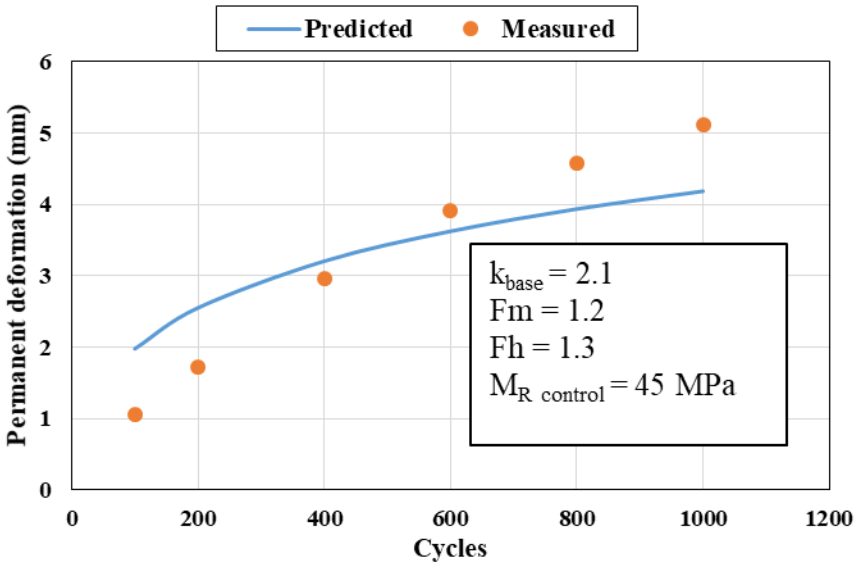

(c) 3% CBR subgrade at 2 hours after rainfall

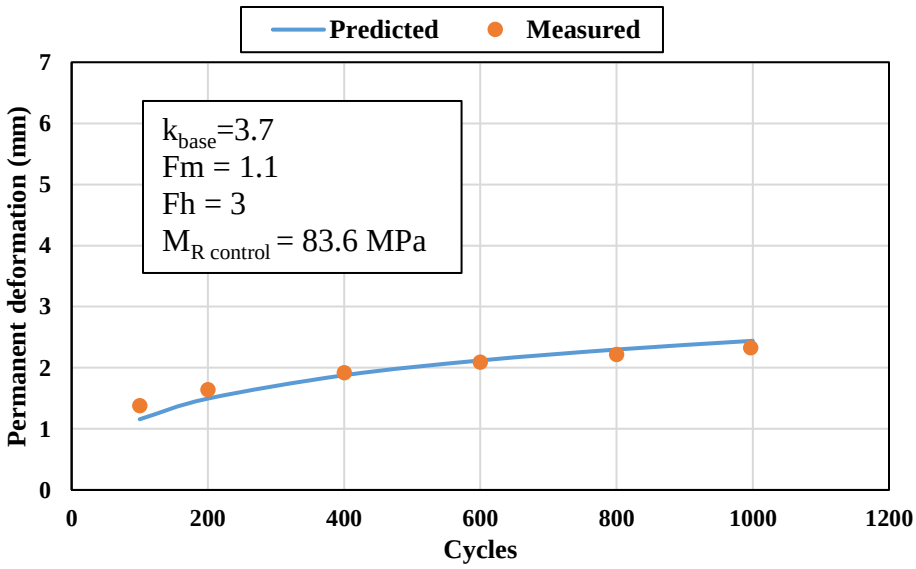

(d) 5% CBR subgrade at 7 days after rainfall

Figure 6.13 Measured and predicted permanent deformations of the wicking geotextile-improved section with the back-calculated hydraulic improvement factor (continued)

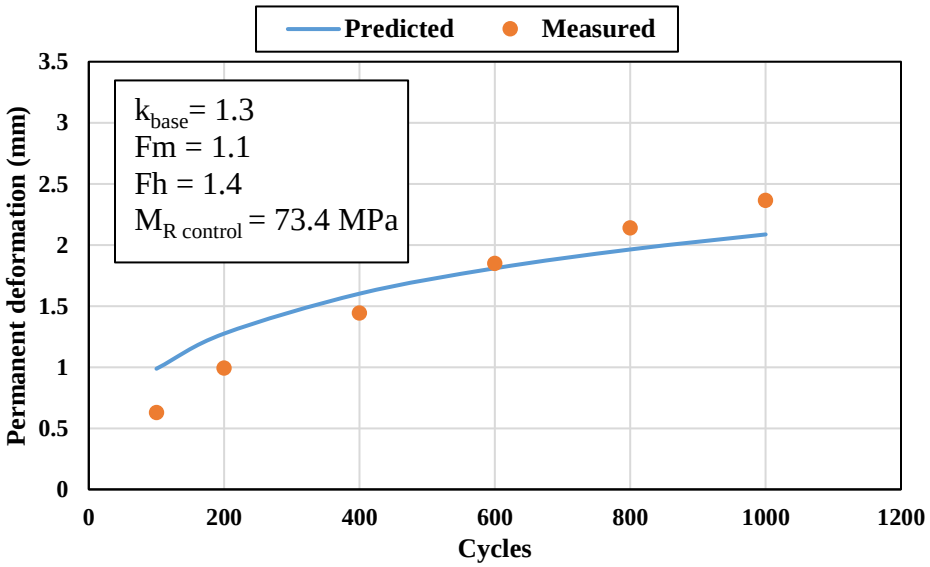

(e) 5% CBR subgrade at 2 days after rainfall

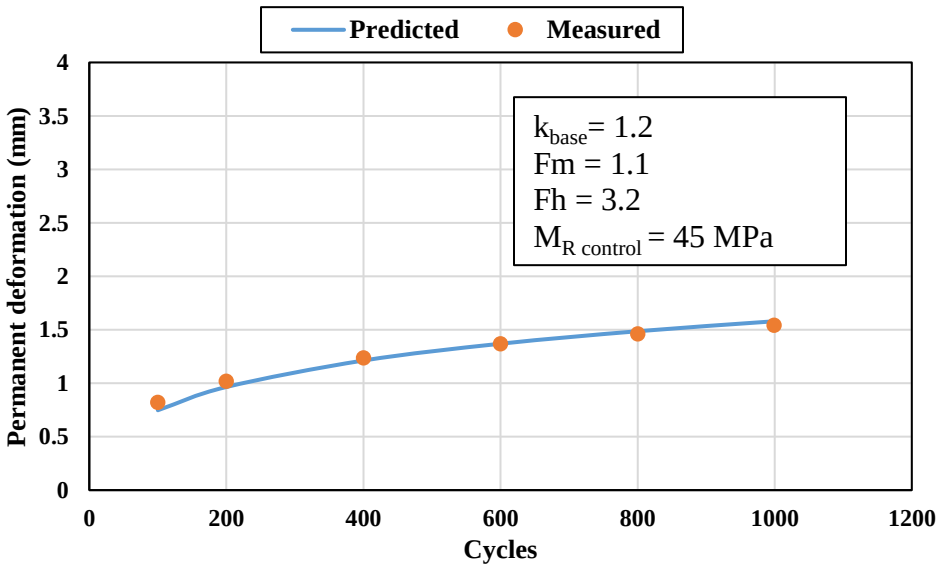

(f) 5% CBR subgrade at 2 hours after rainfall

Figure 6.13 Measured and predicted permanent deformations of the wicking geotextile-improved section with the back-calculated hydraulic improvement factor (continued)

Table 6.4 summarizes the resilient modulus of the base course with no geotextile used in the soil damage model, the calibration factor for the base course, and the improvement factors. When the mechanical improvement factor was assumed the same for all the tests on the same subgrade, the hydraulic improvement factor could be calculated. It is clear that the hydraulic improvement factor of 3.2 for the wicking geotextile on the 5% CBR subgrade at 2 hours after rainfall is not reasonable because no or limited drainage happened within such a time period. To be reasonable and consistent, the hydraulic improvement factor for the wicking geotextile on the 5% CBR subgrade at 2 hours after rainfall is assumed to be 1.0. The corrected hydraulic improvement factor is reported inside the parenthesis.

Table 6.4 Summary of improvement factors

Subgrade		**k**	**M_R (MPa)**	**F_m**	**F_h**	**$F_m \times F_h$**
3% CBR	7 days	9.3	91.7	1.2	4	4.8
	2 days	3.4	77.4	1.2*	2	2.4
	2 hours	2.1	45	1.2*	1.3	1.6
5% CBR	7 days	3.7	83.6	1.1	3	3.3
	2 days	1.3	73.4	1.1*	1.4	1.5

2 hours	1.2	45	1.1*	3.2 (1.0**)	3.5 (1.1**)

* assumed the same as that for 2 days and 2 hours; ** assumed no hydraulic improvement benefit

Based on the analysis of the measured permanent deformations and the resilient moduli of the base course and the subgrade, the overall improvement factor F_w of the wicking geotextile can be defined as the product of the mechanical improvement factor and the hydraulic improvement factor:

$$F_w = F_m \times F_h \tag{6.23}$$

where the mechanical improvement factor (F_m) ranged from 1.1 to 1.2 and the hydraulic improvement factor (F_h) ranged from 4 to 1.3.

The overall improvement factors can be plotted against the time for the wicking geotextile on both subgrades as shown in Figure 6.14, which shows that the over improvement factors increase with the time and decrease with the stiffness of the subgrade.

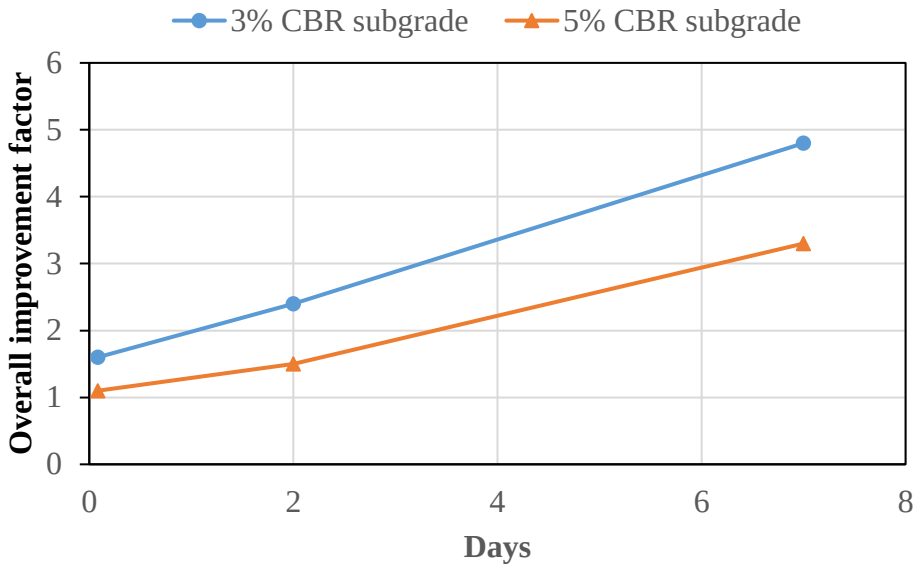

Figure 6.14. Overall improvement factor versus time for the wicking geotextile-improved base course

6.4 Summary

To promote the use of wicking geotextile for roadway applications, design guidelines were proposed in this study by modifying the 1993 AASHTO Pavement Design Guide and the Mechanistic-Empirical Pavement Design Guide. Below is the summary of developing these two modified design methods:

(1) The wicking geotextile increases the resilient modulus of the base course by mechanical stabilization (lateral confinement) and hydraulic stabilization (reduction of water content).

(2) Hydraulic improvement factor (F_h) was proposed to consider the effect of the wicking geotextile in the water content reduction for the 1993 AASHTO Pavement Design Guide. This

factor was developed based on the water content difference between the conventional geotextile-improved base course and the wicking geotextile-improved base course. The effect of the water content on the resilient modulus of the AB-3 aggregate was determined by resilient modulus tests.

(3) To modify the 1993 AASHTO Pavement Design Guide, the relative damage concept was adopted to consider the effect of water content on the resilient modulus of the base course. Based on the relative damage concept, the equivalent resilient modulus improvement factor (F_{heq}) was proposed. The equivalent resilient modulus improvement factor enables the calculation of the equivalent resilient modulus of the base course between major rainfall events. Based on the precipitation data with the equivalent resilient modulus improvement factor (F_{heq}), the equivalent annual resilient modulus of the base course with the wicking geotextile can be calculated so that the layer coefficient ratio is estimated, which can be used for design.

(4) To modify the Mechanistic-Empirical Pavement Design Guide, the mechanical improvement factor (F_m) was calculated with the soil damage model based on the permanent deformations measured in the cyclic loading tests for the control and conventional geotextile-improved sections. The hydraulic improvement factor (F_h) was calculated based on the increased resilient modulus of the base course due to the reduction of water content by the wicking geotextile before cyclic loading. The use of the hydraulic improvement factor by this method over-predicted the permanent deformations as compared with those measured in the cyclic loading tests. The hydraulic improvement factor (F_h) was also back-calculated by matching the predicted permanent deformations from the soil damage model to the measured ones in the cyclic loading tests considering the mechanical improvement factor (F_m). Both the mechanical improvement factor (F_m) and the hydraulic improvement factor (F_h) can be used to adjust the resilient modulus of the

base course considering the effect of the wicking geotextile and predict the permanent deformation of the wicking geotextile-improved base course using the soil damage model.

CHAPTER 7 Conclusions and Recommendations

7.1 Conclusions

To evaluate the performance of wicking geotextile in roadway applications, different types of experimental tests were conducted in this study. Vertical wicking tests were conducted on the wicking geotextile specimens of different widths. The height of water rise in the wicking geotextile was measured. Evaporation tests and horizontal wicking tests were conducted in a temperature and relative humidity-controlled room. The evaporation rates from the wicking geotextile under different temperature and relative humidity were measured. The horizontal wicking distance was determined based on the water content in the geotextile. Rainfall simulations tests were conducted on conventional and wicking geotextile improved-base courses over subgrade in a small box with a dimension of 0.6 m × 0.69 m × 0.53 m (W×L×H), in which the water contents of base course and subgrade were monitored. Soil columns tests were conducted to evaluate water reduction in soil by the wicking geotextile in the temperature and relative humidity controlled room. The soil column had a dimension 0.25 m × 0.25 m × 0.3 m (W×L×H), which was filled with aggregate above conventional and wicking geotextiles. The water contents at different depths were monitored. Large-scale cyclic plate loading tests with rainfall simulation were conducted on control, conventional geotextile-improved, and wicking geotextile-improved base courses over 3% and 5% CBR subgrade in the large geotechnical box of 2 m × 2.2 m × 2 m (W×L×H). The water content of the base course was monitored after each rainfall. The permanent deformations of the test sections under cyclic loading were measured.

The water content reduction over time was compared between the conventional geotextile-improved and wicking geotextile-improved base course. Based on the water content difference, the benefit of the wicking geotextile was quantified in terms of the increase in the resilient modulus of the base course. To incorporate the benefit of the wicking geotextile in 1993 AASHTO Pavement Design Guide and the Mechanistic-Empirical Pavement Design Guide, three improvement factors were proposed: (1) hydraulic improvement factor (F_h), (2) resilient modulus improvement factor ($F_{h\,eq}$), and (3) mechanical improvement factor (F_m).

From this study, the following conclusions can be made:

(1) Due to the micro-channels of the wicking yarns, capillary force develops when it is in contact with water. Water movement within the wicking geotextile is under the action of both gravity and capillary force. When the capillary force is opposite to the gravity, the wicking geotextile could transport water against gravity.

(2) When the soil in contact with the wicking geotextile is fully saturated, gravitational drainage can happen. When the soil is unsaturated, the wicking geotextile can remove water from the soil by capillary force and via evaporation. The wicking yarns suck water into the geotextile to create a wetted area and the water on the wetted area evaporates into the air due to the difference in relative humidity between the geotextile surface and the air. This process continues with time at a certain water removal rate until the suction in the soil is equal to that generated by the geotextile.

(3) Test results showed that the rate of water evaporation from the geotextile surface increased with an increase of temperature and a decrease of relative humidity. The mass transfer-based methods could be used to estimate the evaporation rate from the wicking geotextile. Based

on the mass-transfer methods, the equivalent water evaporation length of a wicking geotextile sample was constant for the tested wicking geotextile and equal to 0.4 m.

(4) The conventional woven geotextile was effective in removing excess water from the aggregate base (AB-3). However, the conventional woven geotextile could not remove water from the AB-3 aggregate when the water content was close to its optimum water content. The wicking geotextile was able to continue reducing the water content of the AB-3 to a lower water content.

(5) The wicking geotextile had little effect on the water content of the compacted subgrade material below the geotextile. To remove the water from the subgrade, the wicking geotextile must generate enough suction to overcome the suction of the subgrade and the gravity. Due to small particle sizes of the subgrade, the suction of the subgrade could be too large for the wicking geotextile to remove water.

(6) Based on the soil column tests and the large box tests, the effective wicking zone of the wicking geotextile was approximately 200 to 300 mm above the geotextile. The water content decreased faster in the effective wicking zone in a wicking geotextile-improved base than a conventional geotextile-improved base.

(7) When compared to a conventional woven geotextile, the wicking geotextile was more effective in reducing the water content in the AB-3 aggregate as more time was allowed.

(8) The wicking geotextile significantly reduced the permanent deformation of the test section under cyclic loading. The reduction in the permanent deformation was more noticeable in the loading test at seven days after the first rainfall simulation.

(9) The wicking geotextile-improved test sections had the lowest measured maximum vertical stresses at the interface of base course and subgrade under cyclic loading, which indicates higher moduli of the base courses.

7.2 Design Guidelines

To promote the use of wicking geotextile for roadway applications, design guidelines following the 1993 AASHTO Pavement Design Guide and the Mechanistic-Empirical Pavement Design Guide were proposed in this study. Below are the summary of these design methods:

(1) The wicking geotextile increases the resilient modulus of the base course by mechanical stabilization and reduction of water content.

(2) A hydraulic improvement factor (F_h) was proposed to consider the effect of the wicking geotextile in water content reduction. The factor was developed based on the water content difference between the conventional geotextile-improved and wicking geotextile-improved base courses. The effect of water content on the resilient modulus of the AB-3 aggregate was determined by resilient modulus tests.

(3) To follow the 1993 AASHTO Pavement Design Guide, the relative damage concept was adopted to consider the effect of water content on the resilient modulus of the base course. Based on the relative damage concept, the equivalent resilient modulus of the base course based on the water content change after every rainfall could be calculated. The equivalent resilient modulus could be used to calculate the resilient modulus improvement factor (W). The equivalent resilient modulus improvement factor enables the calculation of equivalent resilient modulus

between major rainfall events. By analyzing precipitation data with the equivalent resilient modulus improvement factor ($F_{h\ eq}$), the equivalent resilient modulus of each month can be calculated and used for M-E pavement design guide.

(4) To follow the Mechanistic-Empirical Pavement Design Guide, the mechanical improvement factor (F_m) was calculated with the soil damage model based on the permanent deformations measured in cyclic loading tests for the control and conventional geotextile-improved sections. The hydraulic improvement factor (F_h) was calculated based on the resilient moduli of the base course at the water contents before cyclic loading when the conventional geotextile and the wicking geotextile were used. The mechanical improvement factor (F_m) and the hydraulic improvement factor (F_h) can be used to adjust the resilient modulus of the base course and predict the permanent deformation of the base course with the soil damage model.

7.3 Recommendation for future study

(1) The durations of most experimental tests in this study ranged from one week to one month, which are relatively short as compared to actual practice. The effect of the wicking geotextile on the reduction of the water content in the base course over a longer period should be considered. This extension can be achieved by increasing the test duration or conducting a numerical analysis with a longer duration.

(2) Only one type of subgrade and one type of base course material were used in this study. Since the wicking geotextile removes water from soil by suction, soils with different particle size distributions may have different soil-water characteristic curves, which will influence the

effectiveness of the wicking geotextile in removing water. Different types of subgrade and base course should be investigated in the future.

(3) The equivalent resilient modulus improvement factor for the 1993 AASHTO pavement design guide was based on the rainfall intensity that saturated the base course. The low rainfall intensity was not considered in the analysis. The relationship between the water content change after rainfall and with time should be established to account for rainfall with high intensity.

(4) The soil damage model in the Mechanistic-Empirical Pavement Design Guide with the proposed improvement factors over-predicted the permanent deformations of the wicking geotextile-improved test sections. Additional tests and analyses re needed to further improve this method.

References

American Association of State Highway and Transportation Officials (AASHTO) (1993). *AASHTO Guide for Design of Pavement Structures*, Vol. 1.

Aryes, M. Jr. (2002). "*Unbound material rut model modification. Development of the 2002 guide for the design of new and rehabilitated pavement structures*". NCHRP 1-37A. Inter term technical report, 2002.

Azevedo, M., & Zornberg, J. G. (2013). "Capillary barrier dissipation by new wicking geotextile." In *Pan-American Conference on Unsaturated Soils*, 20-22.

Barksdale, R. D. and Itani, S. Y. (1989). ''Influence of aggregate shape on base behaviour.'' *Transp. Res. Rec. 1227*, Transportation Research Board, Washington, D.C., 173–182.

Bathurst, R. J., Ho, A. F., & Siemens, G. (2007). "A Column Apparatus for Investigation of 1-D Unsaturated-Saturated Response of Sand-Geotextile Systems." *ASTM Geotechnical Testing Journal*, *30*(6), 433-441.

Bouazza, A., Zornberg, J. G., McCartney, J. S., & Nahlawi, H. (2006). "Significance of unsaturated behaviour of geotextiles in earthen structures." *Australian Geomechanics*, 41(3), 133-142.

Dalton, J. (1802). "Experimental essays on the constitution of mixed gases: on the force of steam or vapour from water or other liquids indifferent temperature, both in a Torricelli vacuum and in air; on evaporation; and on expansion of gases by heat". *Manchester Lit. Phil. Soc. Mem. Proc.*, 5, 536-602

Dawson, A. R., Thom, N. H., and Paute, J. L. (1996). ‘‘Mechanical characteristics of unbound granular materials as a function of condition.’’ *Flexible Pavements, Proc., Eur. Symp. Euroflex 1996*, Balkema, Rotterdam, Netherlands, 35–44.

F.I.T. (2011). Q-Wick and 4DG Fibers. Retrieved from Fiber Innovation Technology, Inc.: http://www.fitfibers.com/4DG_Fibers.htm

Federal Highway Administration (1992). *Demonstration Project 87: Drainage Pavement Systems, Participant Notebook*, Federal Highway Administration, Publication No. FHWA-SA-929008, Washington, DC.

Garcia, E. F., Gallage, C. P. K., & Uchimura, T. (2007). “Function of permeable geosynthetics in unsaturated embankments subjected to rainfall infiltration.” *Geosynthetics International*, *14*(2), 89-99.

Guo, J., Wang, F., Zhang, X., & Han, J. (2016). “Quantifying Water Removal Rate of a Wicking Geotextile under Controlled Temperature and Relative Humidity.” *Journal of Materials in Civil Engineering*, *29*(1), 04016181.

Han, J. and Shiwakoti, H. (2016). “Wheel tracking methods to evaluate moisture sensitivity of hot-mix asphalt mixtures.” *Frontiers of Architecture and Civil Engineering in China*, DOI: 10.1007/s11709-016-0318-1.

Han, J. (2015). *Principles and Practice of Ground Improvement*. John Wiley & Sons.

Haynes, J. G., and Yoder, E. J. (1963). ‘‘Effects of repeated loading on gravel and crushed stone base course materials used in the AASHTO Road Test.’’ *Hwy. Res. Rec. 39*.

Henry, K.S., (1990). “Geotextiles as capillary barriers.” *Geotechnical Fabrics Report* 8 (2), 30–36.

Hicks, R. G., and Monismith, C. L. (1971). ‘‘Factors influencing the resilient properties of granular materials.’’ *Hwy. Res. Rec. 345*, 15–31.

Ho, A. F., (2000). *Experimental and Numerical Investigation of Infiltration Ponding in One-dimensional Sand-Geotextile Columns*, MSc thesis, Queen's University, Kingston, Ontario, 212pp.

Holtz, R. D., Christopher, B.R. and Ryan R. B. (1997). *Geosynthetic Engineering*. BiTech Publishers, Richmond, British Columbia, Canada.

Huang, Y. H. (1993). *Pavement Analysis and Design*. Pearson Prentice-Hall, Upper Saddle River, NJ

Iryo, T. and Rowe, R. K. (2004). "Numerical study of infiltration into a soil–geotextile column." *Geosynthetics International,* 11(5), 377-389.

Iryo, T. and Rowe, R. K. (2005). "Hydraulic behaviour of soil–geocomposite layers in slopes." *Geosynthetics International,* 12(3), 145-155.

Koerner, R. M. (2012). *Designing with Geosynthetics* (Vol. 1). Xlibris Corporation.

Lee, S. and Bourdeau, P.L. (2006). "Filter performance and design for highway drains." *Joint Transportation Research Program*: 266p.

Lekarp, F., Isacsson, U., & Dawson, A. (2000a). "State of the art. I: Resilient response of unbound aggregates." *Journal of Transportation Engineering*, 126(1), 66-75.

Lekarp, F., Isacsson, U., & Dawson, A. (2000b). "State of the art. II: Permanent strain response of unbound aggregates." *Journal of Transportation Engineering*, 126(1), 76-83.

Lin, C., Zhang, X., and Han, J., (2016). Development of Design Method for H_2Ri Wicking Fabric in Pavement Structures. Internal report, submitted to Tencate.

Linacre, E. T. (1977). "A simple formula for estimating evaporation rates in various climates, using temperature data alone." *Agricultural Meteorology*, 18(6), 409-424.

National Oceanic and Atmospheric Administration (https://www.ncdc.noaa.gov) accessed: 07/06/2017

National Cooperative Highway Research Program (NCHRP) (2004). *Guide for Mechanistic-Empirical Design of New and Rehabilitated Pavement Structures*."

Parish, O.O. and Putnam, T.W. (1997). "Equations for the determination of humidity from dewpoint and psychrometric data". *NASA Technical Note D-8401*, Washington, D.C., 25p.

Penman, H. L. (1948). "Natural evaporation from open water, bare soil and grass". *In Proceedings of the Royal Society of London A: Mathematical, Physical and Engineering Sciences*, Vol. 193, No. 1032, pp. 120-145.

Qian, Y., Han, J., Pokharel, S.K., and Parsons, R.L. (2013). "Performance of triangular aperture geogrid-reinforced base courses over weak subgrade under cyclic loading." ASCE *Journal of Materials in Civil Engineering*, 25(8), 1013-1021.

Seeds, S. B., and Hicks, R. G. (1991). "Development of drainage coefficients for the 1986 AASHTO guide for design of pavement structures." *Transportation Research Record 1307.*

Singh, V.P., and Xu, C.Y. (1997). "Evaluation and generalization of 13 mass-transfer equations for determining free water evaporation." *Hydrological Process*, 11, 311-323.

Stormont, J. C., Henry, K.S. and Evans, T. M. (1997). "Water retention functions of four nonwoven polypropylene geotextiles." *Geosynthetics International*, 4(6), 661-672.

Sun, X., Han, J., Crippen, L., & Corey, R. (2016). "Back-calculation of resilient modulus and prediction of permanent deformation for fine-grained subgrade under cyclic loading." ASCE *Journal of Materials in Civil Engineering*, 29(5), 04016284.

TenCate Geosynthetics (2013). "Case study at St. Louis County, MO." http://www.tencate.com/amer/Images/cs.stlouis_tcm29-32417.pdf (accessed on 06/20/2017)

Thom, N. H., and Brown, S. F. (1987). ''Effect of moisture on the structural performance of a crushed-limestone road base.'' *Transp. Res. Rec*. 1121, Transportation Research Board, Washington D.C., 50–56.

Tingle, J., & Jersey, S. (2005). "Cyclic plate load testing of geosynthetic-reinforced unbound aggregate roads". *Transportation Research Record: Journal of the Transportation Research Board 1936*, Transportation Research Board, Washington D.C., 60-69.

Xu, C. Y., and Singh, V. P. (2001). "Evaluation and generalization of temperature‐based methods for calculating evaporation". *Hydrological processes*, 15(2), 305-319.

Yoder, E. J. and Witczak, M. W. (1975). *Principles of Pavement Design*, Wiley, New York

Zhang, X., & Connor, B. (2013). *Evaluate H2Ri Wicking Fabric for Pavement Application – Year 2*. 2013-S-UAF-0026.

Zhang, X., Presler, W., Li, L., Jones, D., and Odgers, B. (2014). "Use of wicking fabric to help prevent frost boils in Alaskan pavements." ASCE *Journal of Materials in Civil Engineering*, 26(4), 728-740.